

Atomistic study of magnetite thin film interfaces and defects for Spintronic applications

Daniel Gilks

PhD

University of York

Physics

June 2015

Abstract

Fe_3O_4 is a candidate material for future spintronic device applications due to its predicted half metallicity, high Curie temperature and lattice match with current oxide barrier materials. There have been numerous studies on $\text{Fe}_3\text{O}_4(001)/\text{MgO}(001)$ heterostructures and devices in recent years which show structural defect formation has a significant influence on the properties of the grown layers and device performance. In this work I seek to advance our understanding of defect formation and heterostructure interfaces of epitaxially grown Fe_3O_4 layers on a range of substrates. Atomically resolved (S)TEM/EELS has been used as a main experimental techniques to determine the atomic structure of the defects and interfaces in order to model their effect of the functional properties of the thin films magnetite.

Firstly we investigate the MBE growth of (111) oriented $\text{Fe}_3\text{O}_4/\text{MgO}$ thin films. This creates highly ordered, atomically sharp APB defect boundaries rather than the random-like fractal geometry defects which have previously been observed in (001) oriented growth. This has enabled us to undertake atomistic modelling and begin to understand the APBs effect on the magnetic properties of grown films. We show that all APB defects exhibit a high density of high angle Fe-O-Fe bonds with antiferromagnetic coupling.

The $\text{Fe}_3\text{O}_4/\text{MgO}$ structure produces a high density of APB defects, and consequently anomalous properties of the grown films such as negative magnetoresistance and high saturating magnetic fields. In order to avoid crystal symmetry as an origin of APBs we undertook a MBE growth of $\text{Fe}_3\text{O}_4/\text{MgAl}_2\text{O}_4$ a spinel-spinel growth system. However, the presence of the APBs was still observed and their formation was discussed in terms of strain and 3D film growth.

To reduce the density of defects in Fe_3O_4 we employed pulsed laser deposition with subsequent film annealing in a CO/CO_2 atmosphere. This is shown to produce films with bulk like transport properties after a high temperature annealing process. Residual defects including twins were observed. These defects have a low density and the effect on overall film properties is small.

Finally, using the spinel/perovskite model structure of $\text{Fe}_3\text{O}_4/\text{SrTiO}_3$ we show the ability to produce atomically sharp oxide/oxide interfaces which open up the possibility of performing atomic level engineering to tailor potential oxide-oxide device functionality.

Contents

<i>Abstract</i>	2
<i>Contents</i>	3
<i>List of Figures</i>	6
<i>Acknowledgements</i>	15
<i>Declaration</i>	17
Chapter 1. Introduction	18
1.1 Thin film magnetite (Fe_3O_4)	19
1.2 Motivation of this thesis	20
1.3 Overview of Thesis	21
Chapter 2. Theoretical Considerations	24
2.1 The Iron Oxides	25
2.2 Crystal structure of Fe_3O_4	26
2.2.1 Cubic, (001) oriented geometry and atomic structure of Fe_3O_4	28
2.2.2 (111) oriented geometry and atomic structure of Fe_3O_4	30
2.3 Electronic configuration and Hund's rules	34
2.4 Conductivity in room temperature Fe_3O_4	35
2.5 Verwey Transition	36
2.6 Super-exchange interactions (SEI) in metal oxide systems	37
2.7 Antiphase domain boundary (APB)	39
2.8 Polar structures and interfaces	41
2.9 Spintronics	42
2.9.1 Discovery of Electron Spin	43
2.9.2 Giant Magnetoresistance and Tunnelling Magnetoresistance	43
2.10 Magnetite for Spintronic Applications	45
Chapter 3. Methodology	46
3.1 Vacuum Physics and Ultra high vacuum	48
3.1.1 Ultra high vacuum	48
3.2 Thin Film Fabrication	50
3.2.1 Molecular beam epitaxy	50
3.2.2 Pulsed Laser Deposition (PLD)	52

3.2.3 <i>In-situ deposition characterisation</i>	52
3.3 Transmission electron microscopy	54
3.3.1 <i>Electron optics</i>	56
3.3.2 <i>Electron velocity, wavelength and relativistic corrections</i>	60
3.3.3 <i>Electrons interacting with matter</i>	62
3.3.4 <i>High resolution transmission electron microscopy (HRTEM)</i>	63
3.3.5 <i>Selected area diffraction (SAD)</i>	64
3.3.6 <i>Bright Field and Dark field TEM</i>	65
3.3.7 <i>Scanning transmission electron microscopy (STEM)</i>	67
3.3.8 <i>Aberrations</i>	72
3.3.9 <i>Aberration Correction</i>	74
3.3.10 <i>Electron energy loss spectroscopy (EELS)</i>	76
3.3.11 <i>Specimen Preparation</i>	79
3.4 Area Integrated Characterisation Techniques.....	88
3.4.1 <i>Vibrating sample magnetometer and hysteresis curves</i>	88
3.4.2 <i>Magnetoresistance (MR)</i>	89
3.4.3 <i>Raman Spectroscopy</i>	90
3.5 Atomistic magnetic simulations with <i>VAMPIRE</i>	90
3.6 Image Analysis.....	92
3.7 Crystallographic structure models	93
3.8 Image Simulations (HRTEM).....	94
3.8.1 <i>QSTEM image simulations (HAADF-STEM)</i>	97
3.9 Density Functional Theory	98
3.9.1 <i>Determining relaxed structures and lattice vectors</i>	99
3.9.2 <i>Band structures</i>	100
3.9.3 <i>Challenges</i>	100
3.9.4 <i>Implementation using the Vienna code</i>	101
Chapter 4. Fe₃O₄/MgO(111)	102
4.1 Methods	103
4.2 Results	104
4.3 Structural Analysis	105
4.3.1 <i>In-plane rotations</i>	106
4.3.2 <i>Shift Vectors (in-plane)</i>	107
4.3.3 <i>Shift Vectors (out-of-plane)</i>	109
4.3.4 <i>APB Boundary Geometry</i>	110
4.3.5 <i>Non-bulk bonding at the APB</i>	111

4.4 Image simulations	113
4.5 Vampire at Observed Defects	116
4.6 Conclusions.....	120
Chapter 5. Fe₃O₄/MgAl₂O₄(111) symmetry matched spinel's.....	121
5.1 Introduction	121
5.2 Methods	122
5.3 Results	123
5.4 Discussion.....	131
5.5 Conclusion	133
Chapter 6. Fe₃O₄/Y-ZrO₂(111) deposited by PLD methods.....	135
6.1 Methods	136
6.2 Results	137
6.2.1 Rectifying film growth with annealing.....	137
6.2.2 Fe ₃ O ₄ /YSZ interface.....	141
6.2.3 Twin defect structures in Fe ₃ O ₄ /YSZ on the (111) plane.....	144
6.3 Conclusions.....	150
Chapter 7. Fe₃O₄/STO(111) interface structure.....	151
7.1 Introduction	151
7.2 Methods	153
7.3 Results	155
7.3.1 Film deposition quality and epitaxy.....	155
7.3.2 Determining the Fe ₃ O ₄ /SrTiO ₃ interface.....	158
7.4 Conclusions.....	164
Chapter 8. Conclusions and Future Work.....	166
8.1 Future Work	167
<i>Appendix A: List of Publications</i>	<i>168</i>
<i>Appendix B: List of Presentations.....</i>	<i>171</i>
<i>Symbols.....</i>	<i>174</i>
<i>Abbreviations.....</i>	<i>176</i>
<i>References.....</i>	<i>178</i>

List of Figures

- Figure 1: Natural magnetite crystal displayed at the Natural History Museum, London18
- Figure 2: Cubic unit cell of Fe_3O_4 . This cell is composed of 56 atoms representing 8 Fe_3O_4 chemical units. Fe_B is represented by red spheres, Fe_A by yellow, and O by blue.28
- Figure 3: Plane by plane atomic structure of Fe_3O_4 in cubic $\langle 001 \rangle$ geometry as shown in Figure 2. Each diagram (a-d) includes three atomic planes in the z direction with each atomic plane separated by $1/8 a_0$, i.e. each diagram contains ... $\text{Fe}_A/\text{O}-\text{Fe}_B/\text{Fe}_A$... with the Fe_A structure repeated into the proceeding layer. The lowest layer in each diagram is represented with small open circles, the middle layer with filled circles and the highest layer with large filled circles. Fe_A is represented with yellow, Fe_B with red and O with blue.29
- Figure 4: FCC stacking sequence and site positions of Fe_3O_4 along the $[111]$ direction.....31
- Figure 5: Plane by plane atomic structure of Fe_3O_4 along the $[111]$ direction. Along the $[111]$ direction the atomic structure of Fe_3O_4 is defined by 12 equally spaced atomic planes. a) contains the first three planes where $0 \leq z < 3/12a_0[111]$ b) the 4th-6th atomic planes from $3/12a_0[111] \leq z < 6/12a_0[111]$ c) the 7th-9th atomic planes from $6/12a_0[111] \leq z < 9/12a_0[111]$ and d) the 10th-12th atomic planes from $9/12a_0[111] \leq z < a_0[111]$. As in previous diagrams, Fe_B is indicated in red, Fe_A in yellow and O in blue.....32
- Figure 6: Structure of Fe_3O_4 projected into 2D slices as would be imaged by a correctly oriented TEM sample. a) $[11-2]$ zone axis of (111) growth direction Fe_3O_4 . b) $[1-10]$ zone axis of (111) growth direction Fe_3O_4 . c) $[100]$ zone axis of (001) growth direction Fe_3O_434
- Figure 7: Diagram of an APB with reference to structure shown in Figure 3. a) Shows the undisturbed structure of a plane of Fe_3O_4 in the $[001]$ direction, within this configuration only 90° bonds can be found between $\text{Fe}_B-\text{O}-\text{Fe}_B$ indicated in black. b) Shows the same structure with an APB defect created by shifting the right hand side of the structure by $1/2 a_0[100]$. This crystallographic shift is shown with the green arrow and the crystal grain boundary is shown with a green dashed line. This defect returns O sites

to their normal position but gives rise to 180° $\text{Fe}_B\text{-O-Fe}_B$ bonding which generates an antiferromagnetic coupling.....40

Figure 8: Schematic representation of TMR/GMR with half-metallic electrodes showing conduction in the aligned case in (a) and blocked conduction in the anti-aligned case in (b).....45

Figure 9: Schematic diagram of an electron lens around the microscope optical axis. A series of coiled wires are. Soft iron pole pieces sit inside the the hole at the centre of the lens and are surrounded by Cu coils used to pass the lens current. (a) shows the overall schematic of the lens (b) shows the pole piece and the magnetic field lines within the gap [106].58

Figure 10: Optical Lens ray diagrams showing the a) the focal length of a lens f with an incident parallel beam and (b) the formation of a focused image.59

Figure 11: electron wavelength (red-dashed) as a function of accelerating voltage including relativistic correction (black). At typical TEM accelerating voltages of 200 keV electrons are traveling at 69.5% of c making relativistic correction essential and at this voltage amount to $\sim 10\%$ variation between corrected and uncorrected values. Relativistic mass of the electron is shown in (green) and v/c is shown in blue.61

Figure 12: Schematic diagram of the signals generated as an electron beam interacts with specimen material [106].62

Figure 13: Schematic lens diagram for HRTEM operation. Only minor changes in apertures and lens focus values are required to transfer between HRTEM, DF-TEM, BF-TEM and SAD.64

Figure 14: Objective aperture alignments for a) HRTEM b) BF-TEM and c) DF-TEM.....66

Figure 15: Schematic lens diagram for STEM operation. By converging the beam to a point on the sample surface using the Condenser and Objective lenses a sub-angstrom electron probe is formed to analyse tiny regions of the specimen. The resultant signals can be detected with a number of chemical and imaging modes. Scanning coils and the corrector are omitted from this diagram.69

Figure 16: Ray diagrams of a) Perfect lens b) Spherical Aberration and c) Chromatic aberration.73

Figure 17: Post column filter diagram showing the direct, on axis beam being focused and dispersed through a 90° angle using a magnetic field to act as a magnetic prism.....77

Figure 18: in column filter inserted between the two intermediate lenses of a TEM microscope. Four magnetic prisms disperse and then recombine the electron beam

allowing the energy filtered signal to be passed back into the TEM imaging system after filtering or spectra to be collected within the filter.78

Figure 19: Sample geometry taken from Shinkosha Ltd website. In-plane geometry determined from the two notched corners. Blue dashed lines show pattern of cutting required to produce cross sectional specimens in both the [11-2] and [1-10] zone axes. .81

Figure 20: Gluing and cutting sample cross sections from the substrate material. a) Glue the two corresponding substrate pieces together film side to film side to form a sandwich (b). This is cut into ~1mm slices to provide initial, unpolished, cross sections. .82

Figure 21: Preparing cross sections for polishing. Optical Images a) Si padding pieces are glued to the outside of the sample cross section to form the 'H' shaped sample (b) such that the three glue lines in the sample are parallel to one another. After curing the G1 epoxy this sample is glued flat to a clean glass slide (c) for polishing with the glass slide acting as a mechanical support and a tripod for the polishing process (d).83

Figure 22: Optical reflection microscopy images of sample surface after different grade of polishing. a) directly after cutting with diamond saw blade (b) 15 μm lapping pad (c) 6 μm lapping pad (d) 3 μm lapping pad (e) 1 μm lapping pad.....84

Figure 23: Gluing the TEM grid and turning over the sample cross section. (a) The TEM grid is coated in un-cured G1 epoxy and carefully attached to the sample surface (b). c) The glass slide is then placed on the heater to cure the G1 epoxy and melt the crystal bond glue. After approximately 5 mins the sample can be lifted (d), turned (e) and re-glued to the glass slide with the TEM grid glued in place.85

Figure 24: Cross sectional TEM specimen mounted on 3 mm Cu slot grid with 2 x 1 mm aperture. Specimen imaged using transmission optical microscope. Cu grid is opaque and images as dark contrast. The two Si padding pieces have achieved some optical transparency at sub 100 μm thicknesses.86

Figure 25: Ar ion milled sample. The widened glue line can be seen in (a), (b) and (c) with the hole formed in the glue and the optical fringing in the glue line visible in (d). To find these fringes requires the higher magnifications possible on a standard laboratory microscope.87

Figure 26: Considering the electron wave passing through a real and computational sample. a) in a real microscope a beam is formed giving ψ_i which interacts with the TEM specimen to produce an exit wave function ψ_f containing the various interactions discussed above. This is lensed to give diffraction patterns and imaging. b) the computation sample is reduce to multiple layers which convolve with the initial wavefunction and propagation operators to give a sample exit wave. The transfer of the wave throughout the microscope and the formation of the initial wavefunction are

determined by the contrast transfer function of the microscope. c) The iterative plane by plane convolution of wavefunction, propagation and phase grating96

Figure 27: SAD pattern from $\text{Fe}_3\text{O}_4/\text{MgO}(111)$ interface in the a) $[11-2]$ viewing direction, b) $[1-10]$ viewing direction. The relative scale of the lattice constant of Fe_3O_4 (double sized with respect to MgO) is identified here with inverted scale, i.e. g-vectors to Fe_3O_4 reflections are half that of the MgO structure. This is identified by the yellow (Fe_3O_4) and white (MgO) reciprocal lattice vector constructs. [SAD patterns supplied by Dr. Vlado Lazarov]..... 104

Figure 28: Plan view imaging of $\text{Fe}_3\text{O}_4/\text{MgO}(111)$ film (along the $[111]$ viewing direction) a) DF-TEM image generated using a $[4-40]$ type reflection from the Fe_3O_4 diffraction pattern b) HRTEM image of APB defect in the same geometry. Scale bar equal to 2 nm. [Imaging supplied by Dr. Vlado Lazarov] 105

Figure 29: a) Description of all possible in-plane shift vectors of $\text{Fe}_3\text{O}_4(111)$ constructed by shifting the central O site '4' onto non-equivalent O-sites '1-3' in the near vicinity of the rhombohedral unit cell of Fe_3O_4 . b) The reduced set of shifts which can be used to represent all unique APB boundaries determined from atomic structure models. 108

Figure 30: Surface unit cells of Fe_3O_4 in the $[111]$ direction. Possible APB boundaries are highlighted with blue dotted lines and the effect of the APB shifts on the crystal structure are indicated with arrows and accompanying shift vectors..... 109

Figure 31: Cross sectional structure diagrams of out of plane ($\frac{1}{2}a_0[111]$ shift) APB boundaries in a) the $[11-2]$ viewing direction and b) the $[1-10]$ viewing direction..... 110

Figure 32: Geometrical models of $\frac{1}{4}a_0[10-1]$ shifted APB boundaries in both the $[11-2]$ (a and b) and $[1-10]$ (c and d) viewing direction. 111

Figure 33: HRTEM image simulations from the six possible in-plane APB defect geometries, shift vectors are marked with yellow arrows. (a,c,e) show defects sitting on a $(11-2)$ plane, propagating in a $[1-10]$ direction. (b,d,f) show defects sitting on a $(1-10)$ plane, propagating in a $[11-2]$ direction. (a,b,c,d) show a $\frac{1}{4}a_0[01-1]$ shift with the two possible interface variants shown. (e,f) show the $\frac{1}{4}a_0[1-10]$ shift which only incorporates one possible interface for each defect orientation. (f) is reproduced in Figure 35c and is clearly the only defect from this set which can represent the experimental HRTEM result purely from the geometrical positioning on high intensity sites in this figure..... 114

Figure 34: HRTEM image simulations from the eight possible out-of-plane APB defect geometries, shift vectors are marked with yellow arrows. (a,c,e,f) show defects sitting on a $(11-2)$ plane, propagating in a $[1-10]$ direction. (b,d,f,h) show defects sitting on a $(1-10)$ plane, propagating in a $[11-2]$ direction. (a,b) show a $[000]$ out of plane shift.

(c,d,e,f) show a $\frac{1}{4}a_0[01-1]$ shift with the two possible interface variants shown. (g,h) show the $\frac{1}{4}a_0[1-10]$ shift which only incorporates one possible interface for each defect orientation..... 115

Figure 35: Structural Model, simulation and imaging from a $\frac{1}{4}a_0[1-10]$ APB shift structure. a) Atomic modelling of a Fe_3O_4 APB defect in the $[111]$ viewing direction. O shown with blue spheres, octahedral Fe_B sites shown in red, tetrahedral Fe_A sites shown in yellow. The APB shift can be identified structurally by the broken Fe_{ABA} column stacking across the interface. b) HRTEM image cropped from Figure 27b. c) Image simulations produced from the structure in (a) for comparison with (b). This simulation shows how the contrast variations in HRTEM images of this structure are localised around only the Fe_A atomic columns rather than at all the Fe atomic columns. 116

Figure 36: Experimental and simulated M-H data. a) Experimental M-H data shown in blue (dots) from a (111) oriented 10 nm Fe_3O_4 film. Simulated Bulk Fe_3O_4 magnetisation data shown in black. Simulated APB defect magnetisation shown in red. The experimental magnetisation is expressed in emu and is plotted against the right axis, simulated magnetisation is expressed as a ratio of spins aligned against the moment of all spins within the cell shown on the left axis. Four key points from the APB simulation curve are shown in figure (b-f). b) Shows the spatial distribution of the magnetic moment across the simulated cell and corresponds to the spin configurations shown in c-f). c) Shows the spin configuration at high field, i.e. 2500 Oe. d) shows the spin configuration at 0 Oe. e) Shows the spin configuration at zero net magnetisation at -368 Oe f) Shows the spin configuration at -2500 Oe. 119

Figure 37: HRTEM image of Fe_3O_4 film and MgAl_2O_4 substrate in $[1-10]$ zone axis. 123

Figure 38: SAD patterns from a cross-section of the $\text{Fe}_3\text{O}_4/\text{MgAl}_2\text{O}_4$ interfacial region in a) the $[11-2]$ zone axis and b) the $[1-10]$ zone axis 124

Figure 39: in-situ XPS showing the $\text{Fe}2p_{(1/2)}$ and $\text{Fe}2p_{(3/2)}$ peaks characteristic of Fe_3O_4 125

Figure 40: a) *ex-situ* Raman spectra of Fe_3O_4 at 193, 306, 538 and 668 cm^{-1} . Measurements were taken to 1900 cm^{-1} but no further structure is shown in the curves beyond 900 cm^{-1} . Raman Active modes for Fe_3O_4 labelled in non-italic [184] and for MgAl_2O_4 labelled in italic type face [185] b) High resolution reproduction of 200-250 cm^{-1} region of 10 nm film data. This shows a small peak which could be attributed to an Fe_2O_3 Raman active mode at 225 cm^{-1} , however a second Raman active mode for Fe_2O_3 at 245 cm^{-1} is not observed. 125

- Figure 41: a) High field in-plane magnetisation curves from thin film Fe_3O_4 . This data has been taken at 150 K using a cold stage VSM. At 8 T magnetization has not saturated". b) High resolution magnetisation data around 0 T in the 30 nm film sample. 126
- Figure 42 In-plane MR Fe_3O_4 films by four point probe techniques..... 127
- Figure 43: (a) HAADF-STEM image of the interfacial region between Fe_3O_4 and MgAl_2O_4 in the $[11-2]$ zone axis. The matched crystal symmetry across this interface can be seen in the continued structural motif from film to substrate. (b) Bragg filtered $\langle 4-40 \rangle$ image showing dislocation cores (c) Fast Fourier transform of image (a), circled reflection are used to create the Bragg image in (b). Dislocation cores are outlined in both the original and filtered image with circles..... 128
- Figure 44: (a) HAADF-STEM image of the interface between Fe_3O_4 and MgAl_2O_4 in the $[1-10]$ zone axis. (b) Fast Fourier transform of the image in (a), $(22-2)$ reflections used for creating the Bragg image in (c) are outlined. (c) Bragg filtered image with a single dislocation core. Dislocation cores are outlined in both the original and filtered image with circles. 128
- Figure 45: HAADF-STEM image of an APB defect within the Fe_3O_4 film, imaged in the $[1-10]$ zone axis. a) The extended defect region is identified by the disruption of the rhombohedral motif, outlined in the inset upper right corner with the Fe atomic columns denoted as following: large (small) red circle representing double (single) occupied Fe_B columns and yellow circles representing Fe_A atomic columns. b) Atomic model of the APB boundary outlined in (a), the colour code is the same as in (a) with O atoms as blue. (c) Simulated HAADF map of the model in (b). The $\frac{1}{4}\langle 01-1 \rangle$ shift between coalesced Fe_3O_4 grain results in loss of the alternating contrast of Fe columns in '3 Fe_B ' layers indicated by dashed yellow lines in (a). The match between the calculated image and experimental image is illustrated by the inset of model image inside the middle of APB region in (a). 129
- Figure 46: (a) HAADF-STEM image of the $\text{Fe}_3\text{O}_4/\text{MgAl}_2\text{O}_4$ interface with evidence of $\frac{1}{4}\langle 1-10 \rangle$ shift APB defect outlined in the black dashed lines in (a). (b) Schematic diagram of overlapping Fe_3O_4 grains leading to closely packed equivalent atomic projections at the centre of this defect. (c) HAADF-STEM image simulation of the bulk $\langle 11-2 \rangle$ zone axis reproduced to the left of (a). (d) HAADF-STEM simulation of overlapping grains reproduced near the centre of (a)..... 131
- Figure 47 Schematic diagram of four translational vectors, $\frac{1}{4}[01-1]$, $\frac{1}{4}[0-11]$, $\frac{1}{4}[10-1]$ and $\frac{1}{4}[-101]$ that give rise to observable half structural motif shifts and give rise to the observed APB imaging seen above. These can be observed in both the $\langle 11-2 \rangle$ and $\langle 1-10 \rangle$ zone axes though the structural spacing's are much larger in the $\langle 1-10 \rangle$ zone axis as indicated in the schematic..... 132

Figure 48. Magnetisation curves (a) relative magnetoresistance (b), and conductivity of annealed and as grown films (c). (Supplied by K. Matsuzaki of Toyko Institute of Technology).....	137
Figure 49: Low magnification HAADF images of as deposited (a) and post-.....	139
Figure 50: a) HRTEM of interfacial region for as deposited Fe_3O_4 film. Digital ...	140
Figure 51: (a) Atomic resolution HAADF image of the interface region for as	141
Figure 52: (a) HAADF-STEM image of the $\text{Fe}_3\text{O}_4/\text{YSZ}$ interface in the $\langle 1-10 \rangle$ zone axis. (b) Fourier filtered image from (a) showing regular misfit dislocations at the interface related to the highly mismatched interface.	142
Figure 53: HAADF-STEM image of the $\text{Fe}_3\text{O}_4/\text{YSZ}$ interface in the $\langle 11-2 \rangle$ zone axis.	143
Figure 54: high resolution HAADF-STEM imaging of the $\text{Fe}_3\text{O}_4/\text{YSZ}$ interface. Images formed from an image stack and combined using the SDS DSD digital micrograph plugin [145].	143
Figure 55: a) Low magnification MAADF-STEM image of the $\text{Fe}_3\text{O}_4/\text{YSZ}(111)$ interface with a (111) oriented twin structure propagating horizontally through the deposited layer, this is highlighted with yellow dashes for clarity. b) SAD pattern taken from a twinned region showing the characteristic rhombohedral pattern associated with the $\langle 1-10 \rangle$ zone axis of both YSZ and Fe_3O_4 the brightest reflections highlighted with the white rhombus are from the substrate the two rhombohedral constructions in red highlight the two domains of Fe_3O_4 structure and uniquely identify the twinned structure.	145
Figure 56: HAADF-STEM image showing the $\langle 1-10 \rangle$ viewing direction (w.r.t lower half of image), the defect plane is identified by yellow dashed lines at the left and right of the image. In this imaging mode the oxygen atomic sites are not visible, but the various Fe sites are identified around the defect with large red dot = doubly occupied octahedral site, small red dot = single occupied oct. site, small yellow dot = single occupied tetrahedral site, small green dot = single occupied Fe sites in the twinning region.	146
Figure 57: Atomic resolution HAADF-STEM imaging of the (111) twin defect. This figure shows the integrated image intensity from 26 rapidly acquired HAADF-STEM images. The defect plane is again identified by the yellow dashed line.	147
Figure 58: (a) HAADF STEM image of the SMART EELS scan [198] across the twin boundary (red line). Regions 1,2 and 3 represent the onset of the boundary region, the centre of the twin boundary and the far edge of the boundary respectively. These regions are bounded by dashed black lines. (b) Plots of the Fe $L_{2,3}$ (pink) and O K (blue) EELS signals along the linescan, plotted against the HAADF image intensity profile (grey). The drop in the Fe signal along with the small drop of the HAADF image intensity are	

indicative of Fe depletion at the twin boundary. (c) O K and (d) Fe $L_{2,3}$ spectra acquired at and adjacent to the twin boundary (marked with dashed lines in panel a and b) [199]... 148

Figure 59: Structural modelling of the (111) twin defect based on a non-stoichiometric defect interface. a) shows the structural model stabilized with electron holes to give charge neutrality. b) shows the HAADF-STEM image simulation produced using (a) and contains the scale bar for both (b and c). c) shows a HAADF-STEM image comparable to the region shown in (b). 149

Figure 60: HRTEM overview image of the $\text{Fe}_3\text{O}_4/\text{SrTiO}_3$ heterostructure showing uniform film thickness of ~ 80 nm and a sharp interface between film and substrate.... 155

Figure 61: XRD θ - 2θ scan of the $\text{Fe}_3\text{O}_4/\text{SrTiO}_3(111)$ structure showing the single phase nature of the film and the shared (111) planes of both materials. 156

Figure 62: b) SAD pattern from the interface shown in (a). The structural motif of Fe_3O_4 and SrTiO_3 is highlighted with the inset quadrilaterals and major diffraction spots indexed. c) And d) show SAD simulations of Fe_3O_4 (red) and SrTiO_3 (green) depending on whether the Fe_3O_4 structure is mirrored around the vertical axis. c) Shows the undisturbed [1-10] viewing direction for both SrTiO_3 and Fe_3O_4 d) shows the [1-10] viewing direction for SrTiO_3 and the [-110] viewing direction for Fe_3O_4 . The close correspondence between b and d show the Fe_3O_4 overlayer is mirrored from direct cube on cube epitaxy..... 156

Figure 63: HAADF-STEM image of the Fe_3O_4 film and SrTiO_3 substrate in the [1-10] zone axis (with respect to the substrate). The Fe sublattice structure is inset, with octahedral (tetrahedral) Fe sites shown in red (yellow). 157

Figure 64: Integrated STEM-EELS spectra from the region of interest indicated in figure 2. 158

Figure 65: HAADF-STEM and STEM-EELS from interfacial region. a) Region of interest selected from HAADF-STEM imaging. b) HAADF-STEM signal showing atomic resolution imaging. c) Spatially resolved intensity of O K edge signal. For guidance we draw a white dashed line that indicates the structural boundary between the Fe_3O_4 structure and the STO structure based on the O EELS map. d) Spatially resolved intensity of Fe $L_{2,3}$ edge signal with high intensity seen on Fe_B sites. e) Spatially resolved intensity of Ti $L_{2,3}$ signal..... 159

Figure 66: HAADF-STEM interface analysis from relaxed DFT co-ordinates. a) HAADF-STEM image of the $\text{Fe}_3\text{O}_4/\text{STO}$ interface structure. b) Relaxed atomic structure of the $\dots 3\text{Fe}_B/4\text{O}/\text{Fe}_A\text{-Ti}/\text{SrO}_3/\text{Ti}\dots$ interface model c) HAADF-STEM image simulation resulting from the structure in (b). d) Relaxed atomic structure of the $\dots 3\text{Fe}_B/4\text{O}/\text{Fe}_A\text{Fe}_B\text{-SrO}_3/\text{Ti}\dots$ interface model e) HAADF-STEM image simulation resulting from the structure in (d). 160

Figure 67: a) Larger area HAADF-STEM image of the $\text{Fe}_3\text{O}_4/\text{STO}(111)$ interface. b) Averaged site intensities for the interfacial sites a, b and c highlighted in (a). In this figure atomic species are represented by: Sr (large green circles), Ti (grey), Fe_B (red) and Fe_A (yellow)..... 161

Figure 68: Calculated electronic density of states of a bulk Fe_3O_4 supercell (black) and a bulk Fe_3O_4 supercell that has been compressively strained by 6.1% in the (111) plane..... 162

Figure 69: Local spin resolved electronic structure at the $\dots 3\text{Fe}_B/4\text{O}/\text{Fe}_A\text{-Ti}/\text{SrO}_3/\text{Ti}\dots$ interface. a) Shows the spin resolved local density of states at the interface. The presented SDOS is projected for the six structural blocks shown in (b). Section *i* and *ii* represent the states from six atomic planes of Fe_3O_4 which each form a structural and chemical repeat unit of $\dots \text{Fe}_B/\text{Fe}_A/4\text{O}/3\text{Fe}_B/4\text{O}/\text{Fe}_A\dots$. Sections *iii* to *vi* each contain a bilayer of STO of $\dots \text{Ti}/\text{SrO}_3\dots$. Section *ii* and *iii* form the atomic interface between the film and substrate. 164

Acknowledgements

This Thesis has been made possible through the help of many people. I would like to begin by acknowledging my supervisor, Dr. Vlado Lazarov, for giving me the opportunity to work on this project. Without his continued support and supervision this research would not have been possible.

I would also like to thank EPSRC for their funding of my studentship for the past three and a half years. I have also received funding from the IOP, Seagate and the IMC2014 organising committee to attend conferences and workshops

During this work I have been fortunate to visit several laboratories around the world. I would like to thank Prof. Kate Ziemer for allowing me access to the Chemical Engineering Laboratories at North Eastern University, Boston in 2012. I am also grateful to Professors Lian Li and Michael Weinert for accommodating my stay at the University of Wisconsin-Milwaukee in 2012. I also wish to acknowledge the support of Prof. Tomofumi Susaki and Dr Kosuke Matsuzaki for facilitating my work at the Tokyo Institute of Technology, 2013 and there longstanding collaboration in material synthesis and characterisation which has led to a series of publications on PLD grown Fe_3O_4 .

During my PhD I have worked with many members of the UK microscopy community, but particular assistance has been given by Dr. Mike Ward to assist sample preparation at the University of Leeds and Dr. Demie Kepaptsoglou and Prof. Quentin Ramasse at SuperSTEM, Daresbury to perform atomically resolved STEM imaging and EELS analysis.

During the period of my PhD I have been constantly supported at the University of York by the York-JEOL Nanocentre, particularly by Dr. Leonardo Lari who has contributed through tireless microscopy operation, alignment and advice and Mr. Ian Wright who has helped me keep equipment running through every type of unidentifiable failure possible. I am also deeply grateful for the support of Prof. Ed Boyes and Prof. Pratibha Gai, thank you for your time and ideas. I worked closely with the other staff of the York-JEOL Nanocentre, particularly Dr Mike Ward and Mr Tom Martin and the staff and students of Dr. Vlado Lazarov including Dr. Balati Kuerbanjiang, Dr. Ghulam Uddin, Mr. Daniel Pingstone, Mr. Arsham Ghasemi and Mr. Zlatko Nedelkoski. Thank you all for keeping work fun.

Prior to commencing my PhD at York I received support from Dr. Charles Barton, Dr. Steve Tear, Dr Andrew Pratt and Prof. Sarah Thompson to encourage me to continue my studies and to show me a route into academic research both in my time at the University of York and at the National Institute for Materials Science, Tsukuba. During my stay at the National Institute for Materials Science in 2011 I was supported to work in the lab of Prof. Yasushi Yamauchi and Dr. Mitsunori Kurahashi.

I also wish to thank the staff and students of the University of York, past and present, both within and outside the Department of Physics. There are far too many people to name, you know who you are. Thank you for making my time at York so enjoyable during the last eight years. In particular I would like to thank my long suffering housemates Dr James Sagar, Mr James Sizeland and Mr Ben Murphy for hours of entertainment and support.

I would also like to thank Dr Andrew Pratt, Prof. David Jenkins and Dr Chris Kelley for their time and interest in and around the Department of Physics particularly in organising the annual York vs Edinburgh cricket match which would not have been possible without drivers, players, kit and colleagues.

During my eight year stay at York one of the few constants has been Goodricke College Hockey team who form a most effective method of stress relief particularly during thesis writing, particular thanks to Thomas Merriman and Lauren Mitchell for their captaincy and organisation.

This work would not have been possible without the support of my family and friends who have given me the time and encouragement to undertake my PhD and my girlfriend Sophie Taylor who has put up with many years of me living in York as she tries to make her way in Advertising at the other end of the East Coast mainline.

To all those mentioned, and many others

Thank you all very much.



Declaration

I declare that the work presented in this thesis is based purely on my own research, unless otherwise stated, and has not been submitted for a degree in either this or any other university.

All sources are acknowledged as References.

Publication List:

- [1] Kepaptsoglou, D. M., et al., *Microscopy and Microanalysis*, 2015. 21, p1151
- [2] Gilks, D., et al., *Microscopy and Microanalysis*, 2015. 21, p1299
- [3] Moorsom, T., et al., *Appl. Phys. Lett.*, 2014. 105(2), p022408
- [4] Moorsom, T., et al., *Phys. Rev. B*, 2014. 105, p022408
- [5] McKenna, K., et al., *Nat. Comms.*, 2014. 5, p5740
- [6] Liu, Y., et al., *Nat. Phys.*, 2014. 10, p294
- [7] Lari, L., et al., *J. Phys. D: Applied Physics*, 2014. 47(32), p322003
- [8] Lari, L., et al., *J. Phys: Conf. Series*, 2014. 522(1), p012016
- [9] Hasnip P. J., et al., *J. Magn. Soc. Jpn.*, 2014. 38, p50
- [10] Hasnip, P. J., et al., *Materials*, 2014. 7, p1473
- [11] Gilks, D., et al., *J. Appl. Phys.*, 2014. 115(17) p17C107
- [12] Gilks, D., et al., *J. Phys.: Conf. Series*, 2014. 522(1), p012036
- [13] Liu, Y., et al., *Phys. Rev. Lett.*, 2013. 110, p186804
- [14] Gilks, D., et al., *J. Phys. Cond. Matt.*, 2013. 25, p485004
- [15] Gilks, D., et al., *J. Appl. Phys.*, 2013. 113(17), p17B107
- [16] Pratt, A., et al., *Phys. Rev. B*, 2012. 85, p180409(R)

Chapter 1. Introduction

Magnetite (Fe_3O_4) is a naturally occurring mineral first discovered around 2000 BC in Magnesia, part of modern day Greece. This region gives its name to magnetite and by extension magnetism (mining in this region also gave the name of magnesium and manganese). Magnetite has attracted interest since its initial discovery and is likely to have been one of the first examples of magnetism and magnetic materials which humans came into contact with.



Figure 1: Natural magnetite crystal displayed at the Natural History Museum, London

A small proportion of geological Fe_3O_4 crystals are found in a magnetised state which is rare amongst naturally forming minerals [1]. Magnetised Fe_3O_4 fragments have historically been referred to as lodestones which attract small pieces of iron and were used to give compass needles their bearing with respect to the Earth's magnetic field. Naturally occurring magnetite is a common geological ore and can be found in large crystals as shown in Figure 1.

Although humans have been aware of magnetite for millennia there is still much we do not fully understand about the electronic structure, transport properties and phase transformations of this crystal.

At present Magnetite is used for a wide range of commercial and industrial applications [2] often in a synthetic particulate form including as a black pigment [3] and as a catalyst for ammonia synthesis [4]. Fe_3O_4 particles are being researched for biological applications including cancer treatment by magnetic hyperthermia [5, 6] and are used as a contrast agent in MRI scans [7]. Fe_3O_4 has been used as a recording material in magnetic tape [8].

Recent interest in magnetite as a material for future spintronics device applications [9-17] is due to the predicted half-metallic band structure [18-20] of the room temperature Fe_3O_4 structure. The band structure of Fe_3O_4 exhibits a band gap at the Fermi level in the majority states however minority states are present at the Fermi level giving rise to conduction via electron hopping between octahedral Fe sites. This should give rise to 100 % spin polarised conduction within bulk Fe_3O_4 .

Fe_3O_4 undergoes a structural, charge ordering phase transformation at ~122 K known as the Verwey transition [21-23]. This effect is characterised by a distortion from cubic symmetry and leads to electron localisation on specific octahedral sites. This in turn leads to a decrease in conductivity as electron hopping between octahedral sites reduces significantly. The Verwey transition is not a well understood phenomena [24] and demonstrates the complexity of the atomic and electronic structure of this material.

At room temperature Fe_3O_4 crystalizes in the inverse spinel structure with a lattice constant of 0.834 nm and space group $\text{Fd-}3\text{m}$ [25]. The oxygen sublattice forms a fully occupied face centred cubic (FCC) lattice with Fe occupying interstitial sites. The dominant super-exchange interaction in Fe_3O_4 between tetrahedral (Fe_A) and octahedral (Fe_B) sublattices results in their antiferromagnetic alignment [26, 27]. As the unit cell contains twice as many B site cations than A site cations Fe_3O_4 acquires a net magnetic moment of $4 \mu_\text{B}$ /formula unit [28]. Fe_3O_4 exhibits a high Curie temperature of 858 K.

1.1 Thin film magnetite (Fe_3O_4)

The half metallic band structure of Fe_3O_4 is important for spin valve device structures and other spintronics devices where highly spin-polarised materials are required for spin injection or detection. However, device applications require fabrication of thin films and heterostructures. Since the desirable attributes of Fe_3O_4 are bulk properties, these properties of Fe_3O_4 must be retained in thin films after the deposition process. Despite significant effort to prepare thin films of magnetite with bulk like properties in the majority of cases Fe_3O_4 thin films exhibit non-bulk anomalous properties. The most

significant of which are negative magnetoresistance (MR) [25, 29, 30] and exceptionally high saturation fields [31], neither of these properties are seen or expected in bulk crystals of Fe_3O_4 [32]. Growth defects such as anti-phase domain boundaries (APBs) have been identified as the main cause of anomalous thin film behaviour due to the strongly anti-ferromagnetic (AFM) super exchange interactions predicted at the defect boundaries. Magnetite performance when used as an electrode in devices is critically dependent upon realising the full chemical and structural properties of bulk like Fe_3O_4 so significant attention must be given to stoichiometry, single crystal formation and atomic structural order which must be fully realised to give the half metallic properties determined by density functional theory calculations based on bulk structure and chemistry. Controlling the presence of APBs is essential to give bulk magnetite behaviour in device structures [33].

Furthermore, for spintronic device applications the interface structures between Fe_3O_4 and other material layers must be understood at an atomic scale. The electronic states of the device interface and the relative band alignments between the layers of a device will define the functional properties, efficiency and stability of the device.

This means we must work with structurally robust materials which will allow atomically engineered interfaces to be produced and maintained for the useful lifetime of a device. We must also investigate material properties on an atomic scale using theoretical and experimental techniques which can determine chemistry and structure on a site by site basis to complete the understanding given by macroscopic analysis techniques such as spectroscopy and x-ray crystallography. For this work metal oxide materials offer all the properties required.

1.2 Motivation of this thesis

Highly spin polarised materials are one of the most pressing requirements for development in conventional electronics and spintronic device applications. For this Fe_3O_4 offers an almost ideal candidate material; either to be utilised as a layer in a conventional spin valve or to be used as a spin injector or detector in a more advanced spintronics logical device. Fe_3O_4 has a theoretically predicted half metallic band structure which should give rise to 100 % spin polarised conduction, a high Curie temperature which makes stability and integration into a real computational device feasible and shares a lattice match with well-known device barrier oxides.

Furthermore, the stability of oxide structures allows the potential development of all oxide electronics and atomically engineered interface and device properties which are not currently used in conventional electronic devices.

Fe_3O_4 can be utilized either in spin dependent tunnelling devices such as magnetic recording read head technology or future non-volatile memory systems such as magnetic random access memory (MRAM) devices.

With Fe_3O_4 presenting such a wide range of desirable properties, and a material in which to study fundamental science it is clear that for Fe_3O_4 to be a useful material for us we must develop an atomistic understanding of the properties of thin film Fe_3O_4 . This means we can begin to understand the specific effects of APB defects, interfaces and the quality of growth at an atomic scale.

1.3 Overview of Thesis

The chapters of this work are intended to stand alone, so there is some repetition for any reader who reads from cover to cover. Abbreviations and symbols are defined within each chapter and listed at the end of the thesis. The bulk of the document is outlined below.

Chapter 2: Theoretical considerations. Here I describe the state of our current understanding of magnetite and the material physics required to make sense of the results presented in chapters 4-7. This includes a detailed description of the atomic structure of Bulk Fe_3O_4 and by extension other spinel structure materials. Following ordered bulk structure the behaviour of anti-phase domain boundaries (APBs) is explored and the sub-lattice vector structural shifts which define an APB defect are described.

To begin to understand the interplay between structure, conductivity and magnetisation in Fe_3O_4 we study the alteration in these properties as a result of charge ordering and structural transformation at the Verwey temperature. The magnetisation of Fe_3O_4 , like many localised electron oxides is based on super exchange interactions mediated through metal-oxide-metal triplets. This makes the overall magnetic properties of oxides heavily dependent on local atomic co-ordination. To understand non-bulk co-ordination at APBs I explain the properties of super-exchange interactions and the effect of Hund's rules on the cationic Fe sites.

Chapter 3: Methodology. The methodology of this project is broken down into three main sections. Firstly, thin film fabrication using ultra high vacuum (UHV) techniques to allow molecular beam epitaxy (MBE) and pulsed laser deposition (PLD) growth methods. Secondly: Characterisation, ranging from area integrated techniques such as Raman spectroscopy and x-ray diffraction to determine film structure and chemistry through to atomically resolved microscopy techniques using the transmission electron microscope. And, finally, simulation and modelling using experimentally determined atomic structures

to investigate and predict the electronic and structural properties of grown films using density functional theory (DFT), image simulations and atomistic spin modelling.

Chapter 4: $Fe_3O_4/MgO(111)$. Using this well studied spinel/rocksalt interface with MBE growth to deposit Fe_3O_4 we observe well-ordered defect formation when we grow in the polar (111) direction. The ordered nature of APBs in this growth orientation has allowed extended atomistic modelling of the defect boundaries and a thorough examination of the different defect boundary geometries and their effect on the properties of the deposited film. By constructing atomic models of APB defects we are able to perform atomistic spin modelling of a hysteresis curve and show a high degree of agreement between experimental and theoretical results based on predicted APB super exchange interactions.

Chapter 5: $Fe_3O_4/MgAl_2O_4(111)$. The APB formation in Fe_3O_4/MgO is expected as a result of multiple nucleation sites at the interface due to differing atomic structure of MgO and Fe_3O_4 . By changing substrate to another spinel system, in this case $MgAl_2O_4$, we explore the behaviour of APB defect formation when there is only a single stable interface registration. However we still find APB defects in MBE grown Fe_3O_4 on $MgAl_2O_4$. We perform comprehensive chemical and structural analysis using x-ray photoelectron spectroscopy (XPS) and Raman spectroscopy to identify high quality Fe_3O_4 film growth. Finally, we show that pure interfacial strain due to lattice mismatch is mediated through misfit dislocations and does not drive the formation of APB defects at the interface.

Chapter 6: $Fe_3O_4/YSZ(111)$. In this chapter I present the results of pulsed laser deposition of Fe_3O_4 on Y-stabilised ZrO_2 (YSZ). This work follows our attempts to improve and control the overall properties of Fe_3O_4 films by significantly reducing APB defect formation and ensuring high quality chemical uniformity using post-deposition processes. In this work we study the effect of post annealing Fe_3O_4 films in CO/CO₂ conditions to reform phase segregation at the film/substrate interface and provide high quality bulk like Fe_3O_4 .

In this PLD growth mode we do not observe single crystal Fe_3O_4 in the as-deposited films; rather we observe Fe and FeO inclusions at the interface which are removed during the high temperature annealing routines in this work. In the post deposited films we observe significant improvements in film structure, a reduction in APB defect density when compared with MBE grown films and a return to bulk like properties of the Fe_3O_4 material.

The post deposition interface is atomically sharp but contains a very high misfit dislocation density due to the very high lattice mismatch between the film and substrate.

In this PLD growth we observe highly regular crystallographic twinning within the Fe_3O_4 overlayer, both on (111) and (11-2) planes. The atomic structure of (111) plane twins is determined and shown to be non-stoichiometric. These defects are not expected to significantly affect the overall magnetic properties of the Fe_3O_4 film as they do not lead to significantly altered Fe-O-Fe bond geometry within the defect (unlike in the case of APB defects) and have a low defect density within the film.

Chapter 7: $\text{Fe}_3\text{O}_4/\text{STO}(111)$. Having refined the deposition of Fe_3O_4 using the YSZ substrate we can begin to consider the materials we particularly wish to combine Fe_3O_4 with to create functional devices. To do this we utilise perovskite structure SrTiO_3 (STO) due to the conductivity tuning which can be achieved in this material with Nb doping and as a model systems for depositing other spinel/perovskites junctions which allow the combination of ferrimagnets (spinel) with a wide range of material classes including ferroelectrics, insulators and superconductors. In this chapter we demonstrate the realisation of an atomically sharp oxide/oxide interface with well-defined interfacial chemistry.

Chapter 8: Conclusions and Future Work. The final conclusions of this thesis and options for Fe_3O_4 device layers and oxide electronics are discussed alongside suggestions for future experiments.

Chapter 2. Theoretical Considerations

To allow a full appreciation of the results presented in this thesis a number of theoretical considerations are required before continuing directly to the results shown in later chapters.

Firstly, I discuss the other Iron Oxides, how they relate to one another chemically and structurally and how the atomic structures of these materials affect their overall properties. Fe and O are able to bond with each other in different valence configurations based on either octahedral or tetrahedral co-ordinated Fe sites. This makes determining the chemistry of deposited films essential and structural analysis is required to determine the quality of Fe_3O_4 film growth. Following this I will describe fully the Fe_3O_4 atomic structure in both the conventional (001) oriented cubic unit cell and a (111) oriented cell which is more useful for this work. In this section and through this thesis O sites are denoted in blue and Fe sites are shown in red for octohedrally co-ordinated sites or yellow for tetrahedrally co-ordinated sites.

After describing the atomic structure of Fe_3O_4 the electronic configurations of the atomic sties will be considered using Hund's rules. This allows an explanation of the conductivity of Fe_3O_4 at room temperature. This is further examined by understanding the behaviour of Fe_3O_4 at low temperatures (below the Verwey transition) where a charge ordering structural transformation occurs which significantly reduces the conductivity of Fe_3O_4 .

The magnetic exchange interactions of the iron oxides are then discussed with an explanation of the super-exchange interactions exhibited in these materials. The bond lengths, angles and co-ordination of the sites are intrinsically linked to both the strength and sign of the resultant exchange constants.

The effects of antiphase domain boundaries (APBs) in Fe_3O_4 are discussed next. APB defects and their properties are fundamentally linked to the altered atomic structure and thus altered super-exchange constants of the Fe_3O_4 film around these defects.

The final sections of this chapter are less directly related to the physics of Fe_3O_4 and consider how this material may be used for device fabrication, particularly in relation to the use of polar materials for atomically controlled interface engineering. The basis of why this material is useful for spintronic applications and what spintronics means in practice.

2.1 The Iron Oxides

A range of binary iron oxide structures with similar structure, chemistry and composition to Fe_3O_4 can be formed at different temperatures, pressures and stoichiometric composition. In terms of simultaneous deposition of Fe and O onto a substrate the four most likely outcomes are either $\alpha\text{-Fe}_2\text{O}_3$ (hematite), $\gamma\text{-Fe}_2\text{O}_3$ (Maghemite), Fe_3O_4 (Magnetite) and FeO (Wüstite). Whilst the composition and Fe coordination of these materials are very similar [2], the overall properties of these materials are significantly altered, giving rise to ferrimagnetic and antiferromagnetic ordering, conductors and insulators as highlighted in Table 1.

At the highest oxidation level in this series, two polymorphs of Fe_2O_3 exist. Firstly, $\alpha\text{-Fe}_2\text{O}_3$ is a stable naturally occurring mineral with a corundum crystal structure. This material may form if deposition is performed in an oxygen rich atmosphere, however this can be clearly differentiated from Fe_3O_4 due to a significantly altered crystal structure.

The $\gamma\text{-Fe}_2\text{O}_3$ phase is more challenging when trying to grow Fe_3O_4 as both of these materials share the spinel structure. This means regions of $\gamma\text{-Fe}_2\text{O}_3$ and Fe_3O_4 may co-exist and are hard to experimentally verify with crystallographic methods. To identify $\gamma\text{-Fe}_2\text{O}_3$ a chemical approach such as x-ray photoelectron spectroscopy (XPS) or Raman spectroscopy is ideally used. $\gamma\text{-Fe}_2\text{O}_3$ is a ferrimagnetically ordered material like Fe_3O_4 . At room temperatures $\gamma\text{-Fe}_2\text{O}_3$ transforms to the $\alpha\text{-Fe}_2\text{O}_3$ phase though it is possible small inclusions of this structure may exist within a Fe_3O_4 layer.

The Fe sites in both Fe_2O_3 structures are all Fe^{3+} sites if full stoichiometry is achieved and both materials are poor conductors such that they can be classified as insulating materials.

Fe_3O_4 is the only stoichiometric iron oxide which can conduct sufficiently to be treated as a conducting material, though this is achieved by electron hopping between Fe^{3+} and Fe^{2+} sites within the octahedral sublattice and is not a typical metallic style conduction mechanism.

At the lowest oxidation point in this series, FeO is a rocksalt structure can only form as a stable phase above 570 °C [34]. However inclusions of FeO type structure are observed in some Fe_3O_4 growths undertaken in this thesis. Fully stoichiometric FeO should contain only Fe^{2+} sites in octahedral co-ordinations. However, the FeO Wüstite

phase exhibits a wide range of cation deficient non-stoichiometric structures with the chemical formula Fe_{1-x}O where ($0.05 < x < 0.15$) with a tendency for Fe atoms to occupy tetrahedral sites in the case of octahedral Fe Vacancies. Losing a single Fe^{2+} site as Fe content falls generates two Fe^{3+} sites to create charge neutrality. Of the Fe^{3+} sites formed there is a tendency for these sites to move to tetrahedrally co-ordinated geometry. Neutron scattering experiments suggest defects in FeO are similar to the atomic arrangement in magnetite [35]. This means the Fe_3O_4 stoichiometry must be finely balanced on both the O rich and O deficient extremes otherwise secondary phases are liable to form within the crystal. As the FeO phase moves away from stoichiometry is become more conductive but is an insulating material when near stoichiometry.

Since the Fe and O co-ordinations in all these iron oxide materials are extremely similar, (particularly if hexagonal $\alpha\text{-Fe}_2\text{O}_3$ is excluded) the crystal structures are similar, and the lattice constants are similar a high degree of control over the stoichiometry of films is required. Furthermore, the ability of Iron oxides to form non-stoichiometric compounds near to Fe_3O_4 composition based on displacements of single atoms and atomic vacancies makes achieving fully stoichiometric bulk Fe_3O_4 a significant challenge.

The strong dependence of the properties of iron oxides on atomic structure mean subtle changes in stoichiometry lead to completely altered magnetic and transport properties. This makes determining the structure and chemistry of grown films essential.

Table 1: Iron Oxides and there properties. *FeO has a cation deficient structure and therefore full FeO properties are rarely realised.

	$\alpha\text{-Fe}_2\text{O}_3$ [36]	$\gamma\text{-Fe}_2\text{O}_3$ [37-39]	Fe_3O_4 [18, 40, 41]	FeO^* [42-44]
Fe:O ratio	0.66	0.66	0.75	1
Structure	Corundum	Spinel	Spinel	Rock salt
Lattice Constant		0.8352 nm	0.8397 nm	0.433 nm
Valencies	$\text{Fe}^{3+}/\text{O}^{2-}$	$\text{Fe}^{3+}/\text{O}^{2-}$	$\text{Fe}^{3+}/\text{Fe}^{2+}/\text{O}^{2-}$	$\text{Fe}^{2+}/\text{O}^{2-}$
Name	Hematite	Maghemite	Magnetite	Wüstite
Magnetic order	Anti	Ferri	Ferri	Anti-Ferro
Conductivity	Insulator	Insulator	Electron hopping	Insulator

2.2 Crystal structure of Fe_3O_4

Bulk Fe_3O_4 crystallises in the inverse spinel structure. The commonly used cubic geometry unit cell of this material contains 56 atoms (8 chemical formula units of Fe_3O_4) as shown in Figure 2. This material exhibits a face centred cubic (FCC) stacking

sequence with a lattice constant of 0.8397 nm. The spinel structure is defined by the Fd-3m space group [45-47].

Along the [111] direction Fe_3O_4 is chemically and structurally layered with the FCC stacking sequence giving a ...ABCABC... relationship between planes. Further to this, the four plane atomic/chemical structure of ...4O/3 Fe_B /4O/ $\text{Fe}_A\text{Fe}_B\text{Fe}_A$... means this stacking sequence is fully realised only over twelve atomic planes in the [111] direction. In this [111] geometry the unit cell of Fe_3O_4 can be expressed in terms of 42 atomic sites, however, the primitive cell of Fe_3O_4 can be described with only 14 atomic sites but this requires an awkward cell geometry so is unused in this work.

The inverse spinel structure of Fe_3O_4 is composed of three interleaved structural sublattices. The O structure (blue spheres in the structural diagrams) is the simplest forming a fully occupied FCC stacked cubic arrangement as can be seen in Figure 2. The Fe structure is further divided into tetrahedrally co-ordinated Fe_A sites which account for 1/3 of the Fe sites. The tetrahedral sites have a nominal 3+ valence and occupy 1/8 of the available interstitials in this structure. Tetrahedral Fe_A sites are identified with yellow spheres. Octahedrally co-ordinated Fe_B sites account for 2/3 of the Fe content of Fe_3O_4 and have a nominal valence of 2.5+ due to the electron hopping conduction mechanism between Fe_B sites which are an equal distribution of 3+ and 2+ sites. Octahedral Fe occupies 1/2 of the available sites [48]. The two Fe sublattices, Fe_A and Fe_B are anti-ferromagnetically coupled and therefore magnetically oppose one another leading to the ferrimagnetic order of this material when the unequal numbers of each lattice are considered.

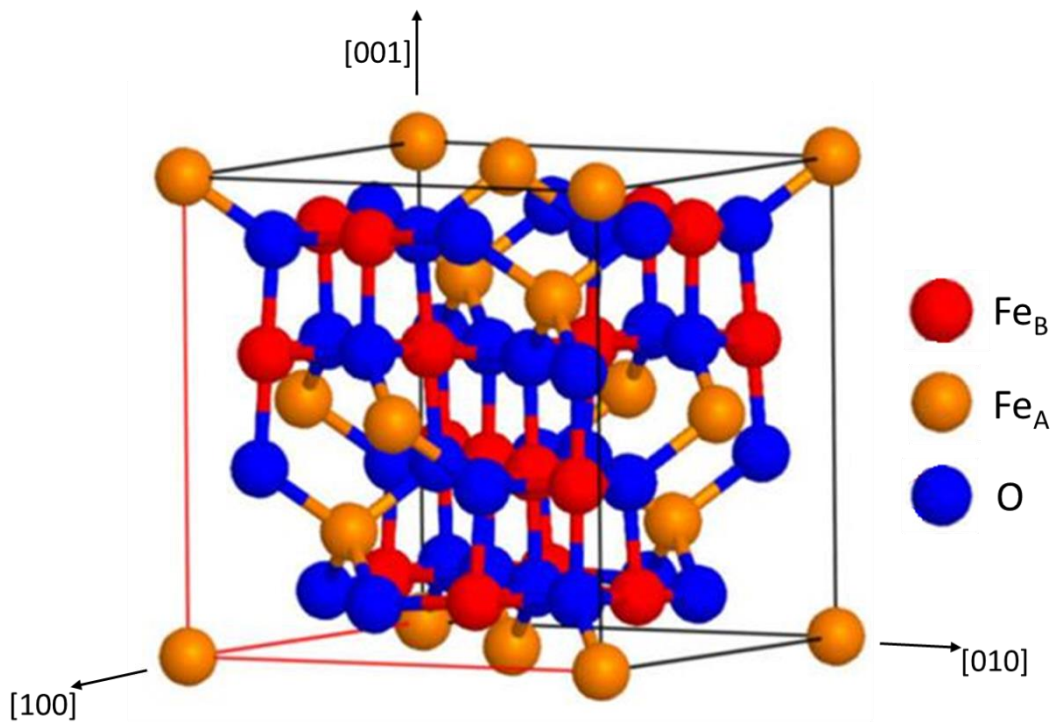


Figure 2: Cubic unit cell of Fe₃O₄. This cell is composed of 56 atoms representing 8 Fe₃O₄ chemical units. Fe_B is represented by red spheres, Fe_A by yellow, and O by blue.

2.2.1 Cubic, (001) oriented geometry and atomic structure of Fe₃O₄

The structure of Fe₃O₄ is generally expressed in the cubic geometry shown in Figure 2 which shows the fully occupied O sublattice and the two Fe sublattices. This structure contains 8 Fe₃O₄ chemical units. Looking closely at Figure 2 it is possible to see the structure is layered with alternating planes of 2 Fe_A sites followed by planes of 4 Fe_B and 8 O sites. To make this structure more clear, it is laid out schematically in Figure 3.

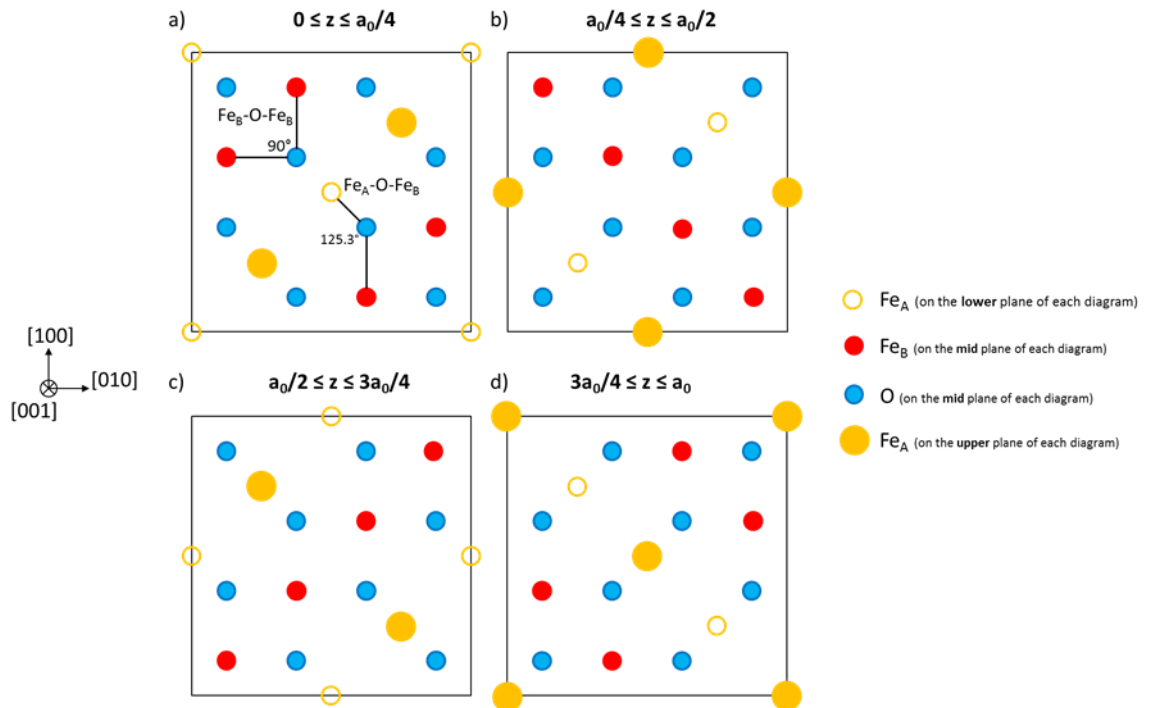


Figure 3: Plane by plane atomic structure of Fe_3O_4 in cubic $\langle 001 \rangle$ geometry as shown in Figure 2. Each diagram (a-d) includes three atomic planes in the z direction with each atomic plane separated by $1/8 a_0$, i.e. each diagram contains $\dots\text{Fe}_A/\text{O-Fe}_B/\text{Fe}_A\dots$ with the Fe_A structure repeated into the proceeding layer. The lowest layer in each diagram is represented with small open circles, the middle layer with filled circles and the highest layer with large filled circles. Fe_A is represented with yellow, Fe_B with red and O with blue.

This $[001]$ oriented structural geometry is conceptually useful when growing on (001) oriented substrates. However observing the sample in cross sectional geometry using the $[010]$ or $[100]$ viewing direction is not generally helpful. In these orientations many of the projected atomic columns are mixed Fe and O making it hard to obtain the full atomic structure of the material. There are six $\langle 001 \rangle$ type directions each at 90° to one another so the imaging condition is equivalent along all the major axes of the cube drawn into Figure 2. To expose a more useful geometry requires the sample to be cut at 45° to show a $\langle 110 \rangle$ type zone axis in which atomic columns of O, Fe_B and Fe_A are spatially separated and single species. The near neighbour Fe-O bonds have been included in Figure 2 as they are helpful for understanding the local Fe-O-Fe superexchange interactions present in this material.

The layered structure shown in Figure 3 shows the Fe_3O_4 structure split into 4 slabs in the z -direction. Each individual layer includes 3 crystal planes of $\dots\text{Fe}_A/\text{O-Fe}_B/\text{Fe}_A\dots$ with the Fe_A layers repeated at the top and bottom of subsequent slabs for clarity. The three layers per slab are identified using unfilled circles to represent the lowest layer, filled circles to represent the middle layer and large filled circles to represent the top layer. In this unrelaxed representation of the Fe_3O_4 structure all sites are found at $(na_0/8)$

fractional co-ordinates in the cubic (x,y,z) geometry where $a_0 = 0.8397$ nm. The first layer of the diagram shown in Figure 3a represents $0 \leq z \leq a_0/4$ with Figure 3(b-c) representing the subsequent quarters of this structure.

By examining the O sites in both Figure 3a and Figure 3c (which are identical) it is clear that this fully occupied sublattice is described by half the unit cell length in z than that required to describe the Fe sublattices (which do not repeat within the layers of the diagram). This relates to the discussion of APB defect formation later in this chapter and shows the FCC O sublattice shares its geometry with the O sublattice of rocksalt structure materials such as MgO and FeO.

The Fe_B atoms (red) occupy sites which run along alternating $\langle 110 \rangle$ directions from plane to plane. This shows the formation of 90° Fe-O-Fe in-plane bonds between various Fe sites without any 180° bond angles present. This is also true for out-of-plane Fe_B -O- Fe_B bonding, but this is less obvious from this schematic.

The Fe_A sites in this diagram are tetrahedrally co-ordinated which requires them to sit between four O sites in an out-of-plane interstitial site with respect to the O and Fe_B sublattices. Across the three planes of each of the diagrams in Figure 3 it can be seen that the Fe_A sites are spatially removed from the Fe_B sites by sitting in the un-occupied $\langle 110 \rangle$ lines left in the Fe_B sublattice.

2.2.2 (111) oriented geometry and atomic structure of Fe_3O_4

The [111] oriented structure can be defined with just 42 atomic sites, i.e. 6 chemical formula units of Fe_3O_4 and is expressed using a rhombohedral cell. In this geometry the FCC stacking sequence is clearer than in the cubic geometry and the positioning of the vacancies and the layered nature of this structure is made obvious.

The FCC stacking sequence and the structural cell is outlined in Figure 4. To fully describe Fe_3O_4 in this geometry requires four 'a-sites', four 'b-sites' and 4 'c-sites' (not to be confused with the Fe_A and Fe_B atomic sites) which are identified in Figure 4 with circles, squares and triangles respectively. As the structure is extended in a layer by layer fashion the rotation of site positioning is similar to the effect of stacking pool balls in three dimensions.

The [111] direction of Fe_3O_4 has a hexagonal in-plane symmetry with six $\langle 1-10 \rangle$ and six $\langle 11-2 \rangle$ directions each separated by 30° in plane. This means that the [1-10] and the [11-2] directions are at right angles to one another as shown in Figure 4 and when films have been grown in this [111] growth direction we have access to two unique viewing directions using perpendicularly cut samples.

The rhombohedral cell described below is aligned horizontally with the [1-10] zone axis and this cell extends for half the distance across the cubic unit cell in the [1-10] direction so is given by the length $a_0/\sqrt{2} = 0.594$ nm. The vertical direction in the diagram is aligned with the [11-2] zone axis. This direction is $a_0\sqrt{3/2} = 1.028$ nm. The out-of-plane direction which is not well visualised in this representation is the [111] direction and the rhombohedral cell runs across the full cubic unit cell, so this length is given by $a_0\sqrt{3} = 1.454$ nm. The general stacking of the twelve layers shown in Figure 5 is based on equally spaced layers so this spacing is $\frac{a_0\sqrt{3}}{12} = 0.121$ nm

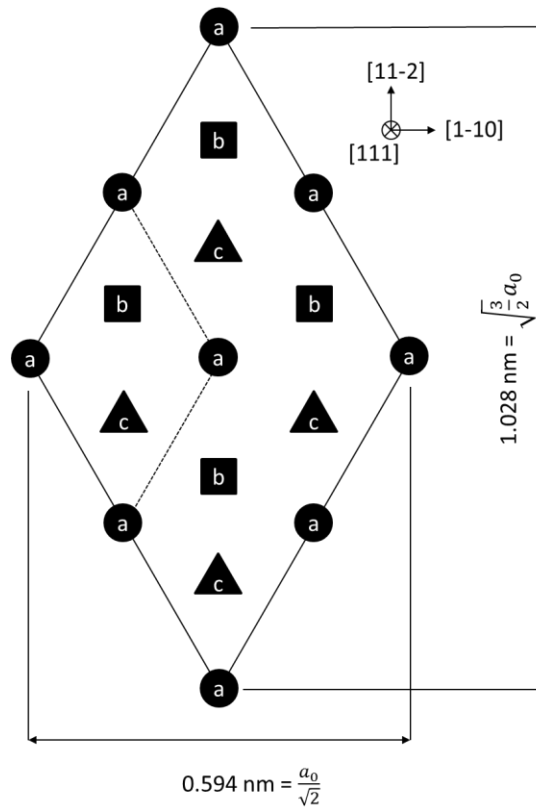


Figure 4: FCC stacking sequence and site positions of Fe_3O_4 along the [111] direction.

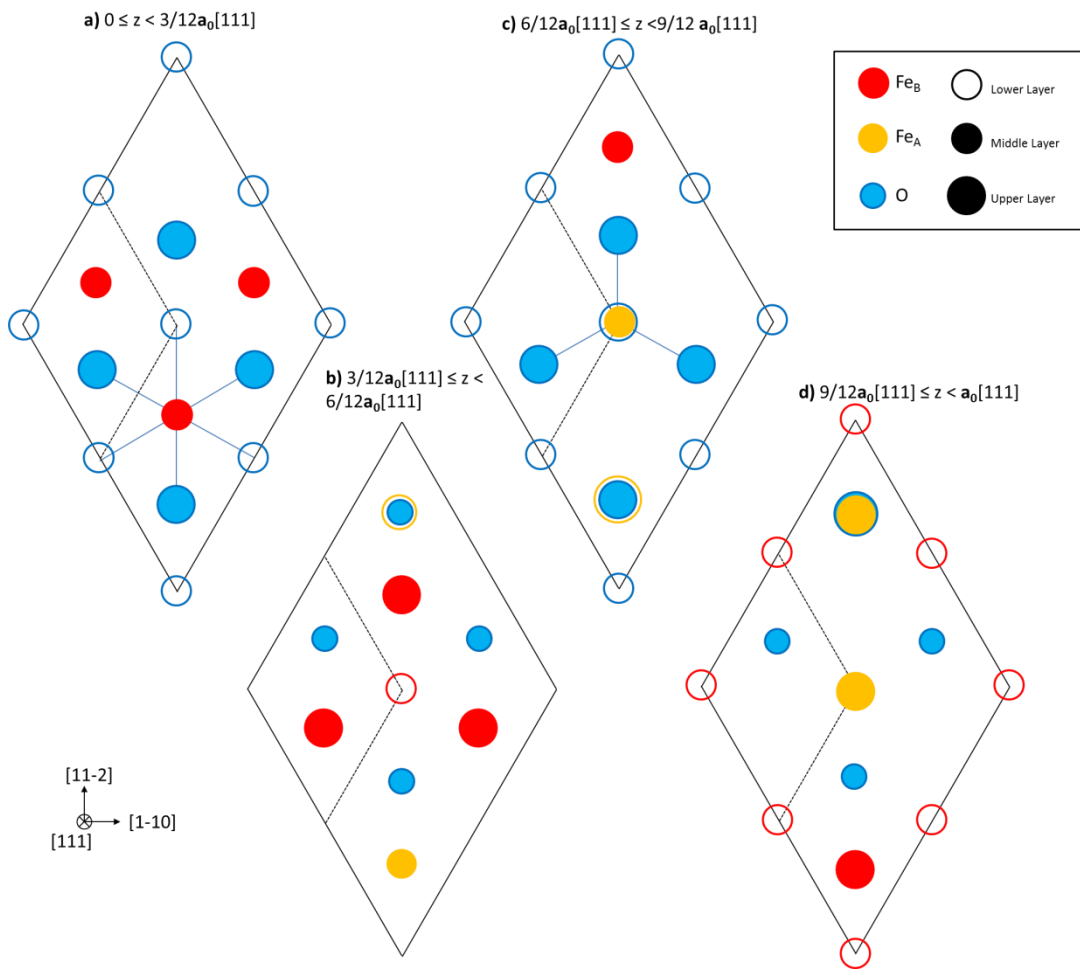


Figure 5: Plane by plane atomic structure of Fe_3O_4 along the $[111]$ direction. Along the $[111]$ direction the atomic structure of Fe_3O_4 is defined by 12 equally spaced atomic planes. a) contains the first three planes where $0 \leq z < 3/12a_0[111]$ b) the 4th-6th atomic planes from $3/12a_0[111] \leq z < 6/12a_0[111]$ c) the 7th-9th atomic planes from $6/12a_0[111] \leq z < 9/12a_0[111]$ and d) the 10th-12th atomic planes from $9/12a_0[111] \leq z < a_0[111]$. As in previous diagrams, Fe_B is indicated in red, Fe_A in yellow and O in blue.

In Figure 5a I show the ...4O/3 Fe_B /4O... layers in the first ...ABC... stacking sequence. The two oxygen planes are simple as they are fully occupied. The nine hollow spheres on 'a-sites' represent the first layer of oxygen on the $Z=1/12$ layer and only represent four full sites due to the four corner sites each representing $1/4$ occupation and the four edge each sites representing $1/2$ occupation. The Fe_B layer shown on the middle plane of this diagram at $Z=2/12$ contains a vacancy and has three occupied Fe_B sites. The following O plane at $Z=3/12$ on 'c-sites' is again simple and contains four occupied sites.

The Fe_B site in the lower half of Figure 5a is highlighted with its six nearest neighbour O bonds to demonstrate the octahedral co-ordination of this site.

In Figure **5b** the structure is slightly more complex as this introduces the first $\dots\text{Fe}_A/\text{Fe}_B/\text{Fe}_A\dots$ layer. This type of layer does not sit completely on the $Z=4/12$ plane in the z -direction, but rather the two Fe_A sites shift out of plane. The lower Fe_A site (hollow yellow circle directly beneath an O) is positioned directly above the Fe_B vacancy from two layers before in Figure **5a**. This atom sits at $Z=7/24$ splitting the layer by layer spacing in half. Furthermore, this site is not an 'a-site' the only 'a-site' atom in the $\dots\text{Fe}_A/\text{Fe}_B/\text{Fe}_A\dots$ layer is the central Fe_B site (red hollow circle) which sits at the equidistant point from the three occupied Fe_B sites below (and above). The final Fe_A site which completes this layer sits into the c-site at the bottom of this diagram and is identified with a filled yellow circle to show this is the higher of the two Fe_A sites; this is positioned at $Z=9/24$. The rest of Figure **5b** is relatively straight forward, the overall stacking of this diagram is $\dots\text{Fe}_A\text{Fe}_B\text{Fe}_A/4\text{O}/3\text{Fe}_B\dots$ on the $\dots\text{ABC}\dots$ stacking sites. The O plane at $Z=5/12$ is shown with filled blue circles and is fully occupied on b-sites, The 3Fe_B is positioned on 'c-sites' at $Z=6/12$ with a single vacancy, this vacancy is again positioned directly above the preceding Fe_A sites seen in Figure **5b** and indicates the site position of the following Fe_A site in Figure **5c**.

Figure **5c** contains the $\dots4\text{O}/\text{Fe}_A\text{Fe}_B\text{Fe}_A/4\text{O}\dots$ structure with the oxygen structure in this diagram identical to that shown in Figure **5a**. The lower O plane is positioned at $Z=7/12$ and the higher O plane is positioned at $Z=9/12$. Once again the $\text{Fe}_A\text{Fe}_B\text{Fe}_A$ does not stay at a single height but instead has the lowest Fe_A site posited at $Z=15/24$ the Fe_B site at $Z=8/12$ and the higher Fe_A site at $Z=17/24$. The Lower Fe_A site is identified with a hollow yellow circle which sits above the 3Fe_B vacancy from the preceding diagram and below the 'c-site' oxygen at the bottom of Figure **5c**. The Fe_B site in this layer is once again positioned at the centre of the six neighbouring Fe_B sites across the two neighbouring 3Fe_B planes. The Fe_A site at the centre of this diagram is highlighted with bonds to the nearest atomic neighbours to demonstrate the tetrahedral co-ordination of this site.

Figure **5d** shows the final three layers of this structure with $\dots3\text{Fe}_B/\text{O}/\text{Fe}_A\text{Fe}_B/\text{Fe}_A\dots$. The 'a-site' 3Fe_B layer on $Z=10/12$ follows as before with a vacancy above the Fe_A site from preceding layers. The b-site O plane on $Z=11/12$ is fully occupied. And the finally $\text{Fe}_A\text{Fe}_B\text{Fe}_A$ positions Fe_A sites into the 3Fe_B vacancies left above and below this layer with the Fe_B sitting on the natural 'c-site' positioning of the plane. Across the twelve planes it can be seen that of the 12 possible a-site, b-site and c-site positions the $\text{Fe}_A\text{Fe}_B\text{Fe}_A$ only occupies three sites, the direction from lowest site to highest site always circulates down the diagram and that the following $\text{Fe}_A\text{Fe}_B\text{Fe}_A$ begins at the same site as the preceding $\text{Fe}_A\text{Fe}_B\text{Fe}_A$ layer ended.

Although the diagram for Fe_3O_4 in this $[111]$ direction can initially look complex it give a much clearer explanation of why the Fe_A sites are tetrahedrally co-ordinated and explains the complex crystallography of Fe_3O_4 very neatly. This also expresses the crystallography which will be used in the $[111]$ oriented growths of Fe_3O_4 in the results sections of this document.

Although the expression of the atomic structure in the cubic (001) and rhombohedral (111) oriented cells is quite different the underlying structure is identical. To provide a three dimensional reference for these structural models Figure 6 shows the in-plane, cross sectional viewing directions associated with these diagrams. Figure 6a shows the view of (111) oriented growth seen down the $[11\bar{2}]$ viewing direction. Figure 6b shows the (111) style growth down the $[1\bar{1}0]$ viewing direction and Figure 6c shows the $[100]$ viewing direct. The cubic geometries in Figure 6 illustrate the different crystallography at 90° inplane rotation in the (111) growth and the identical crystallography at 90° from the $[100]$ viewing direction in (001) oriented growth.

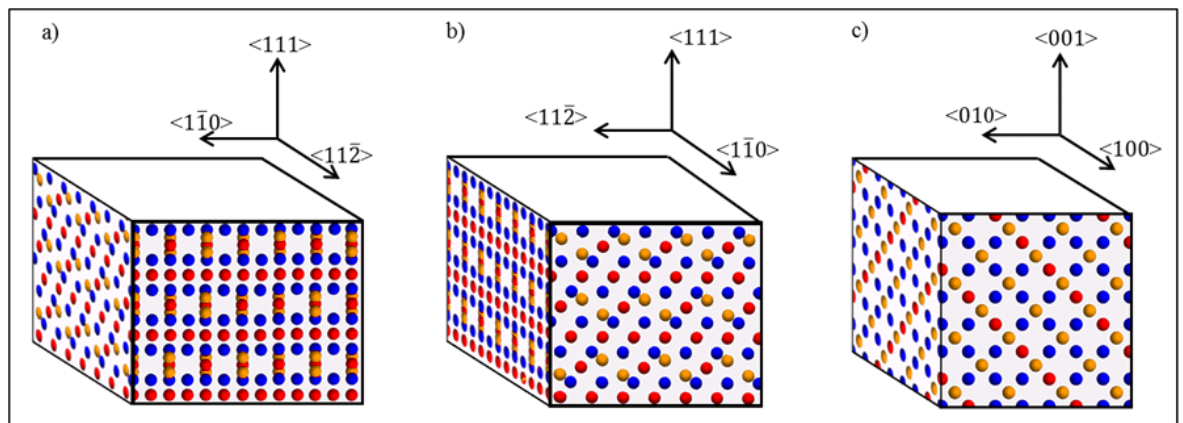


Figure 6: Structure of Fe_3O_4 projected into 2D slices as would be imaged by a correctly oriented TEM sample. a) $[11\bar{2}]$ zone axis of (111) growth direction Fe_3O_4 . b) $[1\bar{1}0]$ zone axis of (111) growth direction Fe_3O_4 . c) $[100]$ zone axis of (001) growth direction Fe_3O_4

2.3 Electronic configuration and Hund's rules

The Fe sites in Fe_3O_4 carry a magnetic moment as a result of the partially filled d-states of this atom. Whilst this is more fully described by spin dependent density functional theory approaches within the context of many atoms in a lattice, a site by site approach based on nominal valence and Hund's rules [49, 50] gives a good insight into some of the transport and magnetic behaviour of Fe_3O_4 . Hund's rule of maximum multiplicity states that electrons in an unfilled electronic subshell will occupy the highest possible spin state as a result of a) electrons filling empty states before forming paired orbits and b) the many half-filled states aligning additively to give a maximum summed spin for the atomic site.

This rule implies that aligned electron spins in different physical orbitals is the most stable and therefore the lowest energy configuration of electrons within a particular atomic sub-shell. Initially this was believed to be a result of minimising electron-electron overlap and therefore reducing Coulombic repulsion between electrons, however later work with refined electron wavefunctions in the 1970s showed the electron-nucleus term dominated this behaviour as electrons in the higher multiplet state are less effectively screened from the atomic nucleus [51].

In the case of Fe ($Z=26$) the general electronic structure of the neutral atom is $1s^2 2s^2 2p^6 3s^2 3p^6 3d^6 4s^2$ with the 4s states lower in energy than the filled d-shell. This can be more easily expressed as $[\text{Ar}] 3d^6 4s^2$ which shows the interesting unfilled shells and valence electrons outside of the noble gas configuration of an Ar atom.

For the two cationic Fe sites in FeO_4 this gives electronic configurations of $[\text{Ar}] 3d^6$ for Fe^{2+} and $[\text{Ar}] 3d^5$ for Fe^{3+} . According to Hund's rule the d-shell of a Fe^{2+} cation has six electrons, of which five are aligned spin up and one aligned spin down. The Fe^{3+} cation has five d-shell electrons, all of which are aligned in a spin up configuration. This leads to a higher magnetic moment on the Fe^{3+} sites than the Fe^{2+} .

Across a full unit cell of Fe_3O_4 ; which contains a Fe^{2+} B-site aligned with a Fe^{3+} B-site, both of which are anti-aligned to a Fe^{3+} A-site, the net magnetic moment is generated entirely from the spin up Fe^{2+} site. Both Fe^{3+} sites have an intrinsic magnetic moment of $5 \mu_B$ however these are opposing one another and therefore net to zero. The remaining Fe^{2+} site has six d-shell electrons, of which five are in a majority spin configuration and one opposes this. Overall this gives a magnetic moment of $4 \mu_B$. As all orbital angular momentum in this crystalline material is quenched the resultant magnetic moment per formula unit of Fe_3O_4 is simply the $4 \mu_B$ from the uncompensated Fe^{2+} octahedral site [52]. This contributes to a saturation magnetic moment of 471 emu/cc for bulk Fe_3O_4 [53, 54].

2.4 Conductivity in room temperature Fe_3O_4

The ionic distribution of sites in Fe_3O_4 is such that the tetrahedral Fe_A sites of Fe_3O_4 are described by Fe^{3+} valences whereas the octahedral Fe_B sites are mixed equally between 2+ and 3+ sites and due to rapid electron hopping between these octahedrally co-ordinated sites are described as $\text{Fe}^{2.5+}$ sites. The conductivity of room temperature Fe_3O_4 is dominated by electron hopping between the Fe_B sites. Since the electron which is most easily donated from the Fe^{2+} site is the single spin down electron, and the only free states to receive an electron on the Fe^{3+} site are also spin down states (in accordance with Hund's rules described above) the electron hopping between the ferromagnetically aligned Fe_B sites is driven entirely by these spin down, minority state electrons. This makes

the conductivity within the bulk of Fe_3O_4 spin polarised. Conductivity behaviour has been calculated by Ihle and Lorentz [55-57].

This spin-down electron hopping between aligned Fe_B sites also makes the electron hopping integral depend directly on the alignment of the spins on neighbouring Fe sites. In the case of magnetic canting or at defect structures which disturb the magnetic order of Fe_3O_4 this hopping integral (t) takes the form $\sigma \propto t^2 = t_0^2 \cos^2 \frac{\phi_{\text{Fe-Fe}}}{2}$ [25] where $\phi_{\text{Fe-Fe}}$ is the angle between neighbouring Fe_B spins. This gives a maximum conductivity with the value t_0 in the case of aligned spins and reduces to zero in the case of perfectly anti-aligned Fe_B spins.

This simplistic explanation of conductivity is borne out by the density functional theory calculations performed on the room temperature structure of this material which gives a half metallic band structure with spin down d-type electrons at the Fermi level meaning Fe_3O_4 can only conduct in the minority spin channel via d-type states.

Numerous theoretical studies have shown the band structure of bulk Fe_3O_4 is half metallic in character [18-20]. This is due to non-symmetric spin split electronic states, which is observed in all ferromagnetic materials. However in Fe_3O_4 this also leads to a band gap in the majority states at the Fermi-level.

2.5 Verwey Transition

Fe_3O_4 undergoes a charge ordered structural phase transformation; the 'Verwey Transition', below the Verwey temperature [21] of approximately 122 K. At this point the Fe_3O_4 structure distorts from cubic symmetry to a monoclinic structure [23] and charge ordering occurs on the octahedral Fe_B sites [55, 58].

A significant reduction in the B-site electron hopping rate leads to charge ordering based on the separation of the octahedral Fe_B sites into two populations, one with a discrete charge of 3+ and the other with a discrete charge of 2+. Above the Verwey temperature this ordering is broken down by electron hopping between octahedral sites giving a nominal charge of 2.5+ on all Fe_B sites.

The Verwey transition also leads to problems in modelling the structure and electronic states of Fe_3O_4 in the cubic room temperature structure. Density Functional Theory (DFT) calculations are 0 K calculations which should give the below Verwey transition electronic and atomic structure of Fe_3O_4 . However, the calculated cell can be forced to be cubic by appropriate selection of cell geometry and structural relaxation. DFT calculations of Fe_3O_4 are generally performed using DFT+U calculations to give an improved representation of the band-gaps presented in this material, however the Hubbard +U term is naturally not an *ab initio* parameter which suggests DFT calculations

are not capable of fully explaining the structure and electronics of room temperature Fe_3O_4 .

The Verwey Transition and the sharpness of its onset as a function of temperature is often used to qualitatively judge the quality of Fe_3O_4 as the full realisation of the room temperature crystal stoichiometry and structure is required to allow the fully charge ordered low temperature state to be realised [59].

2.6 Super-exchange interactions (SEI) in metal oxide systems

Magnetic exchange interactions express the strength of the interaction between close proximity atoms which lead to magnetic ordering. In a metallic ferromagnetic material such as pure Fe or pure Co, the delocalised conduction states at the Fermi-level overlap between atomic sites and lead to standard metallic bonding with delocalised electrons contributing to the exchange interactions. However, in oxide systems such as Fe_3O_4 the electron density is expected to be highly localised and lead to largely ionic bonding between cation (Fe) and anion (O) sites which carry no magnetic moment. This requires a different explanation of the magnetic ordering of metal oxides as a result of oxygen mediated exchange mechanisms than that exhibited in standard metallic ferromagnets. These metal-oxide-metal super-exchange interactions (SEIs) are strongly dependent on the bond angle, bond length and symmetry of the bonding electrons across the interaction triplet.

The theoretical basis for super exchange interactions is derived from the symmetry and physical shape of electron orbitals which are involved in the ionic bonding of the cation and anion sites in the metal oxide. As discussed above, the Fe sites in Fe_3O_4 are either Fe^{3+} or Fe^{2+} sites giving at least one electron in each of the physical orbitals of the 3d sub-shell. Of these five d-orbitals, three have π -type symmetry and give the t_{2g} orbitals and two have σ -type symmetry giving the e_g orbitals. The O sites meanwhile have full $2p^6$ subshells giving rise to 2 π -type symmetry and a single σ -type symmetry orbital, all of which contain two electrons. Orbital overlap is only achieved between electrons of equivalent symmetry [60]. Therefore the two overlapping sets of orbitals are the $p\sigma$ - $d\sigma$ and the $p\pi$ - $d\pi$. With σ type interactions being dominant due to their greater physical overlap [60]. Super exchange is described in much greater detail by Goodenough *et al.* [60-63] and Kanamori [64].

The form of the Heisenberg spin Hamiltonian is shown in Equation 1 where J_{ij} represents the magnitude and the sign of the interaction between the i^{th} and j^{th} spins within the crystal structure. In Fe_3O_4 the spins i and j are only associated with Fe sites, the O site do not contribute any overall magnetic moment but are essential to the bonding which generates the super exchange interactions. To use this form of exchange interactions we

must work in a theoretical framework of localised magnetic moments associated with atomic sites.

We express the magnetic behaviour of Fe_3O_4 in terms of localised spin moments and can therefore use a classical Heisenberg spin model and based on previous work determining the effect of nearest neighbour interactions and further interactions we can neglect all but nearest neighbour interactions from calculations [26]. This helps to justify the highly geometrical basis of the formulation of super exchange as an ionic property between neighbouring atomic sites.

$$\mathcal{H}_{exc} = - \sum_{i \neq j} J_{ij} \mathbf{S}_i \cdot \mathbf{S}_j \quad \text{Equation 1}$$

The magnetic structure of Fe_3O_4 is determined by three exchange constants, J_{AA} , J_{AB} and J_{BB} . Firstly, the 125° bonds between octahedral and tetrahedral sites are strongly antiferromagnetic and dominate the overall magnetic properties of this material. The high strength of the J_{AB} interaction is what must be thermally overcome to reach the Curie temperature and is therefore the reason why this value of $T_c = 868 \text{ K}$ is so high. This interaction makes the Fe_A and Fe_B sublattices align antiferromagnetically and leads to the ferrimagnetic order of the overall material bulk.

Next, the interaction between the Fe_B sites J_{BB} is mediated through 90° bonding across an O site. Overall this interaction is weakly ferromagnetic, however it is challenging to de-convolve the bonding effects of super-exchange from the conduction electron based effects of the double Zener interaction [65, 66] which favours the ferromagnetically ordered case. As this interaction is considerably weaker than the J_{AB} interaction this is not of huge importance to achieving the curie temperature of the overall material.

The final interaction, between Fe_A sites is antiferromagnetic; however, this interaction is relatively weak when compared with the J_{AB} interaction, both as a result of the exchange energy being lower, but also due to the lower density of A-A interactions with the material.

Beyond the complexity of the physical origins of the super exchange interactions, it appears that in orthoferrites a general expression for super exchange is achieved by using a $(-\cos^2 \theta)$ dependency where θ is the angle across the oxygen site [31, 67]. This explains why high angle bonds tend toward antiferromagnetic (AFM) coupling in rock salt structures and across the J_{AB} interaction and why the J_{BB} interaction is both weak and can become ferromagnetic

Various studies have been performed, both experimentally and theoretically to extract values for the three exchange integrals. Margulies *et al.* [31] have used exchange

constants of $J_{AB} = -1.9$ meV (-22K), $J_{BB} = 0.26$ meV (3K) and $J_{AA} = -0.95$ meV (-11K) to explain the properties of APB defects which were extracted from the earlier study of De Grave *et al.* [68] to explain the curie temperature of Fe_3O_4 .

Mazo-Zuluaga *et al.* [27] showed they could reproduce a very accurate Curie temperature using exchange constants of $J_{AB} = -2.92$ meV $J_{BB} = 0.63$ meV and $J_{AA} = -0.11$ meV based on an altered Hamiltonian with an added factor '2' outside the summation $i \neq j$ (not that this alters the physics). With a cubic anisotropy term of 8.43×10^{-2} meV/nm³ implemented in their modelling. The exchange constants used by Mazo-Zuluaga *et al.* constants came from the work of Uhl and Siberchicot [26] working on spin spirals. These two sets of exchange integrals show a significant variation in the three exchange constants depending on the techniques used. In later magnetic modelling we use the exchange values of Uhl and Siberchicot as a starting point [26].

2.7 Antiphase domain boundary (APB)

Antiphase domain boundaries are structural defects defined by fractional lattice vector shifts of the Fe_3O_4 structure between neighbouring grains in the material as shown in Figure 7. These defects are observed with a high density in grown films of Fe_3O_4 and have a significant effect on the overall properties of the grown layer leading to a number of anomalous thin film properties including negative magnetoresistance [69, 70] and very high saturation fields [31, 54]. In previous studies APB densities have been observed which give an average grain size between APB defects of between 5 – 50 nm depending on deposited film thickness [70, 71]. To form an APB requires an extended boundary between two or more neighbouring grains of Fe_3O_4 across which the underlying crystallography is shifted by a fractional lattice vector. This means the boundary is neither twinned, nor visible in diffraction based analysis, however the underlying crystal symmetry is broken which manifests itself in altered bulk properties.

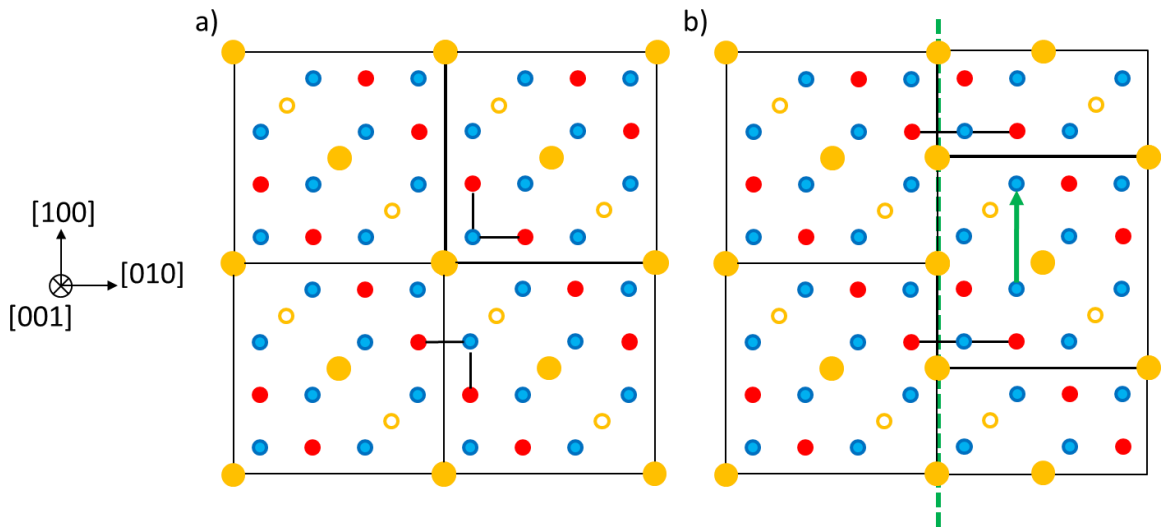


Figure 7: Diagram of an APB with reference to structure shown in Figure 3. a) Shows the undisturbed structure of a plane of Fe₃O₄ in the [001] direction, within this configuration only 90° bonds can be found between Fe_B-O-Fe_B indicated in black. b) Shows the same structure with an APB defect created by shifting the right hand side of the structure by $\frac{1}{2}a_0[100]$. This crystallographic shift is shown with the green arrow and the crystal grain boundary is shown with a green dashed line. This defect returns O sites to their normal position but gives rise to 180° Fe_B-O-Fe_B bonding which generates an antiferromagnetic coupling.

There are a number of reasons why APB defects form in grown films including equivalent growth nucleation sites for the Fe₃O₄ structure on higher symmetry substrates such as MgO, interfacial strain mediation and as a result of the three dimensional growth mode of molecular beam epitaxy (MBE) deposition. Recent work by McKenna *et al.* has shown APB defects in Fe₃O₄ have very low formation energy [72]; this coupled with the many formation mechanisms for such defects means they are found with high densities across a wide range of substrates including MgO [69, 70], MgAl₂O₄ [69, 73, 74], and Al₂O₃ [71].

The large unit cell of Fe₃O₄ with different symmetry sublattices of Fe and O allows antiphase domain boundaries to form [31, 70, 75, 76]. These defects are defined by a structural translation (of a fractional lattice vector) which maps an O site onto the position of an inequivalent O site within the unit cell. Such a translation does not break the O sublattice structure but repositions the Fe_B and Fe_A vacancies across the defect interface giving rise to non-bulk configurations of Fe-O-Fe triplets and therefore altering the Super-exchange interactions locally within the Fe₃O₄.

The most important structural effect of APB defects is in the repositioning of the Fe_B vacancies in the vicinity of the structural defect boundary. This alters the super-exchange interactions and almost universally leads to an introduction of 180° Fe_B-O-Fe_B bonding. As discussed above, this leads to strong AFM coupling across the defect

boundary as expected in materials where 180° configured metal-O-metal triplets are observed, for example all the antiferromagnetic rock salt structures.

This extended, antiferromagnetically coupled, two dimensional nature of an APB leads to a range of unusual properties. APB boundaries are likely to create a persistent magnetic frustration around the site of the defect boundary due to the AFM superexchange interactions around this structure. This makes it almost impossible to magnetically saturate a Fe_3O_4 film with a high APB defect density.

Furthermore, the conductivity of Fe_3O_4 is highly dependent on forming the ferrimagnetic alignment between Fe_B sites on which the double Zener interaction mediated conduction depends. If APB defects are creating AFM coupled boundaries in the material these form a natural block to B-site electron hopping conductivity and suggest an APB could act as a spin valve in its own right [77] leading to the negative magnetoresistance (MR) properties exhibited by thin film Fe_3O_4 .

2.8 Polar structures and interfaces

By growing Fe_3O_4 in the [111] orientation this material becomes chemically layered with single species layers of O, 3Fe_B and $\text{Fe}_A\text{Fe}_B\text{Fe}_A$. Furthermore, these single species planes are electronically polarised with the O planes all being anionic and the Fe layers being entirely cationic.

One of the main obstacles to polar oxide growth is the divergent electrostatic potential of the grown film. This must be mediated in a real heterostructure by a stabilisation mechanism; such as atomic mixing, interface roughening and faceting and/or pure electronic interface reconstructions. For a period of time it was not clear that polar oxides could be grown in a single phase as these materials appeared to phase segregate at the interface or facet to produce neutral surfaces [78-80].

The chemical layering of these materials opens the possibility of tailoring interface structures with atomic control in the Z-direction. Altering the interfacial chemistry and structure of a heterostructure interface would allow a range of unique electronic and functional properties to be generated from a single material pair, this would be useful for tailoring interface properties to optimise spin diffusion or spin tunnelling within a device.

The ultrahigh vacuum (UHV) termination of $\text{Fe}_3\text{O}_4(111)$ is on a relaxed single tetrahedral Fe_A plane [10, 81, 82]. The experimentally determined spin polarisation of this surface is unclear with spectroscopic techniques showing different results for spin polarisation at the Fermi level varying from -80% [83, 84] to +20% [10] depending on the techniques used. This value will certainly be highly sensitive to surface chemistry and structure.

2.9 Spintronics

The success of modern computing has been an astonishing feat of scientific, engineering and corporate endeavour. This has been achieved through continuous efforts to scale down the transistor to allow ever greater processing power with reductions in production cost, energy consumption and physical space required per transistor.

The exponential nature of this increasing technological capability is encapsulated in “Moore’s law”. The observation which became a self-fulfilling prophesy and drove this trend by showing the number of transistors on a chip had doubled every 18 month. This observation has held true from the early 1970’s up until now [85, 86]. Similar laws of exponential increase in data storage and network bandwidth have been observed over similar timeframe.

However, the ability to continually scale down Si and SiO_x based devices will soon reach fundamental size constrains for complementary metal oxide semiconductor (CMOS) and metal oxide semiconductor field effect transistor (MOSFET) technologies. Current gate widths of Si based MOSFET are 22 nm. If this size falls much lower the transistor will be compromised by significant leakage currents, heat build-up and lithographic constraints which prevent ever smaller devices. To continue the rate of earlier development in computing power, or simply to extend on what has already achieve a completely new route to developing computational logic will be required.

One of the various possibilities for developing new computational devices is to develop ‘spintronics’ devices. Current electronic systems are based on manipulating and transporting the electron around a device and thereby carrying the intrinsic charge of the electron around an electronic architecture.

Spintronics seeks to achieve the same, but by exploiting the spin of the electron. This has a number of significant potential advantages. Firstly, the spin of the electron is a two state system with spin either projected ‘up’ or ‘down’ this allows logical operations to be performed on the spin state [87] which cannot be performed on the electron charge. Secondly, spin-transport does not necessarily require electron transport if a spin imbalance can be propagated independent of electron transport then joule heating effects as a result of electrical resistance may be avoided.

Spintronics is currently a well-established research field in condensed matter physics [87] looking to use the intrinsic spin angular momentum of the electron to provide data storage, signal propagation and logical devices.

The first commercial successes of spintronics are in the magnetic read head industry where giant magnetoresistance (GMR) devices are used as a highly sensitive

detector for the local magnetisation of a hard disk drive [88]. GMR devices are explained more fully in the following section.

Whilst this shows the level of interest in spintronic devices and applications, one of the greatest challenges to producing spintronic devices is the development of highly spin polarising materials for spin electrodes and fabricating the atomically controlled interfaces

2.9.1 Discovery of Electron Spin

The discoveries of the early twentieth century have become so fundamental to modern science that it is worth outlining the rapidity and importance of developments of the quantum mechanical treatment of electrons in the 1920's.

The 'spin' of the electron is the intrinsic quantum mechanical angular momentum of the electron and is unrelated to the orbital angular momentum of an atomic electron.

The concept of spin was first suggested by Pauli. However this idea was named and developed by Uhlenbeck *et al.* in 1925 [89, 90]. The essential mathematics of the electron spin were developed by Pauli in 1927 [91] giving the Pauli spin matrix. By 1928 the spin of the electron was an integral part of Dirac's relativistic quantum mechanics [92, 93].

Over this period of just three years, the spin of the electron had been discovered, mathematically explained and become an essential component of relativistic quantum mechanics. The existence of spin in the electron wavefunction completed the information required to formulate the Pauli Exclusion Principle which requires each quantum mechanical state available to a fermion to contain only a single particle.

2.9.2 Giant Magnetoresistance and Tunnelling Magnetoresistance

The physical geometry of GMR and tunnelling magnetoresistance (TMR) based devices are very similar. In both cases, two conducting ferromagnetic (FM) electrodes are separated by a thin spacer layer, when a bias is applied between the two FM electrodes a current may flow depending on the magnetic alignment of the two electrodes. This geometry is a magnetic tunnel junction (MTJ)

In a TMR "spin dependent tunnelling" junction the spacer is an insulating or semiconducting material which electrons must quantum mechanically tunnel across from filled states in the first electrode into empty states in the second electrode. This process was first discovered in 1975 by Julliere [94] based on Fe/Ge/Pb and Fe/Ge/Co junctions at liquid He temperatures of 4.2 K with an observed 14 % variation in resistance.

This process was not accomplished at room temperature for another 20 years [95, 96] due to the challenges of fabricating the ultra-thin barriers required for effective spin

dependent tunnelling. Current TMR ratios of over 600 % have been achieved using MgO tunnel barriers by Ohno *et al* [97].

Giant magnetoresistance does not rely on a tunnelling barrier, but rather a conducting nonmagnetic space. GMR was observed independently by Grunberg *et al.* [98] and Fert *et al.* [99] in the late 1980's leading to the Nobel prize for Physics in 2007. GMR is reviewed by Thompson [88]. These initial discoveries were made due to the observation of a large resistance drop in magnetic multilayer structures based on the alignment of the magnetic layers.

The geometry and concept of spin dependent tunnelling/conduction can be seen in Figure 8 where the magnetic alignment of the FM layers determines the orientation of the spin up and spin down channels within the device. The spin density of states (SDOS) presented here are a schematic representation of Fe_3O_4 which is half-metallic at the Fermi-level with states in the minority (spin down) channel. In Figure 8a the two Fe_3O_4 layers are aligned so there are aligned states available for conduction in the minority channel of both electrode layers. This theoretically allows either conduction or tunnelling (dependent on barrier material) without requiring a spin flipping event. This is compared with Figure 8b, where the available donor states in the left hand side electrode are mismatched for the receiver states on the right side of the diagram as a result of the anti-aligned magnetisation of the two layers.

The GMR/TMR ratio is the percentage change in resistance between the high resistance anti-aligned and low resistance aligned states. To produce success MTJ's requires high quality device fabrication and control over the magnetisation of two neighbouring magnetic layers, this is generally achieved by pinning one of the two FM layers with an anti-ferromagnetic seed layer.

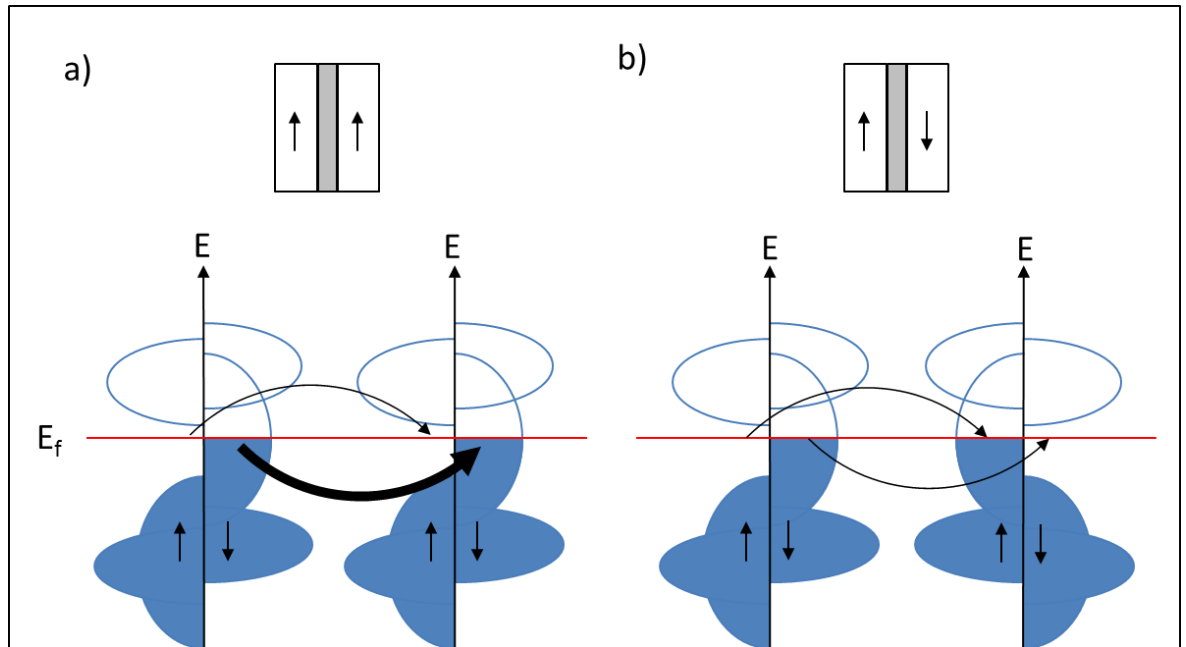


Figure 8: Schematic representation of TMR/GMR with half-metallic electrodes showing conduction in the aligned case in (a) and blocked conduction in the anti-aligned case in (b).

2.10 Magnetite for Spintronic Applications

In Conclusion, Magnetite is an ideal candidate material for spintronic device applications. The high curie temperature of $T_c = 858$ K makes the macroscopic magnetic properties of Fe_3O_4 useable in a room temperature computational operating environment. The predicted half-metallicity of this crystal structure are ideal for ensuring high GMR/TMR values in conventional devices or for using as a spin polarising or spin detecting element in extended novel structures. Furthermore, the material components Fe and O are abundant and cheap making Fe_3O_4 an environmentally and economically viable material.

For implementation in devices; Fe_3O_4 forms stable, atomically sharp interfaces with semiconductors and oxides making integration with current MTJ technology possible. The layered polar nature of this material also makes the future possibility of interfacial atomic engineering and therefore tuned properties are also a key consideration in the selection of Fe_3O_4 as a future functional material.

Chapter 3. Methodology

Forming a correlation between the structures of thin film interfaces and defects at the atomic scale and thin film functional properties at microscopic and mesoscopic length scales is essential to the development of future spintronic devices. This requires a wide range of fabrication, characterisation and analysis techniques to gain a significant understanding of the materials under investigation. Primarily I have used electron microscopy techniques to establish atomic resolution structural and chemical information from specimens prepared to allow the transmission of a high energy electron beam; this however, requires support from a wide range of further techniques.

As this thesis has developed it has been essential to develop from molecular beam epitaxy (MBE) methods to pulsed laser deposition (PLD) to enable the fabrication of high quality Fe_3O_4 . Extensive previous study has been performed on MBE grown Fe_3O_4 on MgO and this forms a starting point for my work, to verify and understand the previous findings within this system, however, within this growth system it is highly challenging to reduce the defect densities which compromise the potential use of Fe_3O_4 in spintronic devices. By moving to crystal symmetry matched $\text{Fe}_3\text{O}_4/\text{MgAl}_2\text{O}_4$ growth it was hoped the defect formation mechanism could be suppressed, however a mixture of lattice mismatch and the fundamental properties of molecular beam epitaxy have shown this is not possible. This lead me to attempt a completely different growth mode with PLD growth and subsequent high temperature annealing. Firstly this was performed on Ytria stabilized Zirconia to allow high temperature post processing and to test the effects of interfacial strain. Success in producing far higher quality Fe_3O_4 films via this methodology led me to continue with PLD grown on strontium titanate, an ideal substrate for testing the viability of spinel/perovskite interfaces which open up the possibility of many multifunctional devices exploiting the wide range of properties available within the perovskite family.

To realise the desired properties of Fe_3O_4 requires the highest possible standards of chemical and structural analysis to ensure defect free, fully stoichiometric structures. This has led to a wide range of high specification characterisations being required.

Firstly I will describe the fabrication methods used in this work, including MBE and PLD. These techniques require high vacuum techniques which allow a significant flux of atoms to travel unhindered to the deposition surface without being either scattered or contaminated by other material species. Both MBE and PLD growth techniques have been used to produce epitaxial single crystal growth.

Grown crystals require analysis using a range of mesoscopic analysis techniques including chemical analysis, magnetic measurements, electron transport measurements and crystallographic analysis on large specimens before commencing microscopy sample preparation which is both physically destructive and limited to sampling incredibly small volumes of the deposited material. This work gives us the experimentally verified structures and properties required for theoretical analysis. At present no one experimental procedure or technique is capable of giving a full view of the behaviour of condensed matter systems on all important length scales.

The final stage in most of this work is to verify the exact atomic structures we observe and then from atomic structure study the macroscopic properties seen in the grown films. To do this we use image simulations and density functional theory (DFT) to optimise experimentally determined atomistic models. With image simulations forming a link between transmission electron microscopy (TEM) data and DFT providing a chemical and energetics related structural refinement tool. Atomistic magnetic simulations have been possible in the case of antiphase domain boundaries (APB) defects where specific atomic configurations can be determined.

Importantly, significant advances have been, and continue to be made across the entire suite of fabrication, characterisation and computational theory branches of this work. This means we can achieve so much more today than would have been possible only ten or twenty years ago, and in areas such as aberration corrected microscopy we can now lift elegant theoretical approaches developed in the 1940's [100] and utilise this work with modern computational power and electrical engineering. The advancement of computational technology has been a major modern miracle for science and humanity and this is observed across the theoretical approaches which can now be utilised for complex modelling of image simulations, magnetic properties and structural and electronic calculations. This state of development also offers great potential for the future, we must assume that in only a few short years' scientists and engineers will once again look back and see the great advancements made in the years to come.

To produce thin film heterostructures, perform sample characterisation, and progress to detailed microscopy and eventual analysis has required input from a wide range of collaborators and technicians around the world. Where contributions from others have been used they are credited within the results sections of this text.

The intention of this form of materials science is to form an ever closer inter relation between physical fabrication of layers and devices, experimental analysis of film properties at a range of length scales and the theoretical underpinning of observed properties.

3.1 Vacuum Physics and Ultra high vacuum.

Vacuum systems are required in this work for both cleanliness and control in terms of high quality sample growth and to form non-interacting regions of space in which molecular beams and electron beams can be formed and propagated without significant interactions with matter.

To this end the MBE and PLD deposition systems described later are inherently dependent on the formation of high quality vacuum conditions. As are the microscope guns and columns which require vacuum for the propagation of electrons and for the formation of high purity electron gun tips.

To maintain vacuum and provide a useable system, elaborate sample transfer mechanisms are required using mechanical arms and load locks operating at various degrees of 'high vacuum'. This is seen in the transfer systems of deposition equipment and the sample transfer systems of electron microscopes. In this thesis vacuum chambers have been used in many circumstances so no specific vacuum diagram is given.

3.1.1 Ultra high vacuum

Ultra high vacuum (UHV) represents the highest possible standards of achievable laboratory vacuum equipment. Generally UHV is quoted to give pressure readings of $< 2 \times 10^{-10}$ mbar a full 13 orders of magnitude lower than atmospheric pressure. To achieve this exacting standard of low pressure most of the pumping equipment, pressure measurement and system engineering requires a rethink from general vacuum systems. The purpose of achieving such high quality vacuum, is that even in a UHV operating condition an atomically clean surface will be coated with one monolayer of contaminants within 8 hours. This allows enough time for most deposition, probe microscopy or chemical analysis techniques to be performed with less than a single monolayer of contaminants being present on the surface. Simply allowing the pressure to rise by one

order of magnitude puts this contamination time below one hour and makes performing a clean experiment almost impossible.

To produce the super low pressure of UHV the design of the chamber and components attached into the system must be UHV compatible. This means no plastics can be placed within the chamber, and soft gaskets cannot be employed. All the equipment in the chamber is either high quality ceramics or metal and joints in the system are sealed with Cu gaskets which are pressure formed into a seal using a UHV knife edge. These materials can all withstand the high temperature of the baking procedure and are not prone to outgassing.

Many procedures can be performed *in-situ* including crystallographic analysis using low energy electron diffraction (LEED) and reflection high energy electron diffraction (RHEED), probe microscopy techniques such as atomic force microscopy (AFM) and scanning tunnelling microscopy (STM) and chemical analysis with x-ray photoelectron spectroscopy (XPS) and Auger electron spectroscopy. Many of the electron beam techniques use LaB₆ electron gun tips which are damaged by contact with Acetone, so this solvent should be avoided for UHV system cleaning.

At the very low pressures of UHV systems much of the behaviour of atoms and molecules needs a considerable re-think. The motion of molecules can largely be considered to be ballistic at such low pressures which makes pumping through a small aperture exceptionally difficult, the residual partial pressure is so low that molecules are not 'pulled' to create a pressure equilibrium in the way they would be in a higher pressure regime. This makes UHV chamber design very important, attention must be taken to ensure bottlenecks and trapped volumes are not being created.

UHV operates at such a low pressure that even a non-leaking system will not achieve UHV without a significant cleaning and outgassing of the internal surfaces of the chamber. This requires baking the entire system at temperatures around 100-140 °C for extended periods of time (12-48 hrs) to raise any residual water, organic molecules or carbon contamination into the chamber to be pumped away. Without performing this process the overall pressure can be compromised by internal reservoirs of material leaking into the chamber volume known as a virtual leak.

The pumping systems used to achieve UHV are not capable of handling high pressure, so a range of pumping systems are required, with backing pumps to provide a differential between atmosphere and the UHV pump exhaust. All UHV systems are pumped to approximately $\times 10^{-4}$ mbar using standard rotary pumps before any of the specialised UHV pumping is added. The mainstay of modern UHV pumping equipment is the turbo pump which can remove significant volumes of gas at a high rate of pumping.

Turbo pumps are based on a series of rapidly revolving (60-75,000 rpm) blades operating in a contra motion which at the higher end of the pressure range will operate as a high powered conventional pump, but at the very low pressure range can effectively bat single atoms or molecules out of the chamber, as the counter rotating blades prevent any material from progressing back into the system from one blade structure to the next. Once UHV conditions are almost achieved a range of highly specialised UHV specific pumping methods can be enabled to create the final high pressure environment. This includes cryo-pumping, Ti sublimation pumping and ion pumping; Cryo-pumping requires an area of the internal chamber to be made cold such that molecules are preferentially likely to stick to the chamber wall. This cooling is generally achieved through passing LN₂ cooled air through the chamber wall into a cold trap. This process can only be effective at very low pressures but is reversible, with trapped material being released as the chamber warms up. This is useful for boosting pressure performance temporarily during an experiment.

Ti sublimation works by depositing a thin layer of Ti on an area of the chamber wall by passing a large current ~40 A through a high diameter Ti filament. This large surface area of Ti is reactive and will slowly form TiO₂ removing oxygen from the chamber. Ti sublimation pumps are fired periodically to replace the metallic Ti surface.

Ion pumping requires atomic or molecular content in the vacuum to pass an ionising filament held within a capacitor configuration. Any ionised molecules or atoms will be pulled to the capacitor plate and therefore be removed from the vacuum.

Further information on vacuums and UHV can be found in A. Chambers' "Modern Vacuum Physics" [101].

3.2 Thin Film Fabrication

Thin film deposition is a heavily researched and developed engineering process which is required for photovoltaic cells, the semiconductor industry and optical coatings. However, the exact specification of the growth, the level of compositional purity and the layer thickness required determine the most appropriate deposition method. In the case of epitaxial metal oxide layers which achieve large areas of single crystal growth we are placing some of the highest possible growth condition constraints in this work.

3.2.1 Molecular beam epitaxy

Molecular beam epitaxy is an essential growth technique for producing the highest levels of control over interfacial structure, film stoichiometry and thickness. MBE is used to produce epitaxial single crystal films directly during deposition. However, this film growth method is relatively slow, potentially allows variations in film characteristics across the

deposited wafer and requires a high degree of calibration and control to ensure the many operating parameters are optimised to give the desired film growth.

In this work on Fe_3O_4 I will show that many of the detrimental film properties we are looking to understand and eventually remove are a result of film growth defects which result from the MBE deposition process. Defect densities in MBE grown films are much higher than that observed in bulk single crystal materials such as that used to form the deposition substrate. A major problem with this is the grown defect structures are not generally a repeatable property of the growth but rather a collection of effects generated from interfacial strain, three dimension growth modes and crystallographic defects within the grown film.

Molecular beam epitaxy is only fully realised when the constituent atoms of the deposited films can be considered to grow in a layer-by-layer fashion with each atom having the freedom to move around the wafer sufficiently to arrive in a low energy configuration. This requires slow growth rates for single crystal Fe_3O_4 . During the deposition process, which can take a number of hours, the flux of Fe and O arriving at the sample surface must be maintained at a constant rate. Furthermore this slow growth mechanism requires incredibly high vacuum levels to ensure contaminants are not incorporated into the film during growth. This operating regime is generally referred to as Ultra High Vacuum (described above) which requires exacting standards of mechanical integrity and leak and pseudo leak detection to be performed alongside chamber baking to remove contaminants and allow the UHV system to be outgassed.

Molecular beam epitaxy was used to produce the $\text{Fe}_3\text{O}_4/\text{MgO}(111)$ and $\text{Fe}_3\text{O}_4/\text{MgAl}_2\text{O}_4(111)$ specimens in this work and was performed in the Chemical Engineering department of Northeastern University, Boston. Fe_3O_4 was deposited by simultaneous deposition of Fe and O from independent sources onto prepared substrates held at 350 °C. MBE base pressure was less than 2×10^{-10} mbar before growth commenced and growth was conducted at a rate of $\sim 1.2 \text{ \AA min}^{-1}$. Fe was deposited via a Knudsen cell and atomic O was supplied to the sample using an RF-assisted plasma source. A partial pressure of 5×10^{-6} mbar was produced by the atomic oxygen source during deposition.

With metal oxides such as Fe_3O_4 great care must be taken to ensure the sample stoichiometry is not adversely affected by annealing and exposure to vacuum, as both these conditions could well lead to oxygen being leached from the film and result in defects or phase transformations.

3.2.2 Pulsed Laser Deposition (PLD)

Pulsed laser deposition does not require the full UHV conditions of MBE deposition as this is a much faster deposition technique which does not generally deliver layer by layer growth of a crystal. However, a high vacuum will improve the cleanliness of the specimen growth and allows the deposition material to travel unhindered to the sample surface. PLD does not achieve layer by layer growth but rather coats the substrate surface in a range of single atoms, and clusters of materials which are vaporised off a sintered target material in a plasma plume by the high energy incident laser beam. Fe₃O₄ has been deposited from a stoichiometric sintered target of Fe₃O₄ composition. Using a KrF excimer laser ($\lambda = 248$ nm with a pulse duration of ~ 20 ns). This laser has been cycled at 10 Hz. With a laser power density of ~ 2.3 Jcm⁻² [102, 103] giving a growth rate of 25 Åmin⁻¹.

To produce high quality Fe₃O₄ growth using PLD requires post-annealing to ensure uniform chemistry and remove growth defects. This has been performed using an image furnace in a mixed CO/CO₂ atmosphere.

Pulsed Laser Deposition has been used to fabricate the Fe₃O₄/YSZ(111) [102, 103] and Fe₃O₄/STO(111) specimens in this work. Layer by layer deposition was determined from *in-situ* RHEED pattern oscillations monitored during growth.

3.2.3 In-situ deposition characterisation

Growth systems generally allow some degree of *in-situ* characterisation of the specimen surface, chemistry and structure both during and after deposition. Electron diffraction based analysis can be performed during deposition using grazing incidence RHEED [104] and post deposition using normal incidence LEED [105] many growth systems are also fitted with XPS and Auger electron spectroscopy (AES) devices. The nature of UHV equipment with multiple chambers, versatile pumping systems and generic UHV flanges make vacuum systems highly adaptable and allows a significant level of chemical and structural analysis to be performed on a specimen before exposure to air. This is essential both at the film growth optimisation stage, to identify where optimum conditions are met for the correct structural and chemical composition of a film and at the final stages of film analysis to provide complementary data to accompany *ex-situ* techniques including transmission electron microscopy.

RHEED and LEED are both based on accelerating a beam of electrons onto the sample surface and detecting the electron diffraction produced after the electrons impinge on the sample. Electron penetration into the specimen in both of these techniques is

minimal with only the surface and very near sub-surface atoms being probed. While both these techniques have been extensively studied and developed as research tools for surface science in their own right, in the scope of this thesis RHEED and LEED are used purely in a supporting role to monitor film growth and crystal structure.

RHEED uses a high acceleration voltage electron beam, generally several keV, in grazing incidence geometry. This means for a RHEED system in a UHV chamber the electron gun and the detector screen are separate systems attached through separate flanges on the chamber. As the beam propagates along a specific in-plane direction it is possible to pick out the different crystallographic symmetries of the sample as it is rotated. The RHEED systems I have used (Tokyo Institute for Technology) are combined with a rotating sample stage which has allowed both the $\langle 1-10 \rangle$ and $\langle 11-2 \rangle$ sample geometry to be visualised sequentially using RHEED.

RHEED can be used during deposition, and with a hot specimen, although this leads to a significant reduction in the sharpness of the diffraction spots. Monitoring RHEED oscillations is one way to identify layer-by-layer epitaxial film growth as the diffraction condition for specific spots is repeatedly met and broken by the full layers and the partial layers of film during the growth.

LEED uses a normal incident electron beam with acceleration voltages between 50 and 300 eV. Electrons which are back scattered are detected by a spherical geometry fluorescent screen positioned around the electron gun. This normal incident geometry is particularly useful for understanding surface structure and surface reconstructions on a film surface however this technique cannot be used during growth or with a hot sample surface, so is performed after deposition rather than during the deposition process.

Auger electron spectroscopy systems are often integrated into a LEED system as they can use the same electron gun. The Auger effect is an atomic interaction with incoming radiation such as a photon or electron which leads to the ionisation of a core electron from the atom. This electronic configuration of the atom is an unstable, excited state and the electron hole will be filled by an electron from an outer shell. As this occurs the energy of the outer electron transitioning to a lower energy state is decreased making the atomic configuration more stable, however, this excess energy must be transferred elsewhere within the atomic electrons and can lead to the emission of another electron if the transferred energy is greater than the ionisation energy of the third electron. Although this is a three electron process all the transitions involved have well defined energies so the emitted electrons are indicative of the chemistry of their source atom.

The Auger electrons have energy $E_k = -E_{core} + E_1 + E_2$ where E_{core} is the energy of the core level ionised by incoming radiation, E_1 is the energy of the orbital donating an

electron to the core state and E_2 is the energy of the final ionised state which must be overcome to ionise the atom and project an atom into the vacuum.

Since the energy levels of atoms are chemical specific the Auger electron spectrum is dependent on the chemistry of the specimen and can be used to identify the atomic species present in a film and their approximate proportions.

Auger electrons are generally low energy, so this technique requires high or ultrahigh vacuum to create significant detection rates with an electron energy analyser. The Auger component of the signal must be picked out as specific energy peaks against a continuous secondary electron background. Due to the low energy of emitted Auger electrons this technique is highly surface sensitive simply as Auger electrons cannot escape from deep within the specimen.

XPS uses a monochromatic beam (of X-rays) directed onto the surface of a sample to ionise atomic electrons using the photoelectric effect. The energies of the resultant ionised electrons are analysed to determine the chemistry of the specimen. In XPS a monochromatic source of X-rays is produced by pumping transitions in a chemical source. In this work the Al K_α has been used to produce 1486.7 eV photons.

The electrons emitted from the sample are detected by a hemispherical electron energy analyser to identify the energy levels present in the observed sample. The photoelectron effect is more simple than the Auger effect with electrons simply absorbing the energy of the photon and being ejected with this energy minus the work-function of the material. From the energy of the detected electrons the chemistry of the sample can be determined.

3.3 Transmission electron microscopy

Modern transmission electron microscopes perform the atomically resolved imaging and chemical analysis on which this project has relied. All transmission electron techniques require carefully prepared specimen foils which allow electron transparency. The capabilities of modern microscopes rely on significant advances in electron optics over the last twenty years, particularly the implementation of aberration correction methods using multipole magnetic lenses and sufficient computational power to assess and adjust aberration values from the images and electron diffraction patterns of amorphous or spherically dispersed media. In this work I will show results acquired using the Japanese Electron Optics Ltd. (JEOL) 2011 operating at 200 keV and the double aberration corrected JEOL JEM-2200FS TEM/STEM operating at 200 keV based at the York JEOL Nanocentre and the aberration corrected NION 100 (SuperSTEM II) operating at 100 keV based at SuperSTEM, Daresbury.

The JEOL JEM-2200FS is equipped with a wide pole piece compared with the standard specification of this model to allow *in-situ* gas experimentation; however, this is not performed within the scope of this thesis. The wide pole piece is able to give high resolution imaging due to the aberration corrections performed at the objective lens.

The three microscopes used within this project have very different capabilities which make it essential to use all three systems. The JEOL 2011 at York is only able to operate in TEM modes. This limits its effectiveness in performing atomically resolved chemically sensitive imaging. However, this microscope is ideal for performing wide area HRTEM and DF-TEM and the simplicity of this machine with direct access to controls allows rapid performance of diffraction and low resolution imaging techniques to assess structure, epitaxy and to identify defects which are shown in DF-TEM modes. This microscope is also the easiest to access and the cheapest to operate so is an essential entry point for training and to test the quality of TEM specimens.

The JEOL JEM-2200FS is a 200 keV (S)TEM equipped with a HAADF-STEM detector. This allows really interpretable $\sim Z^2$ which has been essential for this project. Much of the atomic resolution imaging in this thesis has been performed on this microscope.

The NION 100 at Daresbury operates at 100 keV and therefore has a much reduced sample penetration compared with the 200 keV JEOL machines. This means samples must be produced to a yet higher standard with sample thicknesses of ~ 25 nm being ideal. However, the NION 100 is the most mechanically stable microscope of the three and is fitted with a high performance *enfin*a spectrometer which has allowed atomically resolved EELS. This machine has been used the least in my work, but has yielded some of the most meaningful data as a result of the combined HAADF-STEM, EELS and mechanical stability it offers.

The majority of transmission electron microscopy theory required for this work can be found in "*Transmission Electron Microscopy – A Textbook for Materials Science*" [106] and "*Electron Energy-Loss Spectroscopy in the Electron Microscope*" [107]

All transmission electron microscopes are operated with a vacuum column in which an electron beam is formed, accelerated and lensed to image a specimen. Within the TEM column the first essential component is the electron gun. Conventionally the gun will produce an electron beam with energies between 80 and 300 keV. There are exceptions to this, with very high voltages (1 – 1.25 MeV) used to produce high sample penetration and short wavelength. There are also very low acceleration systems for biological or beam sensitive specimens operating as low as 30 keV.

The technology that has been used in TEM guns has undergone a number of significant developments since the first tungsten hairpin tips to improve source brightness, coherence and energy spread. Modern TEM systems use cold field effect guns (FEG) to offer energy spreads in the beam as low as ~ 0.3 eV making the beam approximately monochromatic. Improvements upon this can be achieved with post-gun monochromation systems; however, these are expensive and generally limited to high resolution electron energy loss spectroscopy (EELS) applications where the gun energy spread is directly related to the detection energy resolution. Modern cold FEG gun technology also provides exceptionally high source brightness and coherency which are major improvements for scanning transmission electron microscopy (STEM) and TEM respectively [108]. For more information of TEM gun technology read *Williams and Carter* [106]

The essential reason to use the TEM over any other microscopy technique or optical technique is the extremely high spatial resolution which can be achieved using high energy electrons, the high speed of data acquisition and the ability to probe specimens in a wide range of geometries after specimen preparation. TEM is also a comprehensive analysis technique, able to access a wide range of magnification length scales, access real and reciprocal space imaging and offer chemical analysis at high resolution.

Electrons have strong interaction with matter which will be discussed later. More details can be found in [106, 109]. The positive properties of TEM analysis can only be accessed where the challenges of dealing with strongly interacting electrons are mitigated by preparing incredibly thin sample foils which have achieved 'electron transparency'.

TEM sample holders offer a high degree of stability and control over the TEM specimen, with 5-axis control used for crystalline cross sectional specimens allowing the zone axes of the sample to be accurately aligned and imaged.

TEM imaging and selected area diffraction (SAD) patterns are commonly recorded using charge-coupled device (CCD) cameras in modern TEM systems, but historically this place would have been taken by a photographic plate.

3.3.1 Electron optics

Much of the discussion of electron optics treatment within the electron microscope is based on the useful analogy made with optical lenses and optical microscopy. Whilst this is an ideal way to frame the necessity for a transition to electron optics to achieve high spatial resolution and benefit from the strong interactions between electrons and matter there are a number of areas where this analogy falls down.

The lenses drawn into the TEM/STEM ray diagrams in the following sections are schematically represented by optical style double convex lenses. This works well to describe two dimensional ray traces but is fundamentally incorrect as a description of electron optics. To focus either light or an electron beam we need a way to influence the local path length or velocity of the beam which can be accurately varied over the extent of the lens region. With light this is achieved through modulating the local refractive index of the beam path by inserting a physical extent of glass or oil or water into the path of a beam. The relative refractive index between the air and the lens material is all that is required to refract and reflect light.

However, in the electron microscope we need a mechanism to modulate the electron beam in a similar fashion to the optical lens. This cannot be achieved by inserting a material into the electron path as you would simply block electrons. Instead to focus an electron beam in a TEM a magnetic field is applied anti-parallel to the beam using cylindrically symmetric electromagnetic lenses. This allows the strength of the lens to be altered by altering the current passed into the electromagnet, however there are also a range of major drawbacks. Firstly, the lens strength must be maintained and controlled with a high degree of precision and stability in time and secondly the ability to construct the exact lens shapes desired is limited by what can be achieved using the stray fields which propagate into the centre of the pole piece as shown in Figure 9. Overall this makes the optical quality of the best electromagnetic lenses lower than achieved in the best optical lenses which can be constructed with high precision to just about any shape desired (particularly when optical coatings and compound lenses are utilised).

As mentioned above for an optical lens, the electron lens needs the capability to modulate the path length and direction of the incoming electron beam. This is achieved as a result of the Lorentz force which deflects an electron in the presence of an electric or magnetic field according to Equation 2. The ramifications of the Lorentz force are that forces exerted upon a moving an electron are not parallel to the direction of the applied magnetic field, a geometrical effect commonly remembered using the 'right hand rule' which results mathematically from the behaviour of the vector cross product between the velocity of the electron, v , and the magnetic field, \mathbf{B} .

$$\mathbf{F} = q(\mathbf{E} + v \times \mathbf{B}) = -e(\mathbf{E} + v \times \mathbf{B}) \quad \text{Equation 2}$$

Within the electron lens, electrons experience an applied magnetic field pointing up the optical axis of the electron microscope. At the centre of the lens, \mathbf{B} should point directly along the optical axis, opposing the direction of the electron beam, in this case

$v \times \mathbf{B} = 0$ and the electron beam on the optical axis is unperturbed as it experiences no force.

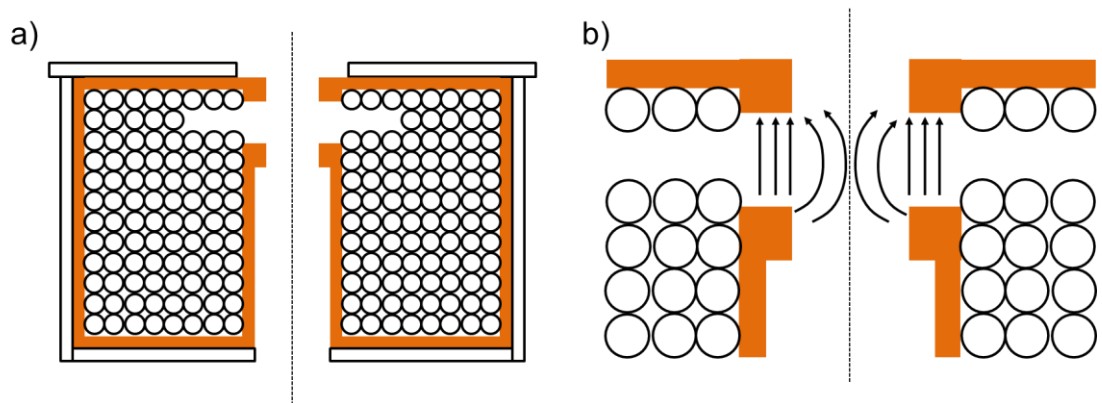


Figure 9: Schematic diagram of an electron lens around the microscope optical axis. A series of coiled wires are. Soft iron pole pieces sit inside the the hole at the centre of the lens and are surrounded by Cu coils used to pass the lens current. (a) shows the overall schematic of the lens (b) shows the pole piece and the magnetic field lines within the gap [106].

However, when an electron enters the magnetic off the optical axis of the lens it experiences a field which fringes away from the optical axis and gives a finite value to $(v \times \mathbf{B})$. This leads to an electron path in which off axis electrons begin to circulate in a helix around the optical axis. As the electron passes through the lens it is accelerated into a helical path on the way into the lens where the stray fields point out of the microscope column and is equivalently decelerated as it leaves the lower portion of the lens where the stray fields point into the optical axis. To ensure these two opposing acceleration values are equivalent electron lens magnetic fields should be highly symmetric vertically.

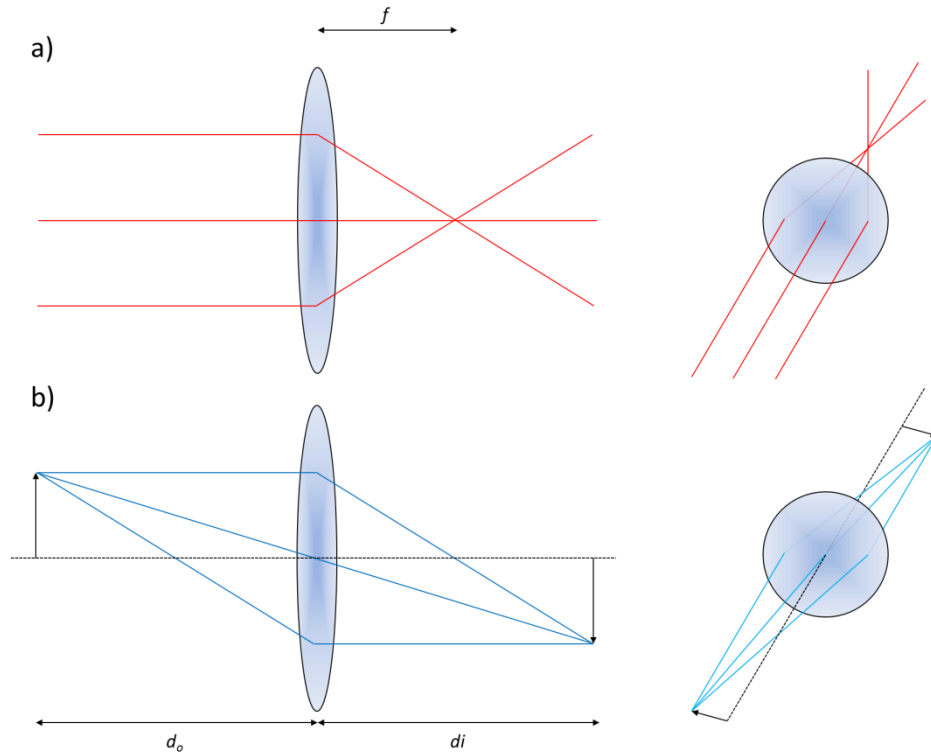


Figure 10: Optical Lens ray diagrams showing the a) the focal length of a lens f with an incident parallel beam and (b) the formation of a focused image.

The full equations which show the ability of the electromagnetic lens to perform a focusing effect require involved mathematics and use of a paraxial approximation. However, this yields two equations, to describe the radial acceleration of the beam which acts to focus the beam shown in Equation 3 and the rotation of the beam around the optical axis (OA) in Equation 4. In these equations $\eta = (e/2m_0c^2)^{1/2}$ [106, 110].

$$\frac{d^2r}{dz^2} + \frac{\eta^2 B^2 r}{2V^{\frac{1}{2}}} = 0 \quad \text{Equation 3}$$

These equations show that the radial motion of the electron is toward the OA and is dependent on the strength of the applied magnetic field, the radius of the electron and the acceleration voltage of the electron. During general operation this makes the strength of the focusing dependent on the magnetic field strength of the lens which is modulated using the lens current.

$$\frac{d\theta}{dz} = \frac{\eta B}{2V^{\frac{1}{2}}} \quad \text{Equation 4}$$

The equation determining the rotation of the electron is simply determined by the magnetic field strength and the acceleration voltage.

3.3.2 Electron velocity, wavelength and relativistic corrections

The most important benefit derived from electron microscopy when compared to optical microscopy is the ability to use the short wavelengths of an accelerated electron beam which bring atomic structure length scales within the diffraction limit.

When an electron is accelerated in an electric field it achieves a kinetic energy equivalent to the accelerating potential difference, in an applied accelerating field of 200 kV, as used in many commercial microscopes, the electron beam is formed of electrons with energy of 200 keV. This energy is related to the wavelength of the electron through the De Broglie wavelength of a particle as expressed in Equation 5 and a standard Newtonian expression for kinetic energy. The relationship between acceleration voltage and the non-relativistic corrected wavelength is plotted with a red dashed line in Figure 11.

$$\lambda_0 = \frac{h}{p_0} = \frac{h}{m_0 v} = \frac{h}{\sqrt{2m_0 eV}} \quad \text{Equation 5}$$

However, when accelerated to 200 keV, an electron is travelling at ~69.5% of the speed of light and therefore the wavelength requires relativistic correction. The relativistic velocity of the accelerated electron can be determined by extracting the γ term from the relativistic kinetic energy equation as rearranged in Equation 6. Without correcting the velocity for relativistic mass gain during acceleration the classic velocity will rapidly exceed the speed of light at high acceleration voltages and thus indicates that relativistic considerations are required.

$$E_k = eV = (\gamma - 1)m_0 c^2$$

$$v = c \left\{ 1 - \left(\frac{m_0 c^2}{m_0 c^2 + eV} \right)^2 \right\}^{\frac{1}{2}} \quad \text{Equation 6}$$

The relativistic velocity of the electron is plotted as a fraction of the speed of light in Figure 11 as a blue curve. The degree of curvature in this line, and the high values of v/c even at modest acceleration voltages require accurate calculations of γ at each acceleration voltage and preclude the use of low velocity $v \ll c$ or high velocity $v \sim c$ approximations in this energy range.

Once the velocity of the electron is known the relativistic mass is simple to extract using Equation 7. The value of m_{rel}/m_0 scales essentially linearly with accelerating voltage in the region 10-400 keV and is almost double at the highest velocities in this range. m_{rel}/m_0 is plotted in green in Figure 11.

$$m_{rel} = \gamma m_0 \quad \text{Equation 7}$$

To identify the relativistic correct to the wavelength we rearrange Equation 8 to give an expression for p_{rel} which can be inserted in place of a classic expression for momentum in Equation 5.

$$E^2 = p_{rel}^2 c^2 + m_0^2 c^4 \quad \text{Equation 8}$$

With some rearrangement this gives Equation 9 which can be rationalised down to a correcting term applied to the classical wavelength value to give the relativistic wavelength of the electron.

$$\lambda_{rel} = \frac{h}{\sqrt{2m_0 eV} \sqrt{1 + \frac{eV}{2m_0 c^2}}} = \frac{\lambda_0}{\sqrt{1 + \frac{eV}{2m_0 c^2}}} \quad \text{Equation 9}$$

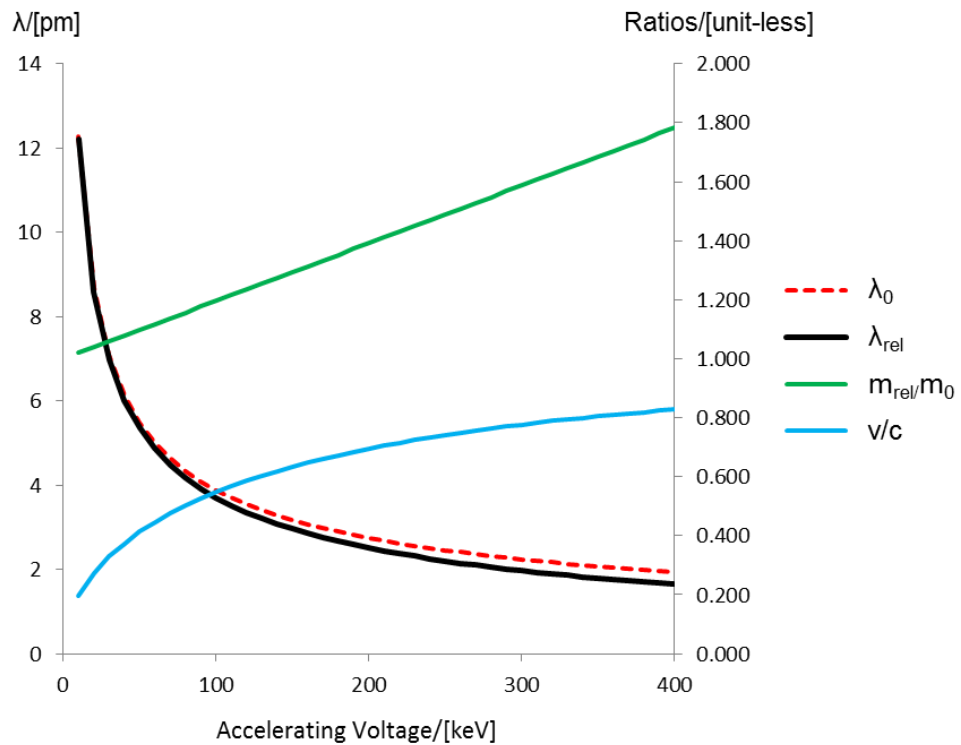


Figure 11: electron wavelength (red-dashed) as a function of accelerating voltage including relativistic correction (black). At typical TEM accelerating voltages of 200 keV electrons are traveling at 69.5% of c making relativistic correction essential and at this voltage amount to ~10% variation between corrected and uncorrected values. Relativistic mass of the electron is shown in (green) and v/c is shown in blue.

This corrected λ_{rel} is plotted in black in Figure 11 and indicates that a significant variance between the relativistic and classical approach begins to emerge at around 100 keV acceleration voltages and gives a small, ~10 % reduction in λ_{rel} compared to λ_0 . This is advantageous for electron microscope as it further extends the diffraction limit at a given accelerating voltage. At 200 keV, $\lambda_{rel} = 2.51$ pm, if we are trying to observe single

crystal materials such as Si which have projected atomic separations of 0.784 Å between dumbbells when imaged in the $\langle 11-2 \rangle$ direction [111] then even in this case of a very small separation our effective wavelength is approximately 30 times smaller than the atomic separation and does not fundamentally limit our spatial resolution from reaching below this atomic separation.

3.3.3 Electrons interacting with matter

Electrons interact strongly with matter of all kinds due to their charge. This means electrons can and will be involved in many energy transfer mechanisms in the physical TEM specimen even if the specimen is incredibly thin.

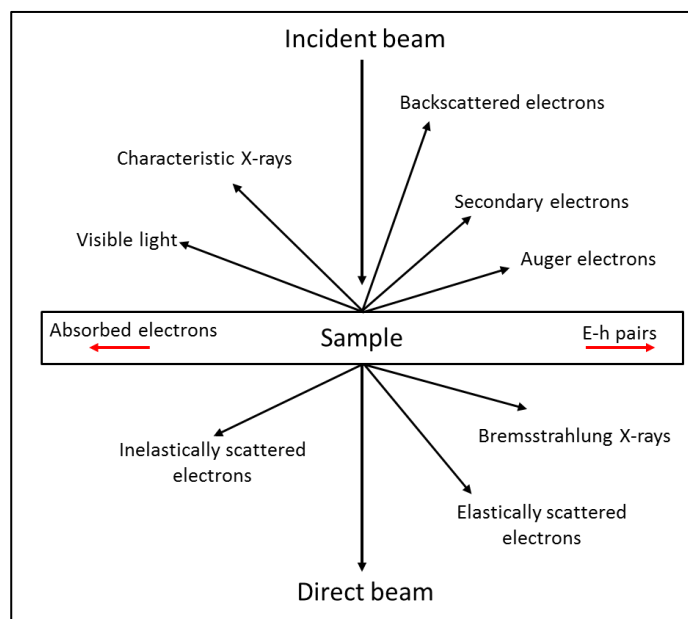


Figure 12: Schematic diagram of the signals generated as an electron beam interacts with specimen material [106].

In Figure 12 the main signals generated from beam-specimen interactions are shown. Many of which are useful for determining the properties of the specimen.

The elastically scattered electrons and direct beam are the most important signal channels for developing imaging and diffraction data as these signals will lens effectively due to the single energy of these signals.

Chemical analysis can be performed using the characteristic x-ray emission to perform energy dispersive x-ray (EDX) techniques and by using the inelastically scattered electrons to perform EELS analysis.

One important consideration is how the intensity of these signal channels varies with specimen thickness. Overall the highest quality imaging and spatial resolution in

chemical analysis is achieved by the thinnest specimens, though at an extreme case this can lead to very low signal and physical difficulties in specimen preparation.

3.3.4 High resolution transmission electron microscopy (HRTEM)

The four basic TEM methods, HRTEM, bright-field (BF)-TEM, dark-field (DF)-TEM and SAD are intrinsically linked and are often cycled between quickly during microscope operation. HRTEM is perhaps the outlier where spot size is minimised leading to a convergent beam for the purpose of imaging very small regions.

High resolution transmission electron microscopy is essentially an analogous technique to a compound lens based transmission optical microscope and therefore the lens system employed can be considered an extension of the physical optics treatment which would also be used to explain lens systems in telescopes and cameras.

The electron beam is focused and converged by the condenser lens assembly which controls the spot size and brightness of the beam at the sample plane. High angle electrons are removed from the beam at this point using the condenser aperture (see Figure 13)

The sample is held within the effective lens region of the objective lens with the objective aperture just below the lens and sample plane. HRTEM is an imaging mode using a wide angle objective lens aperture. In this condition most of the electrons which are diffracted and forward scattered through the sample are focused and used to form an image. This interference of many diffracted beams and the direct beam give a phase contrast image. This condition makes the final image data very rich. DF-TEM and BF-TEM conversely use very narrow objective lens apertures to select specific reflections post-specimen; this can be seen in Figure 14.

Post-specimen the beam passes through the objective aperture and the SAD aperture which are used to limit the beam in reciprocal space (objective aperture) and real space (SAD aperture) before being lensed at the Intermediate Lens array. This lens projects either a diffraction pattern or a real space image forward for imaging.

The projector lens is finally used to project an image onto the image screen or camera of the microscope. The real space imaging and diffraction performed in HRTEM are then recorded using a CCD or photographic plate

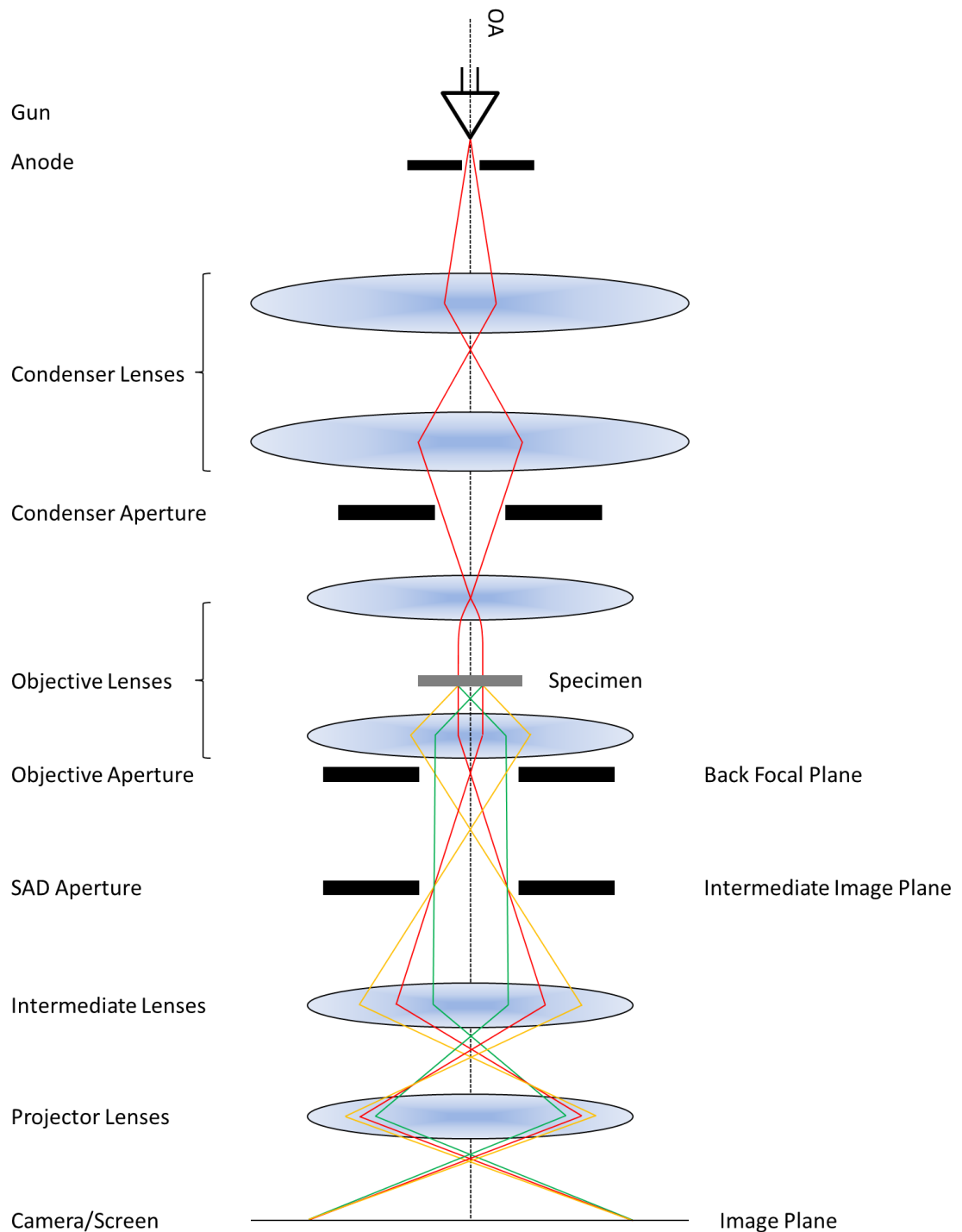


Figure 13: Schematic lens diagram for HRTEM operation. Only minor changes in apertures and lens focus values are required to transfer between HRTEM, DF-TEM, BF-TEM and SAD.

3.3.5 Selected area diffraction (SAD)

SAD is a powerful tool which accompanies the operation of a TEM. A diffraction pattern is acquired by altering the intermediate lens strength such that the back focal

plane of the objective lens rather than the intermediate image plane is projected to the screen or camera.

Whilst this technique can be used in many ways as outlined in [106] my intention has been to extract the crystallographic symmetry at heterostructure interfaces and epitaxial relationships. This has been achieved using standard SAD with parallel illumination of wide regions of the TEM specimen.

Forming an SAD pattern requires a spread electron beam to ensure parallel illumination of the TEM specimen, in generally this means you illuminate a large region of the specimen, often larger than you ideally wish to study, for example in the case of a 30 nm thick film you ideally want 25 – 50 % of your SAD pattern to originate from the film. To achieve this you only wish to allow the diffraction pattern from a 100 nm diameter region. This is achieved by inserting the SAD aperture into the intermediate imaging plane of the microscope. This aperture is imaged as a real circular shape in the imaging mode of the microscope but is not directly visible in the SAD mode.

As the SAD aperture is at a fixed height in the microscope it is essential to align the microscope and specimen such that the focal crossovers demonstrated in Figure 13 are brought to their natural aligned heights within the microscope. When this is achieved it is possible to switch between a focused image (in which you can see a focus SAD aperture) and a focused SAD pattern (in which you can see the in focus objective aperture) at the push of a button based on saved settings within the microscope.

The diffraction patterns achieved using SAD are determined by the wave nature of the incident electron beam and the crystal structure of the underlying specimen material. The most intuitive and straight forward way to understand diffraction is through the phase different/path length changes in the beam as described by Bragg laws [112, 113] shown in Equation 10. However, Bragg's law gives no explanation of forbidden and allowed reflections for which Laue's wave vector approach is required.

$$n\lambda = 2d \sin \theta$$

Equation 10

3.3.6 Bright Field and Dark field TEM

Bright field and dark field TEM are named after the contrast expected from vacuum in the respective imaging conditions. In bright field TEM you image using the un-diffracted (000) direct beam. This means that the vacuum (i.e. a hole in the specimen) which allows incident electrons to pass is imaged as bright intensity. Conversely in dark field TEM imaging, the imaging intensity is taken entirely from a diffracted beam. Since the vacuum

gives no diffraction such regions in dark field imaging give no intensity and are 'dark'. This naming convention is also used in STEM where dark field imaging relates to imaging using off-axis scattered electrons which cannot be produced from vacuum regions, so holes in the specimen are imaged with dark contrast.

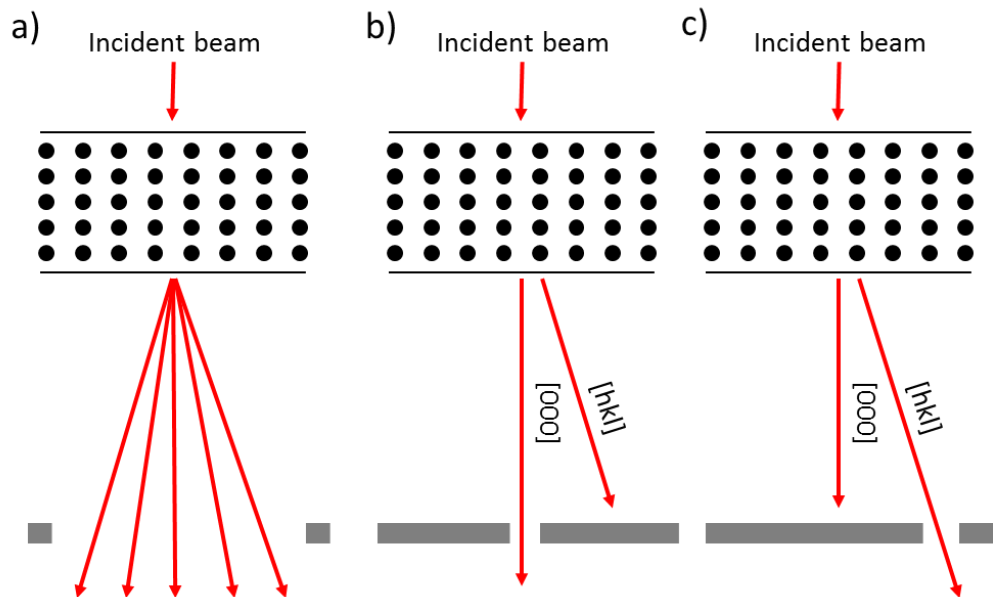


Figure 14: Objective aperture alignments for a) HRTEM b) BF-TEM and c) DF-TEM

Bright field and Dark field TEM are rarely performed at high magnification as imaging must be performed with an in focus diffraction pattern in the optimised back focal plane of the microscope and this requires parallel illumination of the specimen rather than the convergent beam which is generally used to achieve high brightness imaging when operating in HRTEM mode at magnifications over the 300,000 times settings which begin to deliver atomic resolution contrast.

In BF-TEM and DF-TEM imaging a much narrower objective aperture is used to select a specific reflection than is employed in HRTEM. This can be seen in Figure 14 where (a) shows the wide aperture used in HRTEM imaging, this is simply used to remove highly scattered electrons well away from the paraxial approximation and to reduce the background scattering of x-rays and electron from the TEM walls. In BF-TEM shown in Figure 14b a much narrower aperture is required, to select only a single reflection and block all other beams. The configuration in DF-TEM (Figure 14c) is much the same, though the small, single reflection aperture is shifted to the position of the desired reflection. There are often many reflections to choose from so which is ideal is a matter of choice for a specific problem.

The diagrams shown in Figure 14 suggest a physical shifting of the aperture, however, this can also be achieved by deflecting the position of the diffraction pattern

using the dark-tilt controls of the microscope. This is an easier operating mode as BF and DF-TEM can both be readily accessed through the two saved settings.

Since the Dark field reflection chosen is intrinsically linked to diffraction and therefore crystallography this imaging condition is very useful for identifying dislocations, changes in epitaxy and changes in crystallography, for example being used to highlight the spatial extent of a particular layer or phase in a grown film.

The vast majority of the electrons which are forward scattered into either the direct or diffracted beams will be found in the single direct beam, the small amount of diffracted electrons are then shared between many reflections. This means dark-field TEM often has very low imaging intensity and can require very long exposure times to produce a useful image. Often the CCD exposure time for DF-TEM is greater than 20 s. This requires a great degree of stability or the intention to image relatively large features of interest. Often at such low intensity it is challenging to pre-screen the images taken by eye in DF-TEM mode. This makes swapping between DF and BF-TEM essential and most modern microscopes have a dark-tilt setting which allows the microscope operator to deflect the diffraction pattern between the (000) beam and the desired dark field spot (hkl) at the touch of a button. Once set up, this allows rapid interchange between the two operating modes to gain insight into the imaged area and acquire complimentary data.

3.3.7 Scanning transmission electron microscopy (STEM)

Scanning transmission electron microscopy has been an essential tool for this project particularly when coupled with a high angle annular dark field (HAADF) detector. Much of the physical apparatus required for STEM is the same as in the HRTEM and many modern machines are able to operate in both modes. However, as a result of forming a small probe which is then scanned across the specimen the image formation mechanism is fundamentally altered. STEM data is collected in a serial mode with individual pixels probed and intensities collected at different points in time. To affect the beam scanning a set of high accuracy deflectors are required, even in the best STEM systems this leads to scanning instabilities and the potential for time variation in the mechanical position of the specimen. To handle these issues the mechanical and electronic stability of the STEM system must be incredibly high. STEM systems were first developed in the 1930's however the demands upon the mechanical stability, electrical stability and signal processing prevented the early STEM systems from being used for atomic resolution imaging and such systems did not become particularly popular or useful until the 1970's [114]. STEM systems are one of the few experimental techniques which can image single

atoms [115] this is achieved by the incredibly small, sub-angstrom electron probes which can be formed by the STEM system when combined with aberration correction [116].

A schematic diagram of the lens system and detectors used in STEM mode are shown in Figure 15 [106]. The STEM beam is converged to a point at the sample surface. The focus of the microscope is adjusted by altering the convergence angle of the probe which effectively alters the height of the crossing point of the incident beam. As with the TEM, rough focusing is achieved by moving the sample height rather than adjusting the beam characteristics. In general, the focused spot of the beam is referred to as the electron probe. This probe forming method has many parallels with the beam forming mechanism used in scanning electron microscopes (SEM) [117].

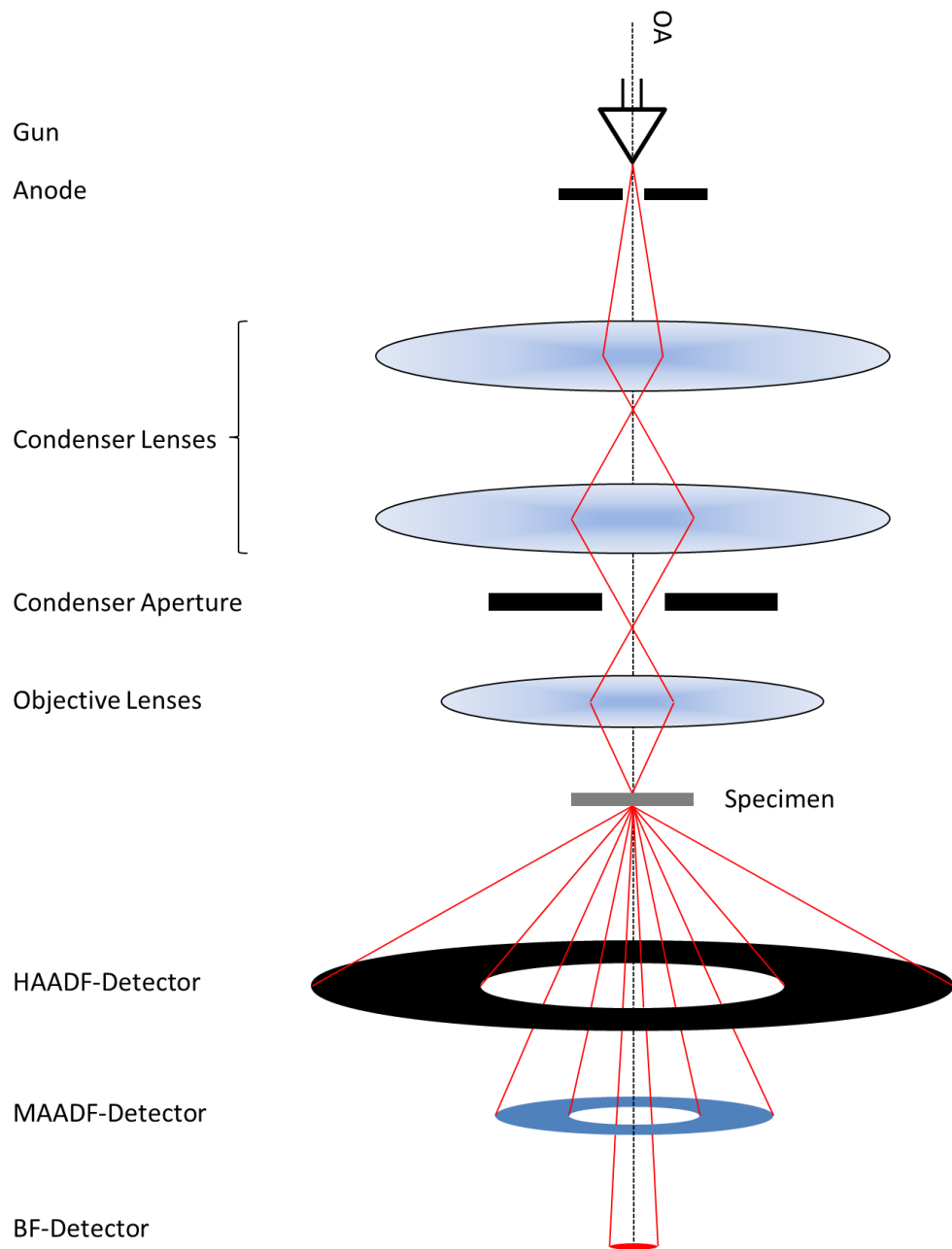


Figure 15: Schematic lens diagram for STEM operation. By converging the beam to a point on the sample surface using the Condenser and Objective lenses a sub-angstrom electron probe is formed to analyse tiny regions of the specimen. The resultant signals can be detected with a number of chemical and imaging modes. Scanning coils and the corrector are omitted from this diagram.

In many ways the lens diagram for STEM is simpler than for HRTEM. The lenses above the sample are the same, with a condenser and objective lens working to form a narrow electron probe. Post specimen, electron intensities are simply measured as a function of the scattering angles required to impinge on the various STEM detectors positioned in reciprocal space post specimen. The lens diagram in Figure 15 omits the corrector and the scanning coils which are used to form raster image. Since the exit of the

STEM sample is relatively free from complex lensing the STEM is an ideal system for capturing multiple signals at the same time. For example the off-axis HAADF-STEM detector can be operated at the same time as a central post column EELS detector, or the HAADF signal can be detected concurrently with medium angle annular dark field (MAADF) and bright field (BF) so long as the electronic feedthroughs and amplification to record these signals are present.

It is worth noting than in STEM mode the concepts of resolution and magnification are completely independent properties. The magnification of imaging or spectroscopic techniques is achieved simply by defining the size of the scanning window produced by the raster scanning. However the microscope resolution depends on the properties of the electron probe, the microscope stability and the ability to detect a significant signal to noise ratio in whatever signal channel is under investigation.

When in focus, the STEM microscope operates with a narrow electron probe; this means there is no real-space imaging which can be easily extracted on a viewing screen. The diffraction pattern from this single point source produces a Ronchigram. However; when the beam is out of focus the probe spreads to illuminate a wider area of the specimen and features can be seen on the TEM viewing screen. The Ronchigram is a diffraction pattern from a single point in the specimen in which virtually every diffracted beam interacts with one another The central region of the Ronchigram when in focus is the infinite magnification image [118].

Due to the serial collection method STEM systems require a large beam current to gain significant signal from each pixel during the acquisition period. This requires high quality gun systems which can deliver high beam currents and leads to more challenges with specimen damage and contamination than TEM imaging modes. This has been overcome mainly due to the advent of field emission guns which can generate current densities 6 orders of magnitude greater than conventional thermionic emission filaments [106].

When the electron probe hit the TEM specimen, the progress of the electron beam through the sample is complicated significantly by its interactions with the sample. This leads to electrons channelling along crystallographic columns in the specimen and also to channel hopping where an electron within the specimen becomes de-localised from the initial point of the electron probe. Channelling effects require the TEM specimen to be aligned with a major crystallographic axis to image with high resolution as providing a crystal direction for channelling through the sample acts to collimate the beam throughout the sample thickness. However as the sample thickness increases the proportion of electrons which undergo one or more scattering events into different channels increases.

This means the while the electron probe is positioned above a single atomic column, and has a probe size small enough to only image this column, imaging intensity and chemical signals will be produced from neighbouring columns to a greater and greater degree as sample thickness extends. This gives us a requirement for super thin specimens for performing atomic resolution work, particularly chemical analysis.

The image contrast given by STEM is highly dependent on the detector used to collect scattered electrons. The detectors used in this work all image in reciprocal space and simply record the intensity captured by a relatively large physical detector over time. The detectors in the STEM do not provide any spatial resolution. Spatial resolution is created by the specimen probe interactions at each imaging pixel.

The HAADF-STEM detector geometry is usually in the range 50 mrad to 200 mrad between the inner and outer detector angles [106]. This high angle means the image intensity is dominated by Rutherford scattering from highly charged atomic nuclei and contains no Bragg scattered electrons [106]. As thermal diffuse scattering is a major source of signal in HAADF mode the image is relatively immune to defocus/thickness effects compared to HRTEM [119, 120]

HAADF-STEM imaging is an incoherent imaging mode [119], in which the intensity of high angle scattered electrons is proportional to Z^n where $1.5 < n < 2$ [115, 121, 122]. This allows rudimentary chemical identification to be performed directly from image intensity, for example in Fe_3O_4 , oxygen has the atomic number 8 and Fe 26. When imaged in a $\sim Z^{1.7}$ regime this gives 7.5 times more intensity to Fe than O, in practice this makes O unobservable in HAADF-STEM as very light atoms barely scatter electrons to the inner angle of the HAADF-STEM detector. This makes HAADF-STEM an ideal imaging technique for the various metal oxide interfaces in this work.

The MAADF-STEM detector images in a similar fashion to the HAADF-STEM detector. However, by operating at a lower angular range, the Z contrast effects of the HAADF detector are reduced giving a less significant increase in brightness for heavier atoms. More importantly, the MAADF detector is able to image crystal strain fields at defects and interfaces and can offer important incite in grown film properties.

The BF detector is an on axis disk which produces coherent imaging which appears very similarly to a HRTEM image. Due to the complex structure of Fe_3O_4 and the wide range of factors which influence the contrast in BF-STEM this has not been used to perform any atomic resolution data acquisition in this project. However BF-STEM allows the possibility to image all atomic species within a sample and with the use of a beam stop, or a purpose built annular bright field detector to remove phase contrast from the

imaging mechanism it is possible to image light elements such as O directly in the STEM [123].

There are two main forms of EELS detectors, in column omega filters which use four magnetic prisms to disperse the electron beam and post-column filters which use a single magnetic prism to disperse the electron beam below the imaging detectors. Both these systems use to energy (velocity) dependent response of an electron to an applied magnetic field to spread the beam into a spatially resolved energy spectrum. The energy resolution of this is essentially limited by the energy spread of the gun and the spatial resolution of EELS is determined by the sample and probe properties.

3.3.8 Aberrations

Aberrations are due to imperfections in lens strength and shape and have a significant effect on the resolution and image quality which can be achieved in a microscope [106].

Optical lenses can be made almost perfect with high quality lens grinding, correction for aberrations using compound lenses with convex and concave elements and optical coatings. However, in a magnetic lens there is no concave lens or optical coatings. Furthermore, the varying current supplied to the magnetic lens means stability cannot be as perfect as that achieved in a physical device. Due to the limitations of what H field can be projected into the pole piece gap we cannot produce all the minor shape variations in the lens which would be required to produce all the lens properties we desire.

Although magnetic lenses are intrinsically more difficult to produce without significant aberrations than optical lenses, a second problem is that a genuine concave lens cannot be produced using magnetic lenses, instead all lensing with magnetic lenses is produce in the form of a double convex style optical lens. This has the effect of making all aberrations additive through the microscope column where in an optical system a compound lens with a mixture of convex and concave elements can be used to mitigate the total effects of aberration within the column this is simply not possible with magnetic lensing. Instead complex arrangements of multipole lenses are required to produce an effective concave lens.

Various aberrations are measured and minimised with various degrees of ease in (S)TEM systems. All TEM operation requires the minimisation of basic aberrations such as focus and two-fold Astigmatism. However some aberrations are more challenging to correct and observe clearly.

The various aberrations present in transmission electron microscopy are a result of imperfect lensing, aperture effects and sample interaction throughout the microscope column.

To simplify matters, the major aberrations present in the microscope are separated and labelled (according to Haider notation in this text [124])

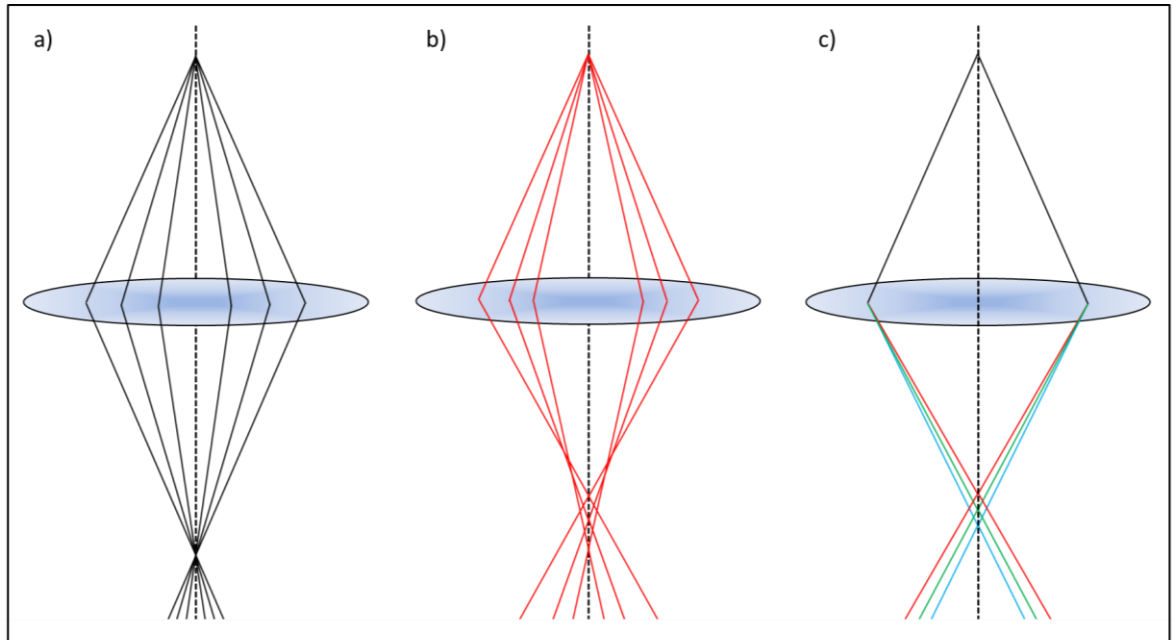


Figure 16: Ray diagrams of a) Perfect lens b) Spherical Aberration and c) Chromatic aberration.

In a perfect lens, shown in Figure **16a** all beams, from an object point are focused at a corresponding infinitely small image point regardless of the wavelength of the beam, the position from which the beam originates, and the region of the lens through which the beam transits, however, in a real lens this is not the case as a number of lens aberrations give rise to imperfect lensing.

Spherical Aberration (C_3 or C_S), shown in Figure **16b** is due to radial imperfections in the magnetic lens and has the effect of over-focusing beams which pass through the lens further from the optical axis. This is an important aberration in the TEM at the objective lens and is one of the most common aberrations to correct in an aberration corrected machine [125-127]. C_3 cannot be corrected manually and would be particularly significant in the wide pole piece design of the JEOL JEM-2200FS operating at York.

Chromatic Aberrations (C_C) relate to the different focal length of the magnetic lens depending on the energy of the electrons within the beam. This can be seen in Equation **3** which shows the focussing power of a lens is proportional to $V^{-\frac{1}{2}}$. This means more energetic electrons have a longer focal length as show in Figure **16c**.

Chromatic aberrations are particularly significant where there is a large energy spread in the incident beam which is very strongly limited due to the low energy spread of the electron gun emission. However, this can be complicated by inelastic sample-electron interactions which produce a wider energy spread post-specimen.

Astigmatism ($A_1 A_2 A_3 A_4 A_5 \dots$) relates to any non-spherically symmetric properties of the lens system and leads to different focal lengths depending on the region of the lens used. This can be a very complex pattern of different lens strengths around the device so is decomposed into two-fold, three fold Astig etc. which allows any inhomogeneity to be captured if using enough A_n coefficients, however, what is important to consider is which aberrations are creating the greatest effect in the imaging condition and in general this is not the high order terms.

Whilst all the lenses in the microscope experience aberrations which feed through into the overall imaging condition, the most significant limiting aberrations in the HRTEM are in the Objective lens. Whereas the most significant aberrations in the STEM are at the probe forming lens (The Condenser lens of the TEM). This is why the JEOL JEM-2200FS is double aberration corrected with CEOS GmbH correctors to correct both these problems.

All the aberrations listed here have the effect of broadening the focus of the magnetic lens from a point to a point spread disk. This is experienced in all lenses and prevents the formation of a perfect lens. However, when attempting to perform scientific analysis at the very edge of device capacity these effects become highly significant.

3.3.9 Aberration Correction

In an aberration corrected (S)TEM, the analysis of imaging aberrations is performed using a monodispersed spherical media such as nanoparticulate matter or amorphous material. For this to be performed successfully, the microscope must first be set to default settings of focus and be well aligned prior to running the aberration analysis algorithms. The specimen is put into an under focused position using z-position stage control to give a convergent beam and an effective negative defocus condition [126].

The aberration correction software has been developed by corrected electron optic system GmbH (CEOS) and operates on an iterative principle of detecting aberrations in the microscope lenses from a tableau of images or diffractograms at a range of beam tilt angles [128] before using a multipolar lens as a 'corrector' to effectively compensate for the observed aberrations, and then repeating this process until the aberrations determined from the imaging tableau are minimised.

This process is undertaken separately from experimental data capture so once aberrations have been analysed and corrected we rely on the microscope to remain stable over a period of time. In the York JEOL JEM-2200FS a sample transfer is required to perform aberration correction so we require ideally 4 - 6 hours of stability after a correction. The Nion UltraSTEM100 can perform correction from the experimental specimen and has a very rapid aberration correction algorithm, so this process can be repeated more often.

Aberration correctors require exceptionally high stabilities and are controlled by software and computational resources which were not available when the theory to correct aberrations were first proposed in 1947 by Scherzer [100]. The correction scheme at York is based on the long hexapole/transfer lens. By using a series of multipole lens acting together the behaviour of a single concave lens can be achieved with negative spherical aberration [126, 127]. Multipolar lenses use a combination of dipole, quadrupole, hexapole and octopole lenses to provide the negative spherical aberration required in the corrector. Correctors use one of two main types of multipole lens systems, either quadrupole-octopole or round lens-hexapole pairs to provide correction [129-132].

For a STEM system, when aberrations are minimised the electron probe is sharp and has a maximum intensity which can be determined by monitoring the intensity of specific pixels within the image. By iteratively correcting the probe a sharpened, high intensity beam can be formed giving the maximum pixel intensities possible [133-135]

The Nion UltraSTEM100 at SuperSTEM is capable of performing rapid aberration correction from the amorphous regions of glue found around the glue line of a conventionally prepared cross sectional sample. As this microscope is only designed for STEM experimentation this is based on a probe corrector which can correct up to C_5 aberrations.

The automated aberration correction procedure of the STEM probe (condenser correction) in the JEOL JEM-2200FS uses an Au nanoparticle sample on a C grid. Probe aberrations are determined from particle size and sharpness. This corrects up to C_3 aberrations in the Probe. The STEM system probe is corrected by using the HAADF-STEM detector, so the alignment specimen requires a sufficiently heavy material to give a high signal at the detector, Au nanoparticles are ideal for this process.

The HRTEM correction in the JEOL JEM-2200FS uses an amorphous alignment specimen to produce a continuous range of spatial frequencies producing spherical FFT results when astigmatism is minimised [136].

3.3.10 Electron energy loss spectroscopy (EELS)

Electron energy loss spectroscopy has a similar physical basis to the other spectroscopic energy loss techniques described in this text (AES, XPS, Raman) in that a material is exposed to monochromatic incident radiation and the energy variations in this signal post specimen are analysed to show the chemical properties of the material under investigation.

EELS can be implemented in both TEM and STEM mode, though the behaviour of the underlying imaging modes leads to different operating modes and results. All the EELS data presented in this work were collected using STEM-EELS at the SuperSTEM facility in Daresbury with the assistance of Dr. Demie Kepaptsoglou and Prof. Quentin Ramasse.

EELS detectors are produced in one of two main geometries, either in-column omega filters shown in Figure 18 or post-column filters described in Figure 17 [106]. The in-column filter allows the most readily available implementation of energy filtered (EF)-TEM by performing energy filtering prior to the conventional imaging CCD detector used in the HRTEM however these systems require four magnetic prisms to disperse and then recombine the electron beam before passing the signal down the microscope column. This makes aligning the detector challenging due to the number of components and means a misaligned filter effects the TEM imaging condition. Conversely, a post-column filter is ideally suited for high spatial resolution STEM-EELS analysis as this detector is spatially separated from the annular dark field detectors of the STEM, and performs energy filtering after the sample interaction and imaging mode of the STEM has been performed this means the detector itself has no impact on the microscope imaging condition [106].

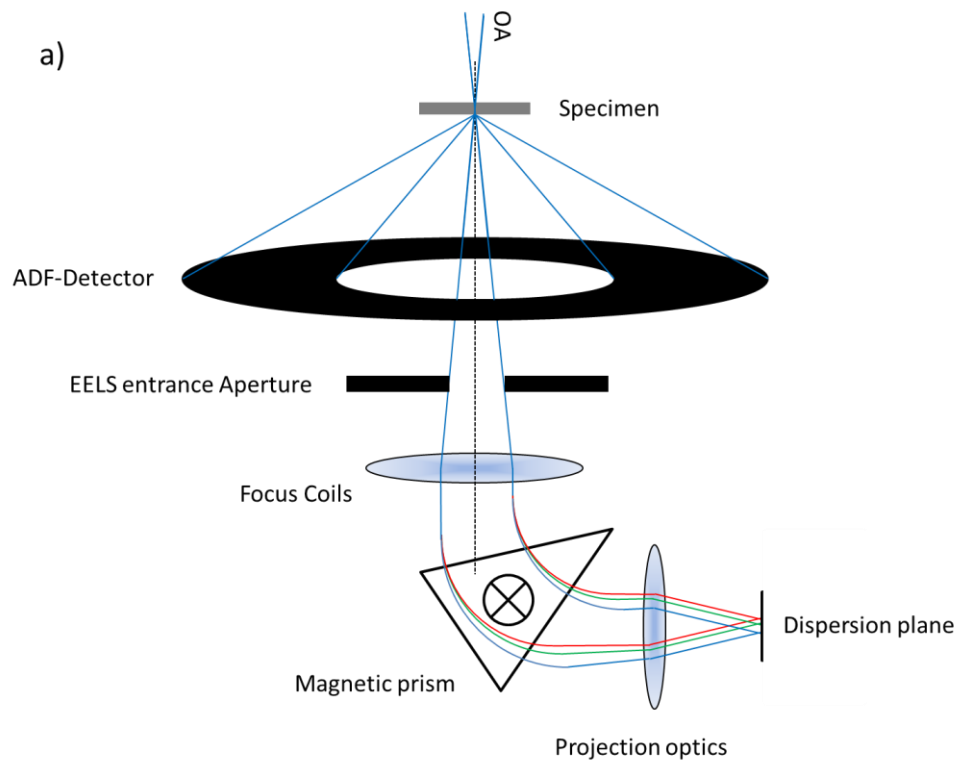


Figure 17: Post column filter diagram showing the direct, on axis beam being focused and dispersed through a 90° angle using a magnetic field to act as a magnetic prism.

EELS analysis has no inherent spatial resolution in terms of the EELS filter and detection mechanism. However, STEM-EELS can be localised at the specimen due to the sub-angstrom electron probe used to study the specimen.

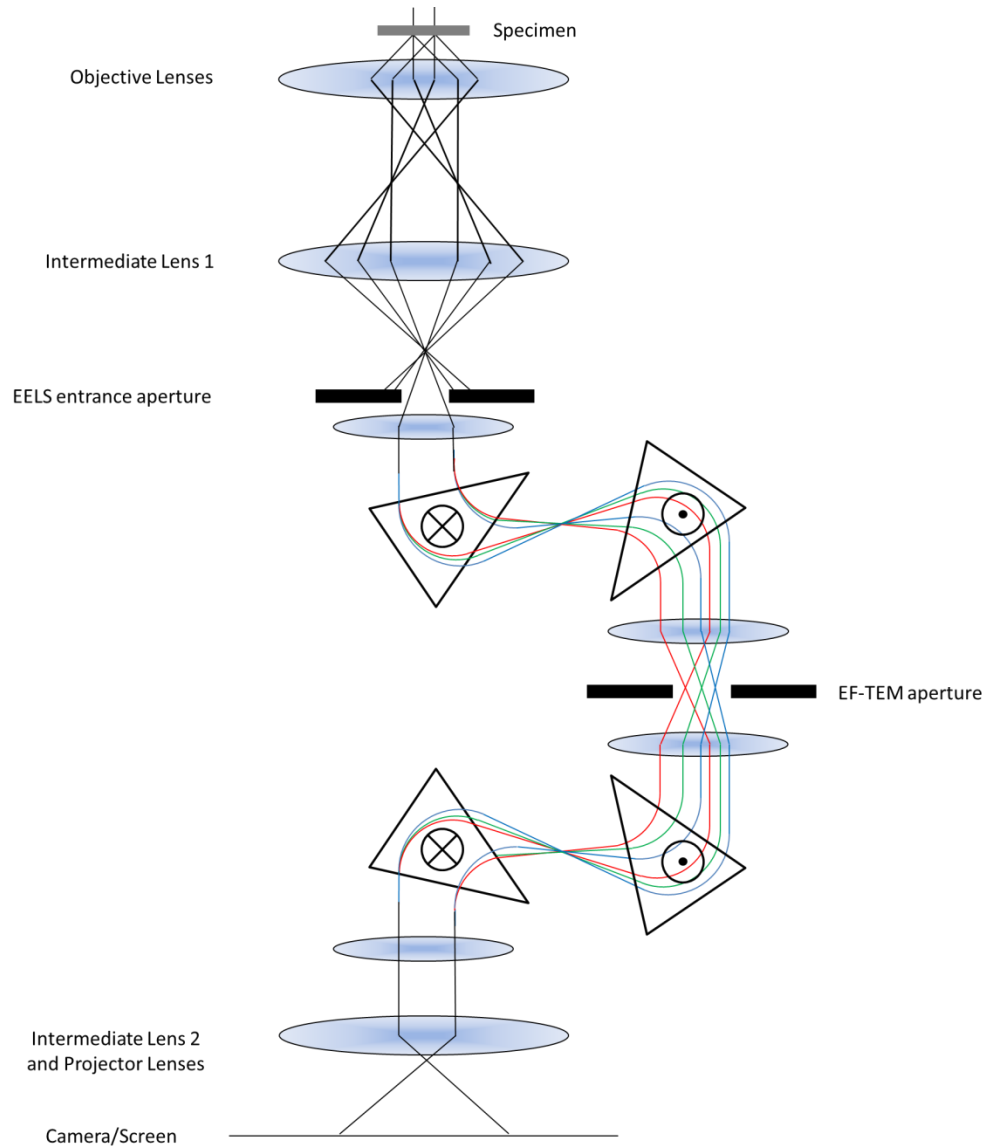


Figure 18: in column filter inserted between the two intermediate lenses of a TEM microscope. Four magnetic prisms disperse and then recombine the electron beam allowing the energy filtered signal to be passed back into the TEM imaging system after filtering or spectra to be collected within the filter.

To perform high resolution and/or atomic resolution EELS using a STEM system requires a method to correlate chemical signals with imaging the spatial distribution of atoms, interfaces and defects within the specimen. This is possible using the annular detectors in the STEM which allow inelastically scattered electrons which are forward scattered in the specimen to be detected through on axis geometry EELS filters. By combining simultaneous atomic resolution imaging with atomic resolution chemical analysis creates a huge amount of highly specific atomic resolution data with which to understand chemistry, atomic structure and allows incredible detail and confidence in later theoretical studies. As mentioned earlier, the effects of signal channelling are incredibly important to maintain an atomically resolved probe through the sample thickness and

understanding the electron beam path through the specimen is required. In this case, ensuring a sample is thin enough that the electron path through the specimen is limited to mainly single-scattering events is essential.

Spatially resolved STEM-EELS is also one of the most effective methods for determining the thickness of a specimen by monitoring the intensity of the zero-loss peak and the intensity detected in the whole EELS spectrum, the thicker the specimen the more electrons undergo energy loss interactions and this gives a local thickness measurement in the specimen.

In TEM mode, spatial resolution in the chemical analysis can be achieved in a similar fashion to SAD by using an aperture or a convergent beam to ensure the detected electrons come from a specific sample region. However, this does not provide the atomic resolution chemical sensitivity of STEM-EELS, in TEM mode a more useful technique is to use the energy filter to perform EF-TEM. This relies on an imaging CCD positioned after the energy filter and is a major motivation behind in-column filtering of the electron beam to allow the same CCD used for general TEM experiments to be implemented for EF-TEM.

EELS data contains energy losses from a wide range of inelastic scattering events within the specimen. This includes plasmon losses, core losses, inter and intra band transitions. This makes EELS a highly sophisticated chemical analysis technique which can be used to understand local atomic valences and bonding configurations as well as simple chemical identification. Furthermore a large background signal is detected in EELS so background subtraction must be performed carefully to extract useful signals in a consistent and rigorous fashion.

In this work I have utilised the spatial distribution of core loss signals to determine chemical composition of atomic columns and I have used zero-loss peak analysis to determine local sample thicknesses.

3.3.11 Specimen Preparation

Preparing samples for TEM study is a challenging, time consuming endeavour. The intention is to prepare thin foils of between 30 and 70 nm of specimen material, such that the material achieves electron transparency to a beam accelerated at over 100 keV [106]. TEM specimens can be prepared in cross sectional and plan view geometry using conventional polishing methods [137] or focused ion beam (FIB) milling [138]. The vast majority of TEM specimen preparation in this work is cross-sectional geometry, mechanically polished (conventional) TEM specimen preparation.

When attempting to generate the highest quality results from a modern, aberration corrected microscope which has the nominal capacity to image and perform chemical analysis on an atomic scale it is often the specimen preparation which is the limiting factor in terms of achieving image quality and chemical information [139, 140].

In general, microscopy demands that TEM specimens are optimal when they are as thin as possible, however in very thin specimen regions the TEM sample material may amorphize and therefore no longer represent the material specimen the was intended for study. Furthermore, the entrance and exit surface of the TEM sample is unlikely to represent the core material which is expected to contain the structure of the deposited film. As samples get thinner, the effect of the sample surfaces becomes more dominant. TEM specimens need to be thin enough to achieve the approximations of 'single scattering events' which allow chemical mapping with a high degree of confidence in the results.

Conventional TEM specimen preparation is a destructive process which requires considerable volumes of sample wafers to be cut, glued and thinned to produce the specimen material required for TEM imaging. From a practical point of view it is therefore generally best to perform this analysis last; once other macroscopic properties have been investigated and specific information is sought from the microscope.

To prepare cross sectional TEM specimens from a 10 x 10 mm² substrate requires sample cutting. In the case of epitaxial films and amorphous or granular specimens it is important to consider the underlying crystallography of the film, substrate or multilayers in question. The specimens shown in this work are grown along the [111] direction, which is orthogonal to the [11-2] and [1-10] in-plane direction. In this work the crystallography of the substrate has been continued into the overlayer with a trivial cube on cube epitaxy, however this is not always the case and must be inferred from RHEED or XRD prior to cutting if a specific sample orientation is desirable. The orientation in which the specimen is cut and cross sectioned will limit which of these viewing directions can be achieved in the final specimen.

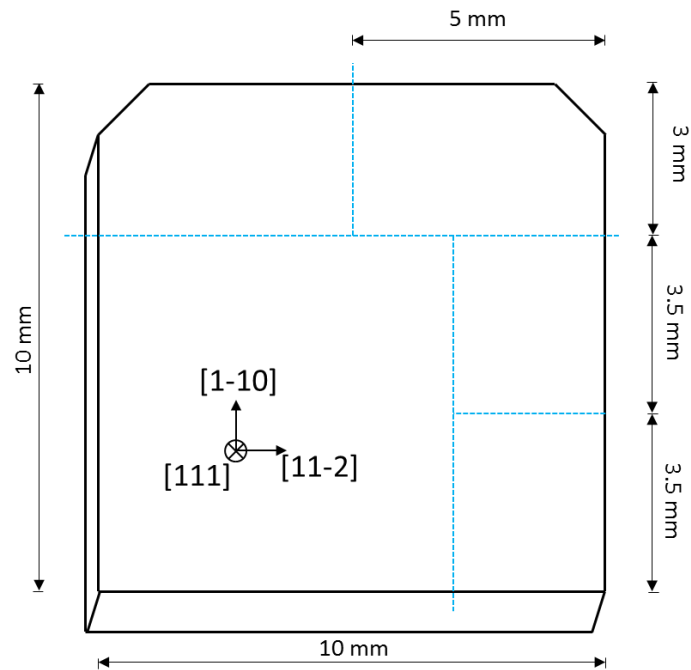


Figure 19: Sample geometry taken from Shinkosha Ltd website. In-plane geometry determined from the two notched corners. Blue dashed lines show pattern of cutting required to produce cross sectional specimens in both the [11-2] and [1-10] zone axes.

The deposited substrate is cut using a diamond edged circular saw blade. The substrate is secured on a glass slide using crystal bond glue which sets to a very hard plastic finish at room temperature and melts to a soft fluid at around 130 °C. This glue is essential for specimen preparation as it allows small sections of sample material to be fixed and supported during cutting and polishing processes. In the case of the [111] oriented substrate material used in this project there are two different crystallographic directions given by the in-plane square edge directions. Using substrates supplied by Shinkosha Ltd. These can be identified using the notched corners as shown above in Figure 19.

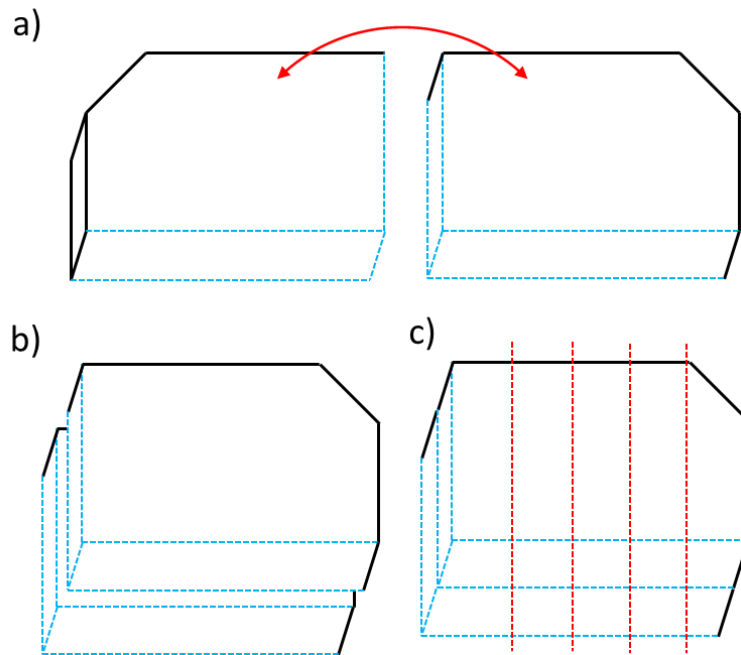


Figure 20: Gluing and cutting sample cross sections from the substrate material. a) Glue the two corresponding substrate pieces together film side to film side to form a sandwich (b). This is cut into ~1mm slices to provide initial, unpolished, cross sections.

The chosen scheme of sample cutting I usually employ is described in Figure 19 with blue dashed lines. This gives four rectangular sections of material (which means the orientation of each piece is clear) and two clear sets of pairs of samples.

After sample cutting, the specimen material is removed from the glass slide by heating on standard laboratory hot plate at ~130 °C to melt the crystal bond glue. To remove residual crystal bond, the sample pieces are placed in acetone which is capable of removing organic and plastic polymer materials. However, this solvent leaves its own residue and the sample must then be washed in ethanol and finally isopropanol (IPA). As the solvents dry they often lead a residue of dissolved glue and fine particles on the material surface. To achieve the cleanest possible surfaces prior to any permanent gluing it is ideal to gently wash any surfaces with IPA and a cotton bud.

High quality TEM specimen preparation glue is used to adhere the two corresponding substrate blocks together. In this work Gatan G1 two part epoxy has been used. This glue is required to withstand plasma cleaning, vacuum conditions, high temperatures, solvents and considerable mechanical strain.

The two part epoxy is mixed in a 1:10 ratio of hardener and resin, and the characteristics of this glue are tested before relevant gluing processes are undertaken. The glue performance depends on the hot plate temperature used for curing and on achieving a consistent, bubble free mixture of resin and hardener in the correct

proportions. To test the glue a sample is left to cure and tested with a cocktail stick. Hardener rich glue crystallises during curing and is brittle, resin rich glue will not set into a hard material.

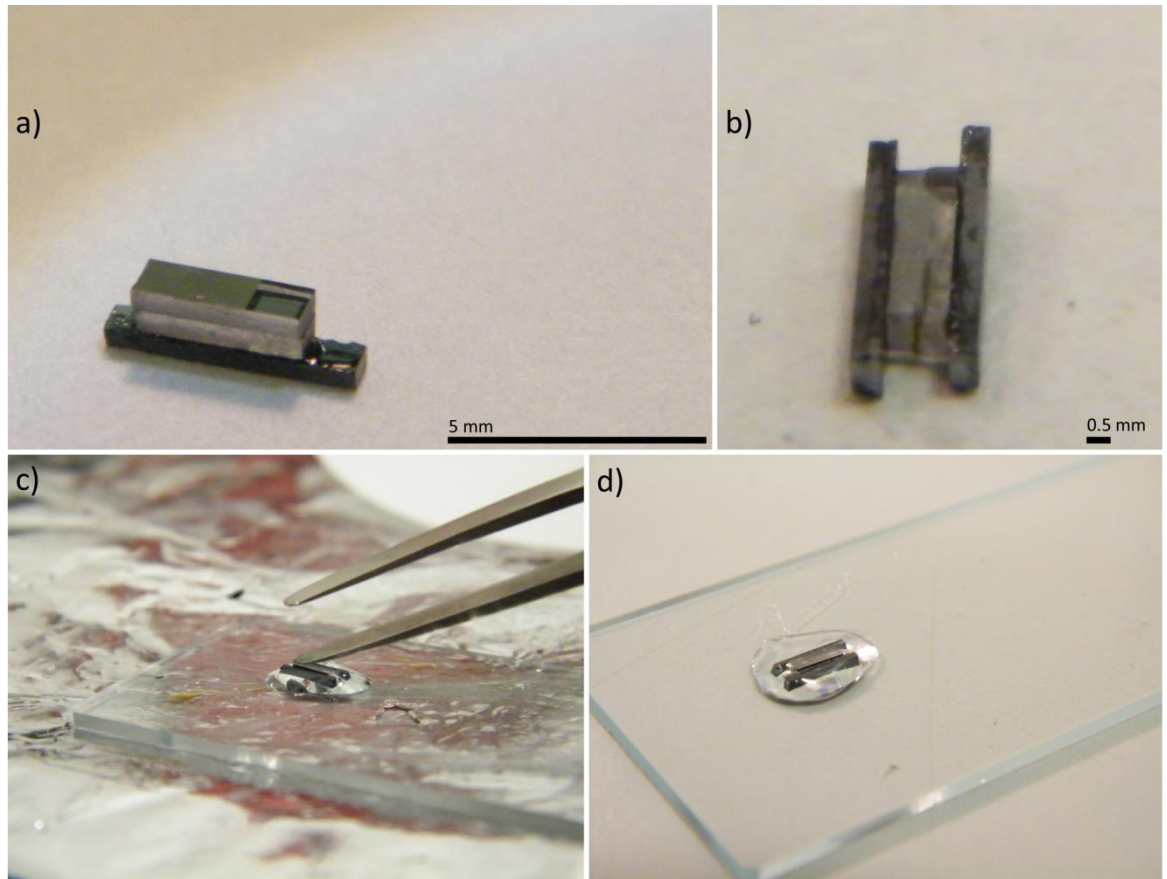


Figure 21: Preparing cross sections for polishing. Optical Images a) Si padding pieces are glued to the outside of the sample cross section to form the ‘H’ shaped sample (b) such that the three glue lines in the sample are parallel to one another. After curing the G1 epoxy this sample is glued flat to a clean glass slide (c) for polishing with the glass slide acting as a mechanical support and a tripod for the polishing process (d).

The pairs of substrate pieces are glued together with film surfaces glued face to face as shown in Figure 20a encasing the film on both substrate pieces within the glue. The un-cured G1 epoxy is applied to the film surface using a cocktail stick to achieve a uniform, thin covering of glue without air bubbles. When the two substrate pieces are positioned together this glue line is then squeezed using tweezers to force any excess glue out of the structure and ensure a uniform well bonded interface. This ‘sandwich’ structure is then placed on the hot plate to cure.

To form cross sectional slices of this material after the G1 epoxy is cured requires the diamond saw to cut ~1 mm sections from the crystal along the long axis of the rectangular crystal block (Figure 20c). These cross sections of sample material must then be cleaned using the hot plate and solvents as before.

Once a neat sample cross section is produced Si padding pieces are added by following the same G1 epoxy gluing procedure as above to provide both mechanical support for the sample and to provide a visible indication of cross-section thickness later in the specimen preparation procedure. The 'H' shaped cross section and Si padding pieces are then fixed to a clean glass slide using crystal bond glue (Figure 21).

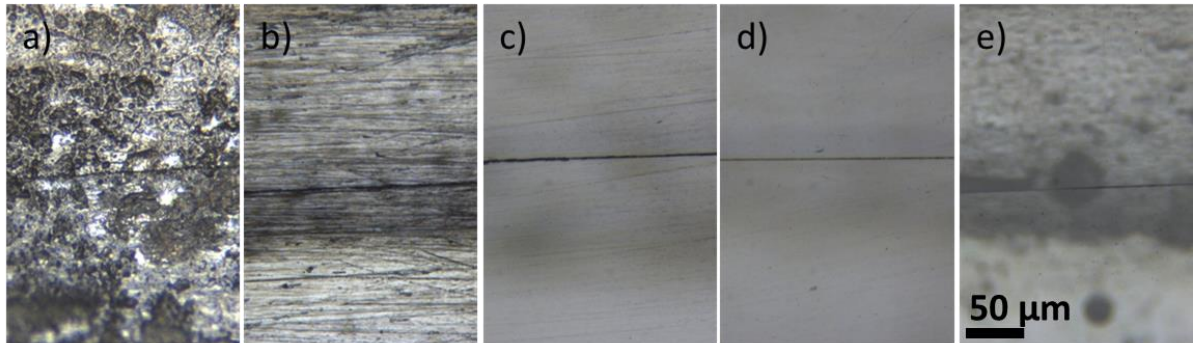


Figure 22: Optical reflection microscopy images of sample surface after different grade of polishing. a) directly after cutting with diamond saw blade (b) 15 μm lapping pad (c) 6 μm lapping pad (d) 3 μm lapping pad (e) 1 μm lapping pad

The cross sectional sample is now polished using a range of diamond lapping pads. Initially the sample surface is rough from the diamond saw and the glue line can be hard to visible identify (Figure 22a). Furthermore, if the Si pieces are not aligned exactly with the substrate material then the four material blocks will need to be squared off to form a single flat surface across the structure. This initial polishing is achieved using a 15 μm polishing pad which results in the surface shown in Figure 22b. Once the sample is squared off, the material is polished subsequently with 6 μm , 3 μm and 1 μm lapping pads until visible asperities on the sample glue lines and surface are fully removed (Figure 22e). In Figure 22e, the marks shown on the sample and around the glue line are actually on the reverse of the sample. During this process the aim is to achieve a highly polished surface which will Ar ion mill effectively at the end of the sample preparation process [106] and to produce a wide region of substrate and Si which is flat to allow a TEM grid to be glue to this surface of the cross-section. As it is not initially important to thin the TEM cross section significantly the progress between different grades of polishing pads is simply determined by the quality of the surface and the glue line.

For cross sectional TEM specimens a slot type grid is used with $\sim 2 \times 1$ mm central aperture. These can be made from a range of materials, but in this work I have used Mo and Cu sample grids. This sample grid is glued to the reverse of the specimen using the G1 epoxy with the grid aperture perpendicular to the glue line as shown in Figure 23. As the G1 epoxy used to fix the sample grid to the specimen requires applied heat, this

process also melts the crystal bond glue which supports the specimen material on the glass slide. Once the G1 epoxy has cured this is also the time to turn over the specimen. It is essential during this process to ensure the sample is mounted squarely on the glass slide to ensure uniform thinning of the specimen.

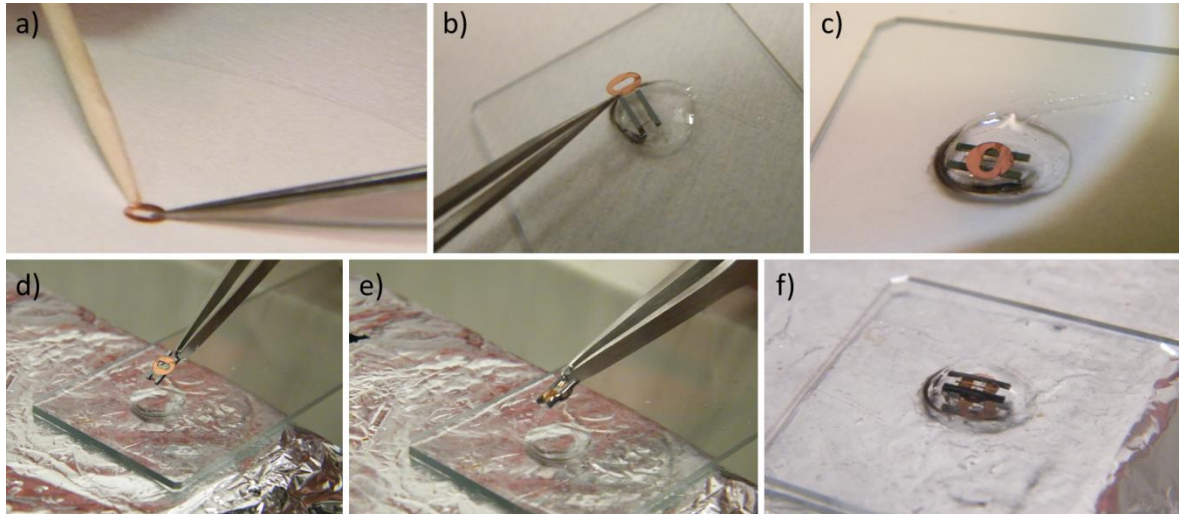


Figure 23: Gluing the TEM grid and turning over the sample cross section. (a) The TEM grid is coated in un-cured G1 epoxy and carefully attached to the sample surface (b). c) The glass slide is then placed on the heater to cure the G1 epoxy and melt the crystal bond glue. After approximately 5 mins the sample can be lifted (d), turned (e) and re-glued to the glass slide with the TEM grid glued in place.

On this second side of the specimen the surface material is again rough, and must be polished to allow successful ion milling, however, this time a second objective of producing a highly thinned cross section must also be achieved during this process. This requires a calibrated micrometre to measure the sample thickness less the glass slide thickness and optical transmission and reflection microscopes to monitor the thinning process.

In general a cross section will be between 450 and 750 μm thick directly after turning the sample over. This measured thickness includes the ~ 40 μm height of the TEM grid. Again the thinning/polishing routine is started with the 15 μm lapping paper. When this paper is new it will rapidly thin the specimen material to a desired thickness of 200 μm as the lapping papers age they become less effective. It is essential to check the specimen during the thinning process to identify sample tilt, cracking or dirt on the specimen and to make sure the polishing is giving a uniform square surface to the sample. Below 200 μm switch to the 6 μm polishing pad to reduce the overall thickness (inc. TEM grid) to 135 μm . Below 135 μm it is possible that misalignment of the TEM specimen can lead to specific regions of the sample being incredibly thin. From this stage onward the sample should be monitored in the transmission optical microscope to identify any regions of Si which begin to show a deep red colour. The structural integrity of the Si

pieces should also be monitored using the optical microscopes. Below 135 μm I use the 3 μm polishing pad to reduce the thickness to 100 μm ; below this thickness sample thinning is performed with the 1 μm pad. The sample is thinned sufficiently when the Si padding pieces show red-yellow colours in the optical transmission microscope as shown in Figure 24.

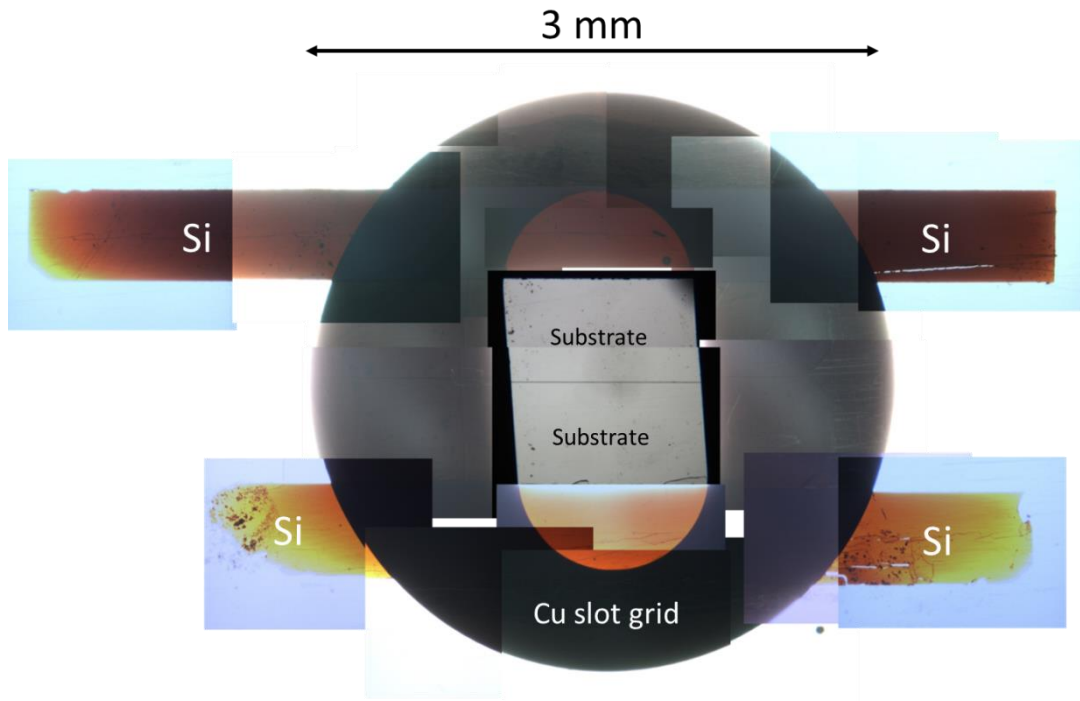


Figure 24: Cross sectional TEM specimen mounted on 3 mm Cu slot grid with 2 x 1 mm aperture. Specimen imaged using transmission optical microscope. Cu grid is opaque and images as dark contrast. The two Si padding pieces have achieved some optical transparency at sub 100 μm thicknesses.

Once the sample is thinned to the point where Si begins to show optical transmission the sample is incredibly delicate and is supported by the strength of the TEM grid. This sample shown in Figure 24 is now ready to be finished using Ar ion milling. To remove the specimen from the glass slide the sample is placed in Acetone to remove the majority of excess crystal bond glue. Then a diamond scribe is used to cut an outline around the TEM grid, removing residual glue and breaking the Si pieces which project beyond the edge of the sample grid. Finally this sample is placed on the hot plate, and once warm enough to melt any final crystal bond, the specimen is carefully removed from the glass to be cleaned in acetone, ethanol and finally isopropanol (IPA).

This specimen is now ready for the final stages of sample preparation using the Ar ion miller. I have used a Gatan 691 precision ion polishing system (PIPS) fitted with low energy guns and a cryo-stage to mill TEM specimens. This system is equipped with two

low angle Ar ion guns which can be set to operate sequentially to avoid sample damage due to local annealing which would be produced if the guns run constantly.

The PIPS sputters material from the specimen using Ar ions accelerated to between 0.3 and 6 keV incident on the specimen at a grazing angle of up to 10°. By milling from both sides of the specimen using the two milling guns the effect of re-deposition is minimised.

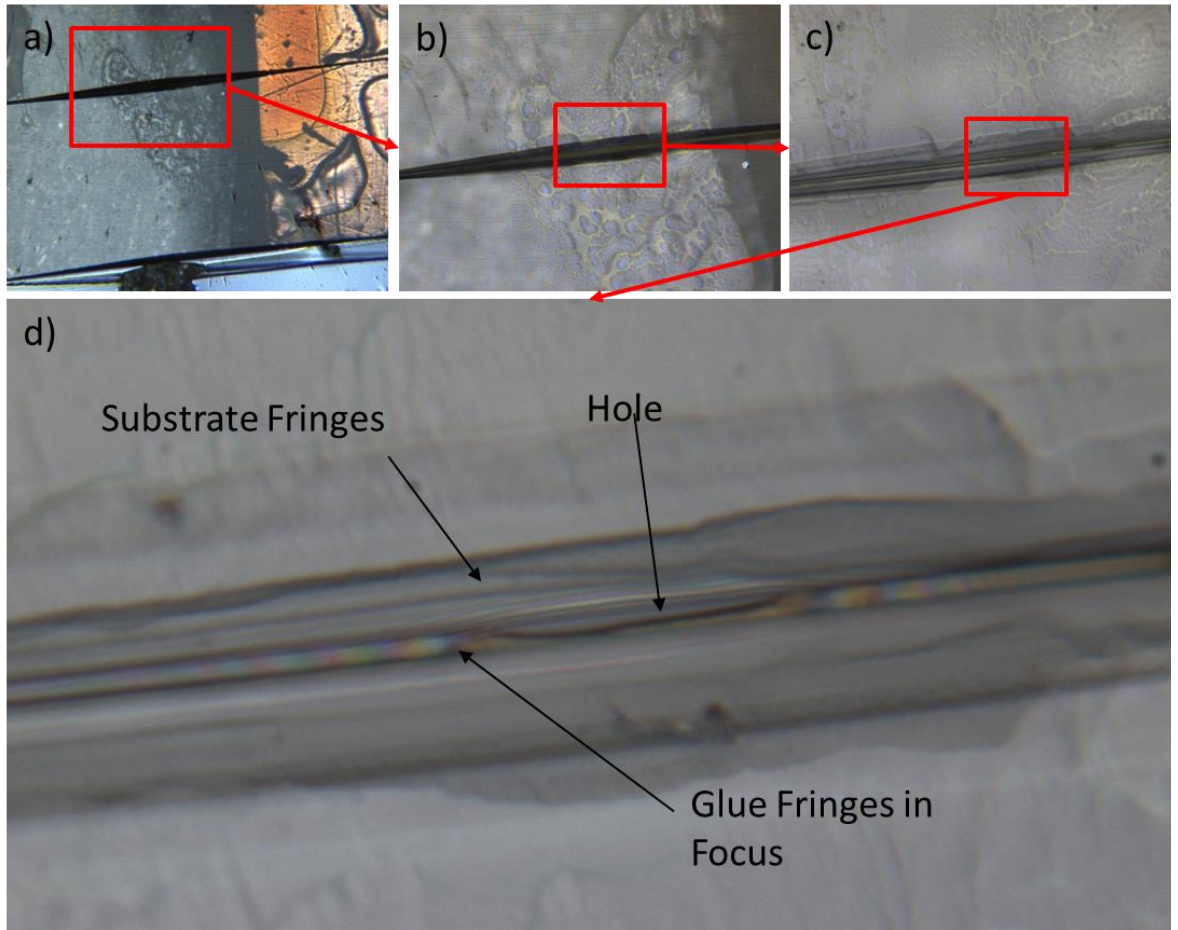


Figure 25: Ar ion milled sample. The widened glue line can be seen in (a), (b) and (c) with the hole formed in the glue and the optical fringing in the glue line visible in (d). To find these fringes requires the higher magnifications possible on a standard laboratory microscope.

In general the milling procedure employed has been to mill at $\pm 6^\circ$ at 3.3 keV for 20 minute time periods. After a number of milling sessions the clean straight glue line seen in Figure 24 widens as the milling process preferentially mills asperities and the softer glue material to leave a widened glue line region as seen in Figure 25(a-c). As this glue line approaches the incredibly low thicknesses required for TEM specimens, optical fringing will begin to appear in the glue line and the substrate material. At this stage the milling time period should be shortened to ~5 minutes until a small hole is opened in the glue line as shown in Figure 25d. This sample is then finished with 3 minutes of milling at 1

keV with the Ar ion guns at 8° followed by 10 minutes of milling at 0.3 keV at 8°. This removes amorphous material and some re-deposited material [141].

This specimen is then prepared for TEM analysis though may be further treated with plasma cleaning, optical baking or solvents to suppress contamination of the specimen in the microscope or be milled further to achieve a thinner sample. Further contamination suppression is achieved in the microscope using a LN₂ cold trap around the TEM specimen and in STEM mode using beam showering.

3.4 Area Integrated Characterisation Techniques

Determining a link between microstructures shown by electron microscopy and general volume properties of a film can be challenging. However, to begin this we require methods to measure the electron transport, magnetisation and chemical properties of our specimens on a large area scale. By assessing larger volumes of the specimen we obtain averaged properties of the material and can use these results to understand the macroscopic properties of deposited films.

3.4.1 Vibrating sample magnetometer and hysteresis curves

The vibrating sample magnetometer (VSM) [142] consists of a non-magnetic rod, an electromagnet and a set of pick up coils. This allows a sample to be mounted at the centre of the magnetic pole pieces in a region of spatially constant applied field and oscillated perpendicular to the applied field. The applied magnetic field leads to a sample magnetisation which generates a further contribution to the magnetic field. The pick-up coils mounted near the pole piece of the electromagnet are oriented such that they do not detect the slowly time varying applied field. However, they do pick up the rapidly time varying magnetisation field as a result of the sample motion. The magnetisation of the sample does not rapidly vary, however, the oscillatory motion of the sample driven through the sample holding rod creates rapid spatial variation in the magnetisation field with respect to the stationary pickup coils. By filtering the pickup coil signal for frequencies comparable to the sample holder driving frequency using a lock-in amplifier it is possible to achieve low noise results for magnetisation as a function of applied field.

The applied field produced in a VSM is calibrated with a Hall probe prior to conducting experimental work and is simply recorded as a function of the current in the electromagnet. Due to the large dimensions of a VSM system a wide range of field strengths can be achieved.

The magnetic moment of the sample is measured as a function of the current produced in the system pick up coils which requires calibration from a standard sample. If

the sample geometry is the same as the calibration standard, sample magnetic moment can be measured to an accuracy of $\pm 1\%$.

Performing a data sweep from high magnetisation, to high reversed magnetisation and back again is used to produce a hysteresis loops from a ferromagnetic material which demonstrates the magnetisation of a material as a function of applied magnetic fields. These results show a number of key properties of a magnetic material including the reversible and irreversible domain wall motion, demonstrating the magnetic saturation field and the sample magnetic coercivity.

VSM experiments can be conducted at York and elsewhere and have been used to argue the presence of structural defects in Fe_3O_4 due to the lack of clear magnetic saturation in grown films. Furthermore it is possible to identify in a rudimentary way the presence of Fe_3O_4 rather than other iron oxides which could be produced in poorly optimised Fe/O deposition due to the characteristic coercivity and magnetisation of Fe_3O_4 .

3.4.2 Magnetoresistance (MR)

Magnetoresistance is a measure of the change in electronic resistance of a material as a result of an applied magnetic field. This terminology has been used earlier in this thesis with reference to tunnel magnetoresistance and giant magnetoresistance, where layered device structures are used to produce significant, non-linear variations in resistance due to the magnetic configuration of many material layers. In terms of simple MR measurements we are looking for variation in the resistance of a single material layer as a result of applied magnetic fields. The value of MR is given as an fraction as shown in Equation 11 where $R(0)$ is the zero field resistance and $R(H)$ is the measure resistance with an applied field.

$$\text{MR} = \frac{R(H) - R(0)}{R(0)} \quad \text{Equation 11}$$

In general MR measurements are made using four contacts arranged in a straight line across the specimen; this allows a voltage to be supplied between the two outer most contacts, and the current flowing to be measured between the two inner contacts this is referred to as Hall Geometry.

Experimental work to measure MR curves has been performed both at York using a simple four point probe with spring loaded Cu contact points combined with a calibrated electromagnet taken from a decommissioned VSM. MR measurements performed on the $\text{Fe}_3\text{O}_4/\text{YSZ}$ samples shown later in this thesis have been performed using a physical

properties measurement system (PPMS) supplied by Quantum Designs Inc. at the Tokyo Institute of Technology [102, 103].

All MR data taken in this thesis has been performed in a constant voltage operating mode allow current across the sample to be the variable during a magnetic field sweep.

The geometry of an MR result is important, the contacts can be aligned with the in-plane crystallography of the sample or with a more sophisticated design can allow out-of-plane MR measurements and the applied field can be positioned either longitudinally or transverse to the current flow.

Whilst the premise of MR measurement is relatively simple, a wide range of physical properties are probed by this technique and understanding the results produced can be non-trivial.

Bulk Fe_3O_4 should not demonstrate any magnetoresistance change with uniform electron transport regardless of applied field, however, in thin film geometry, Fe_3O_4 exhibits decreasing resistance with the application of a magnetic field. This is generally argued to be a result of APB formation, but direct evidence or justification of this is limited

3.4.3 Raman Spectroscopy

Raman Spectroscopy is used to study the vibrational and rotational modes of crystal bonds to identify the chemistry and structure of crystals and molecules.

A monochromatic laser beam is used to illuminate the sample and will then undergo inelastic scattering events with phonons, molecular vibrations and other sample excitations which lead to energy shifts (both up and down) in the incident phonons.

The radiated light is then collected, focussed and dispersed onto a detector in an analogous fashion to an EELS detector.

Only a specific subset of the rotational and vibrational modes of a molecule or crystal can be identified in Raman spectroscopy. These modes are referred to as Raman active modes. To be Raman active there must be a change in the Polarizability of the material in question as a result of the rotation/vibration.

This technique is only used briefly in this thesis to compare thin films with a reference specimen.

3.5 Atomistic magnetic simulations with *VAMPIRE*

To understand atomic scale spin dynamics at defect interfaces within Fe_3O_4 and within bulk Fe_3O_4 structures I have used the 'Vampire' software package developed at the

University of York [143]. This is an open source program which can be downloaded and compiled following the instructions given at:

<http://www-users.york.ac.uk/~rfl500/research/vampire/>.

Vampire allows atomistic spin dynamics calculation using a fully user determined atomic structure and exchange constants and is therefore ideal for studying the behaviour of metal oxide systems which exhibit structurally dependent, highly localised, super-exchange interactions (see theory). Vampire is based on individual atomic spins without considering band-structure

To explore the behaviour of Fe_3O_4 we study fully periodic 20 nm^3 structural cells. Super-exchange interactions are allocated on a site by site basis by performing a conditional three membered loop over all atoms to identify all $\text{Fe}_i\text{-O-Fe}_j$ structures where $i \neq j$ within an interaction cut-off of $\text{Fe-O} < 3.5 \text{ \AA}$ and $\text{Fe-Fe} < 5 \text{ \AA}$. Many of the Fe sites in Fe_3O_4 are surrounded by 6 oxygen sites, which are in turn each surrounded by 3 or 4 further Fe sites. This leads to ~ 20 interactions per Fe site. However, many of these can be reduced both to remove double counting and to fold multiple $\text{Fe}_1\text{-O}_x\text{-Fe}_2$ interactions into a single summed interaction based on linear summing of multiple antiferromagnetic (AFM) and ferromagnetic (FM) exchange couplings.

Within this cell we neglect O sites as these carry no uncompensated magnetic moment based on a site localised magnetic moment.

$$\mathcal{H} = \mathcal{H}_{exc} + \mathcal{H}_{ani} + \mathcal{H}_{app} \quad \text{Equation 12}$$

$$\mathcal{H}_{exc} = - \sum_{i \neq j} J_{ij} \mathbf{S}_i \cdot \mathbf{S}_j \quad \text{Equation 13}$$

Bulk values for the super exchange interactions in Fe_3O_4 have been taken from *Ab Initio* spin spiral studies by Uhl & Siberchicot [26] which were confirmed to give convincing values of the Curie temperature T_c by Mazo-Zuluaga *et Al* [27]. The validity of assigning individual atomic spins to metal sites in these simulations is based on the work of Uhl and Siberchicot [26].

Local super exchange interactions have been determined as effective Heisenberg interactions between near neighbour cation sites based on Fe-O-Fe co-ordinations. All local atomic interactions have been collected computationally on structural cells of ~ 2500 atoms to identify bond angles and bond lengths present within a crystal structure. Super-exchange interaction values have been determined from bulk Fe_3O_4 super-exchange values of $J_{AA} = -0.11 \text{ meV}$, $J_{AB} = J_{BA} = -2.92 \text{ meV}$ and $J_{BB} = 0.63 \text{ meV}$ as determined by Mazo-Zuluaga *et Al*. [27] and Uhl *et Al*. [26] from spin spiral calculations which are verified due to the high correspondence between theoretical and experimental curie temperatures

obtained by simulated annealing. The assignment of non-bulk interactions has been performed through extrapolation of these values using a general form of expected super-exchange interactions given by Sawatzky et al. [67] for orthoferrite materials of $J_{ij} = -\cos^2 \theta$. To ensure correct effective J_{ij} values within the calculations the total interaction values have been divided by the number of contributing $\text{Fe}_i\text{-O}_x\text{-Fe}_j$ triplets which form these interactions in the bulk. In the case of the $90^\circ \text{Fe}_B\text{-O-Fe}_B$ interaction it is intuitively clear that this interaction is mediated by multiple right-angled bonds via an O site which are summed. All interactions between Fe_i and Fe_j are linearly summed across all intermediated O sites which contribute to this interaction.

Cubic magnetocrystalline anisotropy has been incorporated in these simulations using $K_V = 8.43 \times 10^{-2} \text{ meV/nm}^3$ [27].

3.6 Image Analysis

Modern TEM systems (particularly the STEM operating mode) require many software and hardware systems to integrate with one another to control the imaging systems, chemical analysis control and to maintain the aberration corrector systems. In the case of the JEOL JEM-2200FS at York this is largely achieved by many different computational systems, the CEOS correctors are operated using a separate system from the imaging controls. However, the main user interface used for the microscopy data presented in this thesis has been collected using the Gatan Digital Micrograph software suite which integrates offline image analysis and processing with an online TEM control mode. Digital Micrograph saves images as an encoded and metadata integrated “*.tiff” style format which saves as a “*.dm3”.

Digital Micrograph allows a wide range of image analysis and processing including fast Fourier transform (FFT) routines and digital diffraction pattern masking for Bragg filtered imaging. Standard image measurements such as histograms, line profiles and thresholding and particle size analysis routines. However, the ability to write scripts for Digital Micrograph makes this software suite highly adaptable and well suited to controlling high specification image analysis and novel experiments [144].

In this PhD I have used the statistically determined spatial drift (SDSD) digital micrograph plugin provided by Schaffer *et al* [145] to align STEM image stacks. This allows averaged intensities to be calculated on a pixel by pixel basis from a large number of raster scanned images. This process all significant improvements in the imaging signal to noise ratio without incorporating high levels of beam damage or specimen drift which would be produced by slow scanning rate. I have also used the EELSTools [144] software suite to analyse EELS spectra.

Image analysis and presentation has also been performed using the ImageJ software package which offers useful tools for image measurement and image presentation [146].

3.7 Crystallographic structure models

To perform the atomistic theoretical methods on which the analysis of Fe_3O_4 depends requires the creation of three dimensional crystallographic structure models. Simple crystallographic structures have been produced for image simulations, magnetic simulations, density functional theory and diagrammatic interpretation of atomic structures.

These atomic structures take the form of either crystallographic symmetry and atomic basis cells or primitive unit cells to describe bulk co-ordinated crystal structures. When describing larger structures we form supercells which can contain many thousands of atoms and allow the description of extended defects, interfaces or surfaces. Fundamentally crystallographic structure models need to include cell geometry to create a 'box' into which an atomic structure can be created allowing a fully periodic structure which can be extended infinitely in a regular array of cells.

Basic crystal structures have been produced using data held by the chemical database service, Daresbury. These are expressed in terms of space group (which define cell shape, symmetry and repeat structure, lattice vectors and an atomic basis). This structural data is often taken from experimental analysis often based on x-ray crystallography. Structures of this type do not discreetly describe the position of atomic sites but rather the full atomic structure is produced by using the symmetry operations of the structural space group with the atomic basis of the structure which generally comprises only three or four atomic sites. The CrystalKitX software package has been used to expand these details into a real space atomic structure which can be further manipulated and visualised.

The discreet positioning of each atomic site into a primitive cell or unit cell in the case of Fe_3O_4 relies on atomic sites being described in either fractional or absolute co-ordinates within a three dimensional space. The co-ordinate system for describing the positions of atoms is not necessarily the same as the co-ordinate system used to describe the overall cell geometry and in the case of hexagonal or trigonal geometries this can be used to simplify the description of the atomic structure. For unit cell descriptions of atomic structure in either symmetry based or discreet structures the underlying crystallography of the cell is generally incorporated and maintained by the cells allowing an accurate mapping of various crystal planes as the cell is manipulated.

To explore defects, vacancies, interfaces or other crystal defects it is generally preferable to form extended supercell structures containing many unit cells of a crystal. This allows the incorporation of a defect into bulk like crystal structure and can be used to effectively model the electronics, magnetic behaviour or structural refinement of a defect with the bulk crystal matrix. These cells are built either using a software package or with some form of algorithmic approach which allows the manipulation of many atoms in an error free fashion. Supercells generally do not maintain the underlying crystallography of the structure as sites are populated into a large, user specified geometry. Choosing the correct size and structure of a supercell is essential to produce accurate theoretical models which represent the transitions between bulk and defect structure without requiring exceptionally high levels of computational resources.

The atomic structures of all three scales of atomic modelling are based on highly geometric atomic site positions which are a highly accurate first order approximation of site positions. Relaxed co-ordinates have been produced using DFT structural refinements and classical potentials implemented in the general utility lattice program (GULP) code to allow all sites to find their energy minimised positions. In general this does not create 'large' deviations in atomic position but rather allows minor deviations in atomic site co-ordinations.

Many of the programs and codes used to produce and analyse crystal structures rely on program specific cell definitions so a number of java scripts have been produced to convert atomic structures into different formats with different file extensions. However, all the programs use a basic plain text file.

3.8 Image Simulations (HRTEM)

Image simulations are an essential tool to extract structural information from microscope images; particularly in the case of complex atomically resolved HRTEM data. The phase contrast found in HRTEM images is a function of sample thickness, microscope defocus, higher order microscope beam parameters such as astigmatism and convergence semi-angle and the fundamental atomic structure under examination. Local variation in these parameters particularly in the likely case of sample thickness variation across the field of view can lead to complete contrast inversions as a result of only minor sample properties variations.

When image simulations are performed for HRTEM a tableau of defocus and sample thickness values is generally presented, this is often accompanied by an equivalent range of microscope images across a range of experimental defocus values.

All the image simulation techniques used within this thesis are based on the multislice method which reduces the 3D structure of the specimen to a series of closely spaced projected potentials and propagation functions [106, 147-153]

This technique reduces the three dimensional crystal structure representing the TEM specimen material down to a series of two dimensional planes in which the three dimensional potentials of the atomic structure are represented as two dimensional projected potentials. The electron wavefunction (ψ) is passed through this series of two dimensional potentials using an iterative approach which takes the input wave $\psi_i(\mathbf{k})$, convolves this with a Fresnel diffraction, near field, propagation operator $P(\mathbf{k})$ which represents the wavefunction moving the distance in space between two neighbouring x-y planes this incident wave is then convolved with the interaction with the phase grating which represents the projected potential of the next crystal plane $Q(\mathbf{k})$, the mathematics of this iterative convolution is expressed in general in Equation 14. This wave propagation is continued through the material until reaching the crystal exit surface. This final electron wavefunction is then convolved with the contrast transfer function of the microscope which contains a number of microscope parameters to express the final contrast variation in a real space image.

Much of the mathematics of image simulation calculation requires rapid and computationally efficient transfers between real and reciprocal space which is essentially dependent on the fast Fourier transfer routines developed by Ishizuka and Uyeda [154, 155]

$$\psi_{n+1}(\mathbf{k}) = [\psi_n(\mathbf{k})P_{n+1}(\mathbf{k})] \otimes Q_{n+1}(\mathbf{k})$$

Equation 14

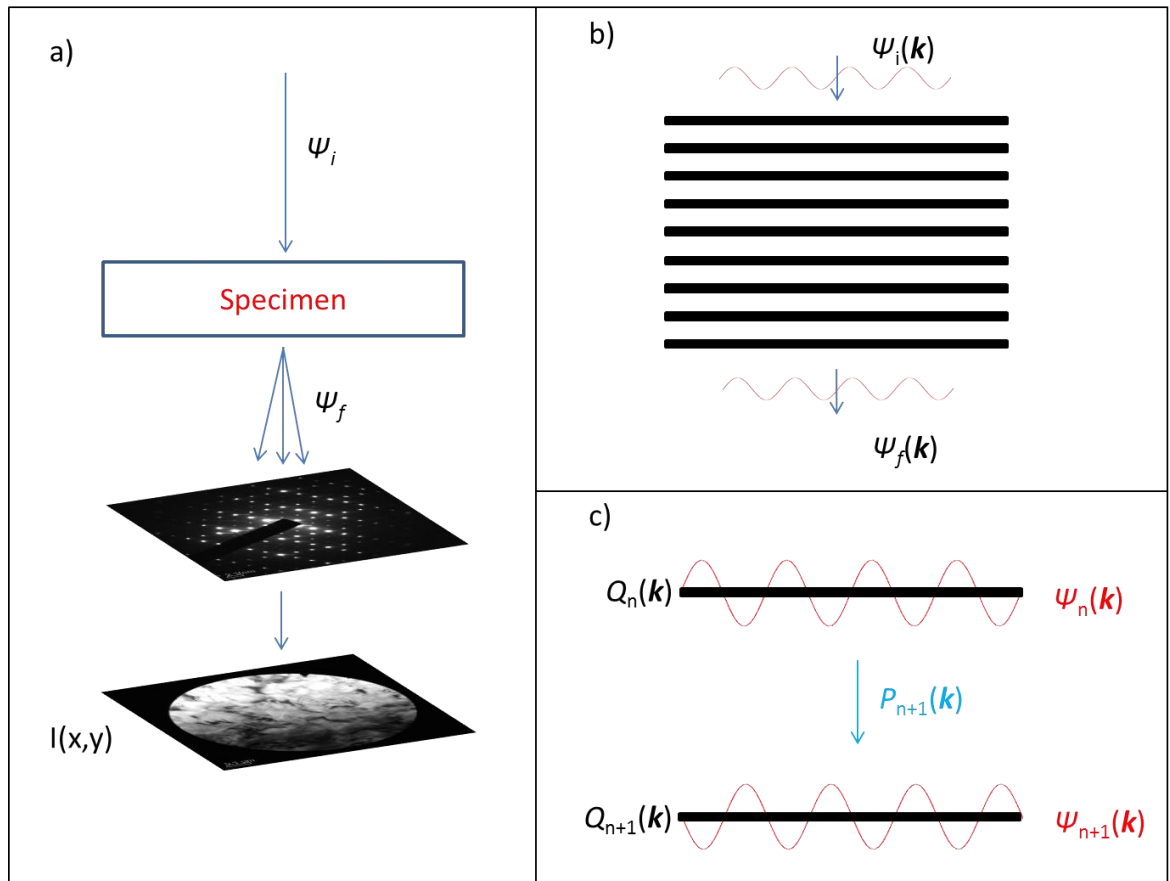


Figure 26: Considering the electron wave passing through a real and computational sample. a) in a real microscope a beam is formed giving ψ_i which interacts with the TEM specimen to produce an exit wave function ψ_f containing the various interactions discussed above. This is lensed to give diffraction patterns and imaging. b) the computation sample is reduce to multiple layers which convolve with the initial wavefunction and propagation operators to give a sample exit wave. The transfer of the wave throughout the microscope and the formation of the initial wavefunction are determined by the contrast transfer function of the microscope. c) The iterative plane by plane convolution of wavefunction, propagation and phase grating.

There are a number of major scientific constrains to using image simulations, firstly we require knowledge about the full crystallographic structure of the sample including sample thickness and atomic structure. Secondly we need to understand the properties of the microscope imaging condition including the defocus value. Often when performing image simulations we do not know these properties with the level of accuracy we would ideally demand, which leads to image simulations being performed on an iterative basis to determine how accurate our predicted model structures are.

HRTEM image simulations in this work are performed using the java electron microscope simulator (JEMS) image software package distributed by Stadelmann [156]. The JEMS software package used also allows SAD simulation and crystal visualisation. This is required to analyse the input structures being studied in the HRTEM simulation.

3.8.1 QSTEM image simulations (HAADF-STEM)

The Quantitative-STEM (QSTEM) software package [157] allows the highest possible levels of user specification for STEM based image simulations. STEM simulations are a modification of the HRTEM simulations and are fundamentally based on the multislice approach outlined above. However, STEM simulations require a pixel-by-pixel approach to image simulation [119] to reflect the incoherent serial nature of data acquisition when producing a STEM image. This greatly increases the computational demand required to produce a STEM simulation compared to a HRTEM simulation as each pixel of the simulation represents a separate calculation.

STEM simulations begin from a function for the probe which is a coherent convergent plane wave set propagating from the probe forming aperture [158]. What is then calculated at the end of the simulation is the proportion of the beam being scattered to specific detector geometry angles. This determines the pixel intensity associated with the probe position of the incident beam.

QSTEM allows full detector geometry to be determined allowing both inner and outer detector angles to be set within the simulation. This makes the simulations of HAADF-STEM, MAADF-STEM and BF-STEM fundamentally very similar, but with different detector geometry applied as the criteria for scattered electron detection within the final image.

Atomic displacement and phononic distortions are contained within this image simulation routine by calculating the effect of thermal diffuse scattering (TDS). These electron-phonon interactions effectively increase higher angle scattering and reduce the intensity of lower angle scattering [159].

Frozen phonons are used to simulate thermal diffuse scattering by implementing random atomic site displacements based on the Debye-Waller factor of specific sites. The simulation routine and the frozen phonon model requires fixed discrete atomic positions which cannot describe the multiple distortions and range of motion of atoms across the duration of the experiment [160], so multiple frozen phonon configurations are used in the simulation to describe the effect of a range of possible atomic positions. For any final image simulations I have used 30 frozen phonon iterations (TDS runs) which also forms a trivial way of parallelising the image simulation process as different TDS runs are essentially independent calculations these can be calculated by different processors, the resultant images are recombined as an average image intensity after the calculation is completed [136]. Frozen phonon were explained by Van Dyck [161] and demonstrated

that such a method could be used for quantitative analysis. The implementation of these absorption processes in QSTEM make it ideal for HAADF-STEM simulations.

The Debye-Waller factors of specific sites can be individually determined or standard values can be used however for surfaces and other non-bulk atomic configurations, Aveyard *et al.* [162] have shown significant variations in atomic displacements depending on the position and co-ordination of atomic sites.

To illustrate the computational demand of STEM simulations, each pixel in the simulation requires an individual multislice calculation for each TDS run, so for a very small, i.e. 25 x 25 pixel simulation with a modest number of 15 TDS runs would require over 9000 individual calculations.

Simulation packages have defaults for atomic scattering form factor $f_i(\theta)$ however atoms oscillate within the crystal matrix effectively smearing out the projected potential of an atomic column. This introduces an absorption term in the electron wavefunction [161, 163, 164].

3.9 Density Functional Theory

Density functional theory (DFT) is a computational theory method to model the quantum mechanics of many body systems. This is used to investigate the ground state electronic structures of many atom (many electron) material systems.

These calculations rely on the Hohenberg-Kohn theorems that demonstrate that the electronic ground state of a system relies only on the three dimensional electron density of the system rather than the $3N$ spatial co-ordinates of N electrons which are required by many body quantum mechanical treatments and that the ground state electron density is determined by the electron density functional which minimises the system energy [165].

Within Kohn-Sham DFT the unsolvable many-body problem of interacting electrons is reduced to a solvable problem of non-interacting electrons in an effective potential. This effective potential includes external potentials and the effects of Coulombic interactions between electrons including the exchange and correlation interactions. Modelling exchange and correlation is the greatest difficult for DFT as the exact behaviour of exchange and correlation is only known in the case of a free electron gas [166].

This requires approximations for exchange and correlation using either the local density approximation (LDA) local spin density approximation (LDSA) or generalised gradient approximations (GGA) to give local solutions for correlation and exchange as a

function of the local electron density and in the case of GGA the local electron density and its local gradient.

Density functional theory is an *ab initio* approach which uses an iterative self-consistent approach to determine the electronic densities of the ground state electronic structures of an atomic arrangement. The many unknown properties of a density functional calculation are approached using iterative self-consistent methods.

3.9.1 Determining relaxed structures and lattice vectors

Structural refinements and lattice vector determination is based on the principle that stability is achieved by minimising the ground state energy of the system.

To determine the relaxed structure of a crystal, a DFT calculation will perform iterative electronic density calculations based on an initial atomic structure to determine the minimum energy electronic state of this structure. As the various iterations of the calculated electronic density decreases in energy and become increasingly self-consistent (until a specified energy difference minima is met) a minimum energy ground state for the initial atomic structure is determined.

From this minimum energy electronic density the Coulombic forces acting upon the atomic sites are calculated and from these forces a small structural step is made in the positioning of the atomic sites.

This whole process from input structure to marginally refined structure is then repeated many times until the input and output structures have also become self-consistent with minimised ground state energy.

In general, structural refinement using DFT is suitable for making minor adjustments to the atomic structure and will get stuck in local energy minima or simply fail to converge in the case of unphysical initial atomic configurations.

If the calculation is not set up correctly, for example in terms of the size of the structural steps taken or the degree of change between successive electronic densities is not suitable the calculation may either never converge on a self-consistent solution and instead oscillate around one or many local energy minima or conversely may take an incredibly large number of iterations to converge. In both cases the computational details of this process have been selected poorly.

The process of determining lattice vector is based on taking an atomic structure, running only a single ground state energy determination for given atomic structure across a range of lattice vectors and determining the point where the lattice constant minimises the ground state configuration energy. This is effectively probing the Young's modulus of the material by determining the energy cost of compressing or stretching the material. For any DFT calculation determining the energy minimised structure of both lattice constants

and atomic co-ordinations is essential to learning anymore about the material. In the case of bulk structures we can then produce band structures and learn about the properties of the structure in question, in the case of large, experimentally motivated defect structures then simply verifying the stability of a structure is a result in its own right.

3.9.2 Band structures

A band structure expresses the range of electronic states which exist within a material as a function of energy and momentum (k) in the case of Fe_3O_4 which carries a magnetic moment and is half-metallic it is important to include spin in the calculation and expresses band structures as a pair, spin up and spin down.

The Band structure of a material shows the positioning of the Fermi energy in a material relative to allowed states and from this goes some way to showing the conduction properties of the material, however standard DFT does not solve a time dependent quantum mechanical model so conductivity is inferred from electrons which exist at the Fermi level.

The Band structure of a solid shows the allowed states for electrons within that material, unlike in an atom, in which a small number of highly specific energy levels are permitted, in a solid, particularly at and around the Fermi level these energy levels are split and broadened to produce a range of $E(k)$ states more readily expressed as bands.

The results of band structures are expressed in many different ways and can be converted into densities of states representing the number of states at a particular energy rather than the momentum of particular states. This can be projected either by considering the states present as a function of energy in particular physical regions of a sample to give local densities of states (LDOS) or total densities of states (DOS). In this work all densities of states are divided into two spin channels giving spin densities of states (SDOS).

Many physical properties of a material can be determined from band structures and densities of states, including the general conduction properties of a material and the spectral properties of materials which allows EELS simulations (not performed here)

3.9.3 Challenges

As DFT finds the ground state of a many body system, this is indicative of a 0 K structure. This is problematic for Fe_3O_4 as the half-metallic room temperature structure of Fe_3O_4 does not exist at 0 K. What is more, conventional DFT struggles to provide the correct band gap energies for many transition metal oxides so requires a +U parameter to be included in the DFT+U style calculations, this however leads to a higher degree of

charge localisation which can produce polaronic distortions to the structure and the electronics.

DFT calculations are a highly demanding computational process and require workstations or super computers to achieve useful results. This demand scales linearly with the number of electrons in the refined structure, so DFT demands cell geometries be kept as small as possible. This can lead to scientific issues with under sampling in the case of defects and interfaces where non enough atomic sites are included to fully describe a defect, within bulk structure.

3.9.4 Implementation using the Vienna code

The density functional theory results presented in this work were performed by Dr. Keith McKenna [72] using atomic structures determined from electron microscopy.

DFT has been performed using the projector augmented wave (PAW) method as implemented within the Vienna *ab initio* simulation package [167, 168]. We use the Perdew-Burke-Ernzerhof exchange correlation functional and calculations have been performed both using both standard DFT and the DFT+U [169] approach to correct for self-interaction error. DFT calculations have been performed using two collinear spin channels to represent the minority and majority states of the materials separately.

Once the energy minimised structure is found by solving multiple structural configurations the electronic structure of the system can be taken to give a band structure. The most important thing is to find the genuine ground state structure to give the correct band structure. In this work the Brillouin zone sampling density has been maintain equivalent to using a 7 x 7 x 7 Monkhorst-Pack k-point grid for the bulk primitive cell of Fe₃O₄ [72] and pseudo-potentials have been employed to separate valence and core electrons within the calculations and to minimise computational demands.

This work has required the use of the Archer Supercomputer.

Chapter 4. Fe₃O₄/MgO(111)

The vast majority of studies in thin film Fe₃O₄ have been performed using (001) oriented MgO crystals as a substrate material [31, 69, 170]. In general MgO is an obvious choice of substrate to grow Fe₃O₄ films for spintronic applications. MgO is a successful tunnel barrier material and has a close lattice match with Fe₃O₄ of ~0.3%. However the different crystal symmetry of MgO (space group Fm-3m, lattice constant 4.212 Å) [171] compared with Fe₃O₄ (space group Fd-3m, lattice constant 8.34 Å) [46] lead to structural growth defects known as antiphase domain boundaries (APBs) as a result of equivalent growth nucleation sites between the film and substrate [31, 40, 75, 172].

By changing the growth orientation in this system to explore the (111) oriented growth we are able to potentially exploit polarity related phenomena in this layered cation/anion structure and can generate a range of atomically controlled interfacial structures if the specific interfacial layer in this structure can be controlled during the first stages of growth nucleation.

The growth conditions required to produce high quality films in the (111) geometry are slightly altered from those used to produce (001) oriented Fe₃O₄ and the surface spin polarisation has been shown to be inverted through spin polarised metastable de-excitation spectroscopy (SP-MDS) studies [10]. In this work we have found a much greater degree of regularity in the morphology and atomic configuration of APB defects when compared with historical Fe₃O₄/MgO(001) growths in which the formation of defects appears to take a complex fractal geometry morphology.

By determining the atomic structure of an APB based on experimental data it is possible to probe magnetic and transport behaviour on the atomic level which is of interest for nanostructured devices. Previously this has been hindered due to the complex fractal network of APBs in (100) oriented thin films and lack of atomic resolution data to verify the atomistic models of APBs in magnetite.

In this work we demonstrate that Fe₃O₄(111) film grown on MgO(111) represents a model system for determining the atomic structure of Fe₃O₄ APBs. Based on these

models we study magnetisation reversal in thin film magnetite based only on the exchange interactions obtained from the geometry of the atomistic models that incorporate APBs.

4.1 Methods

Fe₃O₄ films have been grown at a rate of 0.2 Å/minute in a ultrahigh vacuum (UHV) environment with a base pressure $<2 \times 10^{-10}$ mbar by simultaneous deposition of Fe and atomic O from an e-beam K-cell and radio frequency (RF) assisted gas plasma source respectively. During the deposition the MgO(111) substrate was held at 300 °C and the partial pressure of O was maintained at 5×10^{-6} mbar.

Cross sectional samples have been produced using conventional methods as described earlier, including mechanical polishing and Ar ion milling [137]. Plan view transmission electron microscopy (TEM) specimens were prepared by cleaving the MgO substrate to produce thin (111) oriented foils. High resolution transmission electron microscopy (HRTEM) and dark field transmission electron microscopy (DF-TEM) were performed using a Hitachi H-9000 NAR microscope operating at 300 kV. Dark field imaging was performed using the [4-40] reflections from the Fe₃O₄ diffraction pattern which highlights the APB defect shift vectors with dark contrast and excludes any residual MgO from the imaging condition. In this imaging condition 66% of the $\frac{1}{4}a_0[1-10]$ shift vectors associated with an APB defect are shown in dark contrast [173, 174]

Crystal structures have been performed using rigid shifts and rotations of an unrelaxed Fe₃O₄ structure in CrystalKitX. Automated bond counting and structural analysis exercises have been performed using a C++ routine to determine all possible Fe-O-Fe bonds with Fe-O distances cutoff at 3.5 Å and Fe-Fe distances cut off at 5 Å. Full periodic boundary conditions have been implemented for structural analysis.

HRTEM image simulations were performed using the java electron microscope simulator (JEMS) image simulation software package for multislice simulations [156].

Experimental magnetisation data has been produced using a room temperature vibrating sample magnetometer (VSM) with applied fields of ± 5 kOe. This data has been corrected for substrate contributions using an equivalently shaped MgO specimen to produce a substrate contribution to magnetisation for subtraction.

Magnetic simulations have been performed using a three dimensional atomistic spin model implemented in the VAMPIRE software package [143, 175]. This Heisenberg spin model determines spin configurations as a result of user defined exchange constants and atomic structures. Super exchange interactions have been calculated using accepted exchange values for the three bulk interactions in Fe₃O₄ [26, 27] i.e. the bulk J_{AA} , J_{AB} and J_{BB} values and a $J_{ex} = -A \cos^2\theta + B \sin^2\theta$ relationship (negative is anti-ferromagnetic) fitted

to bulk values of super-exchange interactions at the three known bulk Fe₃O₄ points to extrapolate to non-bulk interactions [31, 63, 67]. Super-exchange interactions are calculated with an interaction cut-off of 3.5 Å between Fe-O and 5 Å between Fe – Fe across the Fe-O-Fe triplet with the angle θ defined by the angle subtended at the O site. Spin configuration images have been produced using POVRAY graphical software.

4.2 Results

Figure 27 shows selected area diffraction (SAD) patterns from the Fe₃O₄/MgO interface in the [11-2] and the [1-10] viewing directions. These patterns show the epitaxial relationship between the film and substrate which is identified as Fe₃O₄(11-2)||MgO(11-2) and Fe₃O₄(1-10)||MgO(1-10) as expected in this almost unstrained cube on cube growth. As a result of the double size Fe₃O₄ unit cell compared with the MgO unit cell, the Fe₃O₄ diffraction pattern has ½ spaced diffraction reflections which can be seen in the SAD pattern. The reciprocal lattice vectors are highlighted with a dashed yellow line (Fe₃O₄) and white solid line (MgO) showing this difference in size. The variation in contrast between the Fe₃O₄ (dimmer/smaller) spots and the mixed Fe₃O₄ and MgO (brighter/larger) spots is clear. As Figure 27b is not symmetrical about the vertical/horizontal axes this diffraction pattern shows that twinned structures are not present in this film.

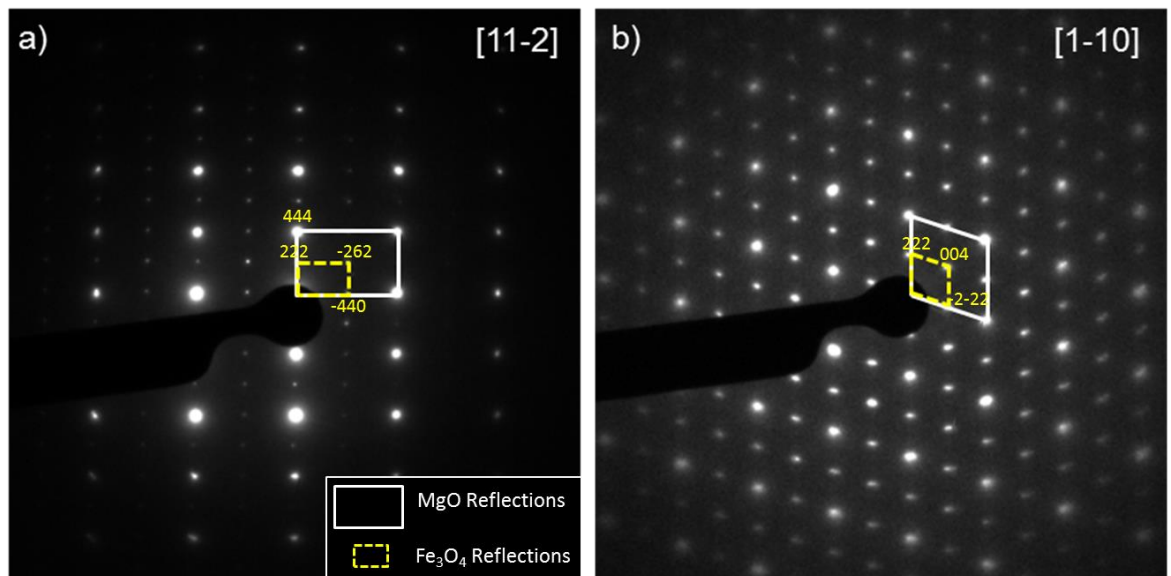


Figure 27: SAD pattern from Fe₃O₄/MgO(111) interface in the a) [11-2] viewing direction, b) [1-10] viewing direction. The relative scale of the lattice constant of Fe₃O₄ (double sized with respect to MgO) is identified here with inverted scale, i.e. g-vectors to Fe₃O₄ reflections are half that of the MgO structure. This is identified by the yellow (Fe₃O₄) and white (MgO) reciprocal lattice vector constructs. [SAD patterns supplied by Dr. Vlado Lazarov]

The plan view DF-TEM image in Figure 28a shows APB defects in Fe₃O₄/MgO(111) which create an ordered network of boundaries that run along the major

crystallographic planes of the grown film. From this image it can be seen that APB defects in this film preferentially propagate along [11-2] type directions and therefore lie on (1-10) planes forming a network of defects with 60° and 120° intersections. By imaging only with the <4-40> reflections from Fe₃O₄ the $\frac{1}{4}a_0$ <1-10> shifted boundaries which constitute an APB defect give dark contrast. From a range of DF-TEM image we see APB defects prefer to lie on (1-10) planes, but a population of (11-2) plane defects are also observed.

Figure 28b shows a HRTEM image of a defect which sits on a single (1-10) plane in this film. The orientation of the defect running through the centre of the image is the same as those shown in Figure 28a. This image shows the APB defect runs along a single atomic plane and maintains a well ordered, regular defect structure at the interface.

The imaging in Figure 28 demonstrates the presence of APB defects running along crystallographic planes within the Fe₃O₄ film. This reduction in the complexity of APB defect geometry makes structural modelling more straightforward and more accurate.

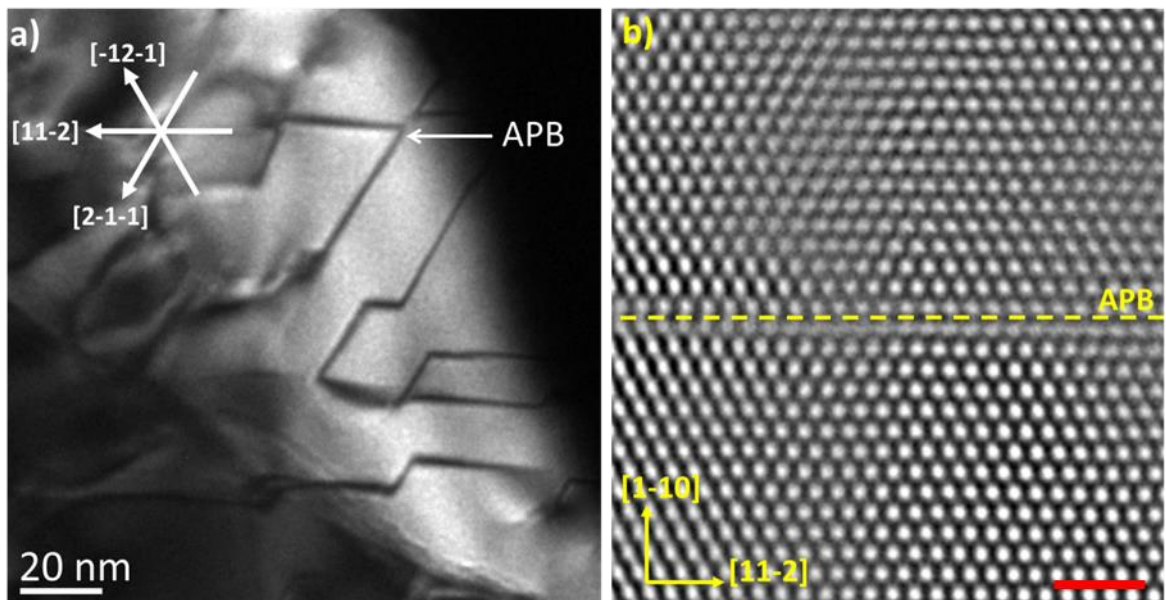


Figure 28: Plan view imaging of Fe₃O₄/MgO(111) film (along the [111] viewing direction) a) DF-TEM image generated using a [4-40] type reflection from the Fe₃O₄ diffraction pattern b) HRTEM image of APB defect in the same geometry. Scale bar equal to 2 nm. [Imaging supplied by Dr. Vlado Lazarov]

4.3 Structural Analysis

With the data from the SAD patterns in Figure 27 and the real space imaging in Figure 28 we can begin to perform structural analysis on the APB defects observed in this film. We know the film exhibits a direct cube to cube epitaxial relationship with the substrate and we know the APB defect is confined to running along major crystallographic directions. We also have a HRTEM image of an APB defect which gives us a method to differentiate between various APB structural models we can generate. What we need to

understand from this information is the atomic structure of APB defects, what possible APB shifts are present in the film and what the specific atomic structure of the interface is. This will allow us to determine the bonding configurations at the APB defect interface and begin to study the effect of these structures on the macroscopic properties present.

The next sections of this work explain the rationalisation of this problem for over 100 possible trial structures to just 14 unique APB models of which many must also be unphysical.

Crystal structures representing the possible APBs in (111) oriented Fe₃O₄ films have been produced using CrystalKitX interface building software which allows rigid translation and rotation of crystal grains. A comprehensive list of possible shift vectors has been produced by studying the crystal symmetry of Fe₃O₄ and the Fe₃O₄/MgO(111) and interface properties.

From the proposed crystal structures we extract all short range Fe-O-Fe bonds with periodic boundary conditions implemented. To model the entire structural repeat of the Fe₃O₄ defect structure we have performed these calculations on cells of between 350 and 600 atoms depending on specific geometry, this gives an output of between 3000 and 6000 unique short range interactions within the interaction range cut off of 5Å from Fe to Fe and 3.5Å from Fe to O.

For each structure the vast majority of Fe-O-Fe bonds are bulk like in nature so we compare the various non-bulk bonding arrangements to identify the prevalence of non-bulk Fe-O-Fe bonds at the model APB defects.

Fortunately this task is simplified as all the bonds studied can be characterised using nominal Fe valence, bond angle and bond length to give a reasonable number of unique bond types including three bulk bonding configurations.

4.3.1 In-plane rotations

From the SAD patterns shown in Figure 27 we can see the clear epitaxial relationship between film and substrate in this Fe₃O₄/MgO(111) growth. Since the substrate used is a single crystal this confines the set of boundary configurations which need to be considered significantly. However, for completeness the possibility of in-plane rotations of Fe₃O₄ must be considered. For both <1-10> and <11-2> type viewing directions there are three related in-plane directions each 120° apart, i.e. [11-2], [1-21] and [-211].

In the case of both (1-10) and (11-2) plane APB boundaries, rotating one side of the defect by a multiple of 120 degrees produces an identical cell with exactly the same atomic positions and hence exactly the same interfacial bonding configurations.

Furthermore, consider an in plane rotation of one grain by 180° so one grain is viewed in the [11-2] direction and the other in the [-1-12] direction for example. In this case, the interface is considerably altered, and when viewed in the [11-2] direction of the substrate this would be very difficult to differentiate using cross-sectional microscopy. However, this type of rotation forms a twinned epitaxial relationship between film and substrate and would be easily identified in the [1-10] direction SAD pattern, since we observe no evidence of twin structures in this sample this type of defect is not studied any further in this chapter. From this initial investigation we can work from the presumption that APB defect boundaries are caused by rigid body, non-rotational shifts of the Fe₃O₄ crystal structure and thus rationalise this problem considerably

4.3.2 Shift Vectors (*in-plane*)

On first inspection, the structural cell of Fe₃O₄ presents a wide range of possible in-plane APB shift vectors between oxygen sites as shown in Figure **29a**. However many of these are equivalent and redundant. The six shorter shift vectors expressed here are of the type $\frac{1}{4}a_0\langle 1-10 \rangle$ and the six larger vectors are of the type $\frac{1}{2}a_0\langle 11-2 \rangle$. By summing two neighbouring $\frac{1}{4}a_0\langle 1-10 \rangle$ type shifts we return the bisecting $\frac{1}{2}a_0\langle 11-2 \rangle$ type shift as shown in Figure **29b** where $\frac{1}{4}a_0\langle 10-1 \rangle + \frac{1}{4}a_0\langle 01-1 \rangle = \frac{1}{2}a_0\langle 11-2 \rangle$. By analysing defect structures produced from all twelve shift vectors at both 11-0 and 11-2 type boundaries it is clear that only two shift vectors are truly unique (excluding a [000] shift vector which gives bulk structure and becomes relevant later) from this analysis it is also clear that the entire APB shift vector scheme can be entirely described by either $\langle 1-10 \rangle$ or $\langle 11-2 \rangle$ style shifts, considering both simply adds redundant complexity to the problem.

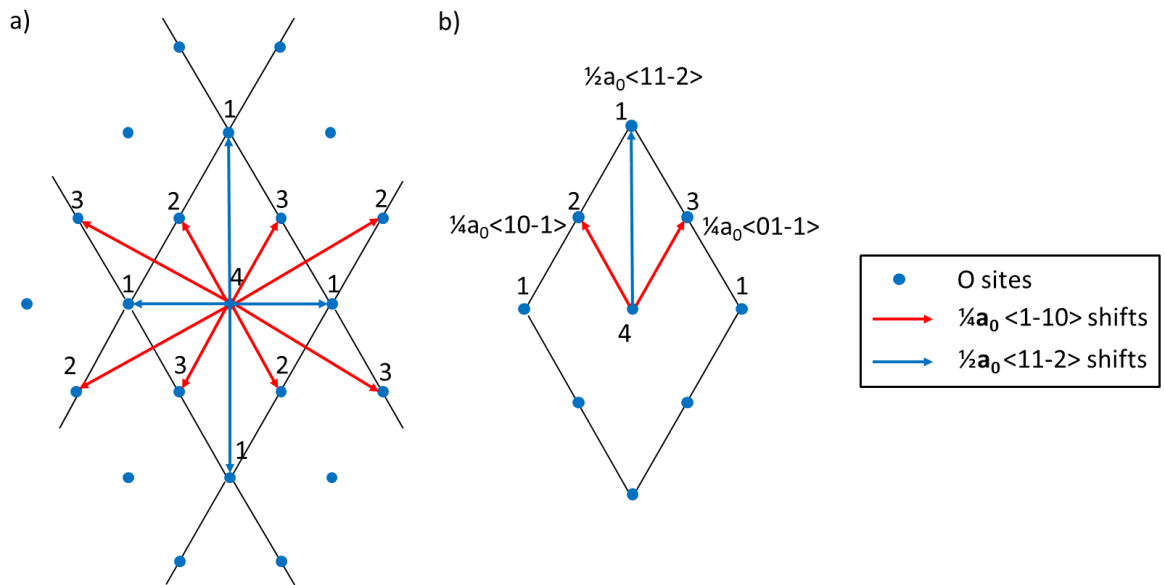


Figure 29: a) Description of all possible in-plane shift vectors of Fe₃O₄(111) constructed by shifting the central O site '4' onto non-equivalent O-sites '1-3' in the near vicinity of the rhombohedral unit cell of Fe₃O₄. b) The reduced set of shifts which can be used to represent all unique APB boundaries determined from atomic structure models.

Firstly, by considering the labelling of oxygen sites 1-4 in Figure 29a which schematically represents the oxygen sites of a single O plane within the rhombohedral 2D cell of Fe₃O₄, it can be seen that all of the twelve shift vectors translate either site 4 to site 1, site 4 to site 2 or site 4 to site 3. And this actually accounts for all the shift vectors that require consideration, as shown in Figure 29b. Furthermore, we find that the $\frac{1}{4}a_0\langle 10-1 \rangle$ and $\frac{1}{4}a_0\langle 01-1 \rangle$, though they translate the structure to a different site, produce identical structures and bonding arrangements. So we can reduce all in-plane APB shifts in (111) oriented Fe₃O₄ to just two, $\frac{1}{4}a_0[01-1]$ and $\frac{1}{4}a_0[-110]$ which are shown in Figure 30.

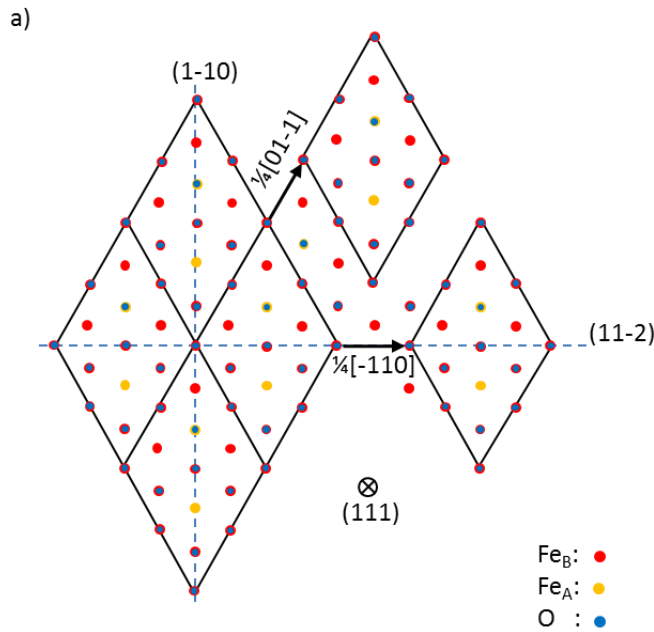


Figure 30: Surface unit cells of Fe₃O₄ in the [111] direction. Possible APB boundaries are highlighted with blue dotted lines and the effect of the APB shifts on the crystal structure are indicated with arrows and accompanying shift vectors.

4.3.3 Shift Vectors (*out-of-plane*)

As a result of step edges on the MgO(111) surface, a second set of APB shifts vectors are created where the Fe₃O₄ structure is translated out-of-plane by a multiple of the inter-oxygen plane spacing at an MgO step. Whilst the (111) direction of Fe₃O₄ is composed of twelve atomic planes of which six contain oxygen as shown in Figure 31, there is only one out-of-plane shift which requires study. The reason for this is that the MgO substrate follows the same stacking sequence as the Fe₃O₄.

By considering Figure 31a which shows the Fe₃O₄ structure in the [11-2] viewing direction it is clear that the Fe planes alternate between Fe_{3B} planes (all red) and Fe_{ABA} (yellow and red) layers. As such, any translation which takes the Fe_{3B} to a second Fe_{3B} layer i.e. a $1/3a_0[111]$ or $2/3a_0[111]$ would have to be accompanied by an in-plane shift to restore of oxygen sublattice and conform to the face centred cubic (FCC) stacking sequence which runs from substrate to film. At this point the structure generated is exactly equivalent to the structures considered before in the purely in-plane shifted structures.

So, the out of plane shifts to be considered are those which translate Fe_{3B} layers to the Fe_{ABA} layer position as is shown in Figure 31. From Figure 31b the oxygen sublattice (blue) can be seen to run continuously through the APB boundary as expected; by the same logic explained for the Fe_{3B} to Fe_{3B} out of plane shifts, an in-plane shift correction is required to ensure this FCC oxygen sublattice is undisturbed, with this correcting shift included the three possible Fe_B to Fe_{ABA} shifts are all equivalent structures. This means

from a set of 6 possible out-of-plane shifts we only have one unique out of plane shift to study and for the advantage of simplicity the $\frac{1}{2}a_0[111]$ shift is selected as in the ...ABCABC... stacking sequence of this FCC material this out-of plane shift is the only Fe_B to Fe_{ABA} shift which does not require an in-plane correction as the stacking sequence is shifted through two full repeats back to equivalent stacking planes either side of the boundary. On top of this out-of-plane shift the in-plane shift vectors discussed above in 4.3.2 must also be considered, this gives us three possible shifts. These are either, $\frac{1}{2}a_0[111]+[000]$ (i.e. the out of plane shift with no in-plane shift), $\frac{1}{2}a_0[111]+\frac{1}{4}a_0[01-1]$ or $\frac{1}{2}a_0[111]+\frac{1}{4}a_0[11-2]$. In total this means the entire system of geometrical APB shift vectors at well-defined crystal boundaries in Fe₃O₄(111)/MgO(111) can be explained in terms of five shift vectors at 2 crystallographic boundary types. This represents a significant rationalisation of the overall problem into something which can be analysed and studied extensively.

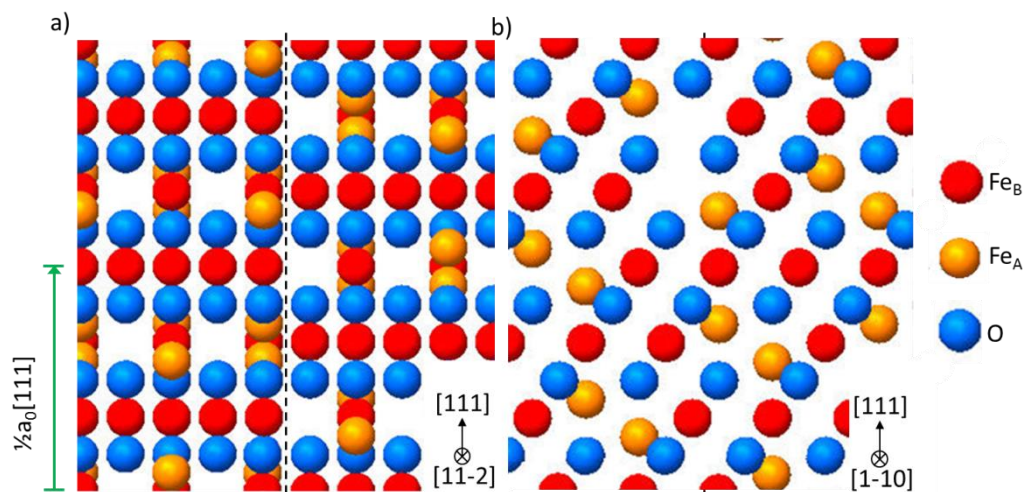


Figure 31: Cross sectional structure diagrams of out of plane ($\frac{1}{2}a_0[111]$ shift) APB boundaries in a) the $[11-2]$ viewing direction and b) the $[1-10]$ viewing direction.

4.3.4 APB Boundary Geometry

With a full set of shift vectors considered and rationalised down to the set of 5 unique shifts (2 in-plane and 3 out-of-plane) we require specific geometries of APB boundaries. From the DF-TEM image in Figure 28a and the HRTEM image in Figure 28b we can clearly see extended, straight line defects on crystallographically oriented planes. However, these images do not inform us of the exact atomic structures at the interface. We are able to identify a viable geometrical structural model and use image simulations to understand how relevant our models are to the real crystal structure. However this is not possible on all boundaries, some of which produce greater levels of complexity. Particularly the oblique $\frac{1}{4}a_0[10-1]$ geometrical shift can be terminated on one of two

boundaries, both of which are non-stoichiometric. The difference between these two boundaries is shown in Figure 32. The clearest example of the two possible interface structures is shown in Figure 32a and Figure 32b where the choice of moving the boundary plane by one atomic site left or right introduces a completely different interfacial structure. The same effect is observed in Figure 32c and Figure 32d, which represents the same shift vector but with the perpendicular defect plane, but is harder to identify. By studying all possible surface terminations through the Fe₃O₄ unit cell, we find this interfacial structure issue is only present in the oblique $\frac{1}{4}a_0[10-1]$ shift and the equivalent out of plane shift. And this leads to two differing structures from the one shift vector. Overall, this gives five possible shift vectors with 2 extra interface configurations, at 2 crystallographic oriented boundaries. A total of 14 models must be considered to study all possible geometric APB boundaries within this set.

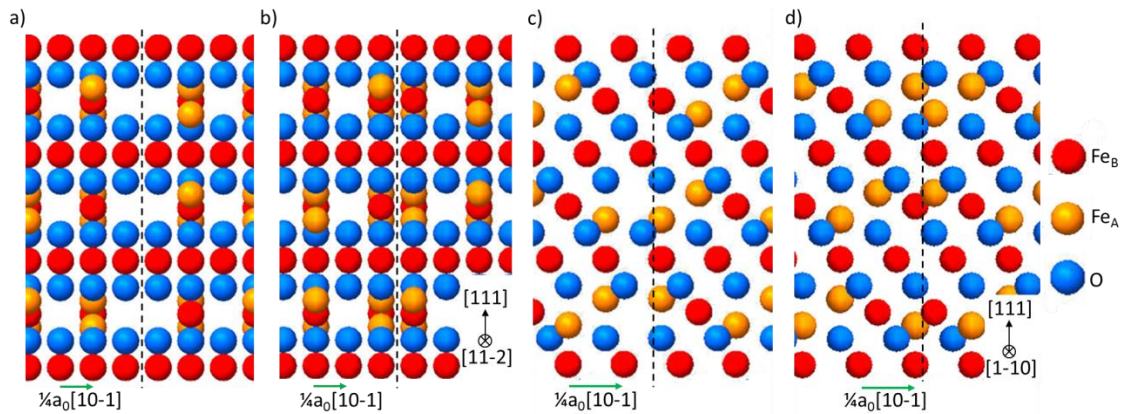


Figure 32: Geometrical models of $\frac{1}{4}a_0[10-1]$ shifted APB boundaries in both the $[11-2]$ (a and b) and $[1-10]$ (c and d) viewing direction.

4.3.5 Non-bulk bonding at the APB

By analysing the geometric bonding calculations at the interface of the 14 Fe₃O₄(111)/MgO(111) APB models we find sets of bonding configurations with many shared characteristics and some important differences between different boundary types. Each of these boundaries gives a large set of non-bulk bonds which can be characterised by their bond lengths, angles and nominal atomic valences.

We find there are 180° Fe_B-O-Fe_B bonds at each of the APB defects studied, regardless of APB geometry, shift vector and growth direction. Since we find no other high angle bonds between the 125.3° Fe_A-O-Fe_B bulk bonds (which are responsible for the Anti-ferromagnetic coupling of the Fe_B and Fe_A sublattices in the bulk Fe₃O₄) and the APB defect specific 180° bond we work on the basis that the majority of the anomalous properties of APB defects will be driven by the density of these specific bonding configurations. However the range of other lower angle non-bulk bonds also requires

some consideration. Here we present the number density of 180° bonds at the various APB defects for comparison.

The APB defect we observe in Figure 28 shows a defect on a (1-10) plane, all the possible (1-10) APB defects are shown in Table 2. This table shows the seven different shift vectors can be broadly grouped into defects which produce 0.266 180° bonds/Å² and the single defect which gives a much higher 0.664 180° bonds/Å². In the first category with lower levels of high angle bonding we find all but one of the geometrical defect structures. These defects are categorised by the many equivalent shift vectors which produce the specific defect so while Table 2 includes 41 different defects, only seven non-identical boundaries are produced. Of these seven boundaries, six actually lead to exactly the same interface density of high angle bonding and none of these interfaces lead to no high angle bonding.

It remains to be seen whether the very high density of high angle bonding at the out-of-plane [000] shifted defect is actually realised in a grown film or whether this leads to defects of this geometry simply being unstable in a grown film or being heavily restructured to avoid this outcome.

Table 2: 180° bonds at (1-10) boundaries in (111) growth direction

Growth Direction	Boundary plane	Shift vector	No. of 180° bonds	Density of 180° bonds/[Å ⁻²]
[111]	(1-10)	V1 [-101],[10-1],[1-21],[-12-1] [01-1],[0-11],[-211],[2-1-1]	48	0.266
		V2 [-101],[10-1],[1-21],[-12-1] [01-1],[0-11],[-211],[2-1-1]	48	0.266
		[1-10],[-110],[11-2],[-1-12]	48	0.266
		$\frac{1}{2}$ [111]+[000]	120	0.664
		V1 $\frac{1}{2}$ [111]+[-101],[10-1],[1-21],[-12-1] [01-1],[0-11],[-211],[2-1-1]	48	0.266
		V2 $\frac{1}{2}$ [111]+[-101],[10-1],[1-21],[-12-1] [01-1],[0-11],[-211],[2-1-1]	48	0.266
		$\frac{1}{2}$ [111]+[1-10],[-110],[11-2],[-1-12]	48	0.266

Table 3 shows a very similar result, with all defects apart from the [000], out-of-plane shift exhibiting the same density of 180° bonding. In the case of (11-2) boundary defects the density of high angle bonding is lower than in the (1-10) case which may

suggest these defects will behave differently in terms of the overall magnetisation (MH) and magnetoresistance (MR) response of the film. However, our observation of the grown film suggests these defects are in the minority. Again, there are 41 tabulated defects in Table 3 which rationalised down to only 7 unique boundaries with only 2 different high angle bonding densities.

This result should go some way to rationalising the problem of APB defects in Fe₃O₄ and demonstrate that this highly complex problem can be broken down into a small number of variables with largely equivalent outcomes.

Table 3: 180° bonds at (11-2) boundaries in (111) growth direction

Growth Direction	Boundary plane	Shift vector	No. of 180° bonds	Density of 180° bonds /[Å ⁻²]
[111]	(11-2)	V1 [-101],[10-1],[1-21],[-12-1] [01-1],[0-11],[-211],[2-1-1]	32	0.188
		V2 [-101],[10-1],[1-21],[-12-1] [01-1],[0-11],[-211],[2-1-1]	32	0.188
		[1-10],[-110],[11-2],[-1-12]	32	0.188
		$\frac{1}{2}$ [111]+[000]	80	0.470
		V1 $\frac{1}{2}$ [111]+[-101],[10-1],[1-21],[-12-1] [01-1],[0-11],[-211],[2-1-1]	32	0.188
		V2 $\frac{1}{2}$ [111]+[-101],[10-1],[1-21],[-12-1] [01-1],[0-11],[-211],[2-1-1]	32	0.188
		$\frac{1}{2}$ [111]+[1-10],[-110],[11-2],[-1-12]	32	0.188

4.4 Image simulations

All image simulations shown here have been initially produced over an 80 nm thickness range and a 50 nm defocus range to identify the best representation of the imaging condition observed in Figure 28b. This was narrowed to a 10 nm thickness range and a 10 nm defocus range in which the HRTEM simulations show similar contrast variation to the imaging and in which the values for thickness and defocus are representative of the sample material; i.e. thickness between 10.11 and 21.67 nm and defocus between -15 and -25 nm.

In Figure 33 and Figure 34 only a single image simulation for each structural model is shown which represents the optimum thickness and defocus values determined for each simulation.

The first important outcome from these image simulations is that only two of the models are close to representing the experimentally observed HRTEM imaging shown in

Figure 28b which is reproduced for convenience alongside the image simulation in Figure 35b. This conclusion is simple to draw as the orientation of the hexagonal intensity pattern immediately disqualifies any of the (11-2) plane defects (left hand column of both Figure 33 and Figure 34). This corresponds with the APB defect geometry identified from the DF-TEM imaging in Figure 28a.

Secondly, it is important to note that the out-of-plane shift in all cases is essentially indistinguishable from the corresponding in-plane shift and the [000] out of plane shift is indistinguishable from the undisturbed Fe₃O₄ structure in this viewing direction. By considering the density of 180° bonds produced at the $\frac{1}{4}a_0[1-10]$ shift and the corresponding out of plane shift we model the magnetic behaviour of this defect on the in plane version as this also corresponds most closely with all other defect structures.

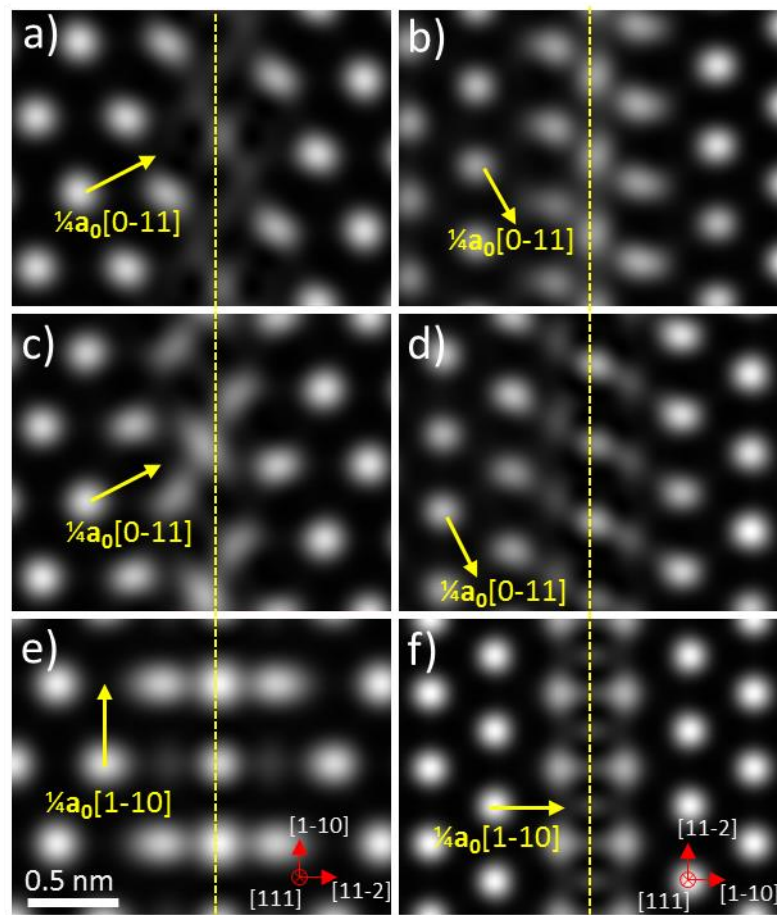


Figure 33: HRTEM image simulations from the six possible in-plane APB defect geometries, shift vectors are marked with yellow arrows. (a,c,e) show defects sitting on a (11-2) plane, propagating in a [1-10] direction. (b,d,f) show defects sitting on a (1-10) plane, propagating in a [11-2] direction. (a,b,c,d) show a $\frac{1}{4}a_0[01-1]$ shift with the two possible interface variants shown. (e,f) show the $\frac{1}{4}a_0[1-10]$ shift which only incorporates one possible interface for each defect orientation. (f) is reproduced in Figure 35c and is clearly the only defect from this set which can represent the experimental HRTEM result purely from the geometrical positioning on high intensity sites in this figure.

Since the oblique $\frac{1}{4}a_0[01-1]$ all lead to non-stoichiometric defect regions such atomic configurations seem naturally less likely than the stoichiometric defects we actually observe. This could mean that the oblique shifted defects may occur but with significant atomic rearrangement at the defect, or it is possible these defects are simply energetically unfavourable and will not occur in a real film.

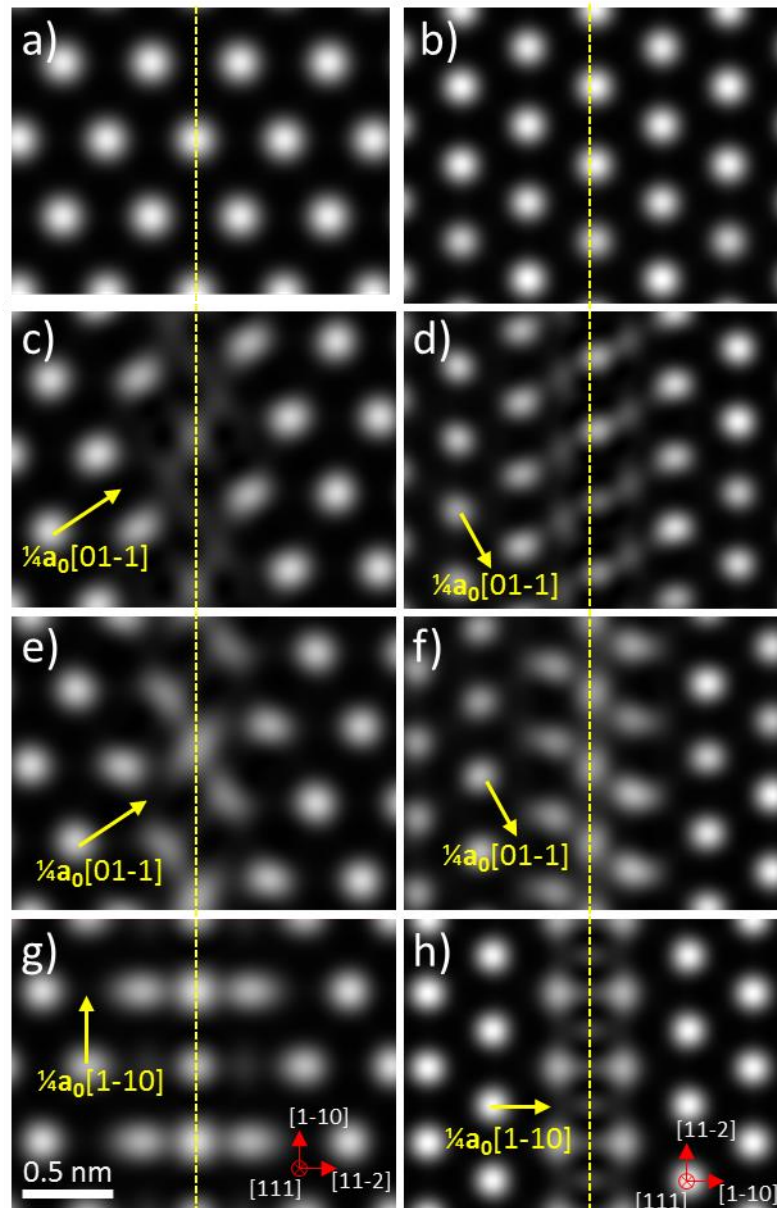


Figure 34: HRTEM image simulations from the eight possible out-of-plane APB defect geometries, shift vectors are marked with yellow arrows. (a,c,e,f) show defects sitting on a (11-2) plane, propagating in a [1-10] direction. (b,d,f,h) show defects sitting on a (1-10) plane, propagating in a [11-2] direction. (a,b) show a [000] out of plane shift. (c,d,e,f) show a $\frac{1}{4}a_0[01-1]$ shift with the two possible interface variants shown. (g,h) show the $\frac{1}{4}a_0[1-10]$ shift which only incorporates one possible interface for each defect orientation.

By studying the HRTEM image and image simulation contrast in Figure 35 with the corresponding structural diagram it is clear that the intensity variation we observe is not related to individual atomic sites, but rather the imaging intensity sits on the tetrahedral Fe sites (yellow in Figure 35) as can be seen by the inlaid hexagon/cube construction. This contrast therefore relates to four atomic columns per intensity peak. In this viewing direction the Fe_A column has a higher atomic density than the other three sites and forms the centre of the imaging intensity.

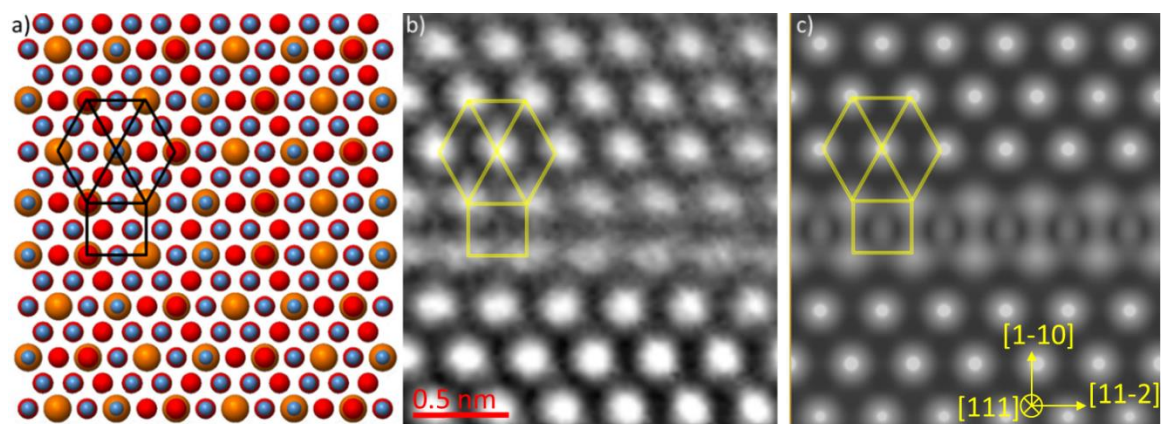


Figure 35: Structural Model, simulation and imaging from a $\frac{1}{4}a_0[1-10]$ APB shift structure. a) Atomic modelling of a Fe₃O₄ APB defect in the [111] viewing direction. O shown with blue spheres, octahedral Fe_B sites shown in red, tetrahedral Fe_A sites shown in yellow. The APB shift can be identified structurally by the broken Fe_{ABA} column stacking across the interface. b) HRTEM image cropped from Figure 27b. c) Image simulations produced from the structure in (a) for comparison with (b). This simulation shows how the contrast variations in HRTEM images of this structure are localised around only the Fe_A atomic columns rather than at all the Fe atomic columns.

Figure 35b shows the high resolution TEM image from Figure 28b cropped to represent the region of the image simulation. The high level of correspondence between this image and the image simulation in Figure 35c shows the structure used for this image simulation is representative of the atomic structure of the defect. Of all structures considered the only other structural shift which fits the experimental imaging of this structure relates to the identical in-plane shift with an added perpendicular out-of plane shift of $\frac{1}{2}a_0(111)$.

4.5 Vampire at Observed Defects

From our understanding of super-exchange interactions we expect the local magnetic ordering in metal oxide structures to be highly dependent on local bond configurations between nearest neighbour metal sites across bridge O sites. This makes the magnetic behaviour of metal oxides fundamentally different from that of soft magnetic

materials and metals. This difference is particularly notable at extended crystal defects. In a metal oxide the non-bulk bond angles and bond lengths generated at a defect can give rise to strong, non-bulk magnetic coupling interactions which persist regardless of the applied magnetic field. In Fe₃O₄ we expect Fe-O-Fe bonds approaching 180° to become strongly anti-ferromagnetic [61] and therefore contribute to the anomalous properties of the Fe₃O₄ film discussed earlier.

The full defect bonding configuration of the in-plane $\frac{1}{4}a_0[1-10]$ shift is listed in Table 4 this corresponds to the defect shown structurally in Figure 35a. In this we see the bulk like bonding configurations are not counted, however all non-bulk bonds are counted within the APB defect. As we have used periodic boundary conditions in this highly geometrical model all the bond counting models lead to multiples of 12 bonds at the boundary.

Aside from the 180° bond angles which we have discussed extensively we also observe a range of lower angled bonds which are not present in the bulk of Fe₃O₄ many of these are based on relatively long range bonding with one of the two Fe-O distances over 3 Å. These bonds are not really significant in terms of the behaviour of this material as these are not nearest neighbour Fe-O-Fe triplets but rather represent more distance Fe sites. However, all bonds have been allocated an exchange constant accounting for the bond angle of the specific triplet to allow atomistic spin calculations.

Table 4: Fe-O-Fe bonds at the $\frac{1}{4}a_0[1-10]$ APB defect on the (1-10) plane

Growth Direction	Boundary plane	Shift vector	Bond Angle	Bond Type	Fe ₁ -O dist. [Å]	Fe ₂ -O dist. [Å]	Fe ₁ -Fe ₂ Dist. [Å]	No.	
[111]	(1-10)	(11-2),(-1-12)	50.5	Fe _A -O-Fe _A	3.46	3.46	2.95	72	
			58.5	Fe _A -O-Fe _A	1.81	3.46	2.95	96	
		(1-10),(-110)	72.5	Fe _A -O-Fe _B	3.46	2.09	3.46	BULK	
			80.0	Fe _A -O-Fe _A	1.81	3.46	3.61	BULK	
		84.8	Fe _A -O-Fe _A	3.46	3.46	4.66	96		
		90.0	Fe _B -O-Fe _B	2.09	2.09	2.95	BULK		
		107.5	Fe _A -O-Fe _B	3.46	2.09	4.54	192		
		109.5	Fe _A -O-Fe _A	1.81	1.81	2.95	24		
		121.5	Fe _A -O-Fe _A	1.81	3.46	4.66	96		
		125.3	Fe _A -O-Fe _B	1.81	2.09	3.46	BULK		
		180	Fe_B-O-Fe_B	2.08	2.08	4.17	48		
		Interfacial unit area [Å²]:				$3^{1/2} \cdot 2.25^{1/2} \cdot a^2 = 180.7$			
		180° bonds/unit area [Å⁻²]:				0.266			

Figure 36 shows the magnetic simulation from the atomic structure in Figure 35a compared with experimental MH data.

Figure 36a shows the simulated magnetisation curve of Fe₃O₄ bulk (black) and defect structure (red) alongside an experimental M-H curve from a 10 nm Fe₃O₄(111)/MgO(111) film in blue where diamagnetic and paramagnetic contributions

from the substrate have been removed using an M-H curve taken from an equivalently shaped MgO piece. The values of magnetisation given for the simulated curves relate to the maximum possible summed spin configuration of all spins within the cell. Since Fe₃O₄ exhibits ferrimagnetic ordering in which two octahedral sites oppose one tetrahedral site per formula unit the maximum possible magnetisation with all spins oriented co-linearly is equivalent to one third of the total magnetic moment aligned to the applied field. It can be seen from the simulation of the APB that this structure saturates at around 0.2 compared to the bulk simulation which saturates at a magnetisation value of 0.29. The experimental curve (blue) is expressed in emu which is shown on the right axis. The coercivity of the modelled APB structure is 388 ± 4 Oe and the coercivity of the experimental film is 248 ± 3 Oe showing a significant variation between the absolute values of coercivity derived from the modelling process and the experimental film, certainly greater than the experimental uncertainty. However, these values show a rough order of magnitude agreement and suggest we are close to understanding some of the behaviour of these Fe₃O₄ films in the low applied field regimes. The simulation fails to show the non-saturated nature of the grown film above ± 1500 Oe.

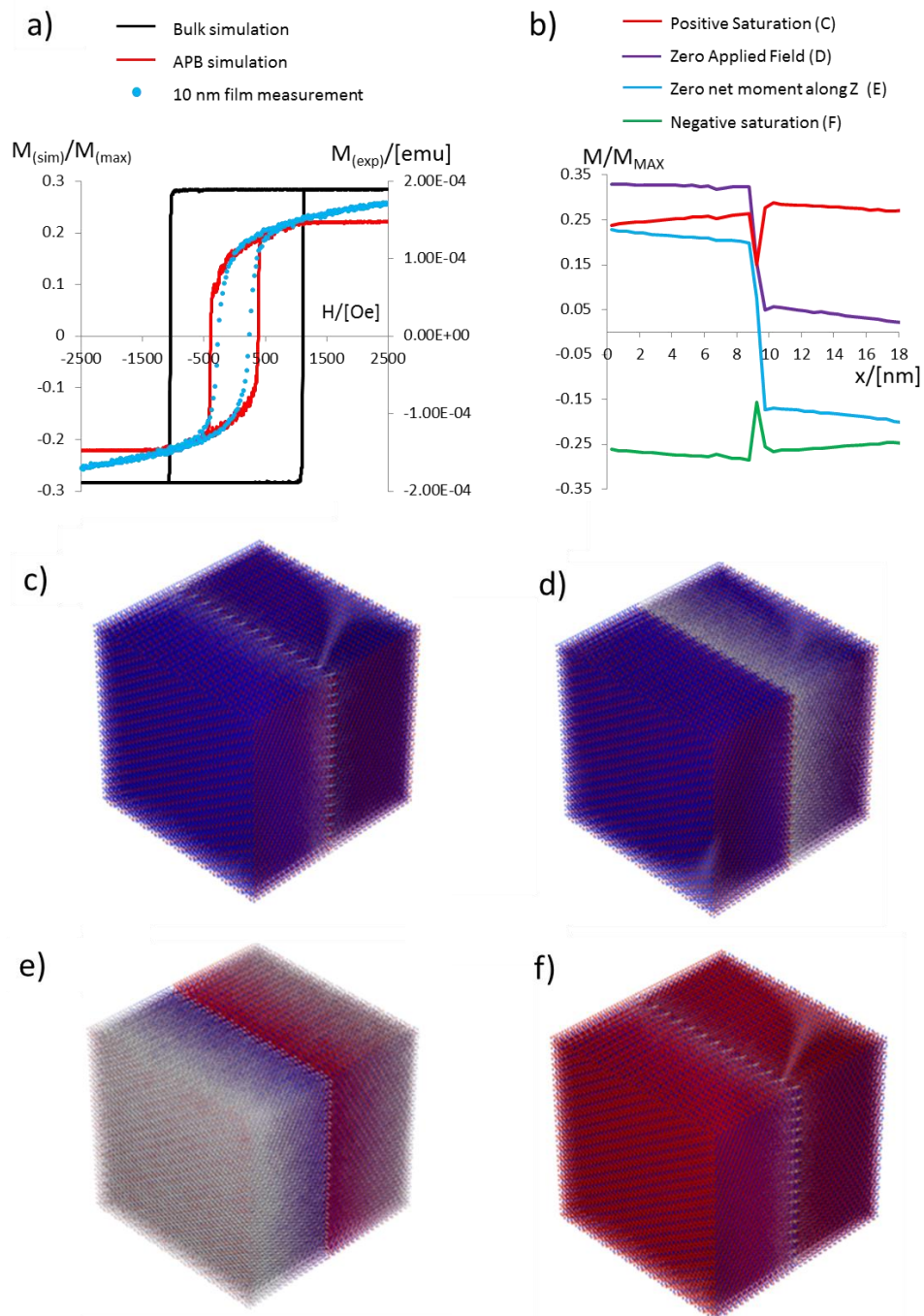


Figure 36: Experimental and simulated M-H data. a) Experimental M-H data shown in blue (dots) from a (111) oriented 10 nm Fe₃O₄ film. Simulated Bulk Fe₃O₄ magnetisation data shown in black. Simulated APB defect magnetisation shown in red. The experimental magnetisation is expressed in emu and is plotted against the right axis, simulated magnetisation is expressed as a ratio of spins aligned against the moment of all spins within the cell shown on the left axis. Four key points from the APB simulation curve are shown in figure (b-f). **b)** Shows the spatial distribution of the magnetic moment across the simulated cell and corresponds to the spin configurations shown in c-f). **c)** Shows the spin configuration at high field, i.e. 2500 Oe. **d)** shows the spin configuration at 0 Oe. **e)** Shows the spin configuration at zero net magnetisation at -368 Oe **f)** Shows the spin configuration at -2500 Oe.

Figure **36 (b)** shows the spatial distribution of the magnetic moment of the simulated cell across the APB defect with positive saturation shown in red (2500 Oe), zero applied field in purple (0 Oe), zero net magnetisation in blue (-368 Oe) and finally negative saturation in green (-2500 Oe). Figure **36 (c-f)** show the atomistic spin configurations of the 20 nm³ cube at the same stages in the simulation as those shown in Figure **36(b)**.

In these graphics the colour of the Fe site relates to alignment with the magnetic field direction. As these cells are ferrimagnetic a mixture of red and blue is always seen however when magnetisation reverses the net change is observed by a general red-blue switch.

4.6 Conclusions

In this work we have shown that the APB defects seen in Fe₃O₄/MgO heterostructures become regularly ordered when grown in the (111) direction. Furthermore we have identified the specific shift vectors which are present in this film through an exhaustive analysis of possible in-plane and out-of-plane shift vectors and image simulations. As this film exhibits highly regular defect structures it has been possible to create a three dimensional structural model for atomistic spin calculations using VAMPIRE software [143, 175]. The comparative data from the magnetic simulations and the experimental MH curve show a high degree of agreement and suggest this model is effectively capturing the physical behaviour of the defect structure and inter-defect effects. This helps to confirm that the general behaviour of the defects as anti-ferromagnetically coupled and highly localised around the defect interface. All the interactions modelled here are based on Fe-O-Fe super exchange interactions derived from simple arguments linking the degree of orbital overlap of d-state electrons in Fe.

The regular arrays of defects shown in this film may be of use for defect functionality devices which could not be implemented in the highly complex fractal geometry defects observed in the defects present in (001) oriented Fe₃O₄/MgO films.

We show that it has become feasible to consider atomic scale defect magnetic behaviour using atomistic modelling. This has reproduced the experimental magnetisation behaviour with a high degree of accuracy and shows the SEI dominates the magnetisation behaviour of thin film Fe₃O₄.

The prevalence of the $\frac{1}{4}a_0[1-10]$ APB boundary indicates this structure may be of lower formation energy than the other possible APB defect configurations generated simply from geometrical models. This corresponds well with recent work by McKenna et al [72] which has shown the low formation energy of a $\frac{1}{4}a_0[1-10]$ defect with a closely matched structure to that used here.

Chapter 5. $\text{Fe}_3\text{O}_4/\text{MgAl}_2\text{O}_4(111)$ symmetry matched spinel's.

This chapter is based on the work published in [74, 176] and forms a natural comparison with the work performed in the previous chapter on $\text{Fe}_3\text{O}_4/\text{MgO}(111)$ as the rationale behind antiphase domain boundary (APB) defect formation is altered in this case.

In the $\text{Fe}_3\text{O}_4(111)/\text{MgO}(111)$ growth by molecular beam epitaxy (MBE) we see APB formation on the basis of multiple nucleation sites of independent Fe_3O_4 grains during growth. The lattice constant of MgO is approximately half that of Fe_3O_4 due to the complexity of the lower symmetry Fe sublattices within the Fe_3O_4 structure. This means in three dimensions there are eight possible registries of Fe_3O_4 to MgO which are all structurally and energetically equivalent, but exhibit translational shifts of the Fe_3O_4 structure where separate grains coalesce.

In the case of $\text{Fe}_3\text{O}_4(111)/\text{MgAl}_2\text{O}_4(111)$ both film and substrate share the same crystal structure and $Fd-3m$ symmetry of space group 227. This means there should be no possible secondary nucleation site from one material to the other as the position of every atomic site in both structures should be fully determined in three dimensions by the underlying substrate structure and stacking sequence.

In this work the film were produced by Prof K. Ziemer and Dr Z. Cai in the Chemical engineering department of Northeastern University, Boston.

5.1 Introduction

APBs in MBE grown heterostructures of Fe_3O_4 are widely explained as a result of crystallographically and lattice mismatched atomic structures, e.g $\text{Fe}_3\text{O}_4\text{-MgO}$ (spinel-FCC) [25, 30], $\text{Fe}_3\text{O}_4\text{-Al}_2\text{O}_3$ (spinel-corundum) [29, 71], $\text{Fe}_3\text{O}_4\text{-GaAs}$ (spinel-zinc blend) [177, 178]. Therefore, $\text{Fe}_3\text{O}_4/\text{MgAl}_2\text{O}_4$ heterostructures are of special interest because both the film and the substrate have the same crystal symmetry and close lattice

constants, with mismatch of ~3%. However, regardless of crystal symmetry and lattice constants with one to one ratio, thin films of magnetite grown on MgAl₂O₄(001) still show anomalous properties [73]. This unexpected behaviour of Fe₃O₄ films on MgAl₂O₄ was attributed to interface originated APBs in this study of (001) oriented growth. However, high resolution scanning transmission electron microscopy (STEM) imaging of the Fe₃O₄(111)/MgAl₂O₄(111) interface does not appear to support strain and misfit dislocations as the origin of APB formation [176]. In this chapter I will show atomic resolution high angle annular dark field scanning transmission electron microscopy (HAADF-STEM) in order to find the origin of the anomalous behaviour of magnetite films when grown on symmetry matched substrates. In this chapter I present direct evidence of APBs in MBE grown Fe₃O₄/MgAl₂O₄(111). The observed APB defects break the symmetry of the Fe octahedral sublattice which results in a significant number of non-bulk superexchange interactions (SEIs) with antiferromagnetic character across the boundary that give rise to anomalous film properties.

5.2 Methods

Fe₃O₄ films of 10, 30 and 50 nm thickness have been grown on (111) oriented MgAl₂O₄ single crystal substrates MBE. Fe and atomic O have been simultaneously deposited by Knudsen cell and a RF-assisted plasma source respectively. MBE base pressure was less than 2×10^{-10} mbar, and the deposition has been conducted at a rate of $\sim 1.2 \text{ \AA min}^{-1}$ in a partial pressure of atomic oxygen of 5×10^{-6} mbar. During growth, the substrate temperature has been held at 350 °C.

Film growth was monitored in real time with reflective high energy electron diffraction and characterised post-deposition using *in-situ* x-ray photoelectron spectroscopy (XPS) with an Al K α source and *ex-situ* infra-red Raman spectroscopy.

In-plane magnetisation vs. applied field (MH) magnetic hysteresis curves, have been measured using a low temperature stage vibrating sample magnetometer in applied magnetic fields up to 9T, with applied field and sample vibration along the [1-10] direction. Magnetoresistance (MR) measurements have been carried out in longitudinal in-plane geometry also along the [1-10] crystal direction using four point probe contact methods at room temperature in applied fields up to 10 kOe.

Structural film characterisation has been performed using high resolution transmission electron microscopy (HRTEM), selected area diffraction (SAD), and HAADF-STEM. Cross-sectional TEM microscopy specimens were produced in orthogonal [11-2] and [1-10] zone axes by conventional methods that include mechanical thinning/polishing followed by low angle Ar ion milling in order to achieve electron transparency [137].

Electron microscopy has been performed using a double aberration corrected field emission JEOL FS-2200 JEM TEM/STEM and a JEOL-2011 TEM both operating at 200kV.

Multislice image simulations [147] have been produced to correlate the experimental (S)TEM atomic column intensities with proposed model APBs atomic structure.

5.3 Results

Figure 37 shows a representative HRTEM image giving an overview of the $\text{Fe}_3\text{O}_4/\text{MgAl}_2\text{O}_4$ heterostructure in the [1-10] viewing direction. The film has uniform thickness (30 nm) and demonstrates the single crystal nature of the film and the abrupt film/substrate interface.

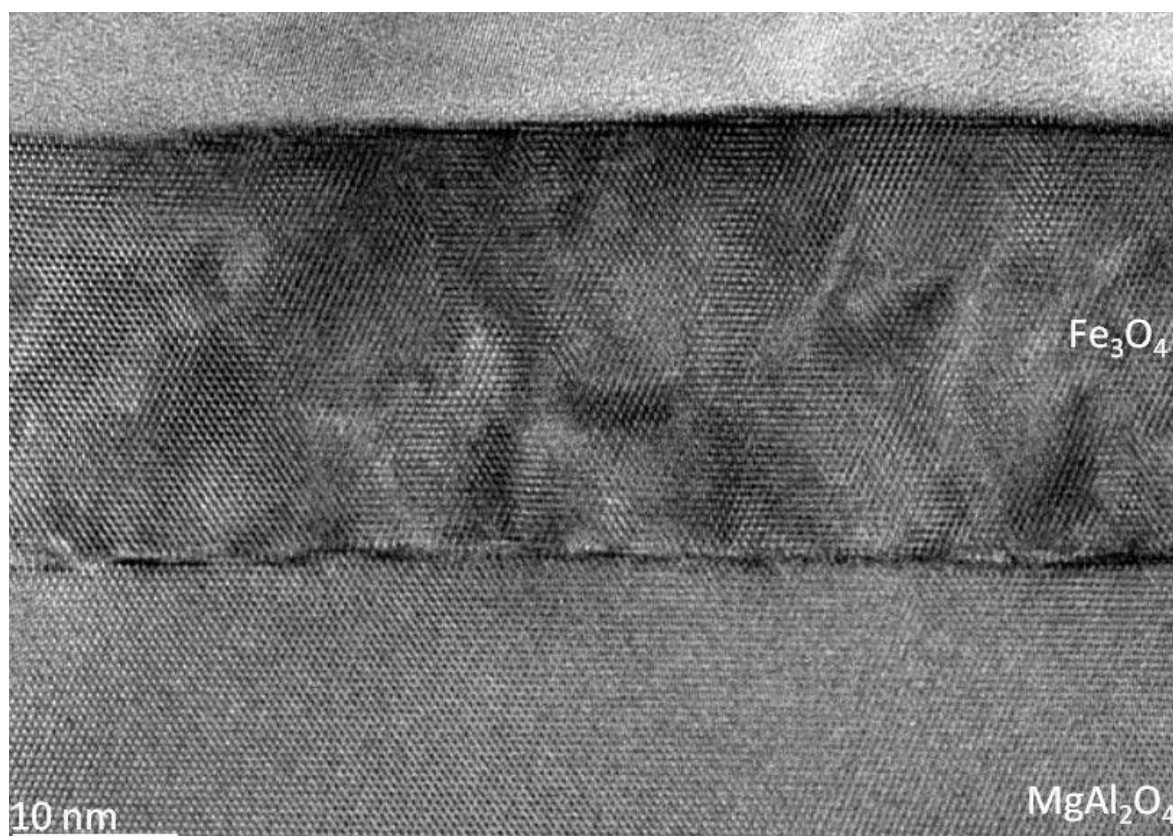


Figure 37: HRTEM image of Fe_3O_4 film and MgAl_2O_4 substrate in [1-10] zone axis.

SAD patterns from the interfacial region of the sample in the [11-2] and [1-10] zone axis are shown in Figure 38a and Figure 38b respectively. The shared crystal symmetry of the film and substrate can be seen through the superimposed film/substrate reflections in both diffraction patterns. The radial separation of diffraction spots which can be clearly seen in higher order reflections corresponds to the 3% difference between the film and substrate lattice constants. These diffraction patterns demonstrate the single crystal

nature of the film and show no evidence of any secondary phases. From the SAD pattern the epitaxial cube to cube relationship between film and substrate is found to be: Fe₃O₄(111)||MgAl₂O₄(111) and Fe₃O₄(1-10)||MgAl₂O₄(1-10) as expected.

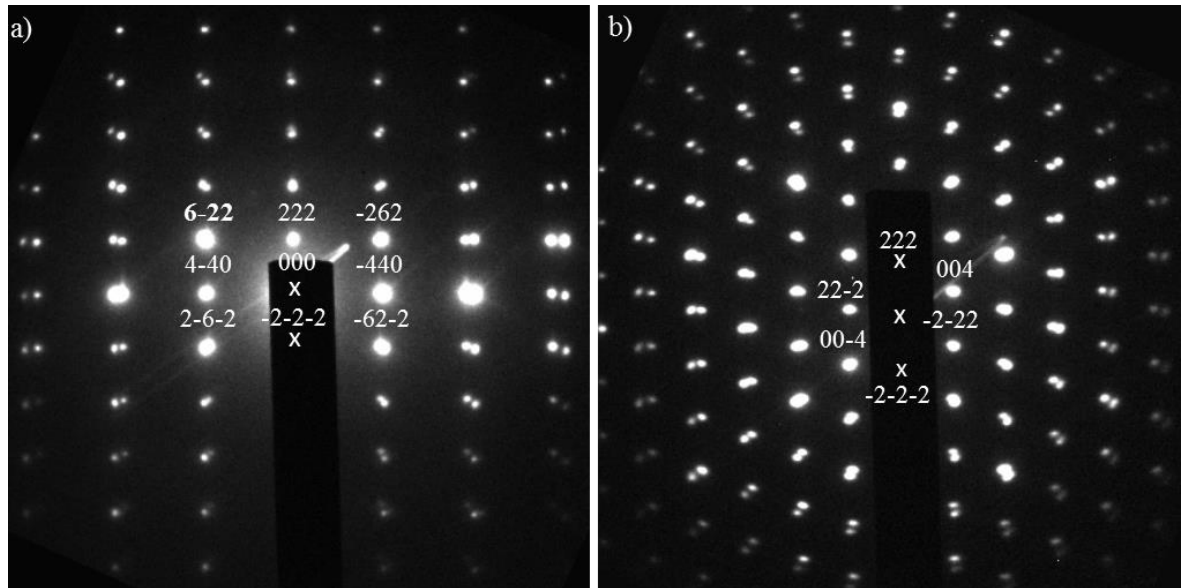


Figure 38: SAD patterns from a cross-section of the Fe₃O₄/MgAl₂O₄ interfacial region in a) the [11-2] zone axis and b) the [1-10] zone axis

The stoichiometry of the film is confirmed by *in-situ* XPS (Figure 39) taken directly after deposition. This data shows the characteristic Fe 2p peak of magnetite with 2p_(1/2) and 2p_(3/2) clearly resolved without the presence of any additional peaks that would indicate the presence of secondary phases [78]. This result indicates the single phase structure of the film with stoichiometric Fe₃O₄ composition, in contrast to previous reports that have found significant phase separation in polar Fe₃O₄ (111) films [179]. As expected due to the low penetration depth of XPS no signal from the substrate was detected. Further confirmation of the films stoichiometry was provided by *ex-situ* infra-red Raman spectroscopy shown in Figure 40. The higher penetration depth of this technique when compared to XPS gives a contribution to the data from the substrate. The shared structure of both film and substrate is shown by the shared vibrational frequency at 668 cm⁻¹. However, the reduction of the 311 cm⁻¹ peak representative of MgAl₂O₄ [180] and the enhancement of the 540 cm⁻¹ peak representative of Fe₃O₄ [181, 182] with increasing film thickness show the transition to a pure Fe₃O₄ signal in the thicker films. The absence of resonant peaks at 245 cm⁻¹ and 500 cm⁻¹ representative of α-Fe₂O₃ and γ-Fe₂O₃ respectively and the absence of a shoulder at 652 cm⁻¹ again show the good stoichiometry of these films without the inclusion of any secondary phases by comparison with previous results [183, 184].

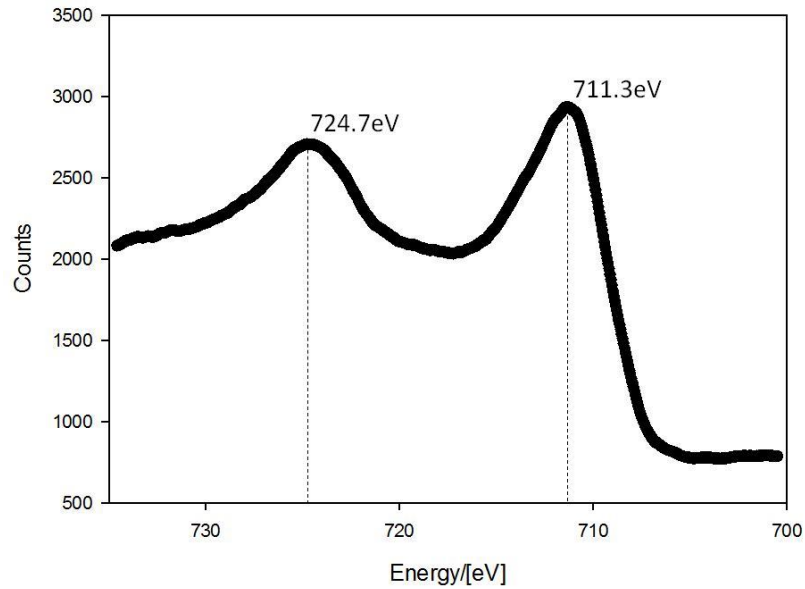


Figure 39: in-situ XPS showing the Fe2p_(1/2) and Fe2p_(3/2) peaks characteristic of Fe₃O₄.

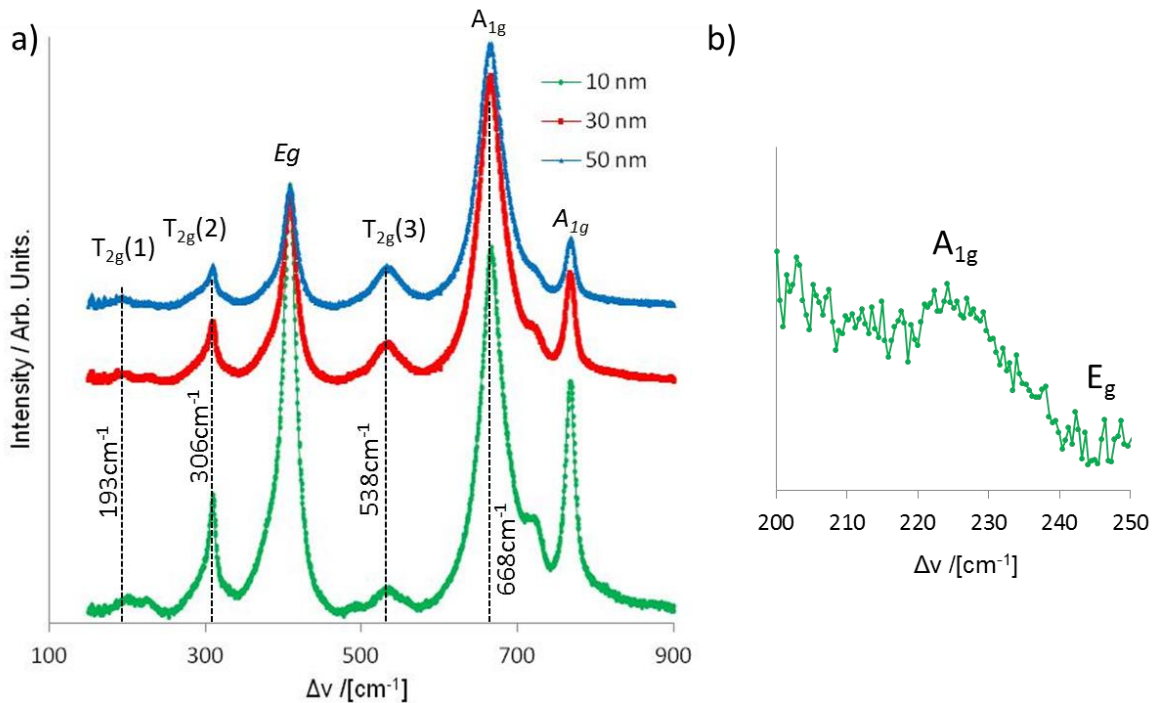


Figure 40: a) *ex-situ* Raman spectra of Fe₃O₄ at 193, 306, 538 and 668 cm⁻¹.

Measurements were taken to 1900cm⁻¹ but no further structure is shown in the curves beyond 900cm⁻¹. Raman Active modes for Fe₃O₄ labelled in non-italic [184] and for MgAl₂O₄ labelled in italic type face [185] b) High resolution reproduction of 200-250 cm⁻¹ region of 10 nm film data. This shows a small peak which could be attributed to an Fe₂O₃ Raman active mode at 225 cm⁻¹, however a second Raman active mode for Fe₂O₃ at 245 cm⁻¹ is not observed.

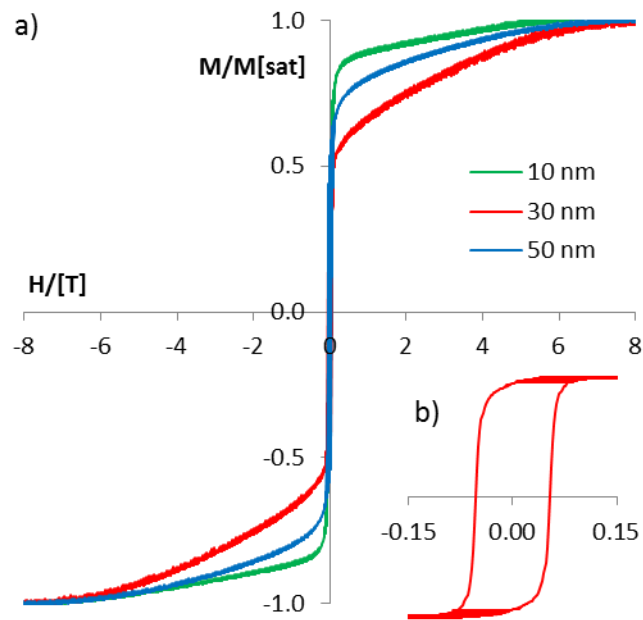


Figure 41: a) High field in-plane magnetisation curves from thin film Fe_3O_4 . This data has been taken at 150 K using a cold stage VSM. At 8 T magnetization has not saturated". b) High resolution magnetisation data around 0 T in the 30 nm film sample.

Next we present the MH and MR results, Figure 41 and Figure 42 respectively. The in-plane magnetisation curves at 150 K clearly show that even at applied fields of 8 T none of the films are saturated, while their coercivity is ~ 50 mT. Furthermore, the room temperature in-plane MR data shows that at applied fields of 8 kOe these films have negative MR in a range between -0.7 and -1 %. Both MH and MR data from these films show the non-bulk like behaviour of thin film Fe_3O_4 , consistent with other reports on thin film Fe_3O_4 properties [25, 31].

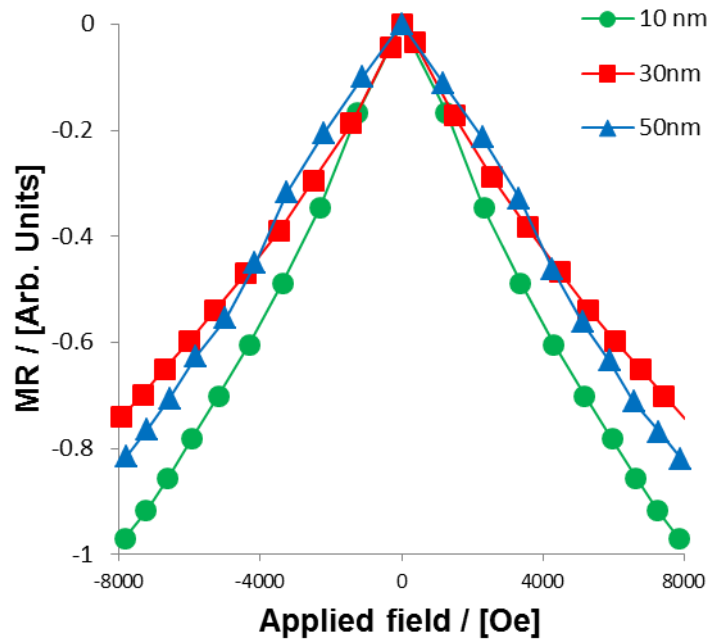


Figure 42 In-plane MR Fe_3O_4 films by four point probe techniques.

In order to understand this anomalous behaviour and correlate structure to properties in these films atomic resolution HAADF-STEM measurements were undertaken. Figure 43 shows a HAADF image of the interfacial region between Fe_3O_4 and MgAl_2O_4 in the [11-2] zone axis. This image clearly demonstrates the crystal symmetry matching of film and substrate as well as the atomically and chemically abrupt nature of this interface. The misfit dislocations at the interface formed due to the film/lattice mismatch are clearly outlined by Bragg filtering of $\langle 4-40 \rangle$ atomic planes. These misfit dislocations lead to relief of the film strain arising as a result of film-substrate lattice mismatch. A similar analysis of the [1-10] zone axis is shown in Figure 44. The interface dislocation here is outlined by Bragg filtering of the $\langle 22-2 \rangle$ planes. These arrays of interfacial misfit dislocations clearly do not change the translational symmetry of the film in the area surrounding the dislocation core. This demonstrates that APBs are not nucleated directly as a result of misfit dislocations. The presence of misfit dislocations at the interface does not enforce a break in the bulk symmetry of the film apart from the dislocation core vicinity.

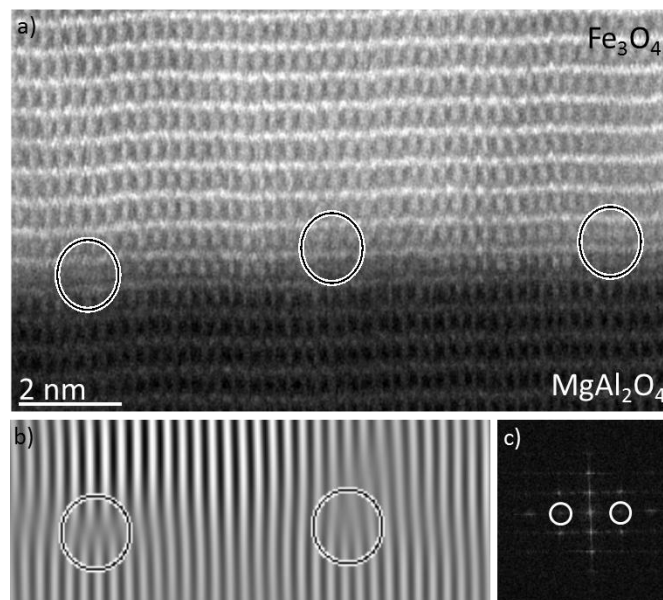


Figure 43: (a) HAADF-STEM image of the interfacial region between Fe_3O_4 and MgAl_2O_4 in the $[11-2]$ zone axis. The matched crystal symmetry across this interface can be seen in the continued structural motif from film to substrate. **(b)** Bragg filtered $\langle 4-40 \rangle$ image showing dislocation cores **(c)** Fast Fourier transform of image (a), circled reflection are used to create the Bragg image in (b). Dislocation cores are outlined in both the original and filtered image with circles.

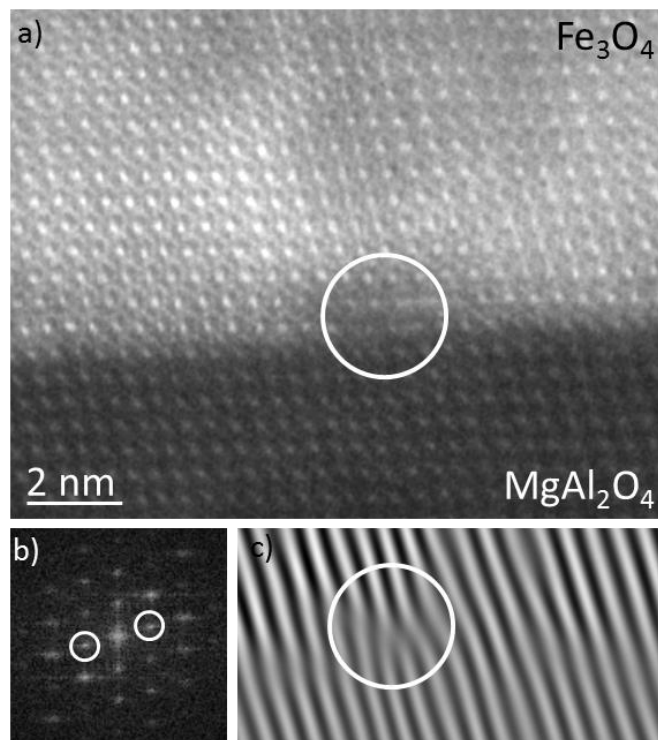


Figure 44: (a) HAADF-STEM image of the interface between Fe_3O_4 and MgAl_2O_4 in the $[1-10]$ zone axis. **(b)** Fast Fourier transform of the image in (a), $(22-2)$ reflections used for creating the Bragg image in (c) are outlined. **(c)** Bragg filtered image with a single dislocation core. Dislocation cores are outlined in both the original and filtered image with circles.

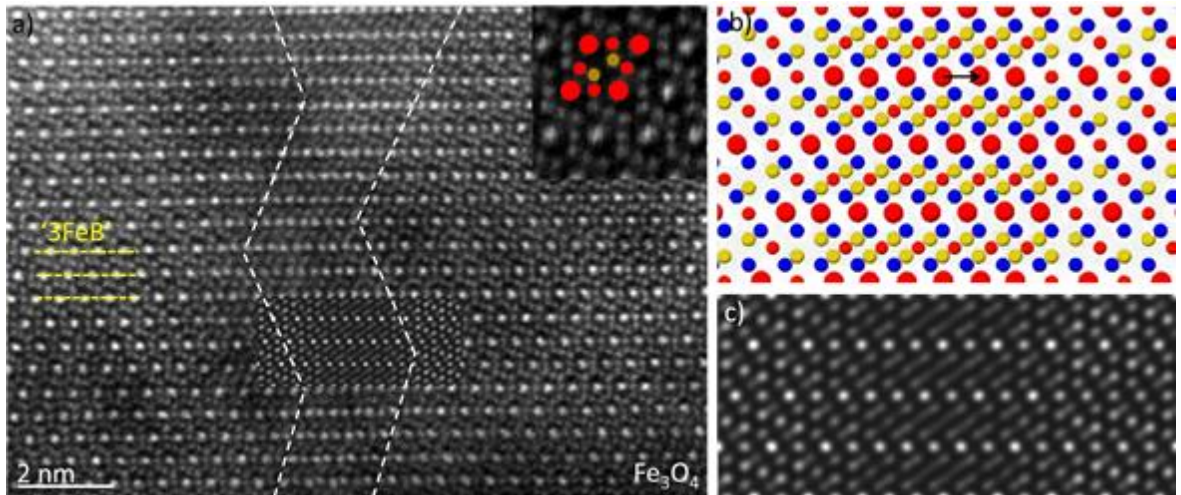


Figure 45: HAADF-STEM image of an APB defect within the Fe_3O_4 film, imaged in the $[1-10]$ zone axis. a) The extended defect region is identified by the disruption of the rhombohedral motif, outlined in the inset upper right corner with the Fe atomic columns denoted as following: large (small) red circle representing double (single) occupied Fe_B columns and yellow circles representing Fe_A atomic columns. b) Atomic model of the APB boundary outlined in (a), the colour code is the same as in (a) with O atoms as blue. (c) Simulated HAADF map of the model in (b). The $\frac{1}{4}\langle 01-1 \rangle$ shift between coalesced Fe_3O_4 grain results in loss of the alternating contrast of Fe columns in ' 3Fe_B ' layers indicated by dashed yellow lines in (a). The match between the calculated image and experimental image is illustrated by the inset of model image inside the middle of APB region in (a).

In order to verify the presence of APBs in the films, detailed analysis of the atomic structure throughout the film has been performed. The result of this analysis is illustrated in Figure 45 which shows an atomic resolution HAADF image, taken from the middle region of the film. An APB running in the film growth direction is clearly seen, the rough outline of the boundary region is presented by white dashed lines.

The presence of the APB has been identified through changes in the atomic column intensities of the ' 3Fe_B ' atomic planes. In the $[1-10]$ viewing direction the iron atomic columns occupancy of the ' 3Fe_B ' layers alternates between double and single occupancy (see the inset in Figure 45a).

As the contrast in the HAADF imaging is $\sim Z^2$; the single to double occupancy of the neighbouring Fe atomic columns in the 3Fe_B layer can be used to determine the conservation of translational symmetry. For bulk like structures the ' 3Fe_B ' layer in the $[1-10]$ projection should alternate between high and low brightness atomic columns. This is clearly illustrated in the areas left and right of outlined region.

However in the middle region (within the dashed lines) this characteristic pattern of well-ordered magnetite film is lost. Instead of alternating Fe_B site intensities, in the boundary region neighbouring sites on the ' 3Fe_B ' planes are all equally bright. This effect is explained by introducing a $\frac{1}{4}\langle 01-1 \rangle$ type shift of the magnetite unit cell between the left and right grain in the field of view. This type of shift is schematically shown in Figure 45b.

Based on this shift atomic models of the APB have been constructed from which HAADF maps were calculated using the multislice methods [147]. The calculated HAADF map is shown in Figure **45c**. As seen from the simulation, the pure geometrical shift between the right and left grain with an overlapping interface region of ~3 nm results in equal intensity of the Fe_B atomic columns within the APB region. This relative shift produces a break in the translational symmetry and hence forms an APB. The APB shown is not edge on with respect to the beam direction; as a result instead of a sharp single atomic plane APB an overlapping region between neighbouring grains is seen across several nanometres in this [1-10] projection.

Figure **46** demonstrates the same type of APB as observed in Figure **45**, but in the <11-2> viewing direction. In this case it is more challenging to observe the defect region as the separation of the vertical atomic planes is much narrower than in the <1-10> viewing direction. However, once again we observe an extended defect region in which the general spacing of the structural motif is halved where two grains overlap in projection.

The lateral extent of this defect of ~2-4 nm is also comparable with the data presented in Figure **45** and suggests once again an off-axis/poorly crystallographically defined propagation of this defect. Figure **46b** shows a schematic structure of two interlocked Fe₃O₄ grains in this <11-2> zone axis. To the edges of this schematic the normal bulk like Fe₃O₄ structure can be observed. This bulk like configuration gives the image simulation shown in Figure **46c**. This is contrasted with the convoluted region at the centre of Figure **46b** which leads to a much closer packed structural motif shown in the image simulation in Figure **46d**. The match between these two simulations and the observed experimental image can be seen by comparing the inset image simulation (Figure **46c**) to the left of Figure **46a** with the local HAADF-STEM imaging and likewise by comparing the simulation (Figure **46d**) inset in the centre of Figure **46a** in the defect region.

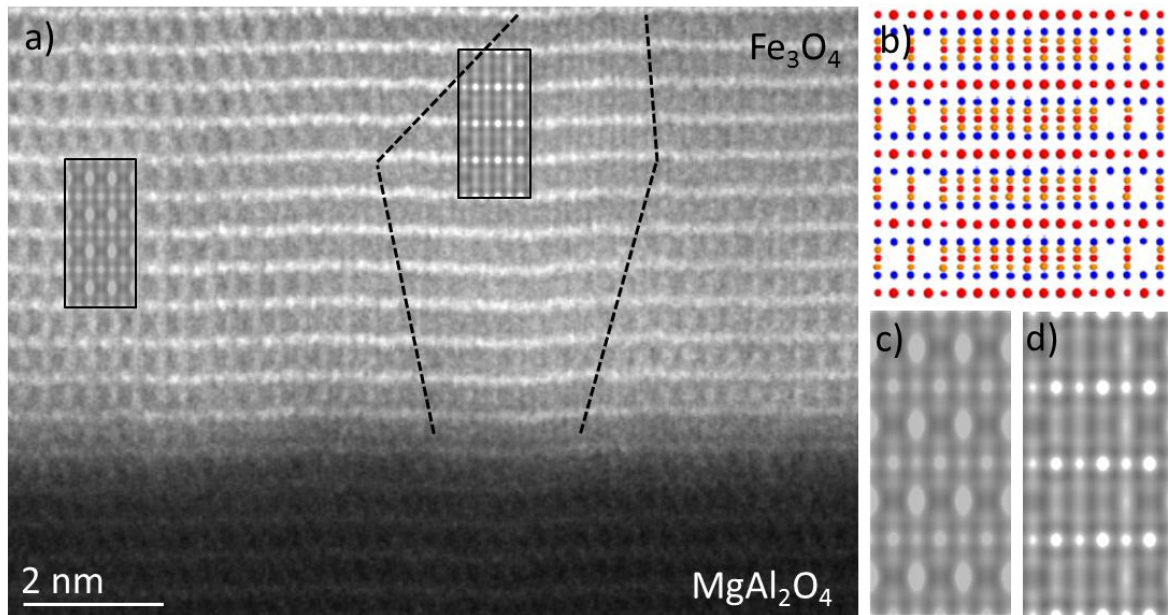


Figure 46: (a) HAADF-STEM image of the $\text{Fe}_3\text{O}_4/\text{MgAl}_2\text{O}_4$ interface with evidence of $\frac{1}{4}\langle 1-10 \rangle$ shift APB defect outlined in the black dashed lines in (a). (b) Schematic diagram of overlapping Fe_3O_4 grains leading to closely packed equivalent atomic projections at the centre of this defect. (c) HAADF-STEM image simulation of the bulk $\langle 11-2 \rangle$ zone axis reproduced to the left of (a). (d) HAADF-STEM simulation of overlapping grains reproduced near the centre of (a).

5.4 Discussion

The results presented clearly show that these Fe_3O_4 films demonstrate anomalous MH and MR properties despite the good structural ordering and stoichiometry determined by the mesoscopic film analysis methods. Furthermore, we have identified the presence of APBs in these films which are not related to interface dislocation formation.

The dominant SEI in bulk Fe_3O_4 that provides the antiferromagnetic (AFM) coupling between the A and B sublattices is the $\text{Fe}_A\text{-O-Fe}_B$ with an exchange integral value of $J_{AB} = -22$ K. The other two important interactions are the $J_{BB} = 3$ K, and $J_{AA} = -11$ K [27, 31, 68]. The magnitude and sign of SEIs depends of the atomic distances and angles of O mediated bonding e.g. the $\text{Fe}_B\text{-O-Fe}_B$ interaction can vary from ferromagnetic (FM) to AFM by varying the bond angle from 90° towards 180° . The effect of the APB defects is in the change of the local atomic co-ordination of Fe_3O_4 , such as altered cation distances and bond angles of SEIs in the region of an APB. These non-bulk SEIs can be dominant and can change the magnetic and magneto transport behaviour of the films.

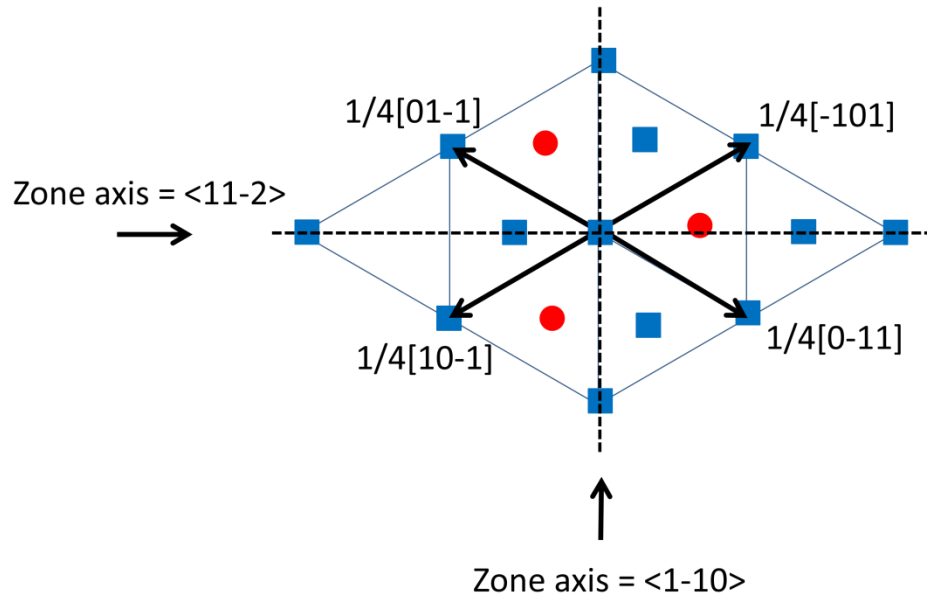


Figure 47 Schematic diagram of four translational vectors, $\frac{1}{4}[01-1]$, $\frac{1}{4}[0-11]$, $\frac{1}{4}[10-1]$ and $\frac{1}{4}[-101]$ that give rise to observable half structural motif shifts and give rise to the observed APB imaging seen above. These can be observed in both the $\langle 11-2 \rangle$ and $\langle 1-10 \rangle$ zone axes though the structural spacing's are much larger in the $\langle 1-10 \rangle$ zone axis as indicated in the schematic.

Based on the experimental evidence we observe only in plane APB shift vectors orthogonal to the $[111]$ growth direction. This shows the crystal symmetry of the substrate is preventing substrate step-edge generated APB formation as considered in the previous chapter. Immediately this limits the set of 14 possible APB defects observed in Fe₃O₄/MgO(111) to just 6. However in this system we observe much less well defined boundaries as a result of APB defects and rather see APB propagating at an angle to major crystallographic planes.

The observed half shift in the positioning of the rhombohedral structural motif (Figure 45a and Figure 46a) is achieved by a shift vector of $\frac{1}{4}a_0[01-1]$, $\frac{1}{4}a_0[0-11]$, $\frac{1}{4}a_0[10-1]$ or $\frac{1}{4}a_0[-101]$, as shown in Figure 47. This means the set of shift vectors observed in this growth are completely different from the $\frac{1}{4}a_0[1-10]$ set observed in the Fe₃O₄/MgO structure.

The ~ 3 nm lateral extent of this defect outlined by white dashed lines in Figure 45 and Figure 46 is due to the 3D nature of film growth. When coalescence between grains occurs the formed APBs are extended onto several planes. For the boundary shown in Figure 45 the region of $(11-2)$ planes that define the APB is ~ 3 nm. Assuming the specimen thickness of ~ 30 nm, the observed APB is 5.7° mistilted with respect to incident electron beam. This is neither on a $\langle 11-2 \rangle$ type plane nor a $\langle 1-10 \rangle$ type plane, this means the APB defect is either genuinely mistilted, or is a result of a physically widened

defect region. As this type of boundary would lead to a non-stoichiometric defect region in the case of an atomically sharp defect boundary, it is possible the boundary is genuinely widened and does not exist on a single atomic plane as shown in Fe₃O₄/MgO in which case the atomic modelling show in the previous chapter is not so simple to perform.

It is possible this film contains $\frac{1}{4}a_0[1-10]$ APB shifts similarly to the Fe₃O₄/MgO growth, however these cannot be easily identified in cross sectional geometry as they would map the structural motif of Fe₃O₄ directly back on to itself in projection and could probably only be identified in plan view or MAADF-STEM imaging by identifying strained regions within the film to determine APBs in directly. However, as shown in the previous chapter the type of APB has very little effect on the overall properties of the film as nearly all defects lead to the same conclusion in terms of high angle bonding and this is confirmed by the anomalous MH and MR properties of this film.

Perturbation of the Fe_B-O-Fe_B interaction has a significant effect on the magneto transport. The conductivity in Fe₃O₄ is limited to electron hopping mechanisms on the B sublattice [57]. The hopping probability is proportional to $\sim \cos(\theta/2)$, implying that 180° Fe_B-O-Fe_B interactions would not contribute to the film conductivity. Also it does explain the increase of the conductivity when H field is applied [25].

These results support the findings of previous work by showing the correlation between APB defects and the anomalous magnetic and magneto transport properties measured in Fe₃O₄/MgAl₂O₄ films.

5.5 Conclusion

Atomic resolution HAADF-STEM images reveal that Fe₃O₄ films show the presence of APBs despite being grown on substrates with the same crystallographic symmetry. It appears that strongly antiferromagnetic Fe_B-O-Fe_B bonds across the boundary are the main superexchange interaction responsible for the anomalous magnetic and magneto transport properties of these Fe₃O₄ films. The APBs found in the film are not uniquely driven by strain relief in the film, since no direct evidence is found to link the misfit dislocation network at the film-substrate interface to APB formation.

We observe a very different pattern of APB formation in Fe₃O₄/MgAl₂O₄ than in Fe₃O₄/MgO with the oblique $\frac{1}{4}a_0\langle 01-1 \rangle$ type shifts observed rather than the $\frac{1}{4}a_0\langle 1-10 \rangle$ shifts. We also see that when using MgAl₂O₄ as a substrate there are no out-of-plane APBs which is to be expected and the APB boundaries are no longer confined to a single atomic planes.

The loss of out-of-plane defects is to be expected as the spinel structure substrate provides a full definition of the interfacial registry of the large Fe₃O₄ unit cell in the z-direction which the rock salt structure MgO cannot. Furthermore, the loss of atomically

sharp APB defects may be a result of the non-stoichiometric defect interface which could in an extreme case could be viewed more as a region of phase segregation to either a mixed iron oxide or to $\gamma\text{-Fe}_2\text{O}_3$ over a very small distance rather than an atomically sharp discontinuity in the Fe_3O_4 structure.

What drives the formation of these defects in both the case of $\text{Fe}_3\text{O}_4/\text{MgO}$ and $\text{Fe}_3\text{O}_4/\text{MgAl}_2\text{O}_4$ remains fundamentally unclear, however, in the case of $\text{Fe}_3\text{O}_4/\text{MgO}$ the behaviour of the substrate with step edges and equivalent nucleation sites for growth appears to be the most likely cause of APB defects whereas in the case of $\text{Fe}_3\text{O}_4/\text{MgAl}_2\text{O}_4$ the interfacial strain as a result of $\sim 3\%$ lattice mismatch is likely to dominate the behaviour of the growth leading to strain in the Fe_3O_4 film and possibly a slight tilt to the growth front which creates a three dimensional growth property with APBs developing away from the film/substrate interface to accommodate this effect.

Chapter 6. Fe₃O₄/Y-ZrO₂(111) deposited by PLD methods

In Chapter 4 and Chapter 5 we have identified antiphase domain boundary (APB) formation in both Fe₃O₄/MgO(111) and Fe₃O₄/MgAl₂O₄(111) [74, 176] heterostructures prepared by molecular beam epitaxy (MBE) growth methods. This corresponds well with previous work in this field [25, 31, 69, 70, 73]. As such we require a different approach to produce Fe₃O₄ films with low defect density. It appears that APB defects are a result of many MBE growth properties. In the case of the MgO substrates defect formation can be justified as a result of substrate nucleation. However, this does not explain the defects formed in the case of the monolithic, symmetry matched spinel interface with MgAl₂O₄. It would appear that APB defects in MBE grown Fe₃O₄ result from at least, multiple interface growth nucleation sites, interfacial strain, local non-stoichiometry during growth and 3D growth modes in the film.

With this in mind, we need a different approach to produce single crystal Fe₃O₄ than MBE growth at 300 °C. In this chapter, and the following Fe₃O₄/SrTiO₃ work we utilise high temperature substrate preparation and high temperature film annealing methods to significantly improve the quality of the grown films

Due to varying concentrations of yttria used to stabilise ZrO₂ properties such as lattice constant and structure are not necessarily well defined for this material.

Yttria stabilised zirconia, Y-ZrO₂, is an insulating ceramic which requires doping with Yttria oxide to create stable crystallisation. This substrate is capable of handling extremely high temperature processing with a melting point of 2500 °C [Shinkosha Ltd.]. This allows aggressive surface processing and annealing to be undertaken.

The lattice constant of Yttria stabilised zirconia (YSZ) supplied by Shinkosha is given as $a_0 = 0.5138$ nm, when compared with the Fe₃O₄ lattice constant of $a_0 = 0.834$ nm [46, 47] it is immediately clear that this will not form unstrained cube-to-cube epitaxy as the lattice mismatch is ~20% based on two lattice constants of YSZ being considerably

larger than a single Fe₃O₄ lattice constant. It is perhaps surprising given this result that our growth indicates direct cube-on-cube epitaxy without either in-plane or out of plane rotations to mediate this interfacial strain effect.

6.1 Methods

Fe₃O₄ thin films have been grown by pulsed laser deposition (PLD) methods on (111) oriented YSZ substrates [59, 103]. Deposition has been achieved using a KrF excimer laser ($\lambda = 248$ nm, pulse duration ~ 20 ns) incident on a sintered, stoichiometric Fe₃O₄ target. During growth the substrate temperature was held at 300 °C in a 2×10^{-4} Pa partial pressure of O. Samples were post-annealed in an image furnace at 1100 °C for 30 minutes in a CO/CO₂ atmosphere with ratio of 1:5000 to facilitate oxidation and reduction within the film to optimise film chemistry [186].

Magnetoresistance (MR) measurements and hysteresis loops have been performed using a quantum designs physical properties measurement system (PPMS) with silver paste contacts made to the Fe₃O₄ surface for MR.

Cross sectional transmission electron microscopy (TEM) specimens have been prepared by conventional means including mechanical polishing and Ar ion thinning to electron transparency [137].

Transmission electron microscopy has been performed using a JEOL 2011, a dual aberration corrected JEOL JEM 2200-FS STEM/TEM and an aberration corrected Nion Ultrastem 100.

Selected area diffraction has been performed using the JEOL 2011. High angle annular dark field (HAADF-STEM) and bright field (BF-STEM) imaging has been performed using the JEOL JEM 2200-FS and the Nion Ultrastem 100. Medium angle annular dark field (MAADF-STEM) and electron energy loss spectroscopy (STEM-EELS) has been performed using the Nion Ultrastem 100.

The image stack and statistically determined spatial drift (SDSD) digital micrograph plug-in has been utilised in combination with rapidly acquired HAADF-STEM data stacks to provide significantly improved signal to noise ratios in imaging data without compromising drift or specimen damage [145].

Density functional theory (DFT) Calculations have been performed using a 168 atom periodic supercell with charge compensation to achieve Fe³⁺ at the non-stoichiometric defect interface achieved using electron holes. DFT calculations have been performed by Dr. Keith McKenna.

HAADF-STEM Image simulations have been performed on DFT refined structural models using the QSTEM image simulation software package [157]. Microscope parameters have been experimentally determined using aberration correction values [72].

Image simulations use 30 thermal diffuse scattering iterations and have been performed to account for experimentally determined specimen thicknesses.

6.2 Results

The results presented here represent the culmination of the work reported in [102, 103, 187]. We show that by altering our growth methods and focusing on post deposition control of chemistry we can achieve a closer match in terms of macroscopic properties between thin film Fe₃O₄ and bulk material properties. Firstly, I consider the effects of high temperature post annealing on the as deposited specimens leading to significant improvements in performance.

6.2.1 Rectifying film growth with annealing

Figure 48 show the effect of post-annealing on magnetisation curves (Figure 48a), MR (Figure 48b), and conductivity versus temperature (Figure 48c). Post-annealing has significantly improved the magnetic properties of the film. Magnetisation saturates in relatively low H field (below 1 T) compared to as grown films that do not saturate even in 5 T. Similarly, MR falls by an order of magnitude at 1 T and falls to 1/20th of the value of comparable MBE grown films [188]. These results together with the sharper Verwey transition of annealed films (Figure 48c) clearly indicate that annealing drastically improves the structural properties of the grown films as will be shown next.

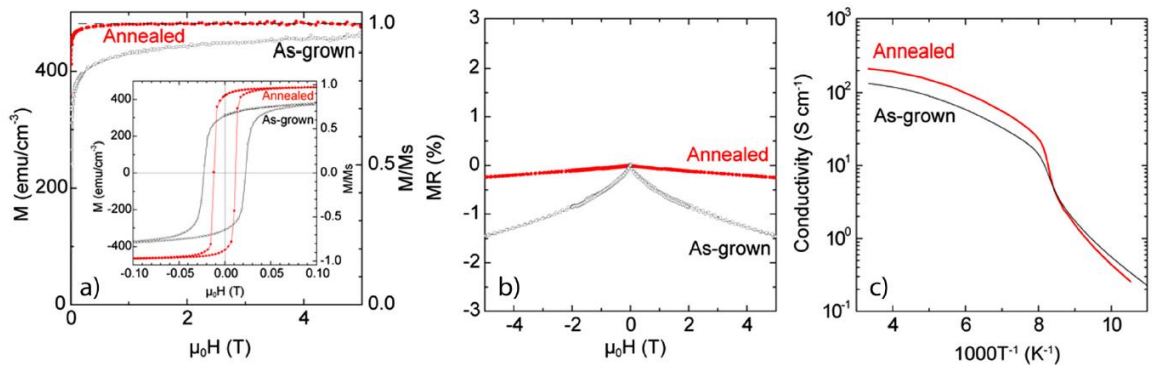


Figure 48. Magnetisation curves (a) relative magnetoresistance (b), and conductivity of annealed and as grown films (c). (Supplied by K. Matsuzaki of Toyko Institute of Technology)

Figure 49(a and b) show low magnification cross-sectional HAADF-STEM images of the as grown and post-annealed films respectively. The film thickness in both films is uniform with abrupt interfaces with the YSZ substrates. Atomic resolution HAADF-STEM imaging from the annealed film (Figure 49c) shows the highly ordered Fe atomic columns of Fe₃O₄ in the [1-10] viewing direction as indicated in the model (Figure 49d). Due to strong $\sim Z^2$ dependence of the scattered electrons, the fully occupied octahedral sites

(denoted as large red circles) appear significantly brighter than the half occupied octahedral (small red circles) and tetrahedral sites (small orange circles). In contrast to post-annealed films, as grown magnetite films show the presence of an interfacial layer ~8 nm in thickness with distinctive contrast from the rest of the film in Figure **49a**. HRTEM of this region is shown in Figure **50**. The clear distinction in the lattice spacing between magnetite film, the interfacial band and substrate is illustrated by the digital diffractograms from representative areas in Figure **50(b-d)** and indicates this region is largely FeO though small areas of Fe are also observed. By calculating the plane separations from the diffractograms, we found the interfacial region consists mainly of FeO with small inclusions of Fe (not shown). Presence of these phases shows that at initial stages of growth, the film is under oxidized. The coexistence of such phases for (111) oriented magnetite films has been also reported when magnetite is grown on polar MgO(111) substrates [78]. The HRTEM data shows that beside the formation of interfacial FeO, the film and substrate are epitaxially related with the following crystallographic relationships: YSZ(111)||FeO(111)||Fe₃O₄(111) and YSZ(1-10)||FeO(1-10)||Fe₃O₄(1-10). For further understanding of the cationic (Fe) ordering in the as grown magnetite film, we performed Z-sensitive atomic column imaging (HAADF-STEM).

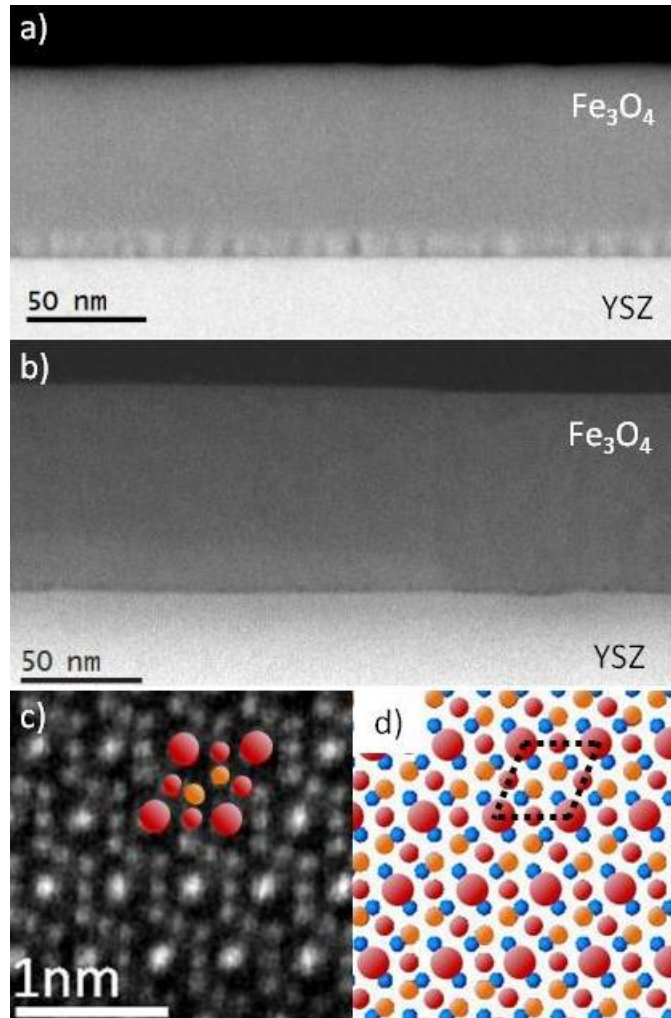


Figure 49: Low magnification HAADF images of as deposited (a) and post-annealed films (b). (c) Atomic resolution HAADF image from the annealed film. Solid circles denotes Fe atomic columns; larger (smaller) red circles representing atomic columns of Fe octahedral columns with full (half) occupancy, and orange circles represent half occupied Fe tetrahedral columns. (d) Atomic positions of Fe₃O₄ in [1-10] viewing direction, oxygen represented in blue (smallest circles), dark dashed line outline the repeat motif in this projection.

Figure 51 shows a region of the film near the interface region. The films appear to have granular structure with regions that have both bulk and more complex non-bulk ordering. For example, the box in the left (right) hand side outlines regions of bulk (non-bulk) ordering. Above each of the selected regions corresponding diffractograms shows characteristic magnetite spacings in [1-10] direction. A selected disordered region is enlarged and shown in Figure 51b. It can be clearly seen that the characteristic ordering of the “3Fe_B” and Fe_AFe_BFe_A is lacking. Instead increased occupancy on the other available Fe_B sites is present, which Fe on some A-sites is missing. This disorder is schematically shown in Figure 51c. In a number of grains, a simple face centred cubic (FCC) (‘FeO’ type) stacking is seen. This suggests that these regions potentially have

antiferromagnetic (AFM) ordering instead of resultant ferromagnetic (FM) coupling when Fe₃O₄ bulk ordering is present. Hence, these disordered regions can also contribute to the anomalous thin film properties of as grown Fe₃O₄ films.

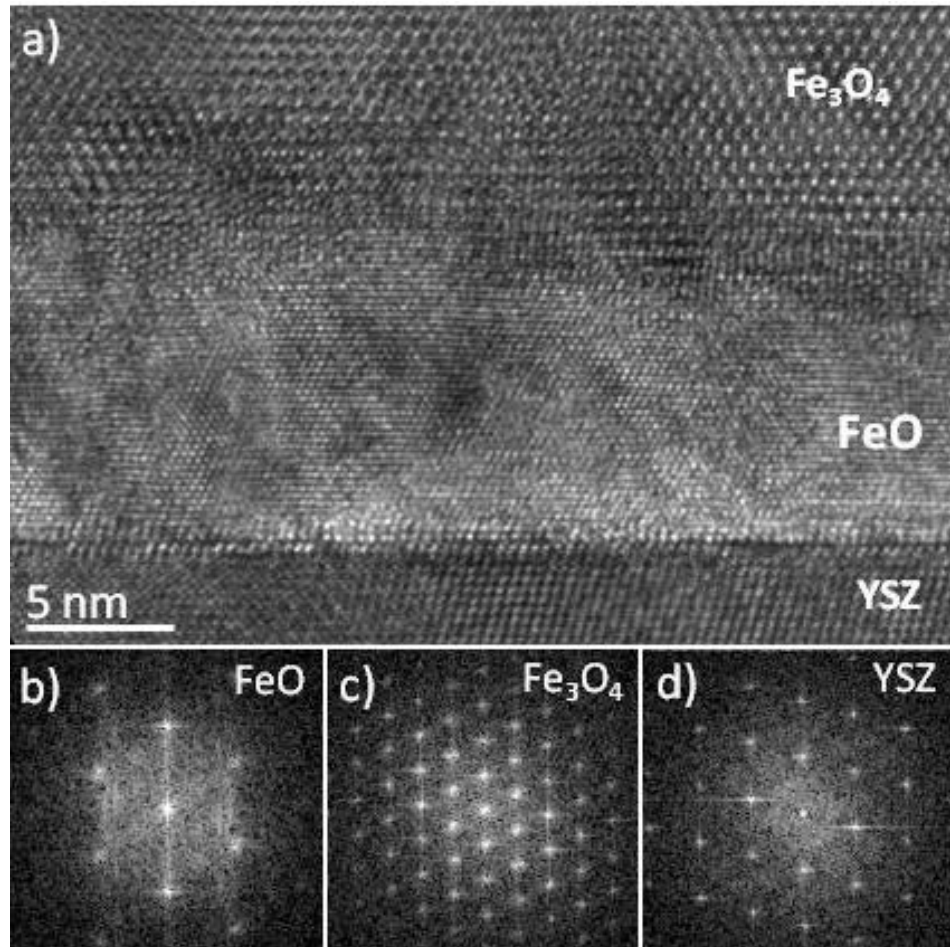


Figure 50: a) HRTEM of interfacial region for as deposited Fe₃O₄ film. Digital diffractograms from the interfacial FeO band, Fe₃O₄, and YSZ substrate are shown in (b), (c), and (d), respectively.

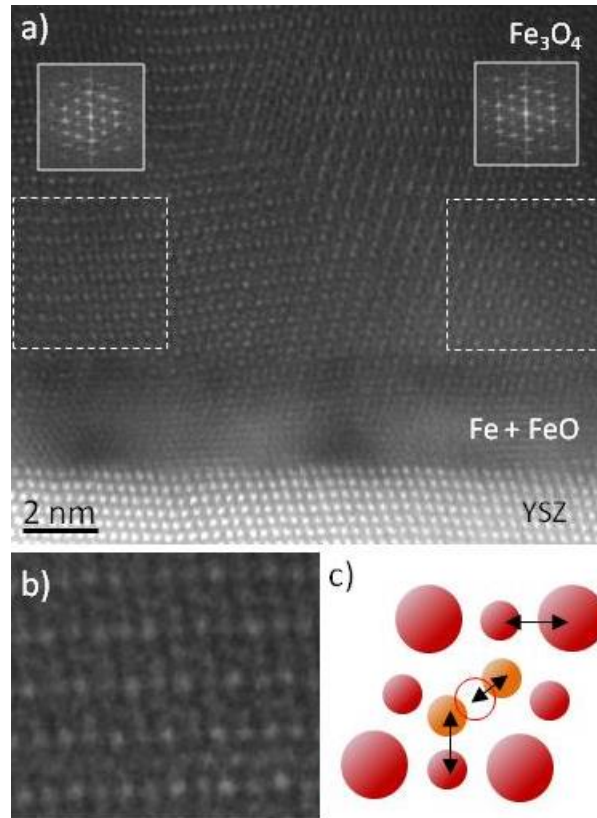


Figure 51: (a) Atomic resolution HAADF image of the interface region for as deposited film. Boxed regions represent areas from which digital diffractograms (insets above) were computed. (b) Region from a grain that shows disordered Fe atomic columns. (c) Potential mixing of the Fe sites leading to disordered cationic sublattices.

In order to fully understand the effect of the disordered regions/grains on the overall film magnetic and magneto-transport properties, quantitative analysis of the HAADF images is necessary in order to build realistic atomistic models which can serve as a starting point for atomistic spin models.

In summary, we have shown that bulk like behaviour in post-annealed films of Fe₃O₄ films in CO/CO₂ atmosphere is due to the structural ordering in the annealed films, which in as grown films, regions with disordered “FeO” like structure are present, and they likely contribute to the anomalous behaviour of the as grown films.

6.2.2 Fe₃O₄/YSZ interface

The Fe₃O₄/YSZ interface is highly strained with lattice constant mismatch of about 20% as described earlier. This is clearly shown in the post-annealed specimen interface shown here in Figure 52 and Figure 54. The interface is atomically sharp based on termination of the Fe₃O₄ on the Fe_{3B} layer. The Fourier filtered image shown in Figure 52b

shows a regular array of misfit dislocations along the interface which occur on the 6th or 5th plane of Fe₃O₄ relative to the 5th or 4th plane of YSZ in this direction.

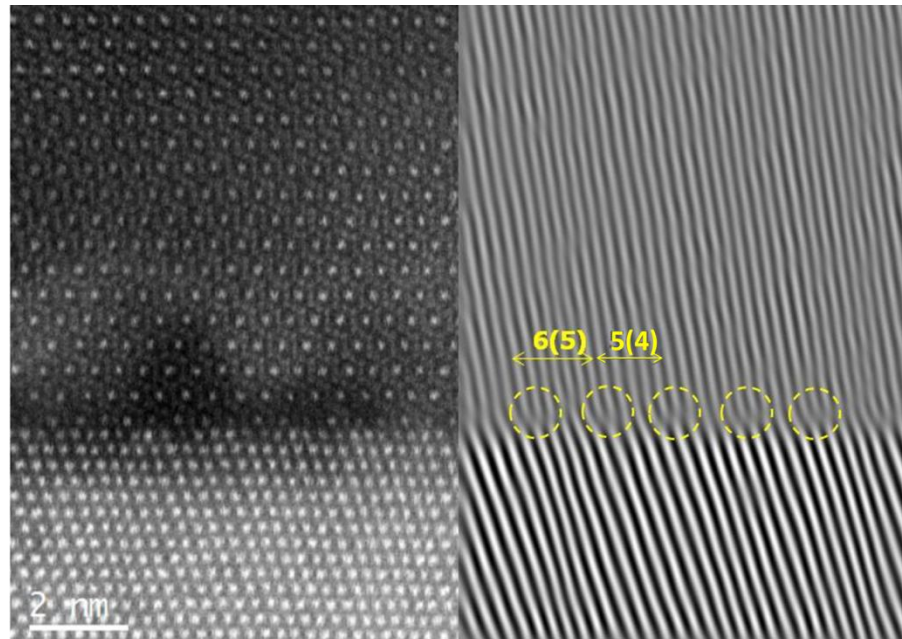


Figure 52: (a) HAADF-STEM image of the Fe₃O₄/YSZ interface in the <1-10> zone axis. (b) Fourier filtered image from (a) showing regular misfit dislocations at the interface related to the highly mismatched interface.

The orthogonal <11-2> zone axis shown in Figure 53 confirms the sharp interface between the substrate and interface and shows a highly regular single crystal of Fe₃O₄ propagating from the interface. Both interfacial images show no indication of APB defects propagating from misfit dislocations.

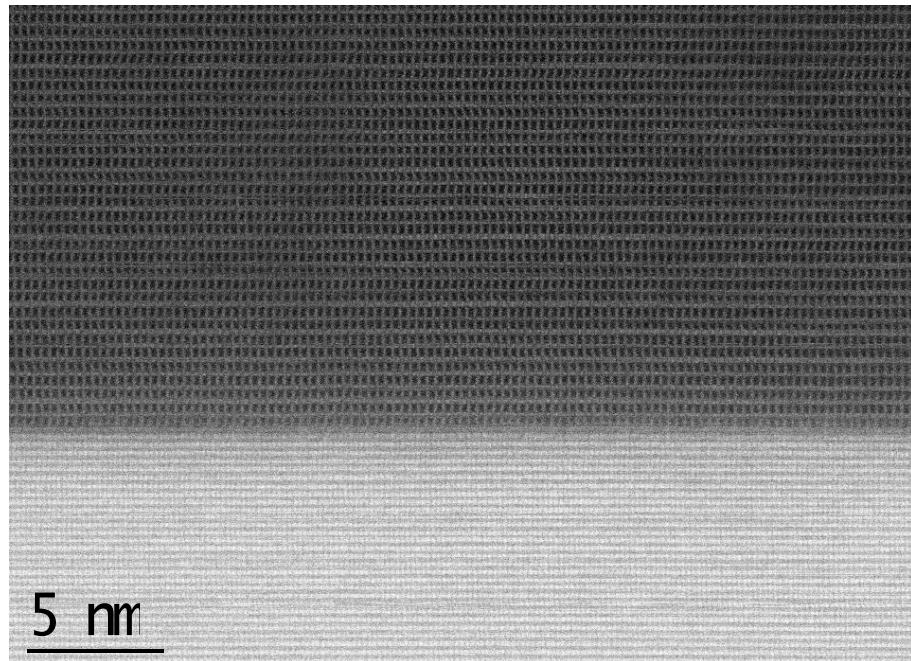


Figure 53: HAADF-STEM image of the Fe₃O₄/YSZ interface in the $\langle 11\bar{2} \rangle$ zone axis.

The higher resolution interfacial image shown in Figure 54 shows further evidence of the Fe_{3B} interfacial plane, however, in this case there is some indication of interfacial mixing on the final plane of YSZ where the HAADF-STEM intensity varies from one site to the next. This may also be a result of interfacial roughness and step edges into the specimen depth.

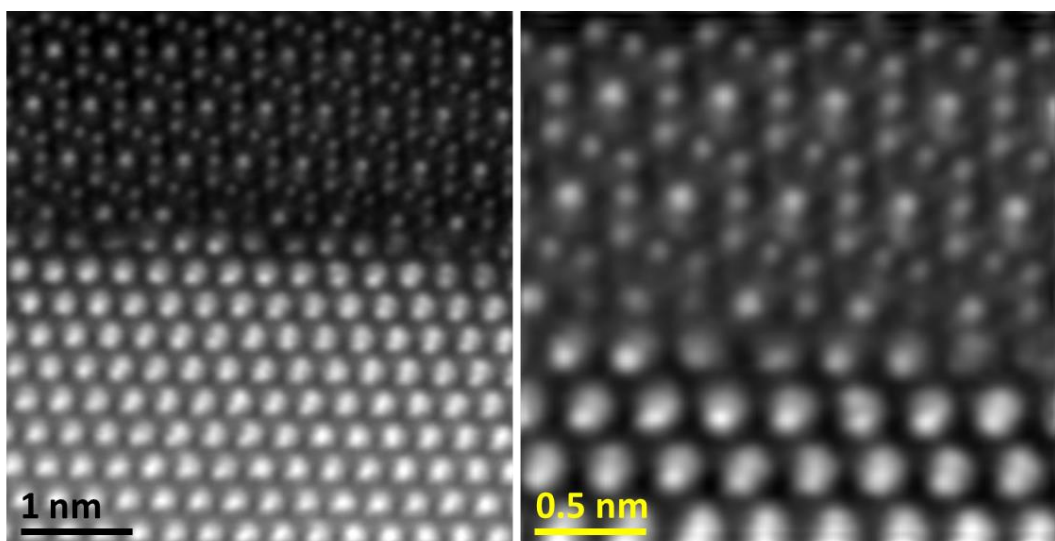


Figure 54: high resolution HAADF-STEM imaging of the Fe₃O₄/YSZ interface. Images formed from an image stack and combined using the SDDS digital micrograph plugin [145].

6.2.3 Twin defect structures in Fe₃O₄/YSZ on the (111) plane

Twin defect structures are prevalent in FCC stacked structures and are observed across a wide range of natural [189, 190] and synthetic specimens [191, 192]. Such defects are essential to the behaviour of shape memory alloys [193] and mediate stress and strain in important functional and mechanical materials.

The formation mechanism of twins in spinel structures remains unclear; however, we show the atomic structure of non-stoichiometric defect formation

Atomistic control of defects and phase segregation in technological materials is an essential challenge for realising predicted functionality in materials science [194], particularly in structural oxides including perovskites [195], spinels and manganite's.

Recent atomistic studies have shown the prevalence and stability of antiphase domain defects in Fe₃O₄ [72] which are thought to dominate the macroscopic properties of most Fe₃O₄ thin film growth [31]. In complex oxides, any disturbances in the crystal structure are liable to significantly alter conductivity and magnetic ordering properties which are highly dependent on local co-ordination and structure due to the localised electron hopping mechanism and super exchange interactions which drive overall properties.

Developing new methods for growing high quality Fe₃O₄ layers for spintronic device applications is essential to realising bulk-like atomic structure and properties in thin film Fe₃O₄ heterostructures. To date all MBE grown films of Fe₃O₄ on MgO [25, 31, 70] and MgAl₂O₄ [69, 73, 74] which are selected as substrates for their success as spin dependent tunnel barriers [196] demonstrate a high density of APBs which lead to non-bulk properties in the film including negative magnetoresistance and inability to reach magnetic saturation in grown films.

Recent developments have shown PLD grown films can be remediated by annealing in a CO/CO₂ atmosphere to reduce APB defect formation and make significant improvements in the overall film performance when compared to bulk-like properties [102]. However, these films show a new form of defect not generally observed in Fe₃O₄ thin film growth.

Figure 55a shows a low resolution MAADF-STEM image of a (111) oriented twin defect in a (111) oriented Fe₃O₄/YSZ heterostructure. In all cases of this growth front twin defect we observe large areas of twinned material with the growth defects often propagating for 200-300 nm on a single atomic plane. Furthermore the highly geometric end point of the defect which angles up to the surface of the film is typical. In this image, the defect can clearly be identified by the high brightness line running horizontally through the Fe₃O₄ layer and highlighted with yellow dashes. At the Fe₃O₄/YSZ interface, the

HAADF intensity of the substrate is greater than the film. This is a result of the high atomic number of Zr ($Z = 40$) in the substrate leading to a strong contribution to the overall intensity of this region. The Fe₃O₄ film surface in this image is not particularly flat and the film has been reduced in thickness to ~60-80 nm, this is a result of Ar ion milling during the final stages of sample preparation and was required to achieve the highly thinned electron transparent films required for this study which allow STEM-EELS acquisition.

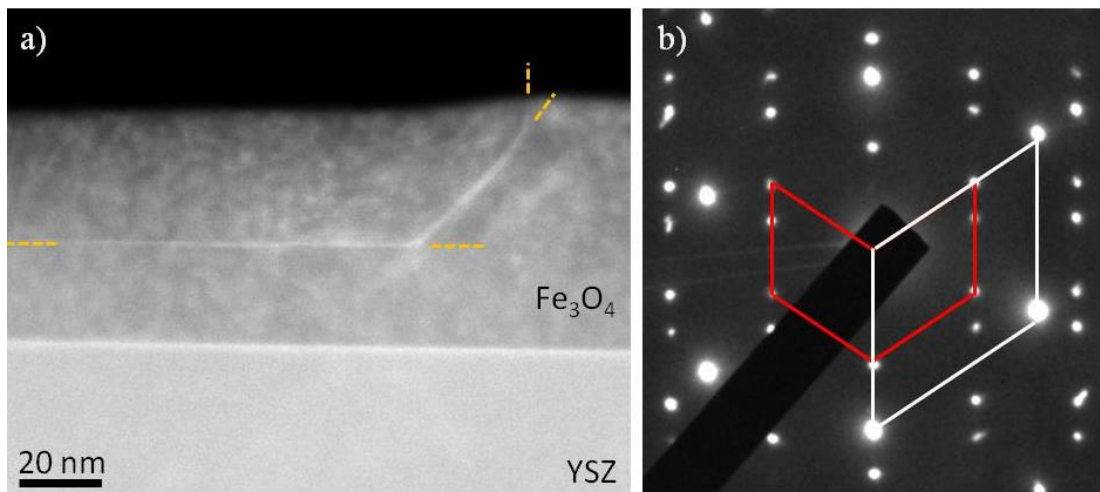


Figure 55: a) Low magnification MAADF-STEM image of the Fe₃O₄/YSZ(111) interface with a (111) oriented twin structure propagating horizontally through the deposited layer, this is highlighted with yellow dashes for clarity. b) SAD pattern taken from a twinned region showing the characteristic rhombohedral pattern associated with the $\langle 1-10 \rangle$ zone axis of both YSZ and Fe₃O₄ the brightest reflections highlighted with the white rhombus are from the substrate the two rhombohedral constructions in red highlight the two domains of Fe₃O₄ structure and uniquely identify the twinned structure.

The selected area diffraction (SAD) pattern shown in Figure 55b demonstrates the highly strained but epitaxial relationship between the Fe₃O₄ and the YSZ(111) substrate. The rhombohedral pattern shows the substrate, film and twinned regions of the film are visualised in a $\langle 1-10 \rangle$ zone axis and a standard cube to cube epitaxy is produced at the interface. The epitaxial relationship between film and substrate is Fe₃O₄(111)||YSZ(111) and Fe₃O₄(1-10)||YSZ(1-10) (except reversed in the twinned region away from the interface).

Figure 56 and Figure 57 show HAADF-STEM images of the (111) twin defect. Figure 56 offers a wider field of view and was formed from a single high resolution HAADF-STEM image. From this it is clear the structure twins at the defect interface simply by studying the structure at a distance away from the defect. We observe a reversal of symmetry in the high intensity; double occupied Fe_B sites at the interface as well as a reversal of the direction of the Fe_A-Fe_B-Fe_A chains across the defect interface. We can

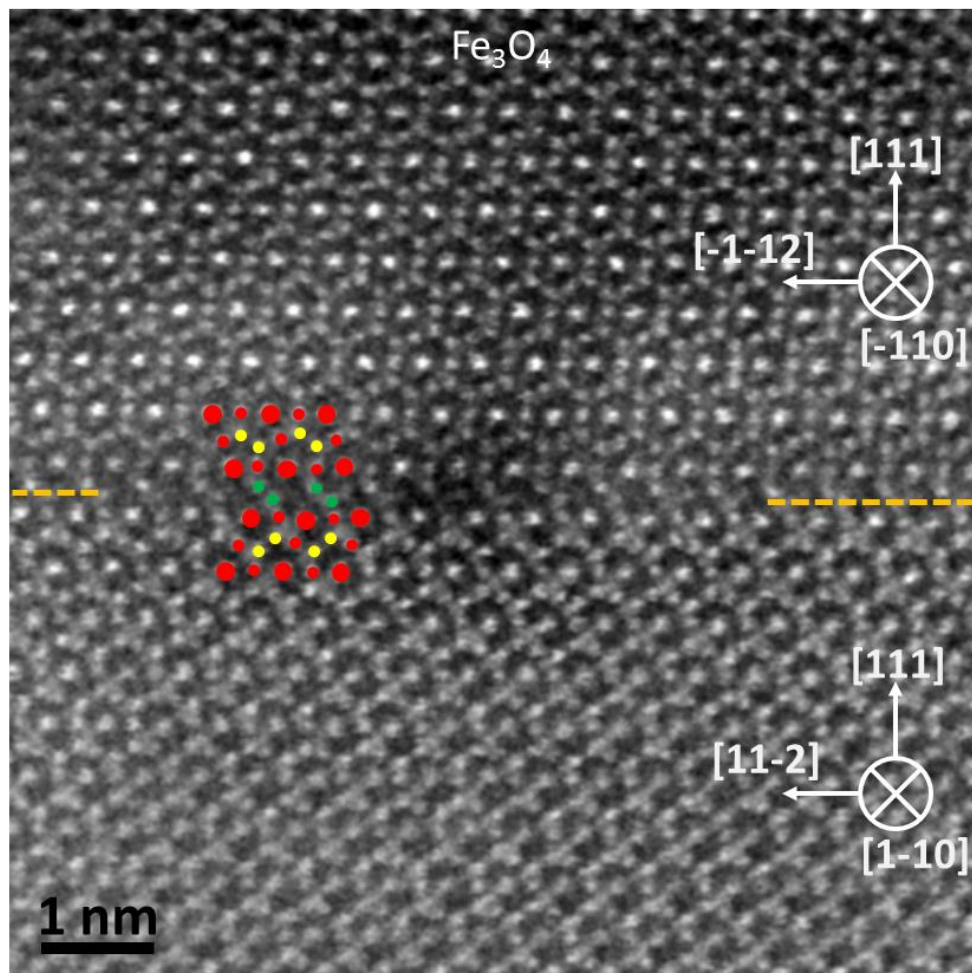


Figure 56: HAADF-STEM image showing the $\langle 1-10 \rangle$ viewing direction (w.r.t lower half of image), the defect plane is identified by yellow dashed lines at the left and right of the image. In this imaging mode the oxygen atomic sites are not visible, but the various Fe sites are identified around the defect with large red dot = doubly occupied octahedral site, small red dot = single occupied oct. site, small yellow dot = single occupied tetrahedral site, small green dot = single occupied Fe sites in the twinning region.

begin to identify the atomic structure of the defect from Figure 56 however Figure 57 gives a much clearer image of this region. Figure 57 is composed of the summed intensity from 26 rapidly acquired HAADF-STEM images which have been aligned using the SDS plugin. This is assisted by the exceptional imaging stability offered by the ultrahigh vacuum (UHV) Nion ultrastem sample mount and imaging system requiring less than 1 Å drift correction across the entire image stack.

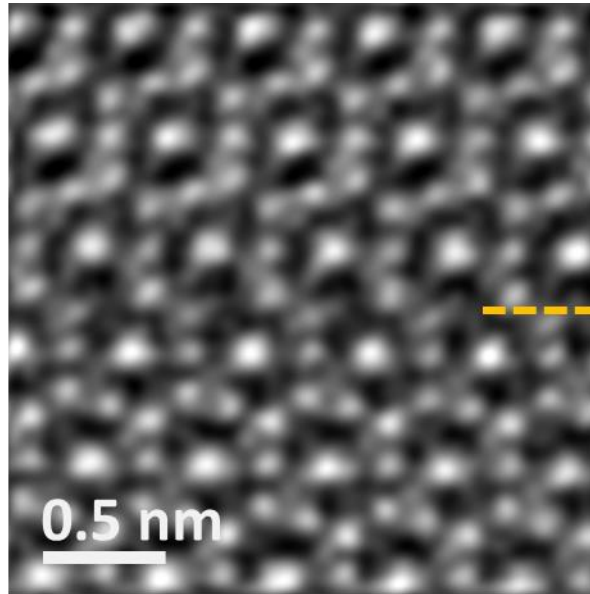


Figure 57: Atomic resolution HAADF-STEM imaging of the (111) twin defect. This figure shows the integrated image intensity from 26 rapidly acquired HAADF-STEM images. The defect plane is again identified by the yellow dashed line.

It is clear from Figure 57 that the twin defect region is incorporated on a Fe_A-Fe_B-Fe_A like structural layer; however, the layer only includes two atomic sites of the singly occupied Fe type (determined by intensity). As such the interface appears to relate to two Fe_A planes terminating together from either side of the defect. In this stacking the interface would be ...Fe_{ABA}/O₄/Fe_{3B}/O₄/Fe_A||Fe_A/O₄/Fe_{3B}/O₄/Fe_{ABA}... with a reversal of the ...ABCABC... structural stacking sequence across this defect. This is of particular interest as it suggests the defect interface is non-stoichiometric if the O content is not reduced at this interface and shows this defect terminates on the same plane (i.e. the single Fe_A plane) as is observed and predicted in vacuum terminated Fe₃O₄(111) surfaces [10, 81, 82, 197].

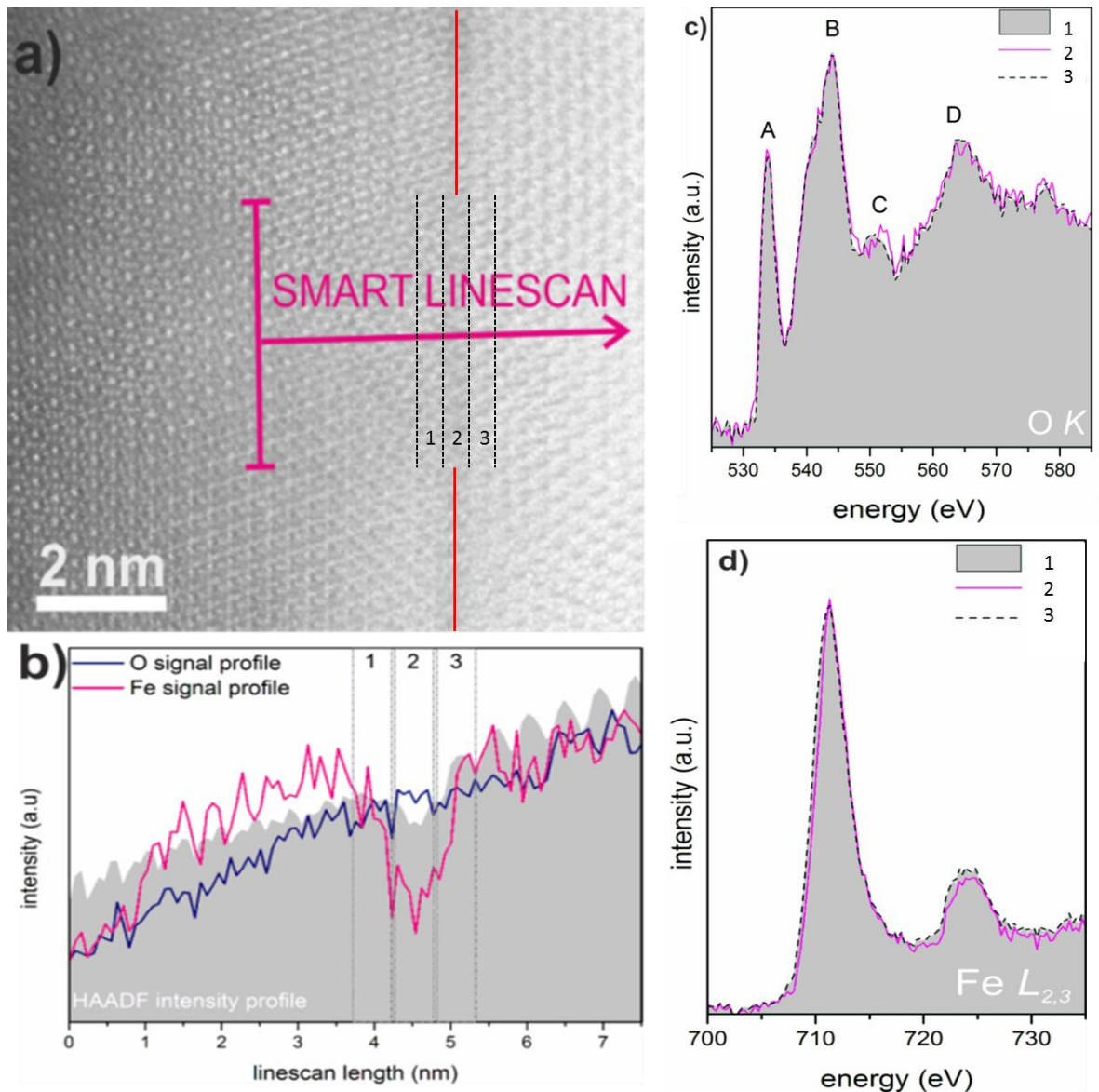


Figure 58: (a) HAADF STEM image of the SMART EELS scan [198] across the twin boundary (red line). Regions 1,2 and 3 represent the onset of the boundary region, the centre of the twin boundary and the far edge of the boundary respectively. These regions are bounded by dashed black lines. (b) Plots of the Fe L_{2,3} (pink) and O K (blue) EELS signals along the linescan, plotted against the HAADF image intensity profile (grey). The drop in the Fe signal along with the small drop of the HAADF image intensity are indicative of Fe depletion at the twin boundary. (c) O K and (d) Fe L_{2,3} spectra acquired at and adjacent to the twin boundary (marked with dashed lines in panel a and b) [199]

STEM-EELS linescan data collected at the twin defect supports the view that Fe content is disturbed at this defect. Figure 58a shows the linescan region with the linear vertical defect being mapped using an ~5 nm lateral integration region which is progressively mapped towards and across the defect. This linescan with perpendicular extent is an ideal way to map this highly geometric defect as it removes the need to put large beam currents through very small regions of the sample as when looking for 2D

atomic resolution data. As can be seen by the increasing imaging intensity in this figure the sample thickness is increasing from left to right as the scan approaches the substrate side of the sample. The comparative HAADF-STEM, O k-edge and the Fe L_{2,3} edge intensity are mapped along this line in Figure 58b. Across this scan the HAADF-STEM intensity (grey) is clearly shown to increase from left to right as expected. The O signal (blue) tracks this increase in the HAADF-STEM signal and shows no evidence of varying O concentration beyond that associated with increasing sample thickness. The Fe signal (pink) shows a significant depleted region in and around the twin defect. The spatial windows identified as 1, 2 and 3 in this plot identify the centre of the twin defect in region 2 and show a clear loss of Fe intensity at the twin. This data is also supported by minor variations in the near edge structure (ELNES) of both the O K-edge (Figure 58c) and the Fe L_{2,3}-edge (Figure 58d). The O k-edge data shows both near defect curves (grey-filled curve and dashed curve) are very similar to one another and that the defect plane region shows a peak position shift in peak 'C'. This, alongside the drop in the Fe L_{2,3} ratio at the defect interface indicates an increase in local oxidation state [199] which in the case of Fe₃O₄ may represent a local shift toward more Fe₂O₃ like chemistry which fits with the likelihood of a missing Fe plane.

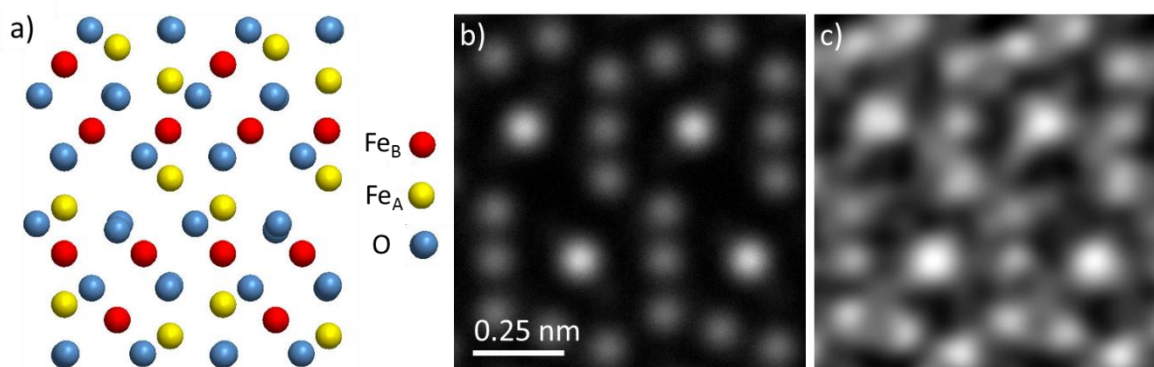


Figure 59: Structural modelling of the (111) twin defect based on a non-stoichiometric defect interface. a) shows the structural model stabilized with electron holes to give charge neutrality. b) shows the HAADF-STEM image simulation produced using (a) and contains the scale bar for both (b and c). c) shows a HAADF-STEM image comparable to the region shown in (b).

By analysing the symmetry of the defect imaging and taking into account the loss of the interfacial Fe site we have produced DFT calculations. These models are stabilised by introducing electron holes to recreate the charge localised anion-cation array expected in this material. This model converges and gives good agreement with atomic scale HAADF-STEM imaging when simulated.

The structural model of this twin interface compensated by electron holes is shown in Figure 59a with a corresponding image simulation shown in Figure 59b. This model

shows a high degree of similarity with the HAADF-STEM imaging data for a comparable defect region shown in Figure 59c.

This defect structure does not have the effect of introducing significant non-bulk bonding configurations as the defect is created mainly by removing the Fe_B plane within the twin. This means the structure remains ferrimagnetically aligned in its ground state and as unlikely to affect the magnetic and MR behaviour of the film, as seen in the bulk like MR and MH properties observed in Figure 48.

6.3 Conclusions

It is clear from this work that PLD and post-annealing techniques can offer very different properties in a grown film than the outcomes achieved by MBE growth. Furthermore, the range of options for chemistry and high temperature processing are altered if the vast majority of sample processing is performed *ex-situ* after the main deposition process has been completed.

It remains to be seen whether specimens deposited by MBE methods can also be reformed post-deposition in this way as that may allow a route back to high levels of accuracy in depositing super thin films which are not easily produced via PLD.

In this chapter we have shown the formation of a highly strained epitaxial interface. That this does not create significant strain and defect propagation into the film overlayer is surprising, as is the resulting cube-on-cube direct epitaxial relationship which is produced.

The films produced are much thicker than the critical thickness of Fe₃O₄ at this level of strain so we would not expect Fe₃O₄ to grown in a directly strained manner, however the behaviour of the overlayer to reform directly after a misfit dislocation is not necessarily expected. If the temperature of substrate processing could be reduced, possibly by implementing very long annealing times then the possibility of returning to semiconductor and oxide barrier materials for substrates could be achieved.

Chapter 7. Fe₃O₄/STO(111) interface structure

Atomic resolution scanning transmission electron microscopy (STEM) and electron energy loss spectroscopy (STEM-EELS) combined with *ab initio* structural and electronic calculations are used to determine the structure and properties of the Fe₃O₄(111)/SrTiO₃(111) polar interface. The interfacial structure and chemical composition are shown to be atomically sharp and of a tetrahedral Fe/Ti nature. Band alignments across the Fe₃O₄ and SrTiO₃ interface pins the Fermi level at the bottom of the SrTiO₃ conduction band. Spin polarisation of the interfacial Fe₃O₄ layer is reduced to 66% but recovers to the bulk value (100%) within the first unit cell. Interfacial mixing is ruled out by both experimental data and theoretical considerations due to high energy barriers calculated for atomic site swapping.

This work has been performed in collaboration with Dr. D. M. Kepaptsoglou and Prof. Q. Ramasse at the SuperSTEM facility, Daresbury (STEM and STEM EELS). Dr K. McKenna at the University of York (DFT calculations) and Dr. K. Matsuzaki and Prof. T. Susaki at the Tokyo institute of Technology (PLD growth and film annealing).

7.1 Introduction

Oxide heterostructures are of interest for developing new functional materials due to their rich physical properties [200-204]. Many oxides are insulators, but oxide materials also provide wide band gap semiconductors [205], superconductors [206], ionic conductors [207], ferrimagnetic [208] and antiferromagnetic [209] materials. As such, oxide multilayer structures provide a broad platform for devices with multifunctional properties. The functionality of oxide devices depends strongly on the atomic scale structural and electronic discontinuities across multilayer heterostructure interfaces; therefore we need an atomic scale understanding of their interfacial properties. In this work we focus on spinel-perovskite heterostructures that have great potential for the development of multiferroic devices by using Fe₃O₄/SrTiO₃ as a model system [210, 211].

This heterostructure is an excellent candidate for spintronic applications due to the half-metallic properties of Fe₃O₄ [18-20] and the tuneable conductivity of SrTiO₃ (STO).

Along the [111] direction both Fe₃O₄ and STO are chemically layered polar materials. STO is defined by alternating SrO₃ and Ti planes. The complex arrangement of Fe sites in the Fe₃O₄ spinel structure gives tetrahedral (Fe_A) and octahedral (Fe_B) sites with six unique atomic planes described by "...4O/3Fe_B/4O/Fe_A-Fe_B-Fe_A..." along the [111] direction. This leads to twelve nominal interfacial terminations between the STO substrates and the grown Fe₃O₄ film which could be exploited for the purpose of interfacial atomic engineering. This could be explored to understand the interface effects on spin-dependent tunnelling/injection in semiconductors. One of the main obstacles to polar oxide growth is the divergent electrostatic potential of the grown film. This interface 'electrostatic catastrophe' must be mediated in a real heterostructure by a stabilisation mechanism; such as atomic mixing, interface roughening and faceting and/or pure electronic interface reconstructions [78-80].

In this work by employing pulsed laser deposition (PLD) growth and atomically-resolved aberration corrected transmission electron microscopy (TEM) and spectroscopy we demonstrate that atomically sharp polar oxide spinel/perovskite junctions can be achieved experimentally.

In contrast to the vacuum/Fe₃O₄(111) interface terminated by a tetrahedrally coordinated Fe_A surface layer which is strongly positively spin polarised, first principle calculations show that experimentally realised Fe₃O₄/STO(111) interfaces have retained the characteristic negative spin polarisation and that ideal 100 % spin polarization of the Fe₃O₄ is recovered within one unit cell from the interface.

The relative stability of oxide/oxide interfaces compared to ferromagnet /semiconductor interfaces [212] makes the implementation of atomically-engineered structures a realistic expectation and opens the possibility of tailoring metastable interface structures with potential for device applications. Finally this work demonstrates the feasibility of atomically-controlled spinel/perovskite heterojunction interfaces, and is an example of a class of materials that can host ferromagnetic and ferroelectric properties, which can be potentially coupled by suitable interface engineering.

SrTiO₃ is an insulating oxide (band gap 3.25 eV) with perovskite structure; however with Nb doping the STO can become an effective semiconducting material and even a metallic conductor [213, 214]. Therefore STO could be used either as a spin tunnel barrier or a medium for spin current diffusion in the insulating and semi-conducting phase respectively.

7.2 Methods

Fe₃O₄ films have been grown on (111) oriented Nb 0.05 wt% doped SrTiO₃ substrates (Shinkosha LTD) by pulsed laser deposition using a KrF excimer laser ($\lambda = 248$ nm) with a pulse duration of 20 ns and power density of 2.3 Jcm⁻² cycling at 10 Hz [102]. Substrates have been prepared for deposition with a buffered NH₄F-HF solution etch to ensure Ti surface termination [215] and a 60 minute anneal at 1050 °C in air to reduce surface roughness and remove surface contaminants. Prior to deposition the substrate condition and orientation has been checked using RHEED. Deposition was performed with the substrate held at 300 °C by the ablation of a sintered Fe₃O₄ target in a background oxygen atmosphere of 2x10⁻⁴ Pa. Post-deposition the sample was annealed at 1000 °C for 60 minutes in a CO/CO₂ atmosphere to improve film crystallinity and stoichiometry [102].

Deposited specimens have been characterised with θ -2 θ X-ray Diffraction (XRD) scans to identify the reflections of Fe₃O₄ and STO and to ensure the growth mode has given correctly oriented, epitaxial growth.

Cross-sectional transmission electron microscopy (TEM) specimens have been prepared by conventional methods that include mechanical thinning/polishing and finishing with low angle Ar ion milling using a cold stage equipped PIPS 691 (GATAN) to achieve electron transparency [137]. These specimens have been prepared in the [1-10] viewing direction with respect to the STO substrate crystallography.

Structural characterisation has been performed by high resolution transmission electron microscopy (HRTEM) and selected area diffraction (SAD) using a JEOL 2011 and a double aberration corrected JEOL JEM-2200FS operating at 200 keV. Scanning transmission electron microscopy has also been performed using bright field (BF-STEM), medium angle annular dark field (MAADF-STEM) and high angle annular dark field (HAADF-STEM) detectors implemented in the double aberration corrected JEOL JEM 2200-FS operating at 200 keV and a C₅ corrected Nion UltraSTEM100 operating at 100 keV in UHV conditions (typical pressures < 2x10⁻⁹ Torr at the sample). Various image collection methods have been used to enhance image quality and suppress noise in the resultant data including the acquisition of series of sequential images of the sample region of interest, which are aligned using the statistically determined spatial drift (SDSD) plugin for Digital Micrograph to correct for any image drift as developed by Schaffer *et. al.* and then summed [145].

Atomically resolved chemical analysis has been performed using a Gatan UHV Enfina spectrometer for electron energy loss spectroscopy (EELS) concurrently with HAADF-STEM imaging using the Nion UltraSTEM100 as above. STEM-EELS was

performed using a 1340 channel detector with 0.3eV/Channel energy resolution comparable to the energy spread of the cold FEG electron gun. EELS maps were generated by integrating the edge intensity above the relevant edge after background subtraction using a power law model. The data was first denoised using principle component analysis, although raw data were systematically checked to ensure the same information was present (albeit noisier).

The resultant microscopy data has been used to inform density functional theory (DFT) calculations which have been performed to study the effect of interfacial strain on the spin polarisation and local magnetisation of the Fe₃O₄ overlayer when compared to bulk. DFT calculations have been performed using the projector augmented wave method and the Perdew-Burke-Ernzerhof (PBE) functional as implemented in the VASP code [167, 168, 216]. The Fe₃O₄/STO interface has been modelled as an inversion symmetric periodic layered structure with ~20 Å blocks of Fe₃O₄ and STO. Wavefunctions are expanded in a plane wave basis with energies up to 350 eV and a 2x2x1 Monkhorst-Pack k-point grid is employed. This approach proved reliable for predicting the structure and stability of antiphase defects in Fe₃O₄ in a previous study [72].

The Fe₃O₄ region of this calculation has been strained in the plane parallel to the interface to lattice match the SrTiO₃ structure as is appropriate to model a Fe₃O₄ overlayer. This requires that Fe₃O₄ is compressively strained by 6.1 %. The cell dimension perpendicular to the interface has been optimized to minimise the total energy of the supercell. The in-plane strain alters the bulk like states of Fe₃O₄ and reduces the 100% spin polarisation of the bulk structure as a result of band broadening and higher energy d-type states in the majority band around the Fermi-level which exhibits a band-gap in the bulk. The comparison between the DOS of bulk Fe₃O₄ and strained Fe₃O₄ can be seen in Figure 68. It is likely the actual Fe₃O₄ interface states in the grown film are more closely matched to the half-metallic states of the bulk configuration as much of the overlayer strain in the grown film is mediated through misfit dislocations at the interface.

HAADF-STEM image simulations of the Fe₃O₄/STO interface have been performed using the relaxed structural data provided by DFT calculations. Image simulations have been performed the multi-slice method implemented in QSTEM image simulation software [147]. Simulations have been performed using 30 thermal diffuse scattering iterations and experimentally determined electron beam parameters relating the the JEOL 2200-FS of, acceleration voltage = 200 kV, chromatic aberration $C_C = 1.6\text{mm}$, spherical aberration $C_s = 0.0011\text{mm}$, fifth-order spherical aberration $C_5 = 1.756\text{mm}$, convergence semi-angle $\alpha = 24\text{ mrad}$ and HAADF-STEM detector acceptance semi-angle 85–170 mrad [72].

7.3 Results

7.3.1 Film deposition quality and epitaxy

Figure 60 shows a HRTEM image of the Fe₃O₄(111)/STO(111) interface as viewed in the [1-10] direction of the STO substrate. This image and others taken show the well-ordered, single crystal nature of the Fe₃O₄ film and demonstrate the abrupt interface and uniform thickness of this growth. When combined with the XRD θ -2 θ scan shown in Figure 61 the epitaxial growth mode is clear, without phase segregation within the film.

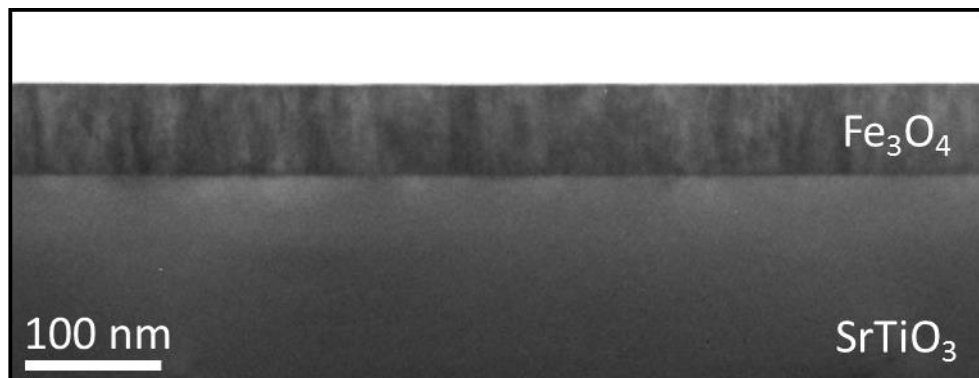


Figure 60: HRTEM overview image of the Fe₃O₄/SrTiO₃ heterostructure showing uniform film thickness of ~ 80 nm and a sharp interface between film and substrate.

Low magnification TEM imaging shows that the film has a uniform thickness (Figure 60) and SAD in Figure 62a and x-ray diffraction (XRD) (Figure 61) show that the film is single-phase with clearly defined crystallographic orientation. In order to determine the epitaxy between the film and substrate we calculate a simple cube-on-cube epitaxy (Figure 62b) and a twinned cube-on-cube epitaxial relationship (Figure 62c). Comparison between the experimental and calculated SAD patterns shows that the Fe₃O₄/STO epitaxy is determined by the twinned cube-on-cube epitaxial relation given by the following relationship: Fe₃O₄(111)||STO(111) and Fe₃O₄(-110)||STO(1-10). Overall the presence of extended structural defects in these films, such as antiphase domain boundaries, have a low density due to the post-deposition film annealing treatments discussed elsewhere [102].

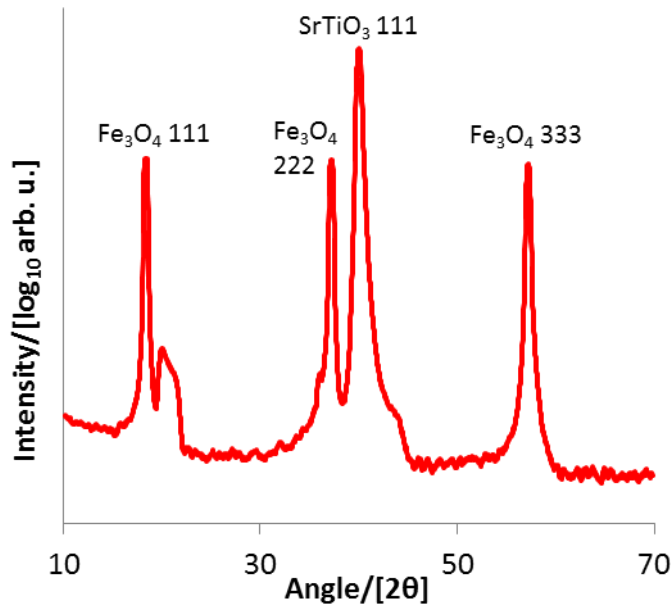


Figure 61: XRD θ - 2θ scan of the Fe₃O₄/SrTiO₃(111) structure showing the single phase nature of the film and the shared (111) planes of both materials.

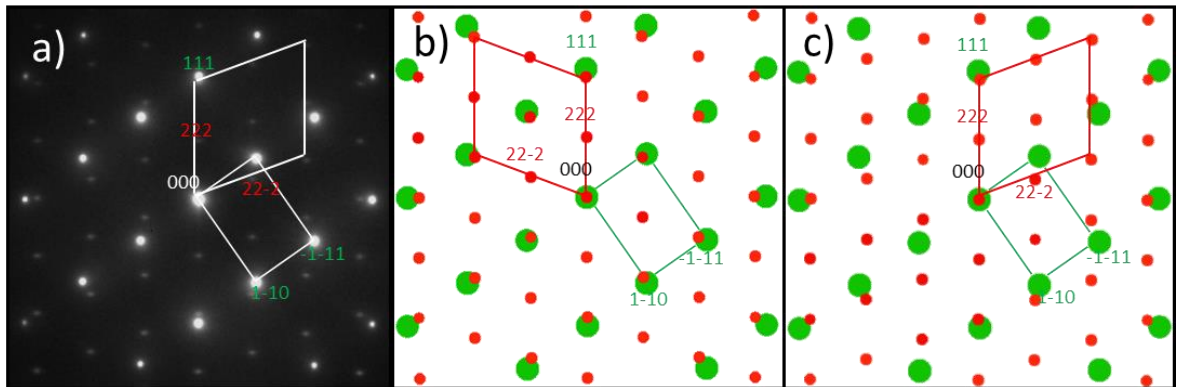


Figure 62: b) SAD pattern from the interface shown in (a). The structural motif of Fe₃O₄ and SrTiO₃ is highlighted with the inset quadrilaterals and major diffraction spots indexed. c) And d) show SAD simulations of Fe₃O₄ (red) and SrTiO₃ (green) depending on whether the Fe₃O₄ structure is mirrored around the vertical axis. c) Shows the undisturbed [1-10] viewing direction for both SrTiO₃ and Fe₃O₄ d) shows the [1-10] viewing direction for SrTiO₃ and the [-110] viewing direction for Fe₃O₄. The close correspondence between b and d show the Fe₃O₄ overlayer is mirrored from direct cube on cube epitaxy.

Firstly we present the interface structure and epitaxial relationship of the experimentally realised Fe₃O₄/STO(111) interface. The structural quality of Fe₃O₄ (111) film grown by PLD is shown in Figure 63. The HAADF-STEM image in Figure 63 shows the interfacial region of this specimen. In this image all the cationic sites (Fe, Ti and Sr) are observed and atomically resolved, while the O atomic columns are not seen due to the low scattering cross section of low Z atomic species. The SrTiO₃ structure shown here is

readily interpretable, the brightest sites are mixed Sr-O columns with high intensity produced from the heavy Sr atoms. The lower intensity sites in the STO region are Ti. The Fe₃O₄ structure is more complex. The inset cationic structural diagram shows the pattern of Fe_A sites in yellow and Fe_B sites in red. The intensity variations between Fe_B sites are a result of the full and half occupation of the octahedral Fe_B columns. This gives the overall rhombohedral structural motif of the brightest atoms. From Figure 63 we observe a sharp interface between Fe₃O₄ and SrTiO₃. Interfacial strain arising from the lattice mismatch between film and substrate is mediated by periodic misfit dislocations.

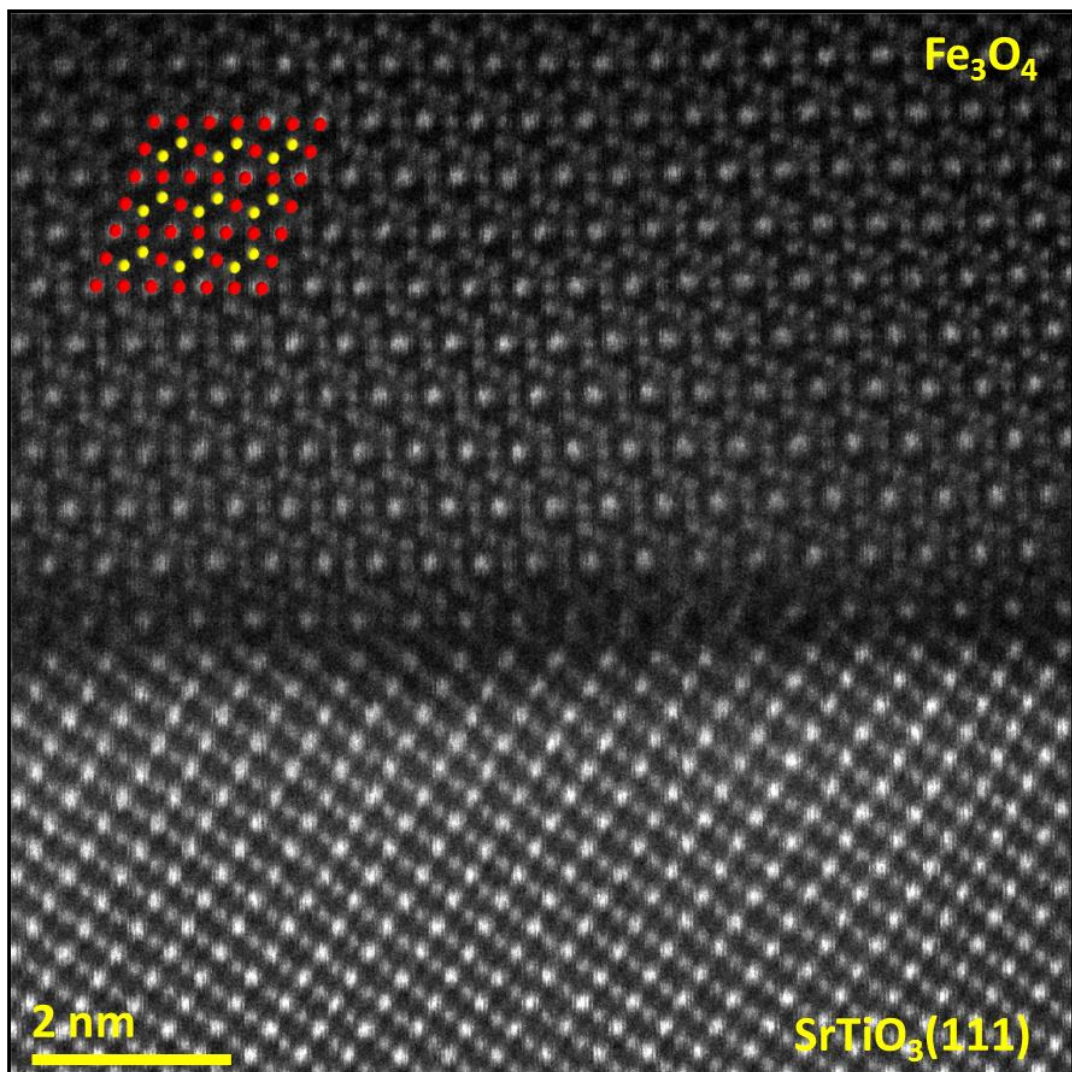


Figure 63: HAADF-STEM image of the Fe₃O₄ film and SrTiO₃ substrate in the [1-10] zone axis (with respect to the substrate). The Fe sublattice structure is inset, with octahedral (tetrahedral) Fe sites shown in red (yellow).

7.3.2 Determining the Fe₃O₄/SrTiO₃ interface

Figure 64 shows the integrated EELS spectra of the region shown in Figure 65. Selecting an energy window for EELS acquisition ranging from 370 eV to 772 eV we are able to include the characteristic peaks for Ti, Fe and O. In this region of the EEL spectra background subtractions have been modelled using a power law model. It is not possible for us to simultaneously identify Sr which can be found at ~1200eV and offers a very weak signal to noise ratio though this has been identified separately and corresponds to the positions of greatest brightness in the HAADF-STEM image as would be expected for the heaviest element in this structure Sr ($Z = 38$).

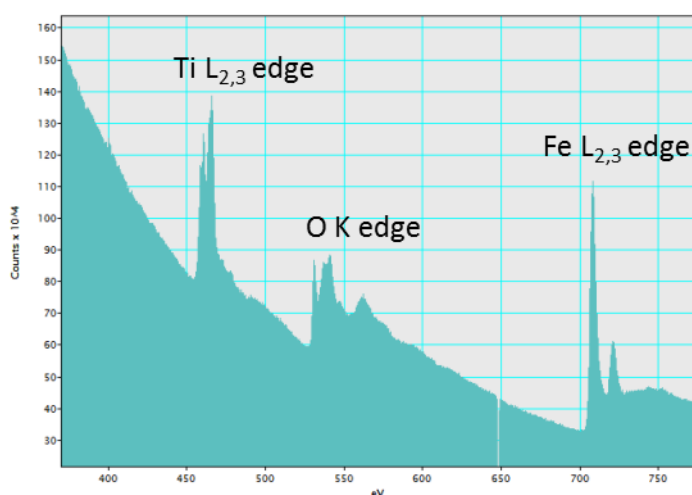


Figure 64: Integrated STEM-EELS spectra from the region of interest indicated in figure 2.

In order to determine the atomic structure of the Fe₃O₄(111)/STO(111) interface we use atomically-resolved (STEM-EELS), shown in Figure 65. The advantage of simultaneously acquiring STEM and EELS is that HAADF-STEM image contrast can be directly correlated with the spectroscopic signal on a pixel by pixel basis in the interface region. The HAADF imaging clearly distinguishes the interface region between the Fe₃O₄ and STO as shown in Figure 65a. Based on the symmetry and the structural patterns of Fe₃O₄ and STO in the [1-10] viewing direction the abruptness of the spinel/perovskite interface is within a single atomic plane. Figure 65b shows the intensity of high angle scattered electrons detected by the HAADF-STEM detector during EELS acquisition. This image forms a reference position for the chemical map of the interface.

In order to determine the chemical nature of the interface we present atomic resolution EELS, shown in Figure 65(c-e). Figure 65c shows that O planes between the STO and Fe₃O₄ are continuous. The [1-10] viewing direction in STO has a mixed Sr-O column, in the HAADF-STEM image, which shows with high intensity due to the high

atomic number of Sr. Similarly the variation of intensities in the O map in the STO reflects the double and single occupancies of O, on either pure O or mixed Sr-O atomic columns, respectively. Following the O atomic column's face centred cubic FCC stacking we define the structural interface as the plane across which O atomic columns are twinned. The twinning of the FCC stacking sequence which has been deduced from SAD (Figure 62) is confirmed in this map with the rhombohedral FCC stacking of O undisturbed away from the interface with the twin structure occurring across a single (111) atomic plane in the interface. Figure 65d shows the elemental map of iron atomic columns, using the Fe $L_{2,3}$ edge. By comparing this data with the HAADF image the rhombohedral motif of Fe occupied sites is identified. The Fe $L_{2,3}$ signal disappears just above the reference interface plane (dotted white line in Figure 65). Similarly Ti is the topmost layer of STO with the Ti $L_{2,3}$ edge map shown in Figure 65e reflecting the expected positioning of Ti atomic columns based on the HAADF image

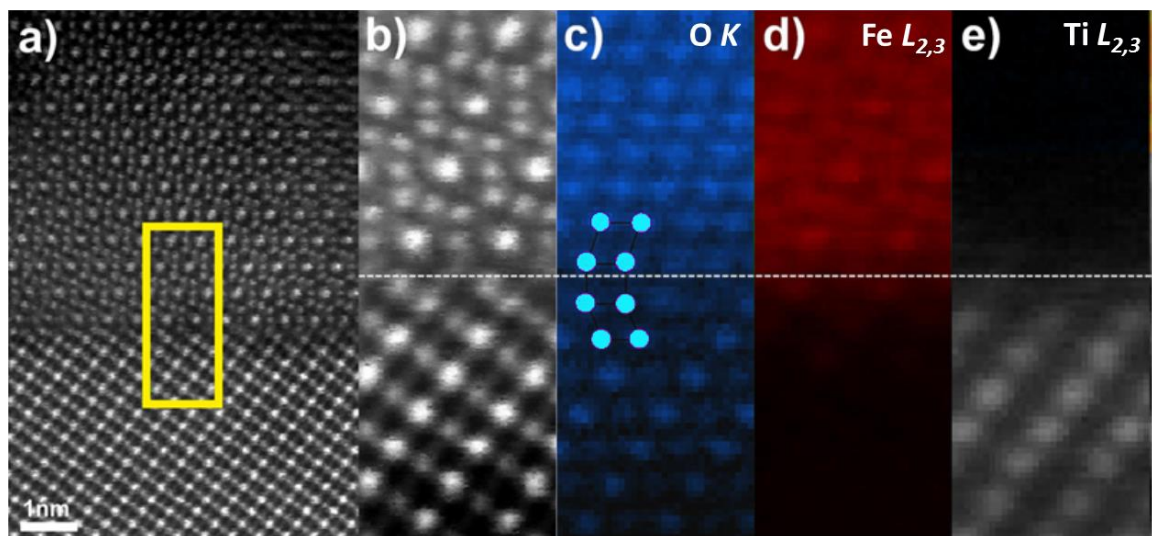


Figure 65: HAADF-STEM and STEM-EELS from interfacial region. a) Region of interest selected from HAADF-STEM imaging. b) HAADF-STEM signal showing atomic resolution imaging. c) Spatially resolved intensity of O K edge signal. For guidance we draw a white dashed line that indicates the structural boundary between the Fe₃O₄ structure and the STO structure based on the O EELS map. d) Spatially resolved intensity of Fe $L_{2,3}$ edge signal with high intensity seen on Fe_B sites. e) Spatially resolved intensity of Ti $L_{2,3}$ signal.

Further insight into the atomic structure of the interface can be extracted from the atomic column intensities at the interface layer(s) based on comparison between the experimental HAADF images and image simulations from candidate structural models. The atomic columns of interest are labelled in Figure 67a. Site 'a' is located in the structural position of a tetrahedral Fe_A atomic column with respect to the Fe₃O₄ structure above and gives strong Fe $L_{2,3}$ signal from STEM-EELS. Site 'b' is positioned such that it sits geometrically in the position of a Ti site w.r.t the STO substrate, but also a singly

occupied Fe_B site w.r.t the Fe₃O₄ structure. Site 'c' is used as a reference site since it is occupied by Sr which is easily identifiable due to its high intensity and direct correlation with bulk Sr atomic sites. Thus we need to determine the atomic species at sites 'b' which is occupied either by Fe and/or Ti.

Based on EELS analysis we create atomic models of two candidate interface as following: ...3Fe_B/4O/Fe_A-Ti/SrO₃/Ti... and ...3Fe_B/4O/Fe_AFe_B-SrO₃/Ti... These models have been structurally optimized using density functional theory (DFT). Based on the relaxed atomic positions obtained by DFT we calculated HAADF image intensities of the atomic columns from both interface models and compare these results to the experimental data (Figure 66). The structural models; ...3Fe_B/4O/Fe_A-Ti/SrO₃/Ti... (resp. ...3Fe_B/4O/Fe_AFe_B-SrO₃/Ti...) are shown in Figure 66b (resp. Figure 66d) and the corresponding image simulations are shown in Figure 66c (resp. Figure 66e), Comparable experimental HAADF imaging is shown in Figure 66a. As expected due to higher Z, the intensity of the Fe atomic column at site 'b' (Figure 66e) is higher than the Ti column (Figure 66c). Comparison between the experimental and simulated images to uniquely identify the atomic structure of the interface is presented in Figure 67a and Figure 67b. The HAADF-STEM images shown in Figure 66a and Figure 67a are formed from image stacks which have been aligned using the SDS digital micrograph plugin [145] and summed using the stack builder tool. This gives a significantly improved signal to noise ratio in the image.

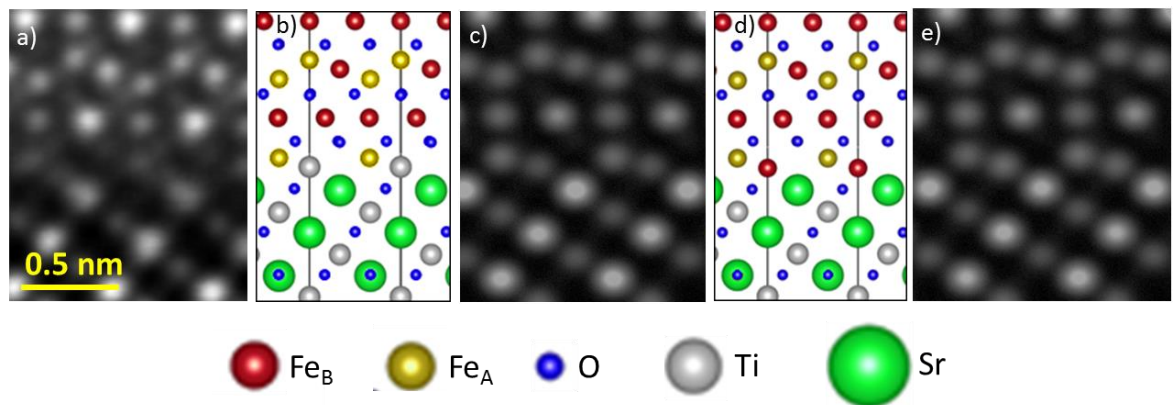


Figure 66: HAADF-STEM interface analysis from relaxed DFT co-ordinates. a) HAADF-STEM image of the Fe₃O₄/STO interface structure. b) Relaxed atomic structure of the ...3Fe_B/4O/Fe_A-Ti/SrO₃/Ti... interface model c) HAADF-STEM image simulation resulting from the structure in (b). d) Relaxed atomic structure of the ...3Fe_B/4O/Fe_AFe_B-SrO₃/Ti... interface model e) HAADF-STEM image simulation resulting from the structure in (d).

The intensities of the three interfacial sites; 'a, b and c' from the experimental HAADF image (Figure 67a) are compared the calculated HAADF maps in (Figure 66c) and (Figure 66e) in the normalised intensity histograms shown in Figure 67b. In the

experimental HAADF-STEM data (black histogram) we find that the interface site 'b' exhibits a drop in intensity of ~22.5 % compared with site 'a'. This drop of intensity is well replicated in the ...3Fe_B/4O/Fe_A-Ti/SrO₃/Ti... interface model (blue histogram) which shows a decrease in intensity of 27.5 %. The decrease in intensity between sites *a* and *b* in the ...3Fe_B/4O/Fe_AFe_B-SrO₃/Ti... simulation (red histogram) is only ~5.1 %. The above analysis is consistent with the conclusions from the EELS mapping that the interface is determined by ...i3Fe_B/4O/Fe_A-Ti/SrO₃/Ti...

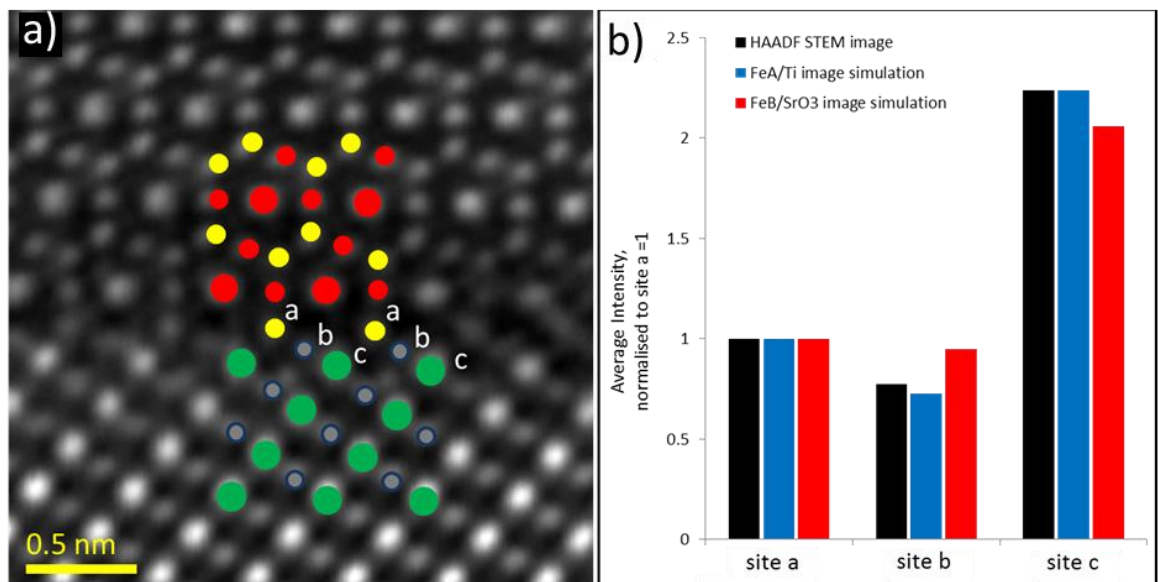


Figure 67: a) Larger area HAADF-STEM image of the Fe₃O₄/STO(111) interface. b) Averaged site intensities for the interfacial sites a, b and c highlighted in (a). In this figure atomic species are represented by: Sr (large green circles), Ti (grey), Fe_B (red) and Fe_A (yellow)

Based on the EELS mapping and HAADF-STEM image analysis a unique determination of the Fe₃O₄/STO interface can be provided in the overlay in Figure 67a; interfacial atomic columns are identified as follows. Ti (grey) is the terminating STO layer, followed by Fe_A in yellow on the Fe₃O₄ side of the interface. The Sr and Fe_B atomic columns are identified with green and red respectively.

To perform DFT calculations of the Fe₃O₄/STO interface we must consider the strain present as a result of the lattice mismatch between Fe₃O₄ and the SrTiO₃ substrate. The bulk unit cells of Fe₃O₄ and SrTiO₃ give optimised lattice parameters of *a* = 8.40 Å and *a* = 3.905 Å respectively when the DFT calculations are converged using the VASP code with general gradient approximations (GGA) and PBE functionals. To create a (111) oriented interface as a commensurate length cell requires a 6.1% lattice mismatch to be

overcome. In this case we strain the Fe₃O₄ to the STO (to model the STO as a substrate). Figure 68 shows the effect this strain has upon the band structure of bulk Fe₃O₄. We see a reduction in the spin polarisation at the Fermi level as the majority band d-states below the Fermi level in the unstrained case begin to move higher in energy. We also observe general band broadening. These effects of strain will not be as significant in the deposited layer as the Fe₃O₄ film has relieved strain through misfit dislocations at the interface so the deposited film will not be as physically strained as we require for a commensurate cell for these calculations.

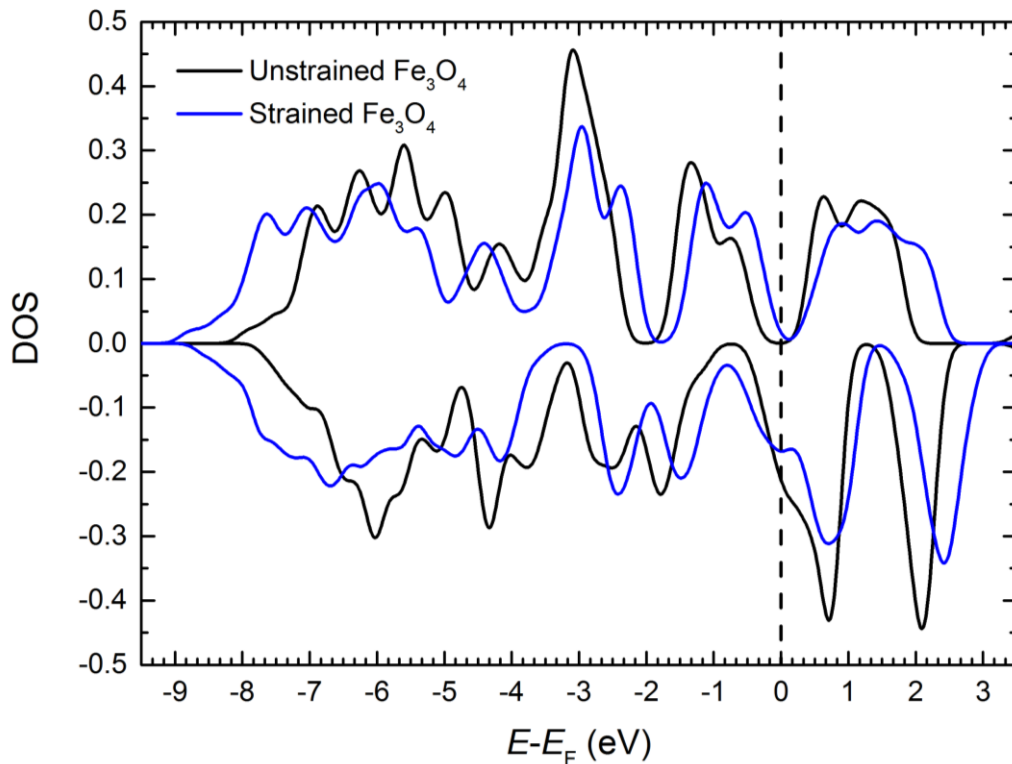


Figure 68: Calculated electronic density of states of a bulk Fe₃O₄ supercell (black) and a bulk Fe₃O₄ supercell that has been compressively strained by 6.1% in the (111) plane.

This interface structure can be related to the surface preparation of the STO substrate. The Ti termination is expected to be prevalent due to the surface pre-treatment of the STO substrate in buffered NH₄F-HF solution which has previously been shown to leave a Ti surface termination on the (111) plane [215]. It is interesting to note that the (111) surface reconstruction of Fe₃O₄ is terminated by 1/3 atomic layer in tetrahedral A-position of Fe [10, 81, 82, 197]. These findings give us opportunity to compare the effect of surface vs interface when the structures are relatively similar with respect to the magnetite film.

In order to determine the electronic structure of the ...3Fe_B/4O/Fe_A-Ti/SrO₃/Ti... interface we performed further first-principles electronic calculations. The spin resolved layer-by-layer density of states (SDOS) of the interface is shown in Figure 69. Partial SDOS are calculated by projecting onto atoms within specific regions in the supercell as indicated by the labels *i-vi* in Figure 69b. These structural regions represent complete formula units of the respective materials, i.e. the upper black plots, (*i* and *ii*) represent Fe₃O₄ blocks away from the interface and the lower red plots (*iii-vi*) represent SrTiO₃ layers. Aside from the two DOS projections on either side of the interface (*ii* and *iii*) the non-interfacial projections show a rapid return to bulk-like electronic structure in both Fe₃O₄ and STO, suggesting interfacial effects are confined to the interfacial region. By analysing the SDOS in Figure 69a we observe the band alignment across the interface puts the Fermi level at the very bottom of the STO conduction band. This property may allow efficient spin diffusion into the conducting states of the substrate. We have also observed that the band alignment in other, hypothetical, sharp interfaces with different atomic structure results in different band alignment *i.e.* a Fermi level positioned in the middle of the STO gap. In addition the SDOS show that very near the interface (~ 6 layers) the band gap is closed and a small number of spin-up density states are present in the Fe₃O₄ structure. This effectively reduces the spin-polarisation at the Fermi level at the interface to values of approximately 66%. However, 6 layers away from the interface, magnetite half-metallicity is restored. Finally we note that swapping of the interfacial Fe and Ti sites is hugely energetically unfavourable (3.7 eV), confirming the stability of the Fe-Ti interface structure.

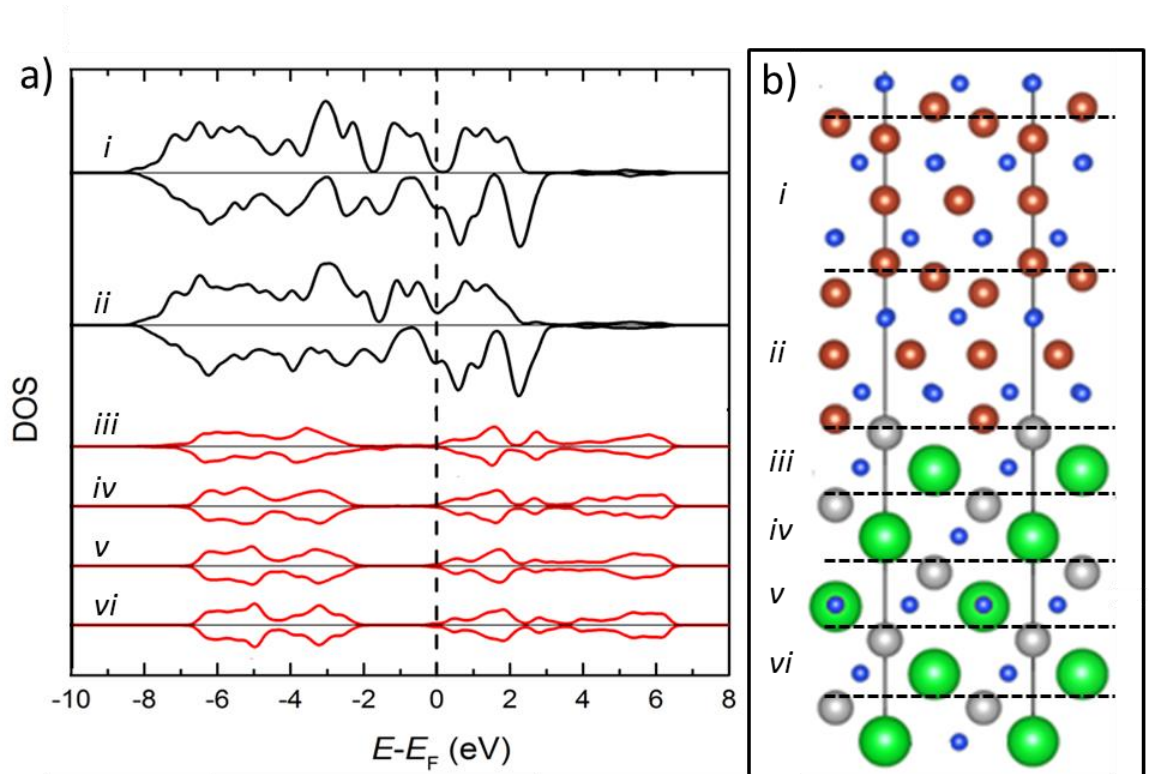


Figure 69: Local spin resolved electronic structure at the ...3Fe_B/4O/Fe_A-Ti/SrO₃/Ti... interface. a) Shows the spin resolved local density of states at the interface. The presented SDOS is projected for the six structural blocks shown in (b). Section *i* and *ii* represent the states from six atomic planes of Fe₃O₄ which each form a structural and chemical repeat unit of ...Fe_B/Fe_A/4O/3Fe_B/4O/Fe_A... Sections *iii* to *vi* each contain a bilayer of STO of ...Ti/SrO₃... Section *ii* and *iii* form the atomic interface between the film and substrate.

7.4 Conclusions

Understanding the electronic and the atomic/chemical structure of the spinel/perovskite interface is an important step in creating multifunctional devices, due to the rich functional properties of materials that crystallize into these two structures. In this work on the Fe₃O₄(111)/STO(111) model system, we have demonstrated that atomically sharp spinel-perovskite heterojunctions are feasible. A STEM/EELS atomic study of the Fe₃O₄/STO interface has shown that the interface is determined by tetrahedral Fe and Ti atomic planes. This particular atomic configuration retains the negative spin polarisation of the magnetite, though at the interface layer is reduced by $\sim 1/3$. Recovery of the strained-bulk like electronic structure of magnetite has been calculated to occur within one unit cell of the interface. This result demonstrates that the experimentally realised Fe₃O₄(111)/STO(111) interface can be used as a platform for studying spin injection from half metals into semiconducting materials. Furthermore, the chemically layered polar nature of this junction may allow interface engineering of different atomic terminations

giving rise to unique electronic properties of interest for applications and fundamental studies. First principle calculations suggest the electronic properties of the Fe₃O₄/STO(111) interface are very sensitive to atomic interface plane terminations. Hence it provides a platform for band engineering and allows the creation of interface electronic structure, which could be useful for studying fundamental properties such as spin injections and tunnelling in model devices.

Chapter 8. Conclusions and Future Work

In this work it has been shown that antiphase domain boundaries (APBs) are present in molecular beam epitaxy (MBE) grown films of $\text{Fe}_3\text{O}_4/\text{MgO}(111)$ and $\text{Fe}_3\text{O}_4/\text{MgAl}_2\text{O}_4(111)$ and in both cases these defects have a significant impact on the overall properties of the grown film as a result of strongly antiferromagnetic 180° Fe-O-Fe bonds at these defect structures. Although the formation mechanisms and the resultant defect structures in these cases are significantly altered the overall functional properties of APB defects and films are broadly equivalent.

Furthermore, we have shown that APB defects in films cannot be easily identified by macroscopic crystallography techniques or determined by spectroscopy techniques. This demonstrates the necessity of atomically resolved analysis when studying grown films and functional interfaces where atomically sharp defects can play a large role in determining overall properties.

An extended analysis of the structures which create APB defects and their properties suggest all APB defects are likely to be persistently antiferromagnetic and therefore any defects of this type are likely to reduce overall spin polarisation and magnetotransport properties when used in a device structure.

The significant role that APB defects play in determining the magneto transport and magnetic response of the film make it essential to control and minimise these defects if we wish to realise the valuable bulk properties of Fe_3O_4 which lead us to study this material for spintronic device applications. Since the MgAl_2O_4 substrate shares the same spinel structure as the grown film yet APB defects still form it appears that MBE growth by itself will not be a suitable method for growing high quality bulk like material.

To produce bulk-like Fe_3O_4 thin films we utilise pulsed laser deposition (PLD) techniques with high temperature CO/CO_2 post annealing to rectify film quality and stoichiometry. This approach has demonstrated the ability to remove interface phase segregation and defect structures such as APBs, hence, providing a route to bulk-like

Fe_3O_4 properties in thin film media. Following this method we have shown that single crystal epitaxial films can be grown on the heavily mismatched YSZ(111) substrate.

Finally we demonstrate a fully epitaxial spinel-perovskite heterostructure with an atomically sharp interface. These findings could provide a way for developing multifunctional oxide/oxide heterostructures with the possibility of interface engineering in order to create new interface driven functionality.

8.1 Future Work

Having produced atomically sharp spinel/perovskite interfaces with fully realised Fe_3O_4 properties we now need to produce device structures using this interface to test the spin polarisation and spin tunnelling at this interface. This would also involve studying more perovskite materials which are well known for their rich physical properties including semiconductors, superconductors, thermoelectric materials and insulators allowing a wide range of functional devices to be created based on this model interface.

Also of significant interest is to attempt to engineer the spinel/perovskite interface to make the Fe_3O_4 structure grow from different interfacial planes which will give different band alignments and different spin polarisation at the interface.

Finding methods to control the spinel/perovskite interface are of significant interest as these properties are once again likely to be transferable to different substrate materials.

Finally, achieving defect free growth with MBE methods is a significant prize to be achieved. Whether this can be produce by combining high quality MBE growth with the post-annealing techniques identified in the PLD growth method would be of significant interest. If these techniques can be developed to be consistent and reliable the potential for Fe_3O_4 based spintronics devices should be of significant interest for developing magnetic random access memory devices which can operate at room temperature and for understanding the physics of half-metallic materials.

Appendix A: List of Publications

K. P. McKenna, F. Hofer, **D. Gilks**, V. K. Lazarov, C. Chen, Z. Wang and Y. Ikuhara, **Atomic-scale structure and properties of highly stable antiphase boundary defects in Fe_3O_4** , *Nature Communications*, **5** 5740 (2014)

<http://www.nature.com/ncomms/2014/141210/ncomms6740/abs/ncomms6740.html>

L. Lari, K. Yoshida, P. L. Galindo, J. Sato, J. Sizeland, **D. Gilks**, G. M. Uddin, Z. Nedelkoski, P. J. Hasnip, A. Hirohata, M. Oogane, Y. Ando and V. K. Lazarov, **Correlations between atomic structure and giant Magnetoresistance ratio in $Co_2(Fe,Mn)Si$ spin valves**, *J. Phys. D: Appl. Phys.*, **47** 322003 (2014)

<http://iopscience.iop.org/0022-3727/47/32/322003/>

T. Moorsom, M. Wheeler, M. T. Khan, F. A. Ma'Mari, G. Burnell, B. J. Hickey and V. K. Lazarov, **D. Gilks** and O. Cespedes, **Effects of spin doping and spin injection in the luminescence and vibrational spectrum of C_{60}** , *Appl. Phys. Lett.*, **105** 022408 (2014)

<http://scitation.aip.org/content/aip/journal/apl/105/2/10.1063/1.4885336>

T. Moorsom, M. Wheeler, M. T. Khan, F. A. Ma'Mari, C. Kinane, S. Langridge, D. Ciudad, A. Bedoya-Pinto, L. Hueso, G. Teobaldi, V. K. Lazarov, **D. Gilks**, G. Burnell, B. J. Hickey and O. Cespedes, **Spin Polarised electron transfer in ferromagnet/ C_{60} interfaces**, *Phys. Rev. B*, **90**, 125311 (2014)

<http://journals.aps.org/prb/abstract/10.1103/PhysRevB.90.125311>

P. J. Hasnip, C. H. Loach, J. H. Smith, M. I. J. Probert, **D. Gilks**, J. Sizeland, K. Yoshida, M. Oogane, A. Hirohata and V. K. Lazarov, **B2 Atomic Disorder in $Co_2Fe_xMn_{1-x}Si$ Heusler Alloys**, *J. Magn. Soc. Jpn.*, **38** 50-55 (2014)

https://www.jstage.jst.go.jp/article/msjmag/38/2-2/38_1402R010/article

P. J. Hasnip, C. H. Loach, J. H. Smith, M. I. J. Probert, **D. Gilks**, J. Sizeland, L. Lari, J. Sagar, K. Yoshida, M. Oogane, A. Hirohata and V. K. Lazarov, **The Effect of Cobalt-**

Sublattice Disorder on Spin Polarisation in $\text{Co}_2\text{Fe}_x\text{Mn}_{1-x}\text{Si}$ Heusler Alloys, *Materials*, **7** 1473-1482 (2014)

<http://www.mdpi.com/1996-1944/7/3/1473>

Y. Liu, Y. Y. Li, S. Rajput, **D. Gilks**, L. Lari, P. L. Galindo, M. Weinert, V. K. Lazarov and L. Li, **Tuning Dirac states by strain in the topological insulator Bi_2Se_3** , *Nature Physics*, **10** 294-299 (2014)

<http://www.nature.com/nphys/journal/v10/n4/full/nphys2898.html>

D. Gilks, L. Lari, J. Naughton, O. Cespedes, Z. Cai, A. Gerber, S. M. Thompson, K. Ziemer and V. K. Lazarov, **Origin of anomalous magnetite properties in crystallographic matched heterostructures: $\text{Fe}_3\text{O}_4(111)/\text{MgAl}_2\text{O}_4(111)$** , *J. Phys.: Condens. Matter*, **25** 485004 (2013)

<http://iopscience.iop.org/0953-8984/25/48/485004/>

Y. Liu, Y. Y. Li, **D. Gilks**, V. K. Lazarov, M. Weinert and L. Li, **Charging Dirac States at Antiphase Domain Boundaries in the Three-Dimensional Topological Insulator Bi_2Se_3** , *Phys. Rev. Lett.*, **110** 186804 (2013)

<http://journals.aps.org/prl/abstract/10.1103/PhysRevLett.110.186804>

A. Pratt, M. Kurahashi, X. Sun, **D. Gilks** and Y. Yamauchi, **Direct observation of a positive spin polarization at the (111) surface of magnetite**, *Phys. Rev. B*, **85** 180409(R) (2012)

<http://journals.aps.org/prb/abstract/10.1103/PhysRevB.85.180409>

D. Gilks, L. Lari, K. Matsuzaki, R. Evans, K. McKenna, T. Susaki and V. K. Lazarov, **A STEM study of twin defects in $\text{Fe}_3\text{O}_4(111)/\text{YZO}(111)$** , *J. Phys.: Conf. Ser.*, **522** 012036 (2014)

<http://iopscience.iop.org/1742-6596/522/1/012036>

L. Lari, I. Wright, D. Pingstone, J. Steward, **D. Gilks** and V. K. Lazarov, **An in-house developed annular bright field detection system**, *J. Phys.: Conf. Ser.*, **522** 012016 (2014)

<http://iopscience.iop.org/1742-6596/522/1/012016>

D. Gilks, L. Lari, K. Matsuzaki, H. Hosono, T. Susaki and V. K. Lazarov, **Structural study of $\text{Fe}_3\text{O}_4(111)$ thin films with bulk like magnetic and magnetotransport behaviour**, *J. Appl. Phys.*, **115** 17C107 (2014)

<http://scitation.aip.org/content/aip/journal/jap/115/17/10.1063/1.4862524>

D. Gilks, L. Lari, Z. Cai, O. Cespedes, A. Gerber, S. Thompson, K. Ziemer and V. K. Lazarov, **Magnetism and magnetotransport in symmetry match spinels: $\text{Fe}_3\text{O}_4/\text{MgAl}_2\text{O}_4$** , *J. Appl. Phys.*, **113** 17B107 (2013)

<http://scitation.aip.org/content/aip/journal/jap/113/17/10.1063/1.4800690?ver=pdfcov>

Appendix B: List of Presentations

“Super-Resolution applied to Magnetite boundaries images”, (Poster), G. Bárcena, M. Guerrero, E. Guerrero, D. Kepaptsoglou, **D. Gilks**, L. Lari, V. K. Lazarov and P. L. Galindo. Presented at the International Microscopy Congress 2014, Prague, Sept. 2014

“STEM and EELS study of Graphene/Bi₂Se₃ Interface”, D. Kepaptsoglou, **D. Gilks**, L. Lari, Q. Ramasse, M. Weinert, L. Li and V. K. Lazarov. Presented at the International Microscopy Congress 2014, Prague, Sept. 2014

“Study of structural defects in Fe₃O₄ thin films: atomic scale correlation between imaging and spin calculations”, (Poster), **D. Gilks**, R. Evans, K. Matsuzaki, K. McKenna, L. Lari, T. Susaki and V. K. Lazarov. Presented at the International Microscopy Congress 2014, Prague, Sept. 2014

“Atomic and electronic structure of Fe₃O₄ oxide heterostructures”, (Poster), **D. Gilks**, L. Lari, K. Matsuzaki, K. McKenna, L. Lari, T. Susaki and V. K. Lazarov. Presented at the International Microscopy Congress 2014, Prague, Sept. 2014

“Atomic level in-situ ETEM gas reaction study of NiO polar and neutral surfaces”, (Poster), L. Lari, K. Yoshida, K. Matsuzaki, **D. Gilks**, T. Susaki and V. K. Lazarov. Presented at the Microscience Microscopy Congress 2014, Jun/Jul 2014

“HAADF image enhancement using Super-Resolution techniques”, (Poster), G. Bárcena, M. Guerrero, E. Guerrero, P. L. Galindo, D. Gilks, L. Lari, D. Kepaptsoglou and V. K. Lazarov. Presented at the Microscience Microscopy Congress 2014, Jun/Jul 2014

“Fe₃O₄ thin films with bulk like magnetic and magnetotransport behaviour” **D. Gilks**, K. Matsuzaki, J. Sizeland, L. Lari, H. Hosono, T. Susaki and V. K. Lazarov. Presented at the 58th Annual Conference on Magnetism and Magnetic Materials, Denver CO, Nov. 2013

“Atomic study of $\text{Co}_2\text{Fe}_x\text{Mn}_{1-x}\text{Si}/\text{Ag}$ interface” P. J. Hasnip, L. Lari, K. Yoshida, **D. Gilks**, M. Oogane, Y. Ando, A. Hirohata and V. K. Lazarov, Presented at the *58th Annual Conference on Magnetism and Magnetic Materials*, Denver CO, Nov. 2013

“Infrared Remote Sensing of Giant Magnetoresistance: Experimental Confirmation of a Strong Correlation Between the Magnetorefractive Effect and Giant Magnetoresistance in the Far Infrared” C. Kelley, S. M. Thompson, **D. Gilks**, S. W. Poon, S. LeFrançois, P. Dumas and J. Matthew. Presented at the *58th Annual Conference on Magnetism and Magnetic Materials*, Denver CO, Nov. 2013

“Mapping Spatial Variations in Iron Oxide Phases in Magnetite Thin Films Using Infrared Reflectance Microspectroscopy” C. Kelley, S. M. Thompson, **D. Gilks**, S. W. Poon, V. K. Lazarov, S. LeFrançois, P. Dumas and J. Matthew. Presented at the *58th Annual Conference on Magnetism and Magnetic Materials*, Denver CO, Nov. 2013

“A STEM study of Twin defects in $\text{Fe}_3\text{O}_4(111)/\text{YZO}(111)$ ” **D. Gilks**, L. Lari, K. Matsuzaki, R. Evans, K. McKenna, T. Susaki and V. K. Lazarov. presented at *EMAG2013*, York, UK. Sept. 2013

“NiO(111)/MgO(111) polar oxide interface and surface analysis by STEM/EELS” (Poster) L. Lari, K. Yoshida, K. Saito, **D. Gilks**, P. J. Hasnip, K. Matsuzaki, T. Susaki and V. K. Lazarov. Presented at *EMAG2013*, York, UK. Sept. 2013

“Atomic study of the $\text{Fe}_3\text{O}_4(111)/\text{SrTiO}_3(111)$ interface” (Poster) **D. Gilks**, L. Lari, K. Matsuzaki, T. Susaki and V. K. Lazarov. Presented at *EMAG2013*, York, UK. Sept. 2013

“Magnetism and Magnetotransport in symmetry matched spinels: $\text{Fe}_3\text{O}_4/\text{MgAl}_2\text{O}_4$ ” **D. Gilks**, J. Naughton, L. Lari, Z. Cai, A. Gerber, S. M. Thompson, K. Ziemer and V. K. Lazarov. Presented at the *12th Joint MMM/Intermag Conference*, Chicago II, Jan. 2013

“Structural and magnetic properties of Fe_3O_4 prepared by post-oxidation of $\alpha\text{-Fe}$ thin films” (Poster) J. Sizeland, **D. Gilks**, S. W. Poon, C. Kelley, L. Lari, O. Cespedes, S. M. Thompson and V. K. Lazarov. Presented at the *12th Joint MMM/Intermag Conference*, Chicago II, Jan. 2013

“Structural study of post-oxidised Fe thin films” (Poster) D. Gilks, C. Kelley, S. W. Poon, J. Sizeland, L. Lari, S. M. Thompson and V. K. Lazarov. Presented at EMC2012, Manchester, UK. Sept. 2012

“On the origin of the anti-phase domain boundaries in crystallographically matched systems: $Fe_3O_4/MgAl_2O_4(111)$ ” D. Gilks, L. Lari, C. Kelley, O. Cespedes, Z. Cai, S. M. Thompson, K. Ziemer and V. K. Lazarov. Presented at CMD-24, ECOSS-29, ECSCD-11, CMMP-12, Edinburgh, Sept. 2012

“Epitaxial Bi_2Se_3 on Graphene/SiC(0001): Structure, growth and defects” V. K. Lazarov, Y. Liu, D. Gilks, M. Weinert and L. Li. Presented at CMD-24, ECOSS-29, ECSCD-11, CMMP-12, Edinburgh, Sept. 2012

“Half-metal Heuslers: order/disorder effects on spin polarisation in films and interfaces” V. K. Lazarov, P. J. Hasnip, J. Smith, J. Sizeland, J. Sato, M. Oogane, D. Gilks, A. Hirohata and Y. Ando. Presented at CMD-24, ECOSS-29, ECSCD-11, CMMP-12, Edinburgh, Sept. 2012

Symbols

a_0	Lattice constant
A_n	n^{th} order astigmatism
B	Magnetic field
c	Speed of light
C_c	Chromatic aberration
C_s/C_3	Spherical aberration
γ	Gamma factor
$-e$	Charge on an electron
E	Electric field
E_{core}	Core level energy relative to vacuum
E_1, E_2	Electron energy levels relative to vacuum
e_g	σ symmetry d-shell orbitals
E_k	Kinetic energy
eV	Electron Volts
F	Force (Lorentz)
$f_i(\theta)$	Atomic scattering form factor
ϕ_{Fe-Fe}	Angle between neighbouring Fe_B spins
h	Planck constant
H	Applied magnetic field
\mathcal{H}	Hamiltonian
\mathcal{H}_{ani}	Anisotropy Hamiltonian
\mathcal{H}_{app}	Applied field Hamiltonian
\mathcal{H}_{exc}	Heisenberg exchange Hamiltonian
J_{AA}	Exchange constant between bulk Fe_A sites
J_{AB}	Exchange constant between bulk Fe_B and Fe_A sites
J_{BB}	Exchange constant between bulk Fe_B sites
J_{ij}	Exchange constant between the i^{th} and j^{th} spin
K	Kelvin
K_v	Cubic magnetocrystalline anisotropy
λ_{rel}	Wavelength

λ_0	Classical de Broglie wavelength
m_{rel}	Relativistic mass of electron
m_0	Rest mass of the electron
$P(\mathbf{k})$	Propagation operator
p_{rel}	Relativistic momentum (of an electron)
p_0	Classical momentum (of electron)
ψ	Wavefunction
$\Psi_i(\mathbf{k})$	Input electron wavefunction in k-space
q	charge
$Q(\mathbf{k})$	Projected potential phase grating
$R(0)$	Resistance in zero applied field
$R(H)$	Resistance in applied field, H
\mathbf{S}_i	Spin on the i^{th} atomic site
σ	Conductivity
t	Hopping integral
t_0	Maximum, aligned hopping integral
t_{2g}	π symmetry d-shell orbitals
T_c	Curie Temperature
μ_B	Bohr Magnetron
v	Velocity
V	Voltage

Abbreviations

AES	Auger electron spectroscopy
AFM	Anti-ferromagnetic
APB	Anti-phase domain boundary
BF-TEM	Bright field TEM
CCD	Charge-coupled device
CEOS	Corrected electron optical systems (GmbH)
CMOS	Complementary metal oxide semiconductor
DF-TEM	Dark field TEM
DFT	Density functional theory
DOS	Density of states
EELS	Electron energy loss spectroscopy
EF-TEM	Energy filtered TEM
FCC	Face centred cubic (crystal structure)
FEG	Field emission gun
FFT	Fast Fourier transform
FIB	Focussed ion beam
FM	Ferromagnetic
FWHM	Full width (at) half maximum
GGA	Generalised gradient approximation
GMR	Giant magnetoresistance
GULP	Generalised utility lattice program
HAADF-STEM	High angle annular dark field STEM
HRTEM	High resolution transmission electron microscopy
IPA	Isopropanol
JEMS	Java electron microscope simulator
JEOL	Japanese electron optics Ltd.
LDA	Local density approximation
LDOS	Local density of states
LEED	Low energy electron diffraction
LSDA	Local spin density approximation
MAADF-STEM	Medium angle annular dark field STEM

MBE	Molecular beam epitaxy
MH	Magnetisation as a function of applied field (hysteresis)
MOSFET	Metal oxide semiconductor field effect transistor
MR	Magnetoresistance
MRAM	Magnetic random access memory
MTJ	Magnetic tunnel junction
OA	Optical axis
PAW	Projector augmented wave
PBE	Perdew-Burke-Ernzerhof
PIPS	Precision ion polishing system
PLD	Pulsed laser deposition
PPMS	Physical properties measurement system
QSTEM	Quantitative STEM
RF	Radio frequency
RHEED	Reflection high energy electron diffraction
SAD	Selected area diffraction
SDOS	Spin density of states
SDSD	Statistically determined spatial drift [145]
SEI	Super-exchange interactions
SEM	Scanning electron microscope
SP-MDS	Spin polarised metastable de-excitation spectroscopy
STEM	Scanning transmission electron microscope
STEM-EELS	See STEM and EELS
STM	Scanning tunnelling microscopy
STO	Strontium titanium oxide (SrTiO_3)
TDS	Thermal diffuse scattering
TEM	Transmission electron microscope
TMR	Tunnelling magnetoresistance
UHV	Ultra high vacuum
VSM	Vibrating sample magnetometer
WPOA	Weak phase object approximation
XPS	X-ray photoelectron spectroscopy
XRD	X-ray diffraction
YSZ	Ytria-stabilised zirconia (Y-ZrO_2)

References

1. Hurlbut, C.S., *Dana's Minerals and How to Study Them (After Edward Salisbury Dana)*. 1998: John Wiley & Sons.
2. Murad, E. and Cashion, J., *Iron Oxides*, in *Mössbauer Spectroscopy of Environmental Materials and Their Industrial Utilization*. 2004, Springer US. p. 159-188.
3. Meng, J., et al., *Synthesis and characterization of magnetic nanometer pigment Fe₃O₄*. *Dyes and Pigments*, 2005. **66**(2): p. 109-113.
4. Pinna, F., et al., *TPR and XRD study of ammonia synthesis catalysts*. *Applied Catalysis A: General*, 1997. **149**(2): p. 341-351.
5. Roca, A.G., et al., *An Analysis of Minor Hysteresis Loops of Nanoparticles for Hyperthermia*. *Magnetics*, IEEE Transactions on, 2011. **47**(10): p. 2878-2881.
6. Roca, A.G., et al., *Progress in the preparation of magnetic nanoparticles for applications in biomedicine*. *Journal of Physics D: Applied Physics*, 2009. **42**(22): p. 224002.
7. Na, H.B., Song, I.C., and Hyeon, T., *Inorganic Nanoparticles for MRI Contrast Agents*. *Advanced Materials*, 2009. **21**(21): p. 2133-2148.
8. Dorniani, D., et al., *Preparation of Fe₃O₄ magnetic nanoparticles coated with gallic acid for drug delivery*. *International Journal of Nanomedicine*, 2012. **7**: p. 5745-5756.
9. Fonin, M., et al., *Magnetite: a search for the half-metallic state*. *Journal of Physics: Condensed Matter*, 2007. **19**(31): p. 315217.
10. Pratt, A., et al., *Direct observation of a positive spin polarization at the (111) surface of magnetite*. *Physical Review B*, 2012. **85**(18): p. 180409.
11. Kado, T., *Large room-temperature inverse magnetoresistance in tunnel junctions with a Fe₃O₄ electrode*. *Applied Physics Letters*, 2008. **92**(9): p. 092502-3.
12. Alldredge, L.M.B., et al., *Spin-polarized conduction in oxide magnetic tunnel junctions with magnetic and nonmagnetic insulating barrier layers*. *Applied Physics Letters*, 2006. **89**(18): p. 182504-3.
13. Kado, T., Saito, H., and Ando, K., *Room-temperature magnetoresistance in magnetic tunnel junctions with Fe₃O₄ electrode*. *Journal of Applied Physics*, 2007. **101**(9): p. 09J511-3.
14. Bataille, A.M., et al., *Crystalline gamma-Al₂O₃ barrier for magnetite-based magnetic tunnel junctions*. *Applied Physics Letters*, 2005. **86**(1): p. 012509-3.
15. Hu, G. and Suzuki, Y., *Negative Spin Polarization of Fe₃O₄ in Magnetite/Manganite-Based Junctions*. *Physical Review Letters*, 2002. **89**(27): p. 276601.
16. Alexe, M., et al., *Ferroelectric Switching in Multiferroic Magnetite (Fe₃O₄) Thin Films*. *Advanced Materials*, 2009. **21**(44): p. 4452-4455.
17. Seneor, P., et al., *Large magnetoresistance in tunnel junctions with an iron oxide electrode*. *Applied Physics Letters*, 1999. **74**(26): p. 4017-4019.
18. Yanase, A. and Siratori, K., *Band-Structure in the High-Temperature Phase of Fe₃O₄*. *Journal of the Physical Society of Japan*, 1984. **53**(1): p. 312-317.
19. Yanase, A. and Hamada, N., *Electronic Structure in High Temperature Phase of Fe₃O₄*. *Journal of the Physical Society of Japan*, 1999. **68**(5): p. 1607-1613.
20. Zhang, Z. and Satpathy, S., *Electron states, magnetism, and the Verwey transition in magnetite*. *Physical Review B*, 1991. **44**(24): p. 13319-13331.

21. Verwey, E.J., *Electronic Conduction of Magnetite (Fe_3O_4) and its Transition Point at Low Temperatures*. *Nature*, 1939. **144**: p. 327-328.
22. Verwey, E.J.W. and Heilmann, E.L., *Physical Properties and Cation Arrangement of Oxides with Spinel Structures I. Cation Arrangement in Spinel*. *The Journal of Chemical Physics*, 1947. **15**(4): p. 174-180.
23. Verwey, E.J., Haayman, P.W., and Romeijn, F.C., *Physical Properties and Cation Arrangement of Oxides with Spinel Structures II. Electronic Conductivity*. *The Journal of Chemical Physics*, 1947. **15**(4): p. 181-187.
24. Wright, J.P., Attfield, J.P., and Radaelli, P.G., *Long Range Charge Ordering in Magnetite Below the Verwey Transition*. *Physical Review Letters*, 2001. **87**(26): p. 266401.
25. Eerenstein, W., et al., *Spin-Polarized Transport across Sharp Antiferromagnetic Boundaries*. *Physical Review Letters*, 2002. **88**(24): p. 247204.
26. Uhl, M. and Siberchicot, B., *A first-principles study of exchange integrals in magnetite*. *Journal of Physics: Condensed Matter*, 1995. **7**(22): p. 4227.
27. Mazo-Zuluaga, J., Restrepo, J., and Mejía-López, J., *Surface anisotropy of a Fe_3O_4 nanoparticle: A simulation approach*. *Physica B: Condensed Matter*, 2007. **398**(2): p. 187-190.
28. Katsnelson, M.I., et al., *Half-metallic ferromagnets: From band structure to many-body effects*. *Reviews of Modern Physics*, 2008. **80**(2): p. 315-378.
29. Ramos, A.V., et al., *Magnetotransport properties of Fe_3O_4 epitaxial thin films: Thickness effects driven by antiphase boundaries*. *Journal of Applied Physics*, 2006. **100**(10): p. 103902.
30. Ziese, M. and Blythe, H.J., *Magnetoresistance of magnetite*. *Journal of Physics: Condensed Matter*, 2000. **12**(1): p. 13.
31. Margulies, D.T., et al., *Origin of the Anomalous Magnetic Behavior in Single Crystal Fe_3O_4 Films*. *Physical Review Letters*, 1997. **79**(25): p. 5162-5165.
32. Coey, J.M.D., et al., *Magnetoresistance of magnetite*. *Applied Physics Letters*, 1998. **72**(6): p. 734-736.
33. van der Zaag, P.J., et al., *On the construction of an Fe_3O_4 -based all-oxide spin valve*. *Journal of Magnetism and Magnetic Materials*, 2000. **211**(1-3): p. 301-308.
34. Press, M.R. and Ellis, D.E., *Defect clusters in wüstite Fe_{1-x}O* . *Physical Review B*, 1987. **35**(9): p. 4438-4454.
35. Roth, W.L., *Defects in the crystal and magnetic structures of ferrous oxide*. *Acta Crystallographica*, 1960. **13**(2): p. 140-149.
36. de Castro, A.R.B., et al., *Magnetic circular dichroism in nanostructured hematite*. *Journal of Magnetism and Magnetic Materials*, 2001. **231**(2-3): p. 287-290.
37. Gao, Y., et al., *Growth, structure, and magnetic properties of $\gamma\text{-Fe}_2\text{O}_3$ epitaxial films on MgO*. *Journal of Applied Physics*, 1997. **81**(7): p. 3253-3256.
38. Frandsen, C., et al., *Interparticle interactions in composites of nanoparticles of ferrimagnetic $\gamma\text{-Fe}_2\text{O}_3$ and antiferromagnetic CoO, NiO materials*. *Physical Review B*, 2004. **70**(13): p. 134416.
39. Ricardo, G.-C., et al., *Vacancy ordering and electronic structure of $\gamma\text{-Fe}_2\text{O}_3$ (maghemite): a theoretical investigation*. *Journal of Physics: Condensed Matter*, 2010. **22**(25): p. 255401.
40. Celotto, S., Eerenstein, W., and Hibma, T., *Characterization of anti-phase boundaries in epitaxial magnetite films*. *The European Physical Journal B - Condensed Matter and Complex Systems*, 2003. **36**(2): p. 271-279.
41. Cox, P.A., *Transition Metal Oxides: An Introduction to Their Electronic Structure and Properties*. 2010: OUP Oxford.
42. Jette, E.R. and Foote, F., *An X-Ray Study of the Wüstite (FeO) Solid Solutions*. *The Journal of Chemical Physics*, 1933. **1**(1): p. 29-36.
43. Roth, W.L., *Magnetic Structures of MnO, FeO, CoO, and NiO*. *Physical Review*, 1958. **110**(6): p. 1333-1341.

44. Anisimov, V.I., Korotin, M.A., and Kurmaev, E.Z., *Band-structure description of Mott insulators (NiO, MnO, FeO, CoO)*. Journal of Physics: Condensed Matter, 1990. **2**(17): p. 3973.
45. Fleet, M., *The structure of magnetite*. Acta Crystallographica Section B, 1981. **37**(4): p. 917-920.
46. Bragg, W.L., *The Structure of Magnetite and the Spinel*. Nature, 1915. **95**: p. 561.
47. Bragg, W.H., *XXX. The structure of the spinel group of crystals*. Philosophical Magazine Series 6, 1915. **30**(176): p. 305-315.
48. Sawatzky, G.A., Coey, J.M.D., and Morrish, A.H., *Mössbauer Study of Electron Hopping in the Octahedral Sites of Fe₃O₄*. Journal of Applied Physics, 1969. **40**(3): p. 1402-1403.
49. Hund, F., *Zur Deutung verwickelter Spektren, insbesondere der Elemente Scandium bis Nickel*. Zeitschrift für Physik, 1925. **33**(1): p. 345-371.
50. Hund, F., *Zur Deutung verwickelter Spektren. II*. Zeitschrift für Physik, 1925. **34**(1): p. 296-308.
51. Shim, I. and Dahl, J., *A new interpretation of Hund's first rule*. Theoretica chimica acta, 1978. **48**(2): p. 165-174.
52. Huang, D.J., et al., *Spin and Orbital Magnetic Moments of Fe₃O₄*. Physical Review Letters, 2004. **93**(7): p. 077204.
53. Landolt, H. and Hellwege, K.-H., *Magnetic and other properties of oxides and related compounds*. Vol. 4. 1970: Springer.
54. Margulies, D.T., et al., *Anomalous moment and anisotropy behavior in Fe₃O₄ films*. Physical Review B, 1996. **53**(14): p. 9175-9187.
55. Ihle, D. and Lorenz, B., *Electron correlation theory of Fe₃O₄*. Philosophical Magazine Part B, 1980. **42**(3): p. 337-347.
56. Ihle, D. and Lorenz, B., *Small-polaron band versus hopping conduction in Fe₃O₄*. Journal of Physics C: Solid State Physics, 1985. **18**(21): p. L647.
57. Ihle, D. and Lorenz, B., *Small-polaron conduction and short-range order in Fe₃O₄*. Journal of Physics C: Solid State Physics, 1986. **19**(26): p. 5239.
58. Friedrich, W., *The Verwey transition - a topical review*. Journal of Physics: Condensed Matter, 2002. **14**(12): p. R285.
59. Gilks, D., et al., *Structural study of Fe₃O₄(111) thin films with bulk like magnetic and magnetotransport behaviour*. Journal of Applied Physics, 2014. **115**(17): p. 17C107.
60. Goodenough, J.B., *Magnetism and the chemical bond*. Vol. 98. 1963: Interscience publishers New York.
61. Goodenough, J.B. and Loeb, A.L., *Theory of Ionic Ordering, Crystal Distortion, and Magnetic Exchange Due to Covalent Forces in Spinel*. Physical Review, 1955. **98**(2): p. 391-408.
62. Goodenough, J.B., *Theory of the Role of Covalence in the Perovskite-Type Manganites [La, M(II)]MnO₃*. Physical Review, 1955. **100**(2): p. 564-573.
63. Wickham, D.G. and Goodenough, J.B., *Suggestion Concerning Magnetic Interactions in Spinel*. Physical Review, 1959. **115**(5): p. 1156-1158.
64. Kanamori, J., *Superexchange interaction and symmetry properties of electron orbitals*. Journal of Physics and Chemistry of Solids, 1959. **10**(2-3): p. 87-98.
65. Zener, C., *Interaction between the d-Shell in the Transition Metals. II. Ferromagnetic Compounds of Manganese with Perovskite Structure*. Physical Review, 1951. **82**(3): p. 403-405.
66. Anderson, P.W. and Hasegawa, H., *Considerations on Double Exchange*. Physical Review, 1955. **100**(2): p. 675-681.
67. Sawatzky, G.A., Geertsma, W., and Haas, C., *Magnetic interactions and covalency effects in mainly ionic compounds*. Journal of Magnetism and Magnetic Materials, 1976. **3**(1-2): p. 37-45.

68. De Grave, E., et al., *Mössbauer study of the high-temperature phase of Co-substituted magnetites, $\text{Co}_x\text{Fe}_{3-x}\text{O}_4$. I. $x \leq 0.04$* . Physical Review B, 1993. **47**(10): p. 5881-5893.
69. Eerenstein, W., et al., *Magneto-resistance and superparamagnetism in magnetite films on MgO and MgAl_2O_4* . Journal of Magnetism and Magnetic Materials, 2003. **258–259**(0): p. 73-76.
70. Eerenstein, W., et al., *Origin of the increased resistivity in epitaxial Fe_3O_4 films*. Physical Review B, 2002. **66**(20): p. 201101.
71. Moussy, J.B., et al., *Thickness dependence of anomalous magnetic behavior in epitaxial $\text{Fe}_3\text{O}_4(111)$ thin films: Effect of density of antiphase boundaries*. Physical Review B, 2004. **70**(17): p. 174448.
72. McKenna, K.P., et al., *Atomic-scale structure and properties of highly stable antiphase boundary defects in Fe_3O_4* . Nat Commun, 2014. **5**: p. 5740.
73. Luysberg, M., et al., *Strain relaxation in $\text{Fe}_3\text{O}_4/\text{MgAl}_2\text{O}_4$ heterostructures: Mechanism for formation of antiphase boundaries in an epitaxial system with identical symmetries of film and substrate*. Physical Review B, 2009. **80**(2): p. 024111.
74. Gilks, D., et al., *Origin of anomalous magnetite properties in crystallographic matched heterostructures: $\text{Fe}_3\text{O}_4(111)/\text{MgAl}_2\text{O}_4(111)$* . Journal of Physics: Condensed Matter, 2013. **25**(48): p. 485004.
75. Voogt, F.C., et al., *Superparamagnetic behavior of structural domains in epitaxial ultrathin magnetite films*. Physical Review B, 1998. **57**(14): p. R8107-R8110.
76. Hibma, T., et al., *Anti-phase domains and magnetism in epitaxial magnetite layers*. Journal of Applied Physics, 1999. **85**(8): p. 5291-5293.
77. Eerenstein, W., Palstra, T.T.M., and Hibma, T., *Spin-valve behaviour of anti-ferromagnetic boundaries in ultrathin magnetite films*. Thin Solid Films, 2001. **400**(1–2): p. 90-94.
78. Lazarov, V.K., Chambers, S.A., and Gajdardziska-Josifovska, M., *Polar Oxide Interface Stabilization by Formation of Metallic Nanocrystals*. Physical Review Letters, 2003. **90**(21): p. 216108.
79. Harrison, W.A., et al., *Polar heterojunction interfaces*. Physical Review B, 1978. **18**(8): p. 4402-4410.
80. Pentcheva, R. and Pickett, W.E., *Avoiding the Polarization Catastrophe in LaAlO_3 Overlayers on $\text{SrTiO}_3(001)$ through Polar Distortion*. Physical Review Letters, 2009. **102**(10): p. 107602.
81. Grillo, M.E., Finnis, M.W., and Ranke, W., *Surface structure and water adsorption on $\text{Fe}_3\text{O}_4(111)$: Spin-density functional theory and on-site Coulomb interactions*. Physical Review B, 2008. **77**(7): p. 075407.
82. Shimizu, T.K., et al., *Termination and Verwey transition of the (111) surface of magnetite studied by scanning tunneling microscopy and first-principles calculations*. Physical Review B, 2010. **81**(23): p. 235429.
83. Dedkov, Y.S., Rüdiger, U., and Güntherodt, G., *Evidence for the half-metallic ferromagnetic state of Fe_3O_4 by spin-resolved photoelectron spectroscopy*. Physical Review B, 2002. **65**(6): p. 064417.
84. Fonin, M., et al., *Spin-resolved photoelectron spectroscopy of Fe_3O_4 —revisited*. Journal of Physics: Condensed Matter, 2008. **20**(14): p. 142201.
85. Schaller, R.R., *Moore's law: past, present and future*. Spectrum, IEEE, 1997. **34**(6): p. 52-59.
86. Moore, G.E., *Cramming more components onto integrated circuits*. Proceedings of the IEEE, 1998. **86**(1): p. 82-85.
87. Wolf, S.A., et al., *Spintronics: A spin-based electronics vision for the future*. Science, 2001. **294**(5546): p. 1488-1495.
88. Thompson, S.M., *The discovery, development and future of GMR: The Nobel Prize 2007*. Journal of Physics D: Applied Physics, 2008. **41**(9): p. 093001.

89. Uhlenbeck, G.E. and Goudsmit, S., *Spinning electrons and the structure of spectra*. Nature, 1926. **117**: p. 264-265.
90. Uhlenbeck, G. and Goudsmit, S., *Naturwiss.* 13, 953 (1925). Nature, 1926. **117**: p. 264.
91. Pauli, W., Jr., *Zur Quantenmechanik des magnetischen Elektrons*. Zeitschrift für Physik, 1927. **43**(9-10): p. 601-623.
92. Dirac, P.A. *The quantum theory of the electron*. in *Proceedings of the Royal Society of London A: Mathematical, Physical and Engineering Sciences*. 1928. The Royal Society.
93. Dirac, P.A.M. *The quantum theory of the electron. Part II*. in *Proceedings of the Royal Society of London A: Mathematical, Physical and Engineering Sciences*. 1928. The Royal Society.
94. Julliere, M., *Tunneling between ferromagnetic films*. Physics Letters A, 1975. **54**(3): p. 225-226.
95. Miyazaki, T. and Tezuka, N., *Spin polarized tunneling in ferromagnet/insulator/ferromagnet junctions*. Journal of Magnetism and Magnetic Materials, 1995. **151**(3): p. 403-410.
96. Moodera, J.S., et al., *Large Magnetoresistance at Room Temperature in Ferromagnetic Thin Film Tunnel Junctions*. Physical Review Letters, 1995. **74**(16): p. 3273-3276.
97. Ikeda, S., et al., *Tunnel magnetoresistance of 604% at 300K by suppression of Ta diffusion in CoFeBMgO/CoFeB pseudo-spin-valves annealed at high temperature*. Applied Physics Letters, 2008. **93**(8): p. 082508.
98. Binasch, G., et al., *Enhanced magnetoresistance in layered magnetic structures with antiferromagnetic interlayer exchange*. Physical Review B, 1989. **39**(7): p. 4828-4830.
99. Baibich, M.N., et al., *Giant Magnetoresistance of (001)Fe/(001)Cr Magnetic Superlattices*. Physical Review Letters, 1988. **61**(21): p. 2472-2475.
100. Scherzer, O., *Ein Elektronenoptischer Apochromat*. Zeitschrift für Naturforschung A, 1948. **3**(8-11): p. 544-545.
101. Chambers, A., *Modern vacuum physics*. 2004: CRC Press.
102. Matsuzaki, K., et al., *Fe₃O₄(1 1 1) thin films with bulk-like properties: growth and atomic characterization*. Journal of Physics D: Applied Physics, 2013. **46**(2): p. 022001.
103. Matsuzaki, K., Hosono, H., and Susaki, T., *Magnetotransport Properties across Verwey Transition in Fe₃O₄(111) Epitaxial Thin Films*. Applied Physics Express, 2013. **6**(7): p. 073009.
104. Nishikawa, S. and Kikuchi, S., *Diffraction of Cathode Rays by Calcite*. Nature, 1928. **122**: p. 726.
105. Davisson, C. and Germer, L.H., *Diffraction of Electrons by a Crystal of Nickel*. Physical Review, 1927. **30**(6): p. 705-740.
106. Williams, D.B.B.C., C. , *Transmission Electron Microscopy: A Textbook for Materials Science*.
107. Egerton, R.F., *Electron Energy-Loss Spectroscopy in the Electron Microscope*. 3rd ed. 2011: Springer.
108. Crewe, A.V., et al., *Electron Gun Using a Field Emission Source*. Review of Scientific Instruments, 1968. **39**(4): p. 576-583.
109. Nicolson, R., et al., *Electron Microscopy of Thin Crystals*, 1965, Butterworth, London.
110. Hawkes, P.W., *Advances in imaging and electron physics*. Vol. 128. 2003: Academic Press.
111. Pennycook, S.J., et al., *Aberration-corrected scanning transmission electron microscopy: from atomic imaging and analysis to solving energy problems*.

- Philosophical Transactions of the Royal Society of London A: Mathematical, Physical and Engineering Sciences, 2009. **367**(1903): p. 3709-3733.
112. Bragg, W.L. *The structure of some crystals as indicated by their diffraction of X-rays*. in *Proceedings of the Royal Society of London A: Mathematical, Physical and Engineering Sciences*. 1913. The Royal Society.
113. Cullity, B., *The elements of X-ray diffraction first ed.*, Addison, 1956, Wesley Publishing company, Inc, United State of America.
114. Crewe, A.V., Wall, J., and Welter, L.M., *A High-Resolution Scanning Transmission Electron Microscope*. *Journal of Applied Physics*, 1968. **39**(13): p. 5861-5868.
115. Crewe, A.V., Wall, J., and Langmore, J., *Visibility of Single Atoms*. *Science*, 1970. **168**(3937): p. 1338-1340.
116. Erni, R., et al., *Atomic-Resolution Imaging with a Sub-50-pm Electron Probe*. *Physical Review Letters*, 2009. **102**(9): p. 096101.
117. Knoll, M., *Charge potential and secondary emissions of electron irradiated bodies*. *Physikalische Zeitschrift*, 1935. **36**: p. 861-869.
118. Cowley, J.M., *Coherent interference effects in SIEM and CBED*. *Ultramicroscopy*, 1981. **7**(1): p. 19-26.
119. Ishizuka, K., *A practical approach for STEM image simulation based on the FFT multislice method*. *Ultramicroscopy*, 2002. **90**(2-3): p. 71-83.
120. Pennycook, S.J. and Jesson, D.E., *High-resolution Z-contrast imaging of crystals*. *Ultramicroscopy*, 1991. **37**(1-4): p. 14-38.
121. Nellist, P. and Pennycook, S., *The Principles and Interpretations of Annular Dark-Field Z-Contrast Imaging*. *Advances in Imaging and Electron Physics*, 2000. **113**: p. 148-204.
122. Krivanek, O.L., et al., *Atom-by-atom structural and chemical analysis by annular dark-field electron microscopy*. *Nature*, 2010. **464**(7288): p. 571-574.
123. Lari, L., et al., *An in-house developed annular bright field detection system*. *Journal of Physics: Conference Series*, 2014. **522**(1): p. 012016.
124. Haider, M., Uhlemann, S., and Zach, J., *Upper limits for the residual aberrations of a high-resolution aberration-corrected STEM*. *Ultramicroscopy*, 2000. **81**(3-4): p. 163-175.
125. Krivanek, O.L., et al., *An electron microscope for the aberration-corrected era*. *Ultramicroscopy*, 2008. **108**(3): p. 179-195.
126. Haider, M., et al., *Electron microscopy image enhanced*. *Nature*, 1998. **392**(6678): p. 768-769.
127. Haider, M., et al., *A spherical-aberration-corrected 200 kV transmission electron microscope*. *Ultramicroscopy*, 1998. **75**(1): p. 53-60.
128. Haider, M., et al. *Development of a spherical corrected 200 kV TEM: current state of this project and results obtained so far*. in *EUROPEAN JOURNAL OF CELL BIOLOGY*. 1997. WISSENSCHAFTLICHE VERLAG MBH BIRKENWALDSTRASSE 44, POSTFACH 10 10 61, 70009 STUTTGART, GERMANY.
129. Beck, V.D., *Hexapole spherical-aberration corrector*. *Optik*, 1979. **53**(4): p. 241-255.
130. Krivanek, O.L., Dellby, N., and Lupini, A.R., *Towards sub-Å electron beams*. *Ultramicroscopy*, 1999. **78**(1-4): p. 1-11.
131. Hawkes, P.W. and Kasper, E., *Principles of electron optics: Wave Optics*. Vol. 3. 1996: Academic Press.
132. Urban, K.W., *Studying atomic structures by aberration-corrected transmission electron microscopy*. *Science*, 2008. **321**(5888): p. 506-510.
133. Krivanek, O.L., et al., *Towards sub-0.5 Å electron beams*. *Ultramicroscopy*, 2003. **96**(3-4): p. 229-237.
134. Batson, P.E., Dellby, N., and Krivanek, O.L., *Sub-angstrom resolution using aberration corrected electron optics*. *Nature*, 2002. **418**(6898): p. 617-620.

135. Nellist, P.D., et al., *Direct Sub-Angstrom Imaging of a Crystal Lattice*. Science, 2004. **305**(5691): p. 1741.
136. Peng, L.M., Dudarev, S.L., and Whelan, J., *High Energy Electron Diffraction and Microscopy*. 2004: Oxford University Press.
137. Lari, L., et al., *Ferromagnetic InMnSb multi-phase films study by aberration-corrected (scanning) transmission electron microscopy*. Journal of Applied Physics, 2012. **111**(7): p. 07C311-3.
138. Li, J., Malis, T., and Dionne, S., *Recent advances in FIB-TEM specimen preparation techniques*. Materials Characterization, 2006. **57**(1): p. 64-70.
139. Srot, V., et al., *Influence of TEM specimen preparation on chemical composition of $Pb(Mg_{1/3}Nb_{2/3})O_3$ - $PbTiO_3$ single crystals*. Micron, 2014. **62**(0): p. 37-42.
140. Özdöl, V.B., Srot, V., and van Aken, P.A., *Sample Preparation Techniques for Transmission Electron Microscopy*, in *Handbook of Nanoscopy*. 2012, Wiley-VCH Verlag GmbH & Co. KGaA. p. 473-498.
141. Barna, Á., Pécz, B., and Menyhard, M., *TEM sample preparation by ion milling/amorphization*. Micron, 1999. **30**(3): p. 267-276.
142. Foner, S., *Vibrating Sample Magnetometer*. Review of Scientific Instruments, 1956. **27**(7): p. 548-548.
143. Evans, R.F., et al., *VAMPIRE: A code for atomistic spin model simulations of magnetic nanomaterials*. arXiv preprint arXiv:1310.6143, 2013.
144. Mitchell, D.R.G. and Schaffer, B., *Scripting-customised microscopy tools for Digital Micrograph™*. Ultramicroscopy, 2005. **103**(4): p. 319-332.
145. Schaffer, B., Grogger, W., and Kothleitner, G., *Automated spatial drift correction for EFTEM image series*. Ultramicroscopy, 2004. **102**(1): p. 27-36.
146. Schneider, C.A., Rasband, W.S., and Eliceiri, K.W., *NIH Image to ImageJ: 25 years of image analysis*. Nat Meth, 2012. **9**(7): p. 671-675.
147. Kirkland, E.J., Loane, R.F., and Silcox, J., *Simulation of annular dark field stem images using a modified multislice method*. Ultramicroscopy, 1987. **23**(1): p. 77-96.
148. Anstis, G.R., *The calculation of electron diffraction intensities by the multislice method*. Acta Crystallographica Section A, 1977. **33**(5): p. 844-846.
149. Goodman, P. and Moodie, A.F., *Numerical evaluations of N-beam wave functions in electron scattering by the multi-slice method*. Acta Crystallographica Section A, 1974. **30**(2): p. 280-290.
150. Self, P.G., et al., *Practical computation of amplitudes and phases in electron diffraction*. Ultramicroscopy, 1983. **11**(1): p. 35-52.
151. Cowley, J.M. and Moodie, A.F., *The scattering of electrons by atoms and crystals. I. A new theoretical approach*. Acta Crystallographica, 1957. **10**(10): p. 609-619.
152. Cowley, J.M. and Moodie, A.F., *The scattering of electrons by atoms and crystals. II. The effects of finite source size*. Acta Crystallographica, 1959. **12**(5): p. 353-359.
153. Cowley, J.M. and Moodie, A.F., *The scattering of electrons by atoms and crystals. III. Single-crystal diffraction patterns*. Acta Crystallographica, 1959. **12**(5): p. 360-367.
154. Ishizuka, K., *Multislice formula for inclined illumination*. Acta Crystallographica Section A, 1982. **38**(6): p. 773-779.
155. Ishizuka, K. and Uyeda, N., *A new theoretical and practical approach to the multislice method*. Acta Crystallographica Section A, 1977. **33**(5): p. 740-749.
156. Stadelmann, P.A., *EMS - A software package for electron-diffraction analysis and HREM image simulation in materials science*. Ultramicroscopy, 1987. **21**(2): p. 131-145.
157. Koch, C.T., *Determination of Core Structure Periodicity and Point Defect Density along dislocations*, 2002, Arizona State University.

158. Watanabe, K., et al., *Atomic-resolution annular dark-field STEM image calculations*. Physical Review B, 2001. **64**(11): p. 115432.
159. Wang, Z.L. and Cowley, J.M., *Simulating high-angle annular dark-field stem images including inelastic thermal diffuse scattering*. Ultramicroscopy, 1989. **31**(4): p. 437-453.
160. Wang, Z.L., *Thermal diffuse scattering in high-resolution electron holography*. Ultramicroscopy, 1993. **52**(3-4): p. 504-511.
161. Van Dyck, D., *Is the frozen phonon model adequate to describe inelastic phonon scattering?* Ultramicroscopy, 2009. **109**(6): p. 677-682.
162. Aveyard, R., et al., *Modeling Nanoscale Inhomogeneities for Quantitative HAADF STEM Imaging*. Physical Review Letters, 2014. **113**(7): p. 075501.
163. Rez, P., *Does phonon scattering give high-resolution images?* Ultramicroscopy, 1993. **52**(3-4): p. 260-266.
164. Rez, P., Humphreys, C.J., and Whelan, M.J., *The distribution of intensity in electron diffraction patterns due to phonon scattering*. Philosophical Magazine, 1977. **35**(1): p. 81-96.
165. Hohenberg, P. and Kohn, W., *Inhomogeneous Electron Gas*. Physical Review, 1964. **136**(3B): p. B864-B871.
166. Kohn, W. and Sham, L.J., *Self-Consistent Equations Including Exchange and Correlation Effects*. Physical Review, 1965. **140**(4A): p. A1133-A1138.
167. Kresse, G. and Furthmüller, J., *Efficiency of ab-initio total energy calculations for metals and semiconductors using a plane-wave basis set*. Computational Materials Science, 1996. **6**(1): p. 15-50.
168. Kresse, G. and Furthmüller, J., *Efficient iterative schemes for ab initio total-energy calculations using a plane-wave basis set*. Physical Review B, 1996. **54**(16): p. 11169-11186.
169. Dudarev, S.L., et al., *Electron-energy-loss spectra and the structural stability of nickel oxide: An LSDA+U study*. Physical Review B, 1998. **57**(3): p. 1505-1509.
170. Arras, R., Calmels, L., and Warot-Fonrose, B., *Electronic structure and interface states at the Fe₃O₄/MgO(100) interface*. Journal of Physics: Conference Series, 2010. **200**(7): p. 072008.
171. Bragg, W.L., *Crystal Structure*. Nature, 1920. **105**: p. 646-648.
172. McGuigan, L., et al., *In-plane magnetic anisotropies in Fe₃O₄ films on vicinal MgO(100)*. Physical Review B, 2008. **77**(17): p. 174424.
173. Bataille, A.M., et al., *Characterization of antiphase boundary network in Fe₃O₄(111) epitaxial thin films: Effect on anomalous magnetic behavior*. Physical Review B, 2006. **74**(15): p. 155438.
174. Eerenstein, W., Hibma, T., and Celotto, S., *Mechanism for superparamagnetic behavior in epitaxial Fe₃O₄ films*. Physical Review B, 2004. **70**(18): p. 184404.
175. Evans, R.F.L., et al., *Atomistic spin model simulations of magnetic nanomaterials*. Journal of Physics: Condensed Matter, 2014. **26**(10): p. 103202.
176. Gilks, D., et al., *Magnetism and magnetotransport in symmetry matched spinels: Fe₃O₄/MgAl₂O₄*. Journal of Applied Physics, 2013. **113**(17): p. 17B107-3.
177. Ram, P., et al., *Electrical and magnetic transport properties of Fe₃O₄ thin films on a GaAs(100) substrate*. Journal of Physics: Condensed Matter, 2007. **19**(48): p. 486212.
178. Watts, S.M., et al., *Transport characteristics of magnetite thin films grown onto GaAs substrates*. Journal of Applied Physics, 2004. **95**(11): p. 7465-7467.
179. Lazarov, V.K., et al., *Atomic and electronic structure of the Fe₃O₄(111)/MgO(111) model polar oxide interface*. Physical Review B, 2005. **72**(19): p. 195401.
180. Cynn, H., et al., *High-temperature Raman investigation of order-disorder behavior in the MgAl₂O₄ spinel*. Physical Review B, 1992. **45**(1): p. 500-502.
181. Gupta, R., et al., *Raman study of stoichiometric and Zn-doped Fe₃O₄*. Physical Review B, 2002. **65**(10): p. 104430.

182. Lübke, M., et al., *Identification of iron oxide phases in thin films grown on Al₂O₃(0001) by Raman spectroscopy and X-ray diffraction*. *Surface Science*, 2010. **604**(7–8): p. 679-685.
183. Zoppi, A., et al., *Al-for-Fe substitution in hematite: the effect of low Al concentrations in the Raman spectrum of Fe₂O₃*. *Journal of Raman Spectroscopy*, 2008. **39**(1): p. 40-46.
184. Chamritski, I. and Burns, G., *Infrared- and Raman-Active Phonons of Magnetite, Maghemite, and Hematite: A Computer Simulation and Spectroscopic Study*. *The Journal of Physical Chemistry B*, 2005. **109**(11): p. 4965-4968.
185. Pascal, T. and François, G., *Ab initio investigation of phonon modes in the MgAl₂O₄ spinel*. *Journal of Physics: Condensed Matter*, 2002. **14**(13): p. 3543.
186. Darken, L.S. and Gurry, R.W., *The System Iron—Oxygen. II. Equilibrium and Thermodynamics of Liquid Oxide and Other Phases*. *Journal of the American Chemical Society*, 1946. **68**(5): p. 798-816.
187. Gilks, D., et al., *A STEM study of twin defects in Fe₃O₄(111)/YZO(111)*. *Journal of Physics: Conference Series*, 2014. **522**(1): p. 012036.
188. Thompson, S.M., et al., *Using the infrared magnetorefractive effect to compare the magnetoresistance in (100) and (111) oriented Fe₃O₄ films*. *Journal of Applied Physics*, 2010. **107**(9): p. 09B102-3.
189. Daneu, N., et al., *Structure and chemistry of (111) twin boundaries in MgAl₂O₄ spinel crystals from Mogok*. *Physics and Chemistry of Minerals*, 2007. **34**(4): p. 233-247.
190. Cahn, R.W., *Twinned crystals*. *Advances in Physics*, 1954. **3**(12): p. 363-445.
191. Yang, Y., et al., *Multitwinned Spinel Nanowires by Assembly of Nanobricks via Oriented Attachment: A Case Study of Zn₂TiO₄*. *ACS Nano*, 2009. **3**(3): p. 555-562.
192. Yan, L., et al., *Nanogrowth twins and abnormal magnetic behavior in CoFe₂O₄ epitaxial thin films*. *Journal of Applied Physics*, 2008. **104**(12): p. 123910.
193. Mohd Jani, J., et al., *A review of shape memory alloy research, applications and opportunities*. *Materials & Design*, 2014. **56**(0): p. 1078-1113.
194. Coll, M., et al., *Low Temperature Stabilization of Nanoscale Epitaxial Spinel Ferrite Thin Films by Atomic Layer Deposition*. *Advanced Functional Materials*, 2014. **24**(34): p. 5368-5374.
195. Kim, Y.-M., et al., *Direct observation of ferroelectric field effect and vacancy-controlled screening at the BiFeO₃/La_xSr_{1-x}MnO₃ interface*. *Nat Mater*, 2014. **13**: p. 1019-1025.
196. Parkin, S.S.P., et al., *Giant tunnelling magnetoresistance at room temperature with MgO(100) tunnel barriers*. *Nat Mater*, 2004. **3**(12): p. 862-867.
197. Paul, M., et al., *Thermodynamic stability and atomic and electronic structure of reduced Fe₃O₄(111) single-crystal surfaces*. *Physical Review B*, 2007. **76**(7): p. 075412.
198. Sader, K., et al., *Smart acquisition EELS*. *Ultramicroscopy*, 2010. **110**(8): p. 998-1003.
199. Colliex, C., Manoubi, T., and Ortiz, C., *Electron-energy-loss-spectroscopy near-edge fine structures in the iron-oxygen system*. *Physical Review B*, 1991. **44**(20): p. 11402-11411.
200. Ramesh, R. and Schlom, D.G., *Whither Oxide Electronics?* *MRS Bulletin*, 2008. **33**(11): p. 1006-1014.
201. Martin, L.W., et al., *Multiferroics and magnetoelectrics: thin films and nanostructures*. *Journal of Physics: Condensed Matter*, 2008. **20**(43): p. 434220.
202. Mannhart, J. and Schlom, D.G., *Oxide Interfaces—An Opportunity for Electronics*. *Science*, 2010. **327**(5973): p. 1607-1611.
203. Dagotto, E., *When Oxides Meet Face to Face*. *Science*, 2007. **318**(5853): p. 1076-1077.

204. Blamire, M.G., et al., *The Materials Science of Functional Oxide Thin Films*. Advanced Materials, 2009. **21**(38-39): p. 3827-3839.
205. Robertson, J., *Band offsets of wide-band-gap oxides and implications for future electronic devices*. Journal of Vacuum Science & Technology B, 2000. **18**(3): p. 1785-1791.
206. Yamane, H., et al., *Y-Ba-Cu-O superconducting films prepared on SrTiO₃ substrates by chemical vapor deposition*. Applied Physics Letters, 1988. **53**(16): p. 1548-1550.
207. Li, M., et al., *A family of oxide ion conductors based on the ferroelectric perovskite Na_{0.5}Bi_{0.5}TiO₃*. Nat Mater, 2014. **13**(1): p. 31-35.
208. Ramos, A.V., et al., *Artificial antiphase boundary at the interface of ferrimagnetic spinel bilayers*. Physical Review B, 2009. **79**(1): p. 014401.
209. Sugiyama, I., et al., *Ferromagnetic dislocations in antiferromagnetic NiO*. Nat Nanotechnol, 2013. **8**(4): p. 266-70.
210. Ghosh, K., et al., *Positive giant magnetoresistance in a Fe₃O₄/SrTiO₃/La_{0.7}Sr_{0.3}MnO₃ heterostructure*. Applied Physics Letters, 1998. **73**(5): p. 689-691.
211. Zheng, J.G., et al., *Epitaxial Fe₃O₄ on SrTiO₃ characterized by transmission electron microscopy*. Journal of Vacuum Science & Technology B, 2007. **25**(4): p. 1520-1523.
212. Kohn, A., et al., *The structure of sputter-deposited Co₂MnSi thin films deposited on GaAs(001)*. Journal of Applied Physics, 2007. **101**(2): p. 023915.
213. Hashimoto, S., Poulsen, F.W., and Mogensen, M., *Conductivity of SrTiO₃ based oxides in the reducing atmosphere at high temperature*. Journal of Alloys and Compounds, 2007. **439**(1-2): p. 232-236.
214. Guo, X.G., et al., *Electronic band structure of Nb doped SrTiO₃ from first principles calculation*. Physics Letters A, 2003. **317**(5-6): p. 501-506.
215. Biswas, A., et al., *Universal Ti-rich termination of atomically flat SrTiO₃ (001), (110), and (111) surfaces*. Applied Physics Letters, 2011. **98**(5): p. 051904.
216. Perdew, J.P., Burke, K., and Ernzerhof, M., *Generalized Gradient Approximation Made Simple [Phys. Rev. Lett. 77, 3865 (1996)]*. Physical Review Letters, 1997. **78**(7): p. 1396-1396.